CBrAVIC2017

Congresso Brasileiro de Aplicações de Vácuo na Indústria e na Ciência

XXXVIII Congresso Brasileiro de Aplicações à Vacuo na Indústria e na Ciência (CBRAVIC)

III Workshop de Tratamento e Modificação de Superfícies

21 a 24 de agosto - São José dos Campos - SP

LIVRO DE RESUMOS

INPE

Sociedade Brasileira de Vácuo

MINISTÉRIO DA CIÊNCIA, TECNOLOGIA, INOVAÇÕES E COMUNICAÇÕES

BRASIL GOVERNO FEDERAL

XXXVIII Congresso Brasileiro de Vácuo na Indústria e na Ciência
III Workshop de Tratamento e Modificação de Superfícies

É com grande satisfação que anunciamos a 38ª edição do Congresso Brasileiro de Vácuo na Indústria e na Ciência – CBRAVIC, a ser realizado nas dependências do Instituto Nacional de Pesquisas Espaciais (INPE), em São José dos Campos, entre os dias 21 a 25 de agosto de 2017, mantendo a tradição do Instituto em sediar renomados eventos científicos.

A comissão organizadora envidará todos os esforços para propiciar um ambiente oportuno para ricas discussões e debates entre pesquisadores, professores e estudantes de pós-graduação e de graduação, público alvo deste evento, contando com excelente infraestrutura de auditórios e salões para a realização de palestras convidadas, palestras técnicas de empresas expositoras, sessões orais, apresentação de pôsteres e para exposição de empresas. Ademais, o Congresso contará com minicursos, abordando temas relevantes nas áreas de pesquisa e desenvolvimento em Ciência e Tecnologia de Vácuo, visita técnica ao Laboratório de Integração e Testes (LIT/INPE) e eventos sociais.

Palestrantes nacionais e internacionais apresentarão os últimos desenvolvimentos científicos e tendências futuras, englobando as áreas de Engenharias, Física, Química, Ciência dos Materiais e assuntos interdisciplinares.

É nosso maior objetivo que o CBRAVIC ofereça a oportunidade a seus participantes de apresentar e discutir seus trabalhos e que seja instrumento para estimular novas e frutíferas colaborações.

Esperamos encontrá-lo em breve em São José dos Campos, uma cidade rica em parques e atividades culturais e com povo muito hospitaleiro.

Dr. Rogério Moraes de Oliveira
Presidente do CBRAVIC2017

Prof. Dr. Rogério Pinto Mota
Presidente da SBV

TEMAS DO CONGRESSO

a. Aplicações de Vácuo na Indústria;

b. Biomateriais;

c. Ciência Atômica e Molecular;

d. Ciência e Tecnologia dos Materiais;

e. Ciência e Tecnologia de Plasmas;

f. Ciência e Tecnologia de Sensores e Dispositivos;

g. Ciência e Tecnologia de Vácuo;

h. Ciência e Tecnologia Aeroespacial;

i. Energia: Fontes renováveis e tecnologia;

j. Instrumentação e Metrologia;

k. Nanociência, Nanotecnologia e Nanomateriais;

l. Superfícies, Interfaces e Filmes Finos;

m. Tratamento e Modificações de Superfícies.

n. Semicondutores

TEMAS DOS MINICURSOS

1. Plasma Assisted Surface Modification

2. Filmes Finos: Deposição, Caracterização e Aplicações

3. Ciência e Tecnologia do Vácuo

4. Aprendizagem Ativa: Uma Abordagem que Faz Pensar

PROGRAMAÇÃO

	Segunda-feira 21/08/17	Terça-feira 22/08/17	Quarta-feira 23/08/17	Quinta-feira 24/08/17	Sexta-feira 25/08/17
8h30		Abertura da secretaria	Palestra convidada **Ronny Brandenburg**	Palestra **José Alexandre Diniz**	Programação Especial para alunos do ensino fundamental e médio
9h15		**9h00** Abertura oficial	Apresentação oral **ID 63**	Apresentação oral **ID 116**	
9h35		**9h30** Palestra convidada **Odylio Denys Aguiar**	Apresentação oral **ID 180**	Apresentação oral **ID 127**	
9h55			Apresentação oral **ID 156**	Apresentação oral **ID 37**	
10h15		Coffee break	Coffee break	Coffee break	
10h45		Apresentação oral **ID 136**	Apresentação oral **ID 114**	Apresentação oral **ID 179**	
11h05		Apresentação oral **ID 73**	Apresentação oral **ID 78**	Apresentação oral **ID 147**	
11h25		Apresentação oral **ID 167**	Apresentação oral **ID 31**	Apresentação oral **ID 25**	
11h45		Palestra convidada **Ian Brown**	Palestra convidada **Luc Pichon**	Palestra convidada **Maria Cecilia Salvadori**	
12h30		Almoço	Almoço	Almoço	Almoço
14h00		Palestra convidada **Alexandre Tallaire**	Palestra convidada **Michael Stueber**	Palestra **José Sérgio Almeida**	Programação Especial para alunos do ensino fundamental e médio
14h45		Apresentação oral **ID 177**	Apresentação oral **ID 111**	Visita no LIT	
15h05		Apresentação oral **ID 170**	Apresentação oral **ID 120**		
15h25		Apresentação oral **ID 140**	Apresentação oral **ID 107**		
15h45		Coffee break	Coffee break	Coffee break	
16h00		Sessão de pôster 1	**16h15** Assembleia e eleição SBV	Sessão de pôster 2	
18h00	Abertura da secretaria e Coquetel de Recepção				
20h00			Jantar de Confraternização		

PALESTRAS CONVIDADAS

DATA	PALESTRANTE	TÍTULO
22/08 9h30	**Odylio Denys Aguiar**	LIGO and its impressive vacuum system
22/08 11h45	**Fiorenza Fanelli**	Surface engineering and functionalization at atmospheric pressure using dielectric barrier discharges
22/08 14h00	**Alexandre Tallaire**	Controlling defects during the growth of large size diamond single crystals by plasma assisted chemical vapour deposition
23/08 8h30	**Ronny Brandenburg**	Dielectric barrier discharges: known since 160 years, but still a lot of potential for innovations
23/08 11h45	**Luc Pichon**	Understanding the behavior of nickel-based superalloys during low temperature plasma immersion nitriding
23/08 14h00	**Michael Stueber**	DLC and carbon based nanostructured composite coatings – an overview of thin film design and process approaches

		towards high performance engineering applications
24/08 8h30	**José Alexandre Diniz**	Ultra-thin and thin films for nano and micro technologies
24/08 11h45	**Maria Cecilia Salvadori**	Surface modification by ion implantation and plasma treatment
24/08 14h00	**José Sérgio Almeida**	INPE-LIT thermal-vacuum testing facilities for spacecraft qualification

APRESENTAÇÕES ORAIS

DATA	PALESTRANTE	TÍTULO
22/08 10h45	**Aline Capella de Oliveira**	ID136: 300 maraging steel welded by plasma process
22/08 11h05	**Silvia Sizuka Oishi**	ID73: Deposition of micro and ultrananocrystalline diamond on reticulated vitreous carbon for use in the nitrate electroreduction
22/08 11h25	**Mauricio Antonio Algatti**	ID167: Optical absorption spectra of vanadium modified barium zirconium titanate and zirconium-doped calcium copper titanate powders
22/08 14h45	**Milena Kowalczuk Manosso Amorim**	ID177: Optical and chemical characterization of a-C:H:Si:O:Cl thin films obtained by plasma enhanced chemical vapor deposition
22/08 15h05	**Nilson C. Cruz**	ID170: Growth of hydroxyapatite coatings on tantalum by plasma electrolytic oxidation
22/08 15h25	**Vladimir Jesus Trava Airoldi**	ID140: An overview of modified PECVD technique for DLC growth and its new areas of research and application
23/08 9h15	**Gelson Biscaia de Souza**	ID63: H-Implantation changes stoichiometry and hydroxylation states of nitride titanium surfaces
23/08 9h35	**José Leonardo Ferreira**	ID180: Study Development and Qualification Tests of Permanent Magnet Hall Thrusters for Future Brazilian Space Missions
23/08 9h55	**Adriana de Oliveira Delgado Silva**	ID156: Deposition of HMDSO-based films on etched cellulose for creation of superhydrophobic surfaces
23/08 10h45	**Deivison Daros Paim**	ID114: The effects of cycling the atmosphere nitriding ability on the structure of the nitride region of an AISI 1015 steel plasma nitrided
23/08 11h05	**Ing Hwie Tan**	ID78: Construction of a photoelectron beam for calibration of space plasma electrostatic analyzers
23/08 11h25	**Konstantin Georgiev Kostov**	ID31: Development of cold atmospheric pressure plasmas jets for surface modification and medical applications
23/08 14h45	**Anaftália Felismino Moraes**	ID111: Partially tri-sulfated chitosan films using sodium sulfate salt and cytotoxicity evaluation on human neutrophils
23/08 15h05	**Elidiane Cipriano Rangel da Cruz**	ID120: Tailoring surface properties of polyamide 6 by plasma processes
24/08 9h15	**Pedro Augusto de Paula Nascente**	ID 116: Influence of the 316L stainless steel substrate roughness on the magnetron sputter deposition of Ti-Nb coatings

24/08 9h35	**Rafael Parra Ribeiro**	ID127: Effect of plasma treatment on the corrosion resistance of carbon steel
24/08 9h55	**Adriano Gonçalvez dos Reis**	ID37: Microstructural evaluation of maraging 300 steel laser treated
24/08 10h45	**Camili Ambrosio**	ID179: High vacuum brazing and microstructural analysis of junction CuAG/Cu with SN100C alloy
24/08 11h05	**Evaldo José Corat**	ID147: CVD diamond and carbon nanotubes nanocomposites production and applications
24/08 11h25	**Mario Ueda**	ID25: Experiments on high current, low voltage, hollow cathode discharges for plasma immersion ion implantation (and deposition) inside Ti6Al4V 1.1 cmØ tube

APRESENTAÇÕES DE PÔSTERES

ID	TÍTULO
4	INCREASE OF ELECTRICAL CONDUCTIVITY BY METAL DEPOSITION IN BRAZILIAN ACTIVATED CARBON FELT
6	ELECTROCHEMICAL AND STRUCTURAL CHARACTERIZATION OF AA5052 ALUMINIUM ALLOY TREATED BY PLASMA ANODIZATION USING BORAX ELECTROLYTE
6_1	CORROSION BEHAVIOR OF AA5052 ALUMINIUM ALLOY TREATED BY PLASMA ELECTROLYTIC OXIDATION IN SILICATE AND PHOSPHATE-CONTAINING SOLUTION
7	THERMAL STABILITY OF THE γN PHASE PRODUCED IN SUPERDUPLEX STAINLESS STEEL THROUGH PLASMA BASED NITRIDING
11	Influence of zirconia nanoparticles suspensions on tribological properties of Diamond Like Carbon films produced by DC-PECVD.
11_1	INFLUENCE OF THERMALLY FUNCIONALIZED NANODIAMOND SUSPENSIONS ON HYDROGEN CONTENT OF DIAMOND LIKE CARBON FILMS PRODUCED BY DC-PECVD WITH ACTIVE SCREEN
13	COMPARATIVE STUDY OF SHIELD MASK TECHNIQUES KAPTON® TAPE AND TIO2 FOR THIN FILM THICKNESS MEASUREMENT
13_1	THIN FILM THICKNESS MEASUREMENT USING TAPER SECTIONING METHOD
16	DEVELOPMENT OF A HYBRID CORONA-DIELECTRIC BARRIER DISCHARGE FOR SURFACE PROPERTIES MODIFICATION OF TEXTILES
19	LANGMUIR PROBE DIAGNOSTICS OF A DC GLOW DISCHARGE USED AT INPE
26	Structural and morphological characterization of the foam powder
29	Scratch and corrosion morphology studies in NiTi 60 and Ti6Al4V alloys with coating diamond-like carbon after immersed in synthetic urine
33	AA7050-T7451 aluminum alloy characterization: microstructure and fatigue behavior
34	COMPARISON OF NITROGEN AND ARGON PLASMA IMMERSION ION IMPLANTATION (AND DEPOSITION) INSIDE AND OUTSIDE STAINLESS STEEL 304 TUBES
38	STUDY OF THE RELATIONSHIP BETWEEN PLASTIC DEFORMATION AND CORROSION RESISTANCE
39	Obtaining niobium nitride for reentrant niobium cavities via plasma Immersion Implantation and HiPIMS
40	Investigation of wc-co hardmetal surfaces prepared by boriding processes
41	TIO2 FILMS OBTAINED FROM HEAT TREATMENT OF TI FILMS DEPOSITED ON SODA-LIME GLASS SUBSTRATE
43	TREATMENT OF MAIZE BIOMASS SURFACE PLASMA FOR LIGNIN BREAKING
44	TRIBOLOGICAL BEHAVIOR OF NIOBIUM TREATED BY HIGH TEMPERATURE

	NITROGEN PLASMA BASED ION IMPLANTATION
45	MECHANICAL CHARACTARIZATION OF NITRIDE LAYERS ON NITI SUBSTRATE
46	INFLUENCES OF PLASMA JET PARAMETERS ON SEEDS TREATMENT
49	REAL AND VIRTUAL LEAKS IN VACUUM SYSTEMS
54	SO3 formation from the irradiation of SO2 ice by X-rays: Experiments and investigations in theoretical Chemistry
55	316L STEEL TRIBOCORROSION PROPERTIES WITH SIC
56	DEVELOPMENT OF A NOVEL THERMAL PLASMA PROCESS FOR THE DEPOSITION OF HIGH PERFORMANCE OVERLAY COATINGS
57	EFFECT OF NITROGEN PLASMA IMMERSION ION IMPLANTATION ON SURFACE DISCHARGE BREAKDOWN VOLTAGE OF ALUMINIZED POLYIMIDE
58	HOLLOW CATHODE DESIGN FOR A BRAZILIAN ION THRUSTER
59	Electrical properties of TiOx thin films deposited by triode magnetron sputtering for application as transparent and conductive oxide
60	FRICCION AND WEAR BEHAVIOR OF TI-W PVD COATING ON STEEL AISI 316L
60_1	INFLUENCE OF TiW INTERLAYER IN ADHESION OF THE DLC COATINGS ONTO AISI 316L STAINLESS STEEL
62	SURFACE CHARACTERIZATION OF HMDSO FILMS DEPOSITED BY ATMOSPHERIC PRESSURE PLASMA JET ON SAE 1020 STEEL
65	EVALUATION OF THE PHYSICAL-MECHANICAL PROPERTIES OF CEMENT-BASED COMPOSITES REINFORCED WITH SURFACE-MODIFIED CELLULOSE PULP
67	HYPERSPHERICAL COORDINATE POTENTIAL ENERGY SURFACE FOR THE Rg3 COMPLEX, WITH Rg=Ne, Ar, Kr AND Xe
67_1	POSSIBLE PATHWAYS IN THE FORMATION OF FORMYL RADICAL HCO
69	EVALUATION OF Cr-N THIN FILMS DEPOSITED BY REACTIVE PLASMA IMMERSION ION IMPLANTATION AND DEPOSITION (PIII&D) AND HOLLOW CATHODE DISCHARGE
72	PRODUCTION OF CARBON FIBER/REDUCED GRAPHENE OXIDE/NICKEL OXIDE COMPOSITE FOR ELECTROCHEMICAL APPLICATIONS
72_1	GROWTH AND CHARACTERIZATION OF BDD/CF1000 AND BDD/CF2000 MODIFIED WITH TIO2 TO IMPROVE THEIR PHOTOCATALYTIC RESPONSES
74	DEVELOPMENT OF A REACTOR FOR MEASUREMENTS OF PHOTOCATALYTIC ACTIVITY OF THIN FILMS
76	MORPHOLOGICAL CHARACTERIZATION OF S-DOPED TiO2 THIN FILMS
77	MORPHOLOGY OF THE PLASMA NITROCARBURIZED LAYER ON DIN 100Cr6 STEEL
79	APPROACH TO DEPOSITION OF FILMS OBTAINED FROM HYDROCARBONS AND HEXAMETHYLDISILOXANE BY PLASMA
81	USE OF LOW COST SENSORS ARRAY AND SMALL DEVICES NOT ONLY ON RESEARCH BUT ALSO FOR TEACHING
82	ACTIVE SCREEN PLASMA SYSTEM: FLOATING POTENTIAL AS A FUNCTION OF SCREEN OPEN AREA
83	MODELING AND EXPERIMENTAL ANALYSIS OF THE SUBSTRATE TEMPERATURE INFLUENCE ON THE REACTIVE MAGNETRON SPUTTER DEPOSITION
84	STUDY OF THE REDISTRIBUTION OF SOLUTE IN EUTECTIC LEAD-TIN ALLOYS SOLIDIFIED UNDER HIGH ACCELERATION
85	EXPERIMENTAL DETERMINATION OF THE PERMITTIVITY AND PERMEABILITY OF AN ARRAY OF SPLIT-RING RESONATORS IN A X-BAND WAVEGUIDE
86	Carbon fiber preparation for metal matrix application
87	EFFECT IN THE CREEP BEHAVIOR OF Ti-6Al-4V ALLOY BY THE MODIFICATION OF THERMAL BARRIER COATING WITH LASER REMELTING TREATMENT
89	WETTABILITY AND SURFACE ENERGY OF TiOx FILMS DEPOSITED BY REACTIVE MAGNETRON SPUTTERING
90	INFLUENCE OF THE SYNTHESIS METHOD ON THE MORPHOLOGICAL AND ELECTROCHEMICAL PROPERTIES OF PANI / CARBON FIBER COMPOSITE

91	EFFECT OF STRESS CONCENTRATIONS ON THE FATIGUE STRENGTH OF AISI 4140 STEEL USED IN OIL AND GAS COMPANY
95	CARBON FIBERS FUNCTIONALIZATION THROUGH N2-H2 PLASMA AS A PRETREATMENT FOR POLYANILINE POLYMERIZATION
96	PROJECT, MODELING AND CONSTRUCTION OF VACUUM OVEN WITH CONTROLLED TEMPERATURE
101	INFLUENCE OF THE SILICON INTERLAYER DEPOSITION PROCESS IN THE ADHESION OF THE DLC COATINGS DEPOSITED ON NITRIDED MARTESNITIC STAINLESS STEEL
102	POROSITY AND MORPHOLOGY OF HVOF SPRAYED WC-12CO-4CR COATINGS USING DIGITAL IMAGE PROCESSING
103	THEORETICAL STUDIES OF THE REACTIONS OF H2 + CN: COMPETITION BETWEEN H-ABSTRACTION IN H + HCN/HNC CHANNELS.
103_1	THEORETICAL STUDY OF THE KINETICS AND MECHANISM OF THE CH3CH2OH + H2O REACTION
104	POTENTIAL ENERGY SURFACES FOR INTERACTIONS OF H2...HX AND H2...X2 SYSTEMS, USING A (HYPER)SPHERICAL HARMONICS REPRESENTATION
105	REACTION RATE OF H+HOC = H2+CO
108	HFCVD DIAMOND PARAMETERS GROWTED ON TOOL STEEL APLAING VANADIUM CARBIDE INTERMEDIATE LAYER
110	GROWTH OF DLC FILM IN A METALLIC TUBE WITH HIGH ASPECT RATIO
112	TI-6AL-4V ALLOY FATIGUE BEHAVIOR SUBJECTED TO SHOT PEENING AND PLASMA IMMERSION ION IMPLATATION (PIII) TREATMENTS
113	THE INFLUENCE OF CONTROLLED THERMAL OXIDATION ON THE MORPHOLOGY AND PHOTOLUMINESCENCE OF POROUS SILICON
117	MICROHARDNESS ANALYSIS NI NI35TI50CU15 BY POWDER METALLURGY MODIFIED BY PLASMA IMMERSION ION IMPLANTATION TECHNIQUE
119	COMPOSITE FILMS OF BARIUM-STRONTIUM TITANATE / SILVER DEPOSITED BY RF SPUTTERING: NEW SYSTEM TEST
122	ELECTROCHEMICAL BEHAVIOR OF HMDSO POLYMER FILM DEPOSITED BY ATMOSPHERIC PRESSURE PLASMA JET
123	Effects of Plasma Immersion Ion Implantation On Fatigue Properties of Titanium Alloy Surfaces
124	SiC/Cr THIN FILMS DEPOSITED BY HiPIMS ON Ti-6Al-4V USED AS PROTECTIVE COATING IN CREEP TESTS
128	ATMOSPHERIC PLASMA TREATMENT FOR PCB ADHESION ENHANCEMENT
130	STUDY OF ALUMINOS REFRACTORY MICROSTRUCTURE AFTER USE IN RACE CHANNEL
132	PLASMA POLYMERIZATION OF AMINE-CONTAINING THIN FILMS IN LOW PRESSURE ATMOSPHERES OF ETHYLENEDIAMINE (EDA) / ACETYLENE (C2H2) MIXTURE
135	DRY TRIBOLOGICAL BEHAVIOR OF LASER TEXTURED 4340 STEEL
138	RELATION BETWEEN SUBSTRATE FLOATING POTENTIAL AND GRID-TO-TARGET DISTANCE IN GRID ASSISTED MAGNETRON SPUTTERING
139	PRODUCTION OF LOW COST COMPOSITE BASED IN ATIVATED CARBON FIBER PARTICULATES APPLIED IN RADIATION ABSORBING MATERIALS IN X BAND FREQUENCY
139_1	RADAR ABSORPTION MATERIAL BY POROUS CARBON PARTICULATE IN POLYMERIC MATRIX
141	CRYOGENIC UHV FAST-ENTRY CHAMBERS AT THE BRAZILIAN SYNCHROTRON LIGHT LABORATORY/LNLS
142	PLASMA POLYMERIZED HMDSO THIN FILMS INCORPORATED WITH CHLOREXIDINE FOR DRUG RELEASE
143	STRUCTURAL AND MORPHOLOGICAL CHARACTERIZATION OF DLC FILMS DEPOSITED BY PLASMA IMMERSION ION IMPLANTATION AND DEPOSITION (PIII&D) WITH MAGNETIC FIELD INSIDE TUBES

145	DEPOSITION AND CHARACTERIZATION OF THIN FILMS BY ATMOSPHERIC PLASMA MICRO DISCHARGE
148	WEAR RESISTANCE ANALYSIS NI50,8TI SMA BY POWDER METALLURGY MODIFIED BY PLASMA IMMERSION ION IMPLANTATION TECHNIQUE
151	CARBON NANOTUBE FUNCTIONALIZATION BY RF PLASMA
152	DYNAMIC FRICTION COEFFICIENT MEASUREMENT AND CONSTRUCTION OF A TRIBOMETER ROTARY WITH AGAINST SPHERICAL BODY
155	CORROSION MORPHOLOGY STUDY OF DENTAL RESINS IMMERSED IN REFRIGERANTS COLA TYPE
160	ALOE VERA INCORPORATION INTO ELECTROSPUN NANOFIBERS
162	SYNTHESIS OF N-DOPED TiO2 THIN FILMS BY MOCVD AND ITS CHARACTERIZATION
164	CHARATERISTICS OF DOUBLE GAS INJECTION NEEDLE MICRO DISCHARGES
164_1	INTEGRATED LIGHT EMISSION STUDY ON ATMOSPHERIC NEEDLE PLASMA DISCHARGES
165	SILICON INTERLAYER INFLUENCE IN ADHESION OF DLC FILM DEPOSITED ON AA 7075 SUBSTRATE USING A MODIFIED PULSED-DC PECVD TECHNIQUE
169	THE EFFECT OF VOLTAGE AND TIME ON THE FABRICATION OF TIO2 NANOTUBE ON TI-30TA ALLOY BY ANODIC OXIDATION
171	EFFECT OF THE TEMPERATURE ON CORROSION BEHAVIOR OF PLASMA-ANODIZED ALUMINIUM ALLOY
175	ANALYSIS OF GRANITE POWDER USING SEM
176	INFLUENCE OF THE PROCESS AGENT ON THE HIGH ENERGY OF 7075T6 ALUMINUM ALLOY CHIPS.
184	A fully automated bakeout system for the new SIRIUS synchrotron

ORGANIZAÇÃO

Comitê Organizador
Rogério de Moraes Oliveira (Presidente)
Carina Barros Mello (Vice-Presidente)
Nazir Monteiro dos Santos
Mario Ueda
André Ricardo Marcondes

Comitê Científico
Adriano Gonçalves dos Reis - UNESP SJC
Aline Capella de Oliveira - UNIFESP SJC
Álvaro José Damião - IEAv
Antonio Renato Bigansolli - UFRRJ
Argemiro Soares da Silva Sobrinho – ITA
Carina Barros Mello - INPE
Carlos Roberto Grandini - UNESP Bauru
Clodomiro Alves Júnior - UFERSA
Danieli Aparecida Pereira Reis - UNIFESP SJC
Deborah C. Ribeiro dos Santos - FATEC Pinda
Elidiane Cipriano Rangel - UNESP Sorocaba
Evaldo José Corat - INPE
Fernando L. Campos Carvalho - UNESP SJC
Gelson B. de Souza - UEPG
Francisco T. Degasperi – CEETEPS/FATEC SP
Gilberto Petraconi Filho - ITA
Graziela da Silva Savonov - INPE
Ing Hwie Tan - INPE
José Eduardo May - INPE
Konstantin G. Kostov - UNESP Guaratinguetá
Leide Lili G. Silva Kostov - FATEC Pinda
Luís César Fontana - UDESC
Marco Antonio Ramirez Ramos - UNIVAP
Maria Lúcia Pereira da Silva - USP
Maria Margareth da Silva – ITA
Mario Ueda - INPE
Mauricio A. Algatti - UNESP Guaratinguetá
Milton Eiji Kayama - UNESP Guaratinguetá
Nazir Monteiro dos Santos - INPE
Nilson Cristino Cruz - UNESP Sorocaba
Pedro Augusto de Paula Nascente - UFSCar
Rodrigo Sávio Pessoa – UNIVAP
Rogério de Moraes Oliveira - INPE
Rogério Pinto Mota - UNESP Guaratinguetá
Vladimir Jesus Trava-Airoldi - INPE
Wisley Falco Sales - UFU

Comitê Acadêmico
Ana Claudia Pinheiro da Silva Cruz - Aluna PG INPE
Carla da Silva - Aluna PG INPE
Eliene Nogueira de Camargo - Aluna PG ITA
Fabricio Iusuti de Medeiros - Aluno PG INPE
Lilian Hoshida - Aluna PG INPE
Michel Felipe Lima de Araújo - Aluno PG INPE
Plinio Ivo Gama Tenório - Aluno PG INPE
Raquel Alvim de Figueiredo Mansur - Aluna PG IEAV
Thayara Ceregatti - Aluna PG UDESC

Diretoria da Sociedade Brasileira Vácuo – SBV
Presidente: Prof. Rogério Pinto Mota
1° Vice-Presidente: Prof. Alvaro José Damião
2° Vice-Presidente: Angelo L. Gobbi
Diretor Cultural: Prof. Carlos Roberto Grandini
Diretora Científico: Prof. Maria Lúcia Pereirra da Silva
1° Secretário: Prof. Francisco Tadeu Degasperi
2° Secretário: Luciano Rugério Silva
1° Tesoureira: Prof. Nazir Monteiro dos Santos
2° Tesoureiro: Prof. Konstantin Georgiev Kostov

PATROCINADORES

APOIO

REALIZAÇÃO

Sociedade Brasileira de Vácuo

LIGO AND ITS IMPRESSIVE VACUUM SYSTEM

Odylio Denys Aguiar
Divisão de Astrofísica - DAS, Coordenação Geral de Ciências Espaciais e Atmosféricas - CEA, Instituto Nacional de Pesquisas Espaciais - INPE

LIGO's advanced twin detectors performed a third detection of gravitational waves on January 4, 2017, at 8:11 am: 58.6 Brazilian summer time, with a signal-to-noise ratio of the order of 13 and a false-alarm less than 1 in 70,000 years, demonstrating that a new window in astronomy has been firmly opened. As in the case of the first two detections, gravitational waves were generated when two black holes collided to form a larger black hole. The new black hole, formed by the fusion of two black holes with masses of ~ 31.2 M⊙ and ~ 19.4 M⊙, respectively, has a mass of about 49 times that of our Sun. This fills a gap between the masses of the two previously formed black holes detected by the LIGO, with solar masses of 62 (first detection) and 21 (second detection), confirming a population of black holes with masses larger than those observed in binary X-ray emitting systems. The recent detection appears to be the furthest from Earth, with black holes located about 3 billion light-years away (redshift ~ 0.18) (black holes on the first and second detection were located at 1.3 e 1.4 billion light-years away, respectively). In the GW170104 event detected, at least one of the black holes appears to be out of alignment compared to the orbital motion, which favors the model that these black holes have latched together late into a dense star cluster. No evidence of wave dispersion was found, and a maximum limit was established for the graviton mass ~ 36% less than the threshold given by previous detections. In all cases, it has been found that GW170104 is consistent with general relativity [1] [2] [3].

This fantastic scientific achievement has only been achieved thanks to the impressive performance of the Advanced LIGO detectors, which circulate high-power laser beams (hundreds of kWatts) over 16 km of arms, several times round trips, thanks to a vacuum of the order of 10^{-9} Torr, maintained in a total volume of about 18 thousand cubic meters [4]. “The world's largest precision optical instruments and the world's second-largest vacuum systems, LIGO is a marvel of engineering and human ingenuity” [5]. “It took 1100 hours (40 days) of constant pumpdown to evacuate the chambers to their optimal operating pressure. “[6] Maintaining this vacuum requires sophisticated monitors and controls as well as the constant operation of ion pumps that extract molecules outgassing from the tubes and other structures inside the vacuum systems. Stray water molecules are also removed by continuously operating liquid nitrogen cryopumps”[6]. A strict control of the materials and their quantities that can be used in the LIGO guarantee the maintenance of the vacuum necessary for the performance of the detectors [7]. LIGO is one of the greatest examples of the use of man-made artificial vacuum for the development of sciences. This presentation will cover not only the part of the gravitational wave detections but also the impressive vacuum system of LIGO.

[1] http://journals.aps.org/prl/abstract/10.1103/PhysRevLett.116.061102
[2] http://journals.aps.org/prl/abstract/10.1103/PhysRevLett.116.241103
[3] https://journals.aps.org/prl/abstract/10.1103/PhysRevLett.118.221101
[4] http://iestjournal.org/doi/abs/10.17764/jiet.1.32.6.v237n70970288926?journalCode=jiet.1
[5] https://www.ligo.caltech.edu/page/facts
[6] https://www.ligo.caltech.edu/page/vacuum
[7] https://dcc.ligo.org/E960050/public

*Corresponding author: odylio.aguiar@inpe.br

SURFACE ENGINEERING AND FUNCTIONALIZATION AT ATMOSPHERIC PRESSURE USING DIELECTRIC BARRIER DISCHARGES

Fiorenza Fanelli[1]* and Francesco Fracassi[1,2]
[1]*Institute of Nanotechnology (NANOTEC), National Research Council, Bari, Italy*
[2]*Department of Chemistry, University of Bari "Aldo Moro", Bari, Italy*

1. Introduction

Over the last two decades there have been considerable advances in the utilization of atmospheric pressure cold plasmas for the surface modification of materials. In particular, dielectric barrier discharges (DBDs) have attracted much interest and, in recent years, efforts have been directed toward the development of a large variety of processes which exploit different DBD electrode geometries for the direct and remote processing of materials [1-2]. In this contribution, a brief overview of our recent advances in surface processing using DBDs will be presented with particular focus on the aerosol-assisted deposition of hybrid multifunctional coatings, the surface modification of three-dimensional (3D) porous materials and the plasma jet deposition of thin films containing carboxylic acid groups.

2. Experimental

Different atmospheric pressure reactors with DBD electrode configuration have been utilized for the direct and remote surface modification of materials. Plasma-treated surfaces have been characterized by various techniques such as X-ray photoelectron spectroscopy (XPS), Fourier-transform infrared spectroscopy (FTIR), scanning electron microscopy (SEM), transmission scanning electron microscopy (TSEM), atomic force microscopy (AFM), water contact angle (WCA) goniometry, etc..

3. Results and Discussions

First, our study of the growth and structure of hybrid organic/inorganic nanocomposite coatings deposited by using an aerosol-assisted process will be briefly reviewed. Specifically, hydrocarbon polymer/ZnO nanoparticles nanocomposite coatings have been deposited by DBDs fed with helium and the aerosol of a dispersion of oleate-capped ZnO NPs in hydrocarbon solvents [3-4]. The coatings show multifunctional behavior due to the combination at the nanoscale level of the specific properties of the organic and inorganic components [5]. Then, representative results about the modification of both the outer and inner surfaces of open-cell polyurethane foams will be reported; examples will include the plasma-enhanced chemical vapor deposition (PECVD) of fluorocarbon coatings [6] and the plasma treatment through chemical grafting of oxygen-containing functional groups and variation of the surface roughness. Finally, the DBD jet deposition of thin films containing carboxylic acid groups will be presented with special focus on the improvement of the chemical and morphological stability of the coatings upon immersion in water [7].

4. References

[1] F. Massines, C. Sarra-Bournet, F. Fanelli, N. Naudé, N. Gherardi, Plasma Process. Polym., **9**, 1041-1073, (2012).
[2] F. Fanelli, F. Fracassi, Surf. Coat. Technol., **322**, 174-201, (2017).
[3] F. Fanelli, F. Fracassi, Plasma Chem.Plasma Process., **34**, 473-487, (2014).
[4] F. Fanelli, A. M. Mastrangelo, F. Fracassi, Langmuir, **30**, 857-865, (2014).
[5] F. Fanelli, A. M. Mastrangelo, N. De Vietro, F. Fracassi, Nanosci. Nanotechnol. Lett., **7**, 84-88, (2015).
[6] F. Fanelli, F. Fracassi, Plasma Process. Polym., **13**, 470-479, (2016).
[7] P. Bosso, F. Fanelli, F. Fracassi, Plasma Process. Polym., **13**, 217-226, (2016).

Acknowledgments

This research was supported by the Italian Ministry for Education, University and Research (MIUR) under grant PONa3_00369 and Regione Puglia under grants "ATTIV'AZIONE" (grant code S8R8930, call "Aiuti a Sostegno dei Cluster Tecnologici Regionali") and "LIPP" (grant no. 51) within the Framework Programme Agreement APQ "Ricerca Scientifica", II atto integrativo - Reti di Laboratori Pubblici di Ricerca.

*Corresponding author: fiorenza.fanelli@cnr.it

CONTROLLING DEFECTS DURING THE GROWTH OF LARGE SIZE DIAMOND SINGLE CRYSTALS BY PLASMA ASSISTED CHEMICAL VAPOUR DEPOSITION

Alexandre Tallaire
Laboratoire des Sciences des Procédés et des Matériaux, CNRS, Université Paris 13, Paris, France

The synthesis of large-size high-quality diamond single crystals still remains an important challenge. Indeed, due to its wide band-gap, high thermal conductivity, high carrier mobilities and good chemical stability, diamond is foreseen as the ultimate material for power devices operating at very high voltages and currents, under harsh environments. More recently, there has also been an increasing interest surrounding luminescent defects in diamond such as the nitrogen-vacancy centers that can be manipulated through optical and microwave fields, and that are holding a great promise for the development of quantum technologies.

The plasma assisted chemical vapour deposition technique (PACVD) has witnessed tremendous progresses over the last decade. Diamond growth rates can now reach up to several tens of micrometers per hour while the crystalline quality of the material produced is starting to be compatible with electronic applications [1]. The past few years have thus seen the introduction of thick CVD diamond material into the market although its availability remains limited.

Nevertheless diamond has yet not been widely adopted as a semiconductor material for active electronic applications. In fact, the available area is usually limited to a few mm^2 which complicates the processing steps of the material. Point and extended defects are also difficult to control especially to the high level of purity required by electronic applications. In this presentation the growth of thick single crystal diamond films by PACVD will be detailed particularly in the light of the remaining challenges. Strategies aiming at controlling defects will be presented.

[1] A. Tallaire, J. Achard, F. Silva, O. Brinza, A. Gicquel, Growth of large size diamond single crystals by plasma assisted chemical vapour deposition: Recent achievements and remaining challenges. Comptes Rendus Physique, 14 (2013) 169-184.

*Corresponding author: alexandre.tallaire@lspm.cnrs.fr

DIELECTRIC BARRIER DISCHARGES: KNOWN SINCE 160 YEARS, BUT STILL A LOT OF POTENTIAL FOR INNOVATIONS

Ronny Brandenburg
Leibniz Institute for Plasma Science and Technology - INP - Greifswald, Germany

160 years ago, the inventions of the Dielectric Barrier Discharge (DBD) for the generation of ozone by Werner Siemens started the development of nonthermal plasma chemistry. Up until know the DBD is a plasma source with high technological relevance as well as the subject of fundamental studies. DBDs are generated in configurations with an insulating (dielectric) material between the electrodes. The dielectric barriers are responsible for the self-pulsing operation and the generation of a nonthermal atmospheric pressure plasma. Besides the generation of ozone, they have opened up many other fields of application, e.g. lighting, exhaust gas treatment, flow control or analytical devices.

The presentation will give a review on the progress in the development of DBD arrangements and on the understanding of its physical mechanisms within about the last two decades. Therefore, the main principles and different modes of discharge generation are summarized. Then a selected collection of known as well as special electrode configurations and reactor designs, e.g. for the treatment of gases, liquids, complex bodies or for life science applications will be presented and demonstrate the broad possibilities of this discharge type. The progress on the investigation of different aspects of breakdown and plasma formation will be discussed in the third part of the presentation. In particular, the recent new insights on the elementary volume and surface memory mechanisms in filamentary DBDs will be discussed.

*Corresponding author: brandenburg@inp-greifswald.de

UNDERSTANDING THE BEHAVIOR OF NICKEL-BASED SUPERALLOYS DURING LOW TEMPERATURE PLASMA IMMERSION NITRIDING

L. Pichon, J.B. Dubois, S. Chollet, J. Cormier, P. Villechaise, C. Templier
Institut P', UPR 3346 CNRS, Université de Poitiers, ISAE-ENSMA, France

Widely employed in aeronautics and energy industry, nickel-based superalloys are materials developed to resist to harsh thermal, chemical and mechanical solicitations. As with other metallic alloys (Fe-based alloys for instance), surface treatments may enable to improve some properties of the bulk alloys, like fatigue-fretting, wear or erosion resistance for instance. Performed with various plasma or ion assisted process, low temperature nitriding was already shown to be particularly efficient on austenitic stainless steels (ASS) thanks to the formation of an "expanded γN" phase [1]. The γN phase is formed by insertion of nitrogen in the octahedral sites of the initial γ phase, a FCC Fe-cell with various alloying elements (Cr, Ni) in substitution solid solution. As the matrix of many nickel-based superalloys has the same γ structure (with FCC Ni-cell and Cr as main alloying element), it was pertinent to determine whether nitriding may bring them similar interesting improvements. Various nickel-based superalloys were then nitrided for few hours by low temperature plasma immersion at moderate temperature (350-400°C) and a similar γN phase was observed on few micrometers [2]. However, in the nickel-based superalloys, an intermediary phase close to Ni_4N seems to precede the γN formation. Moreover, if the γN phase is highly stable in ASS as long as the temperature remains lower than 450°C, it tends to decompose – even at 400°C – in nitrides (CrN) and a released γ phase poorer in Cr. Another difference of many nickel-based superalloys with the solid-solution strengthened ASS is the presence of various strengthening precipitates dispersed in the γ matrix, aiming to improve the bulk alloy mechanical properties. They are obtained by adjunction of specific alloying elements (Al, Ti, Ta, Nb…) and specific heat and metallurgical treatments. The main kind of these precipitates is composed of the γ' Ni_3(Al, Ti) phase, corresponding to the L12 cubic Ni_3Al, with various level of substitution of Al by Ti, Ta or even Nb. Interestingly the behavior of these γ' precipitates was shown to be significantly different from one alloy to another one: some exhibit similar nitrogen content than the surrounding γN phase (25-30 at%) whereas others do not incorporate any nitrogen [2,3]. Several reasons were studied to explain this scattering behavior: size of precipitates, coherency of the γ/γ' interface, anisotropic effect in single crystal superalloys and chemical composition. This last one was shown to be in fact the determinant characteristics; however additional experiments enable to conclude that the nitrogen incorporation is not controlled by thermodynamics stability variation with the γ' precipitates composition, but by composition controlled kinetics limitations of the nitrogen diffusion in the γ' phase.

[1] H. Dong, S-phase surface engineering of Fe-Cr, Co-Cr and Ni-Cr alloys, Int. Mater. Rev. 55 (2010) 65–98. doi:10.1179/095066009X12572530170589.

[2] S. Chollet, L. Pichon, J. Cormier, J.B. Dubois, P. Villechaise, M. Drouet, A. Declemy, C. Templier, Plasma assisted nitriding of Ni-based superalloys with various microstructures, Surf. Coat. Technol. 235 (2013) 318–325. doi:10.1016/j.surfcoat.2013.07.060.

[3] L. Pichon, J. Cormier, A. Declemy, S. Chollet, P. Villechaise, J.B. Dubois, C. Templier, Plasma nitriding response at 400 degrees C of the single crystalline Ni-based superalloy MC2, J. Mater. Sci. 48 (2013) 1585–1592. doi:10.1007/s10853-012-6915-z.

*Corresponding author: Luc.Pichon@univ-poitiers.fr

DLC AND CARBON BASED NANOSTRUCTURED COMPOSITE COATINGS – AN OVERVIEW OF THIN FILM DESIGN AND PROCESS APPROACHES TOWARDS HIGH PERFORMANCE ENGINEERING APPLICATIONS

Michael Stueber
Karlsruhe Institute of Technology (KIT), Institute for Applied Materials (IAM), Hermann von Helmholtz-Platz 1, D-76344 Eggenstein-Leopoldshafen, Germany

Diamond like carbon coatings have nowadays reached high quality standards and are widely used in various industries. However, steadily increasing demands for advanced surface functionalities in high performance engineering applications require permanent progress in both thin films design and properties and related deposition techniques. Besides the enormous achievements made on amorphous carbon and DLC coatings enormous know-how and expertise has been collected on the new class of carbon-based nanostructured composites. In a fundamental view, these materials are at least two-phase composites, containing a nanocrystalline transition metal carbide and an amorphous carbon phase. Depending on their microstructural design (i.e. volume fractions of the crystalline and amorphous phases, grain size of the carbide phase, nature of the carbon phase, e.g. hydrogenated or non-hydrogenated) these new coating materials exhibit interesting multifunctional properties, making them promising candidates for various applications. Until today, these materials have been considered for and tested in selective technical environments only. In this presentation, major phases and achievements of the development of such materials will be discussed. The latest state-of-the-art and new developments in the field of both DLC and carbon based composite thin films will be addressed, with a focus on wear and friction applications. Fundamental materials science issues as well as thin film design concepts, tribological performances, deposition techniques and scale-up measures will be considered.

*Corresponding author: michael.stueber@kit.edu

ULTRA-THIN AND THIN FILMS FOR NANO AND MICRON TECHNOLOGIES.

J.A.Diniz[1]*, L.P.B.Lima[2], A. Leonhardt[2], C.V. Carnio[1], A. M. Rosa[1], C.R. Almeida[1], A. M. Pascon[1], A. R. Silva[1], F. H. Cioldin[1], L.B. Zoccal[3], I. Doi[1] and L. T. Manera[1].

[1]School of Electrical and Computer Engineering (FEEC) and Center for Semiconductor Components and Nanotechnologies (CCSNano), University of Campinas (UNICAMP), Campinas, SP 13083-970, Brazil

[2]IMEC, Kapeldreef 75, 3001 Leuven, Belgium. [3]UNIFEI, Itajubá, MG 37500-903, Brazil

1. Introduction

This work presents the formation and characterization of different films (Pt, TiN, TaN, TiAlO, TiAlON, SiNx, SiO2 and SiON), which were obtained using different vacuum systems, such as: Sputtering, Electron Cyclotron Resonance (ECR)-Chemical Vapor Depositon (CVD), Electron Beam Evaporator (EBE) , Focused Ion Beam (FIB) and Electron Beam Lithography (EBL). These films can be ultra-thin and thin, with thickness values, respectively, between 1.5 nm and 20 nm, and thicker than 20 nm up to 300 nm. Furthermore, these films are used to obtain electronic devices based on MOS (Metal-Oxide-Semiconductor), HBT (Heterojunction Bipolar Transistor) and Graphene technologies, with nano and micron dimensions. It is important to notice that, these technologies and facilities are developed and installed, respectively, at University of Campinas in Brazil.

Today, the MOS transistors, which are used in actual high performance integrated circuit, have three crystalline planes of conduction channel into the silicon nano wires (SiNW) and are named 3D MOS transistors. In this work, to define the SiNWs, FIB milling of Si substrate is used. Thus, we can fabricate two kinds of 3D MOS transistors, JunctionLess (JL) and FinFETs (Fin Field Effect Transistors). The metals, which are used in these devices for drain, source and gate electrodes, are Pt (100 nm), deposited by FIB, TiN (20 nm) and Al (100 nm), deposited by sputtering. The gate dielectrics are the traditional SiO_2, obtained by FIB deposition and thermal oxidation of Si, and high-k insulators, such as SiON (3 nm), obtained by plasma oxynitrdation in ECR system, and TiAlON (8nm), obtained by Ti (0.7nm)/Al (0.3nm) deposition using EBE with additional plasma oxynitridation in ECR system. HBT devices are used for high frequency (> 10 GHz) applications. To get the high performance for these frequencies, the surface passivation, mainly, between emitter and base regions, allows the leakage current reduction, which results the current gain. Our HBTs are based on III-V semiconductors (InGaP/GaAs) and the passivation layer (60nm) is SiNx, obtained by ECR-CVD. FET devices with Graphene conduction channel (GraFETs) are fabricated using Graphenes obtained by CVD and TiN (100 nm) or TaN (100 nm) electrodes for source and drain contacts, deposited by Sputtering.The structural characteristics of all films are extracted from SEM (Scanning Electron Microscopy) and OM (Optical Microscopy), for surface analysis. The electrical characteristics of all devices are extracted from Current versus Voltage (I-V) curves.

2. Experimental

2a.3D MOS devices-JunctionLess (JL) 3D nMOS transistors (Figure 1) were fabricated on SOI substrates using 30 keV Ga+ FIB system for Si milling to define SiNWs and for depositions of 10-nm-thick SiO_2 (as gate dielectric) and 100 nm-thick Pt layers (as gate, drain and source electrodes). Width, length and height dimensions of SiNWs were about 100 nm, 4 μm and 50-80 nm, respectively (Figure 1(a))

Using 30 keV Ga+ FIB system for Si milling to define SiNWs (width of 50nm), different FinFETs were fabricated with different 3D MOS structures, such as Al/TiN/SiO_2/Si (Figure 2(a)), Al/TiN/SiON/Si (Figure 2(b)) and Al/TiN/TiAlON/Si (Fig.2(c)).

2b. HBT devices-HBTs were fabricated on InGaP/GaAs substrate (Fig.3) and the passivation layer (60nm) is SiNx, obtained by ECR-CVD, with low process pressure of 2 mTorr and ECR power of 250 W (both parameters leads to low surface bombardment) to active a N2/Ar/SiH4 plasma.

2c. GraFETs- Field effect transistors (Fig.4) based on CVD monolayer graphene (GraFET) deposited between source and drain TaN metal electrodes. In our devices, graphene lays on top of TaOx gate dielectric deposited on n+ Si substrate, which is used as the back gate electrode.

3. Results and Discussions

Some structural analyses, such as SEM and OM, are presented in Figures 1,2,3 and 4. Other analyses will present in CBRAVIC event. Figures 5 (a), (b), (c), (d), (e) and (f) present I-V curves of the JL, FinFET with Al/TiN/SiO2/Si, FinFET with Al/TiN/SiON/Si, FinFET with Al/TiN/TiAlON/Si, HBT and GraFET devices, respectively, which indicate that the devices are working. JL, FinFETs and GraFET are Field Effect Transistors, which are controlled by gate voltages (Vgs). This behavior occurs in the drain current (Id) x drain voltage (Vds) curves (for different Vgs values) presented in Figures 5 (a), (b), (c), (d) and (f),

*Corresponding author: jadiniz@unicamp.br

respectively. However, only IdxVds curves (Fig. 5(b), 5(c) and 5(d)) for FinFETs present similar behavior of traditional planar MOS transistor. The curves (Fig. 5(a) and (f)) for JL and GraFET devices present the inappropriate inclination, which can be due to the high Pt and TaN source and drain contact resistances, respectively. These inclinations can be reduced using a longer time of contact sintering process. Finally, our fabrication method using FIB process steps can be used to obtain prototypes of JL and FinFET devices. Furthermore, Fig.5(e) presents the curves of collector current (Ic) x voltage between collector and emitter (Vce), with different values of voltage between base and emitter (Vbe), for HBTs with (passivated device - black line) and without (unpassivated device - red line) SiNx passivation layer. These curves indicate that the distortions in saturation region occurred for unpassivated device, which are from leakage current between base and emitter for this device.

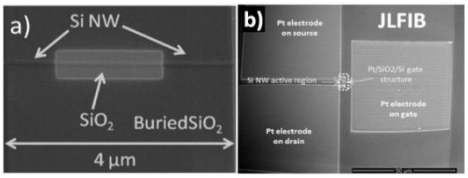

Fig. 1. *SEM analyses of JL Transistor: in (a) SiNW with SiO2 as gate dielectric; in (b) JL transistor after Pt deposition.*

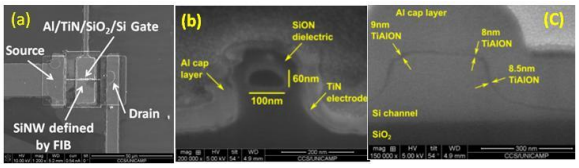

Fig. 2. *SEM analyses of FinFETs with different 3D MOS structures; in (a)Al/TiN/SiO2/Si (top view); in (b)Al/TiN/SiON/Si(cross-section); and in (c)Al/TiN/TiAlON/Si(cross-section).*

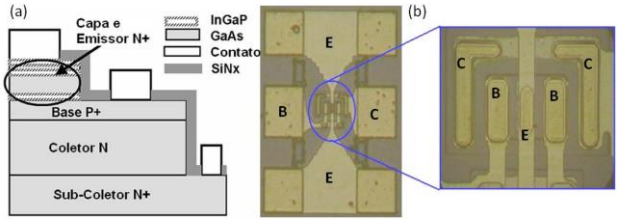

Fig. 3. *HBT: in (a) Schematic; in (b) Optical Microscopy Images (Emitter area of 20 x 6µm^2).*

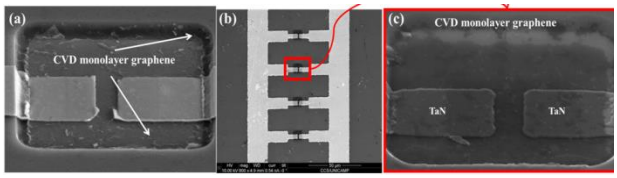

Fig. 4. *SEM analyses of GraFET: in (a) and (c) show the CVD graphene region and TaN electrodes; (b) GraFET arrays.*

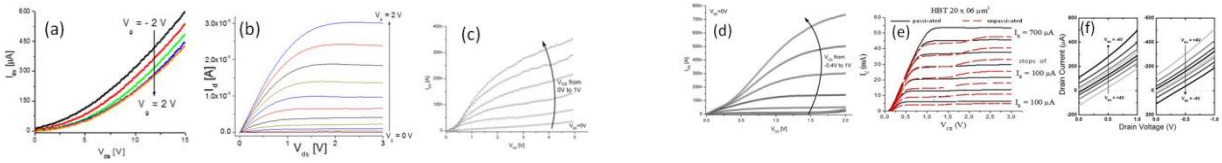

Fig. 5. *I-V curves of nMOS JL in (a)[1], FinFET with Al/TiN/SiO2/Si in (b)[1], FinFET with Al/TiN/SiON/Si in (c)[2], FinFET with Al/TiN/TiAlON/Si in (d)[2], HBTs (passivated (black line) and unpassivated (red line) devices) in (e)[3], and GraFET in (f)[4].*

4. Conclusions

This work presented the applications of different thin films for 3D MOS, HBT and Graphene Technologies. Traditional and alternative, such as FIB steps to define the SiNWs, processes were carried out to fabricate the devices. Thus, it can be concluded: (i) our fabrication method using FIB process steps can be used to obtain prototypes of JL and FinFET devices; (ii) SiNx passivation layer in HBTs improves the device performance; (iii) our fabrication method for GraFETs must be improved, however, allows that the devices work. It is important to notice that these nano and micron technologies, which are in improvement, are developing in CCSNano at Unicamp, Brazil.

5. References

[1] L.P.B.Lima, Joint-PhD Thesis, FEEC/Unicamp, Brazil, and KU Leuven, Belgium (2015).
[2] A. Leonhardt, Master Thesis, FEEC/Unicamp, Brazil (2016).
[3] L.B. Zoccal, PhD Thesis, FEEC/Unicamp, Brazil (2007).
[4] A.M. Pascon de Marque, PhD Thesis, FEEC/Unicamp, Brazil (2016).

Acknowledgments

The authors would like to thank the CCS staff for device processing and characterization. The work is supported by FAPESP, INCT-NAMITEC, CNPq, and CAPES.

*Corresponding author: jadiniz@unicamp.br

SURFACE MODIFICATION BY ION IMPLANTATION AND PLASMA TREATMENT

Maria Cecilia Salvadori
Institute of Physics, University of São Paulo, São Paulo, Brazil

In this work, plasma treatment and ion implantation are presented as techniques for surface modification.

Metal ion implantation was performed in different substrates for surface modification, where the implanted metal self-assembles into nanoparticles. During the implantation, the excess of metal atom concentration above the solubility limit leads to nucleation and growth of metal nanoparticles [1]. The nanoparticles nucleate near the maximum of the implantation depth profile (projected range) that was estimated by computer simulation using TRIDYN code [2, 3]. This program is a Monte Carlo simulation based on the TRIM code (Transport and Range of Ions in Matter); though TRIDYN takes into account compositional changes in the substrate due to two factors: previously implanted dopant atoms, and sputtering of the substrate surface. Our study suggests that the nanoparticles form a bidimensional array buried few nanometers below the substrate surface. More specifically we have studied the systems Au/PMMA (polymethylmethacrylate) [4-7], Pt / PMMA [8], Au /DLC [9], Au / alumina [10], Ti / alumina [11,12] and Ag / SU-8 (epoxy photoresist) [13].

Two examples can be mentioned for the nanocomposites formed by ion implantation. The first one refers to the ability in fabricating high-voltage insulators, controlling the surface resistivity (sheet resistance) of the material [14]. And the second example is to obtain obtained tailored SERS (surface-enhanced Raman spectroscopy) substrates [15].

Plasma treatment was proceeded on diamond and DLC (hydrogen free diamond-like carbon) for surface modification. DLC is an amorphous carbon material with high content of sp3 bonds, providing properties similar to diamond [16].

In diamond surfaces, we formed adjacent regions with different terminations. Initially diamond films were deposited by microwave plasma-assisted chemical vapor deposition, generating surface with hydrogen terminations. Following the surface was masked using lithographed electron-resist and then an oxygen plasma treatment was performed, using a small hollow-cathode plasma gun [17]. Kelvin Probe Force Microscopy (KPFM) showed an electrical potential difference of about hundred millivolts between the two different regions [18].

The DLC samples were deposited by Metal Plasma Immersion Ion Implantation and Deposition (MePIIID) and, posteriorly, treated with oxygen plasma and sulfur hexafluoride (SF6) plasma, in separate samples, generating surfaces with oxygen terminations (DLC-O) and fluorine terminations (DLC-F).

Cell growth was performed on diamond and DLC surfaces and modified surfaces. In both cases, the surface with oxygen terminations presented better results [13, 19].

References

[1] A. L. Stepanov, D. E. Hole and P. D. Townsend, J. Non-Crystalline Solids 260, 65 (1999).
[2] W. Möller and W. Eckstein, Nucl. Instrum. Meth. Phys. Res. B 2, 814 (1984).
[3] W. Möller, W. Eckstein and J. P. Biersack, Computer Physics Communications 51, 355 (1988).
[4] M. C. Salvadori, M. Cattani, F. S. Teixeira and I. G. Brown, Appl. Phys. Lett. 93, 073102 (2008).
[5] F. S. Teixeira, M. C. Salvadori, M. Cattani and I. G. Brown, J. Appl. Phys. 105, 064313 (2009).
[6] F. S. Teixeira, M. C. Salvadori, M. Cattani and I. G. Brown, J. Vac. Sci. Tech. A 28, 818 (2010).
[7] F. S. Teixeira, M. C. Salvadori, M. Cattani and I. G. Brown, J. Appl. Phys. 111, 104311 (2012).
[8] M. C. Salvadori, F. S. Teixeira, M. Cattani and I. G. Brown, J. Appl. Phys. 110, 114905 (2011).
[9] M. C. Salvadori, F. S. Teixeira, W. W. R. Araújo, L. G. Sgubin, R. E. Spirin, M. Cattani and I. G. Brown, J. Appl. Phys. 112, 074312 (2012).
[10] M. C. Salvadori, F. S. Teixeira, L. G. Sgubin, M. Cattani, I. G. Brown, Nuclear Instruments and Methods in Physics Research B 310, 32 (2013).
[11] M. C. Salvadori, F. S. Teixeira, M. Cattani, A. Nikolaev, K. P. Savkin, E. M. Oks, H.-K. Park, L. Phillips, K. M. Yu and I. G. Brown, J. Appl. Phys. 111, 063714 (2012).
[12] R. E. Spirin, M. C. Salvadori, F. S. Teixeira, L. G. Sgubin, M. Cattani, and I. G. Brown, Journal of Applied Physics 116, 184306 (2014).
[13] W. W. R. Araujo, F. S. Teixeira, G. N. da Silva, D. M. F. Salvadori and M. C. Salvadori, Journal of Applied Physics 115, 154701 (2014).

*Corresponding author: mcsalva@if.usp.br

[14] F. Liu, M. R. Dickinson, R. A. MacGill, A. Anders, O. R. Monteiro, I. G. Brown, L. Phillips, G. Biallis, and T. Siggins, Surf. Coat. Technol. 103/ 104, 46 (1998).
[15] J. Ferreira, F. S. Teixeira, A. R. Zanatta, M. C. Salvadori, R. Gordon, O. N. Oliveira Jr., Physical Chemistry Chemical Physics 14, 2050 (2012).
[16] M. C. Salvadori, F. S. Teixeira, W.W.R. Araujo, L. G. Sgubin, I. G. Brown, Diamond and Related Materials 25, 8 (2012).
[17] A. Vizir, E. M. Oks, M. C. Salvadori, F. S. Teixeira, I. G. Brown, Review of Scientific Instruments 78, 086103 (2007).
[18] M. C. Salvadori, W.W.R. Araújo, F.S. Teixeira, M. Cattani, A. Pasquarelli, E.M. Oks, I.G. Brown, Diamond and Related Materials 19, 324 (2010).
[19] S. E. Duailibi, M. T. Duailibi1, L. M. Ferreira, K. I. L. C. Salmazi, M. C. Salvadori, F. S. Teixeira, A. Pasquarelli, J. P. Vacanti, P. C. Yelick, Tissue Engineering 19, 2537 (2013).

Acknowledgments
We are grateful for the contribution of Fernanda S. Teixeira, Leonardo G. Sgubin, Wagner W. R. Araújo, Roman Spirin, Glenda N. da Silva, J. Ferreira, Silvio and Monica Duailibi, Efim Oks, Mauro Cattani and Ian Brown.

*Corresponding author: mcsalva@if.usp.br

INPE-LIT THERMAL-VACUUM TESTING FACILITIES FOR SPACECRAFT QUALIFICATION

Almeida, Jose Sergio
National Institute for Space Research - INPE
Integration and Testing Laboratory - LIT
São Jose dos Campos, SP
Brazil

The Integration and Testing Laboratory - LIT, from the National Institute for Space Research - INPE, located in the campus of Sao Jose dos Campos, SP, was built back in 1987 when it was primarily equipped with four (4) thermal-vacuum chambers, all of them aiming to support the testing campaigns of Brazilian and of international cooperation programs of satellites in terms of reproducing the harsh environment found in Earth orbit, including high vacuum and at the same time the extremes of high and low temperatures. These were accomplished by dedicated horizontal cylindrical vessels, being a 3m dia. x 3m long chamber, a 1m dia. x 1m long chamber and two 250-liter chambers. All of them are rated to the same vacuum level, typically in the 10^{-6}mbar range, and practically the same temperature range such as from -180°C to +150°C. Fitted with cryogenic and turbomolecular pumps in the high-vacuum department aiming to minimize chances of chemical contamination, all four chambers are still in good operational condition up to this day. Giving support to this Laboratory, helium leak detectors, mass spectrometers and quartz crystal microbalances are included in these testing facilities.

From the year 2008 onwards a large Space Simulator was added to this Thermal-Vacuum Laboratory bringing new capabilities in terms of size and mass of spacecraft to be space qualified, but also including new philosophy of multi temperature zones in the thermal shroud, that provides significant advantages on the development of thermal tests of spacecraft. This large thermal-vacuum chamber, built in a mailbox shape and with internal dimensions of 6m wide by 8m long by 7,5m of height is also fitted with cryogenic and a turbomolecular pump for the high-vacuum conditioning, system that is able to take the volume to the 10^{-7} mbar range, and with the same temperature range of the smaller ones.

All these testing facilities successfully provided and continues to positively support space programs such as the first generation of the Brazilian satellites - the SCD (Data Collecting Satellite) program, the SACI (Scientific Satellite) and SATEC (Technological Satellite) projects, the current Amazonia-1 project, but also the international undertakings such as the CBERS (China-Brazil Earth Resources Satellite) program with the Popular Republic of China and the SAC (Scientific Application Satellites) series of spacecraft with Argentina and with the USA/NASA.

This presentation will provide some technical details about all these thermal-vacuum chambers, including some notes of their performance, and the proper use INPE programs are making from these testing facilities.

Figure 1: LIT-INPE Thermal-Vacuum Chambers

Corresponding author: jsergio@lit.inpe.br

ID 4: INCREASE OF ELECTRICAL CONDUCTIVITY BY METAL DEPOSITION IN BRASILIAN ACTIVATED CARBON FELT

A.C. Rodrigues[1]*, E.Leal da Silva[2], S.F. Quirino[2,3], J.T. Matsushima[2,4], J.S. Marcuzzo[2,4], A. Cuña[5], E.S. Gonçalves[1], M.R. Baldan[1,2]

[1]*Instituto Tecnológico de Aeronáutica, São José dos Campos, SP, Brazil,*
[2]*Instituto Nacional de Pesquisas Aeroespaciais, São José dos Campos, SP, Brazil,*
[3]*ETEP Faculdades, São José dos Campos, SP, Brazil,*
[4]*Faculdade de Tecnologia Professor Jessen Vidal, São José dos Campos, SP, Brazil,*
[5]*Cátedra de Fisicoquímica, DETEMA, Facultad de Química, Universidad de la República, Montevideo, Uruguay.*

1. Introduction

Activated carbon fibers from polyacrylonitrile (PAN) have a variety of applications in industry and have been increasingly studied to exploit their various characteristics. Because of their high specific surface area, chemical and thermal stability, pore size distribution and conductivity is largely used in energy storage devices [1]. Recent studies show that is possible to increase the conductivity of carbon materials with a deposition of metals [2]. The aim of this work is to deposit various metals to improve electric conductivity of an activated carbon fiber obtained from polyacrylonitrile textile.

2. Experimental

The activated carbon felt were immersed in deionized water with a solution of $AgNO_3$, $Cu(NO_3)_2$, $Fe(NO_3)_3$, $NiSO_46H_2O$ and $PdCl_2$ for 24 hours. After the spontaneous process of deposition, the samples were washed and dried in a vacuum oven at 100 ºC for 2 hours. The composite obtained of activated carbon felt and the metals (ACF, ACF + Ag, ACF + Cu, ACF + Fe, ACF + Ni and ACF + Pd) were characterized by Field Emission Gum (FEG), thermal gravimetric analysis (TGA) curves, x-ray photoelectron spectroscopy (XPS) and DC electrical resistivity.

3. Results and Discussions

After the deposition of metals on activated carbon felt, the surface changed significantly, in some cases forming a film that covered the entire surface of the fiber filaments and in other cases metallic particles of various sizes are distributed homogenously. The TGA analyses show that the amount adsorbed on the surface of the ACF was low, less than 10 %. On the other hand, this quantity of metal adsorbed on the surface was enough to change the structure of the material in question and in all cases increased the felt conductivity, how is it possible observer in Tab. 1. XPS analyses showed that the way the metals were deposited varied in each case, made of metallic particles (silver sample) and oxides films.

Tab. 1. *Data from resistance, resistivity and conductivity of samples obtained by DC electrical resistivity.*

Sample	RS (Ω)	Resistivity (Ω.m)	Conductivity (S/cm)
ACF	2.434	$2.07\ 10^{-03}$	4.83
ACF + Ag	1.127	$9.58\ 10^{-04}$	10.44
ACF + Cu	1.641	$1.39\ 10^{-03}$	7.17
ACF + Fe	1.341	$1.14\ 10^{-03}$	8.77
ACF + Ni	2.131	$1.81\ 10^{-03}$	5.52
ACF + Pd	1.183	$1.01\ 10^{-03}$	9.94

The sample that showed significant conductivity improvement was ACF + Ag. In Fig. 1a is possible view the metal clusters on the surface of the ACF. This sample presents the greater quantity of metallic particles and few in oxide form, which possibly explains their significant improvement of conductivity.

*Corresponding author: alinerodrigues_1@msn.com

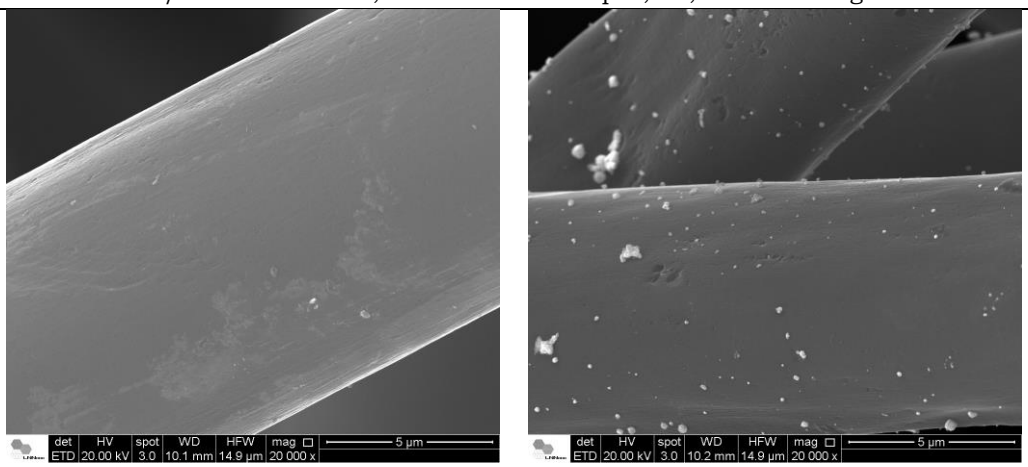

a) b)

Fig. 1. *a) Activated carbon felt and b) activated carbon felt with particles of silver*

4. References

[1] G.B. Baur et al Catalysis Today, **249**, 252-258, (2015).
[2] M. Mirzaeian et al J. Colloids and Surfaces A: Physicochem. Eng. Aspects, **519**, 223-230, (2017).

Acknowledgments

The author would like to thank BEVA-PCI-MCTI (Institutional Process Number 454779/2015-1 and Individual Process Number 170136/2016-7) and Capes for financial support, ITA and INPE for the support and infrastructure.

*Corresponding author: alinerodrigues_1@msn.com

ID 6_1: CORROSION BEHAVIOR OF AA5052 ALUMINIUM ALLOY TREATED BY PLASMA ELECTROLYTIC OXIDATION IN SILICATE AND PHOSPHATE-CONTAINING SOLUTION

Santos, D. C. R*; Reis, G. S.; Lucas, R. R.; Silva, L. L. G
CEETEPS – Fatec Pindamonhangaba – College of Technology

1. Introduction

Plasma electrolytic oxidation (PEO) is a novel method for anodizing valve metals. It is performed at high voltage (hundred to thousand volts), short time and alkaline solutions [1]. PEO layers present excellent properties, but they are strongly dependent on combination of the electrolytic parameters, such as voltage, current, temperature, process time, electrolyte and alloy composition [1]. When PEO is accomplished for treatment of aluminium alloys, the grown oxide layer is alumina (Al_2O_3) and it can be a barrier coating against corrosion and wear [2]. This work evaluated the corrosion performance of AA5052 aluminium alloy treated by PEO feed by DC power supply.

2. Experimental

Polished substrates of AA 5052 aluminium alloy (20 mm x 20 mm x 2 mm) were washed with isopropyl alcohol in ultrasonic bath. Then, they were anodized by PEO in alkaline solution prepared with 6.0 g of trisodium phosphate (Na_3PO_4), 15 g of sodium silicate (Na_2SiO_3) and 1000 ml of distilled water. PEO process was performed for 8.0 min under both currents of 0.5 and 1.0 A, and temperature below 40°C. The deposition rate of the oxide layers was evaluated by mass measurements made in analytical balance (0.0001 g). The corrosion behavior of the treated samples was investigated by exposure to NaCl solution (3.5 wt%), in electrochemical cell composed by a Pt counter-electrode and Ag/AgCl reference-electrode.

3. Results and Discussions

PEO performed in 1.0 A current promoted a deposition rate trifold than the produced in 0.5 A process, which is explained by electric charge ($Q = i\ t$) involved in the process electrochemical reactions. Fig. 1 shows Tafel curves obtained from corrosion tests. Both PEO processes increased the corrosion resistance of the anodized samples relative to untreated AA5052 Al alloy (E_{cor} = -0.78 V and I_{cor} = 4 x 10^{-8} A/cm^2), but the higher current PEO process led to most noble corrosion potential, E_{cor} = -0,20 V, and lower corrosion current density, I_{cor} = 3 x 10^{-10} A/cm^2. This is interpreted as effect of a stable crystalline structure of the alumina deposited in the adopted parameters.

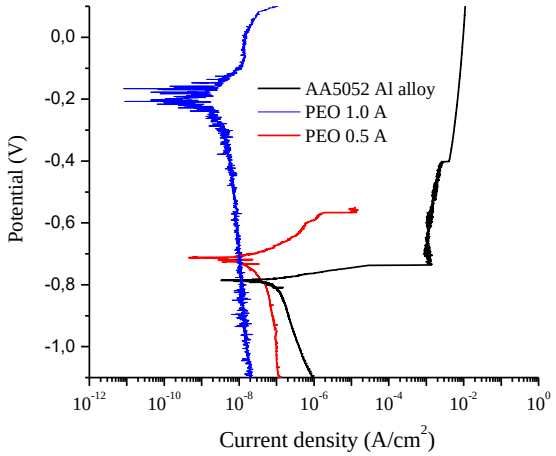

Fig. 1 – Polarization curves of AA5052 alloy anodized by PEO process.

4. References

[1] Denhavi *et al.* Phase transformation in plasma electrolytic oxidation coatings on 6061 aluminum alloy. **Surface & Coatings Technology 251** (2014) 106–114.
[2] Zhu *et al.* A mechanism for the growth of a plasma electrolytic oxide coating on Al. **Electrochimica Acta 208** (2016) 296–303.

Acknowledgments

The authors thank to FAPESP for financial support.

*Corresponding author: deborah.santos@fatec.sp.gov.br

ID 6: ELECTROCHEMICAL AND STRUCTURAL CHARACTERIZATION OF AA5052 ALUMINIUM ALLOY TREATED BY PLASMA ANODIZATION USING BORAX ELECTROLYTE

Santos, D. C., R.*, Reis, G. S. and Silva, L. L. G
[1]*CEETEPS – Fatec Pindamonhangaba*

1. Introduction

Corrosion of metallic materials deserves attention due to damages in their physical integrity and durability. Because of this, surface treatments are commonly performed for protection to the corrosion, such as the anodizing applied in aluminium alloys. The conventional anodizing involves some steps and acid electrolytes, such as sulfuric, phosphoric, nitric or chromic acids [1]. A novel anodizing, called plasma anodizing or plasma electrolytic oxidation (PEO), is sustained by high power source, being performed in a single step and employing alkaline electrolytes [2]. This work shows the results about the plasma anodizing of AA5052 aluminium alloy, using borax (sodium tetraborate – $Na_2B_4O_7.10\ H_2O$) as electrolyte.

2. Experimental

Substrates (20 mm x 20 mm) were prepared from 2 mm-sheet of AA5052 aluminium alloy, being properly washed and polished. The anodizing was performed in a stain steel cell connected to power source (20 kW DC) as cathode. The electrolytic solution was prepared in distilled water using 10 g/l of borax. The anodizing was carried out in different currents, varying from 0.5 A to 2.5 A, and 10 min of process time. The effect of the treatments on the electrochemical behavior of the samples was evaluated via open circuit potential (OCP) and polarization curves (PC) essays, using NaCl solution (3.5% w/w). Besides, structural characterization of the samples was performed by X-ray diffraction (XRD).

3. Results and Discussions

XRD analysis revealed that oxide layers are composed by α-Al_2O_3 e γ-Al_2O_3. Diffraction peaks of those crystalline structures were intensified as anodizing current increased, which is interpreted as the growth of the layers. Measurements of the sample mass, before and after the anodizing, confirm the increase of deposition rate. The anodized alloy samples showed higher corrosion resistance compared to the standard aluminium alloy, except the sample treated at 2.5 A. The corrosion potentials, showed in Fig. 1, increased from – 0.79 V up to – 0.20 V related to the AA 5052 alloy and the sample treated at 1.0 A, respectively. The corrosion current density decreased from 5 x 10^{-8} A/cm^2 for untreated sample up to 7 x 10^{-10} A/cm^2 for the sample treated at 1.0 A. These results show that current beyond 1.0 A does not promote better corrosion behavior, probably duo to increase of temperature that promote defect points through the oxide layers.

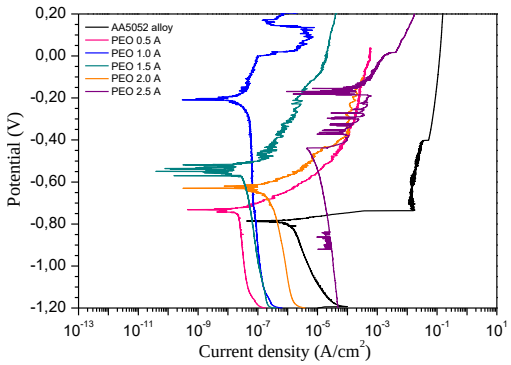

Fig. 1 – *Polarization curves of AA5052 alloy anodized in borax electrolytic solution at different currents*

4. References

[1] Sheasby, P. G.; Pinner, R. **The surface treatment and finishing of aluminum and its alloys.** ASM International Finishing Publications Ltda, vol. 1, 6th ed., 2001.
[2] Li, Q., Liang, J., Wang, Q. **Plasma Electrolytic Oxidation Coatings on Lightweight Metals**. **In** Modern Surface Engineering Treatments. Edited by Mahmood Aliofkhazraei. InTech 2013. https://www.intechopen.com/books/modern-surface-engineering-treatments.

Acknowledgments

The authors thank to FAPESP for financial support, and INPE – S. J. Campos for XRD analysis.

*Corresponding author: deborah.santos@fatec.sp.gov.br

ID 7: THERMAL STABILITY OF THE GAMMA-N PHASE PRODUCED IN SUPERDUPLEX STAINLESS STEEL THROUGH PLASMA BASED NITRIDING

Willian R. de Oliveira*[1], Guilherme M. Valadão[1], Gelson B. de Souza[1], Francisco C. Serbena[1]
[1]*Departamento de Física, Universidade Estadual de Ponta Grossa, Ponta Grossa, PR, Brazil*

1. Introduction

The stainless steels applicability is wide, as they present excellent wear properties, corrosion resistance and hardness [1, 2]. Super duplex stainless steel (SDSS) is composed by ferrite and austenite in balanced proportions, being suitable for the oil and gas exploration. It is known that nitrogen in solid solution increases the surface corrosion resistance of these materials [3,4]. Nitrogen was implanted on SDSS through a high-voltage pulsed plasma system or "Plasma Based Ion Implantation" (PBII), which was compared with the plasma nitriding or glow discharge process (GD). In the work reported here, changes in the nitrogen-expanded austenite phase after tempering the nitrided SDSS were investigated. The phase decay after a short period at 400 ºC were noticeable, and correlated with thermodynamic conditions running on both austenite and ferrite phases. The careful study of the expanded austenite formation using X-ray diffraction (XRD) is been carried out [4,5,6]. However, this metastable phase decay is also of interest to help explaining the formation of layers during nitriding. Here, a high energy process was compared with a low energy one, aiming at geting insights which could be valid for other nitriding processes as well.

2. Experimental Procedure

Samples of super duplex stainless steels UNS S32750 (or SD2507), labelled as F3 *bt* and GD *bt* (where *bt* stands for "before tempering") were nitrided under conditions summarized in Table 1, which preparation was detailed by Oliveira [7].

Table 1. Nitriding conditions for the samples in study

	Implantation method	Voltage (V)	Current (A)	Pressure(Pa)	Temperature (ºC)
F3 *bt*	PBII	9849 ± 60	0.74 ± 0.01	1.91 ± 0.03	351 ± 4.7
GD *bt*	GD	428 ± 7	0.127 ± 0.01	473 ± 20	352 ± 4

Nitridings were carried out under 50%N_2 and 50%H_2 atmosphere for 3 hours. Samples were then cut and one of the halves submitted to the tempering process in argon atmosphere for 4 hours at 400ºC, (a temperature high enough to the formation of chrom nitride [2,3]), creating the F3 *at*, and GD samples (where *at* means "after treatment"). Such heating aims at simulate extreme working conditions for the nitrided steel. The crystalline structure were investigated through XRD using CuKα radiation (0.15406 nm) in the Bragg-Brentano geometry, scanning the 35º-75º range in 0,02º steps during 6s.

3. Results and Discussions

X-rays diffractograms of nitrided samples before and after tempering are shown in Fig. 1. Before heat treatments, the expanded phase gamma-N was identified in either PBII or GD samples. Such phase may lay in austenite and ferrite grains, as discussed elsewhere [7]. The nitride phases ε and γ´were more evident in the GD *bt* sample, which precipitated preferentially in ferrite grains [7]. Expanded ferrite (alpha-N) may have been formed in ferrite grains, but this was not evident and needs further investigation.

An increase in γ_N peaks after tempering was clearly observed on F3 *at* and GD at, notably in the expanded austenite associated with the (200) plane, since, in this position, neither CrN nor Cr_2N contribute with the diffractogram. In addition, the gamma-N peaks shifted to higher diffraction angles, approaching the γ peak. The tempering causes the nitrogen on the surface to diffuse deeper into the substrate, decreasing its concentration, shifting the gamma-N peak closer to the gamma peak due to a smaller lattice expansion [8,9]. This effect gives rise to an expanded austenite with lower nitrogen content. Such smaller lattice expansion results in very different corrosion properties, worse than that with high nitrogen content [6]. Both samples (Fig. 1 and Fig.2) presents similar γ_N peak shifts, but the sample nitrided with lower energy (GD *at*) was more susceptible to the formation of CrN and Cr_2N.

When the nitrogen supply from the plasma to the surface is very high, as in the GD sample case compared to the F3 one, the transport of all nitrogen to inside the bulk is compromised due to a temperature-limited material diffusivity [6]. Hence, the amount of nitrogen entering the GD surface is larger than that which diffuses into the material. This causes a nitrogen supersaturation [10], eventually leading to the fast formation of CrN and Cr_2N (Fig. 2).

*Corresponding author: oliveira.willianrafael@gmail.com

It is possible to observe an additional peak at approximately 36 ° in the diffractograms of the F3 *at* and GD *at* samples. This peak may be iron oxide or chromium oxide, although the oxide stoichiometry was not indubitably indexed. It may have been formed by small flow of argon inside the quartz tube (where the treatments were made).

The in situ XRD analyzes during heating are planned as a continuation of the present study.

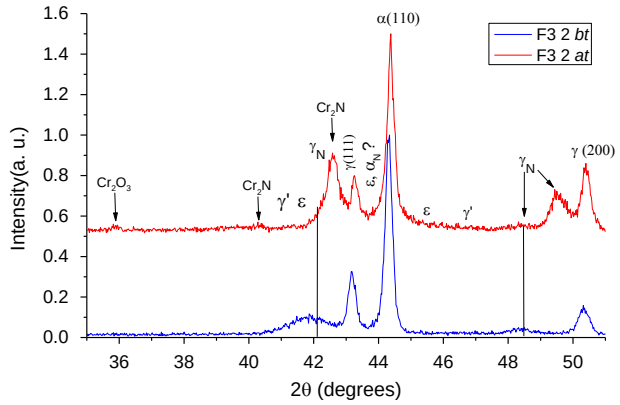

Fig. 1. *X-ray diffractograms of the F3 bt and F3-2 at samples. Nomenclature: γ is austenite, α is ferrite, γ_N is expanded austenite; γ´ is Fe_4N; ε is $Fe_{2-3}N$ and the possible α_N phase. Lines are only guides to the eyes.*

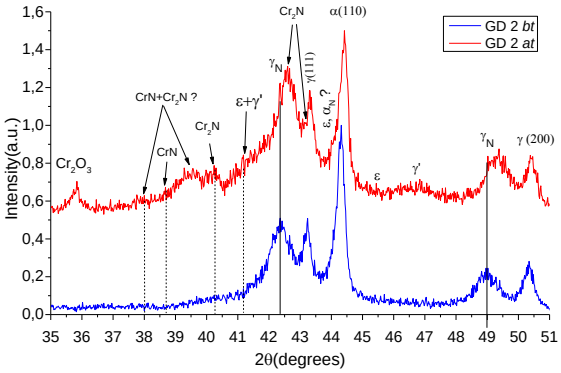

Fig. 2. *X-ray diffractograms of the GD-2 bt and GD-2 at samples. Nomenclature: γ is austenite, α is ferrite, γ_N is expanded austenite; γ´ is Fe_4N; ε is $Fe_{2-3}N$ and the possible α_N phase. Lines are only guides to the eyes.*

4. References

[1] H. Lo, C.H. Shek; J.K.L. Lai, Materials science and engineering R, **65**, 39-104, (2009).
[2] H. Dong, *"S-phase surface engineering of Fe – Cr , Co – Cr and Ni – Cr alloys"*, International Materials Review, **55**:2, 65-98 (2010).
[3] J. C. Lipold, D.J. Kotecki *"Welding Metallurgy and Weldability of Stainless Steels."*, Hoboken (2005).
[4] D. Manova , F. Scholze, S. Mändl, H. Neumann, Surf. & Coat. Tech. **129, 286**-289, (2011).
[5] S. Mändl , R. Dunkel, D. Hirsch, D. Manova, Surf. & Coat. Tech. **258,** 722-726, (2014).
[6] D. Manova, S. Mändl, H. Neumann, B. Rauschenbach, Surf. & Coat. Tech. **312,** 81-90, (2016).
[7] W. R. De Oliveira *"Influência dos parâmetros de implantação iônica por imersão em plasma na eficiência da nitretação do aço inoxidável super duplex"*, Ponta Grossa, (2016).
[8] S. Mändl, R. Günzel, E. Richter, W. Möller, B. Rauschenbach, Surf. & Coat. Tech. **128,** 423-428, (2000).
[9] O. Öztürk, D. L. Williamson, Surf. & Coat. Tech. **158-159**, 288-294, (2002).
[10] H. Dong, Int. Mater. Rev. **55**, 65–98 (2010).

Acknowledgments

Authors are grateful to C-LABMU/UEPG for the analysis facilities, FINEP (contract nº 01.10.0634.02 - REVESPETRO) and CNPq (grants nº 456729/2014-3 and 310819/2015-6). W. R. de Oliveira thanks CAPES and G. M. Valadão thanks CNPq for their scholarships.

*Corresponding author: oliveira.willianrafael@gmail.com

ID 11_1: INFLUENCE OF THERMALLY FUNCIONALIZED NANODIAMOND SUSPENSIONS ON HYDROGEN CONTENT OF DIAMOND LIKE CARBON FILMS PRODUCED BY DC-PECVD WITH ACTIVE SCREEN

Jesús Manuel Gutierrez Bernal[1]*, Thalita Sani-Taiariol[2], Gil Capote Rodríguez[3], Vladimir Jesus Trava-Airoldi[4].

[1]*Facultad de Ingeniería: Universidad Nacional de Colombia, Bogotá.*
[2] *Instituto de Ciência e Tecnologia. Universidade Federal de São Paulo (UNIFESP), São José dos Campos, Brasil*
[3]*Facultad de Ciencias: Universidad Nacional de Colombia, Bogotá.*
[4] *Laboratório Associado de Sensores e Materiais (LAS), Instituto Nacional de Pesquisas Espaciais (INPE), Brasil.*

1. Introduction

Research and development of Diamond-like Carbon (DLC) films with nanostructures is a new field for applications on different industries as automotive, aerospace, biomedical and electronic. DLC films have attracted attention due to their low friction coefficient, chemical inertness, high hardness and biocompatibility [1]. Some authors have reported better properties for DLC films when they are doped with nanoparticles [2]–[4]. However, they have produced films with heterogeneous mixtures although without stability during the synthesis process [4]. DLC films do not have good adherence on metallic surfaces due to a relatively high internal compressive stress in the films and also by the difference in the thermal dilatation coefficient values between substrates and films. Nanoparticles are materials with very good properties that could help to improve the DLC films properties, not only with decrease of stress and friction coefficient but with increase of hardness, biocompatibility and adhesion [5]–[9].

2. Experimental

Thermal functionalization for nanodiamond particles (Sigma-Aldrich, size particle 3-5 nm) was made in a closed oven at 420°C for oxidizing surface functional groups to carboxyl group (-COOH). Fourier Transform Infra-Red (FTIR) technique was employed for finding superficial functional groups and analyzing their changes before and after of functionalization process. Suspensions made from nanodiamond detonation in different solvents as hexane and methanol were obtained by agitation with ultrasound (Vibra-Cell 750®, amplitude 60%). Times from 15 to 60 minutes were used. Some films were deposited on flat polish silicon (100) substrates from drops of the suspensions obtained and solvent evaporation in air. Particle sizes on the films were measured using a High Resolution Field Emission SEM (TESCAN) and image digital treatment with software (MIRA3®, TESCAN) for making histograms as showed in figure 1. An amorphous silicon interlayer was synthesized using gas silane (SiH_4) as precursor in order to improve the film adhesion. DLC films doped with nanoparticles were deposited using a pulsed-DC Plasma Enhancement Chemical Vapor Deposition (PECVD) system with an active screen as additional cathode [1], [10] and nanodiamond suspensions. Hydrogen content and total compressive stress in the films were determined by Raman spectroscopy (LabRam HR evolution) and Stones equation (Optical perfilometer), respectively. Coefficient of friction (COF) in DLC films was determined employing a CETR UMT2 tribometer with the ball on disc technique in linear reciprocated mode with a ZrO_2 ball. A constant force of 10N was applied on the samples at room temperature and under 40% relative humidity. The adhesion test were made using a CETR UMT-2 tribometer with a Rockwell C indenter with a 200 μm which increased over time from 0 to 50N, while maintaining a constant displacement rate of 0.1 mm/s. The critical load was determined as the value of the applied load at which film began to be pulled from the substrate.

3. Results and Discussions

Ultrasound process helped to improve the deagglomeration process in functionalized nanodiamond. Infrared results suggested changes in functional groups on the nanoparticle surface to a preferential carboxyl group (-COOH) because an oxidation process was observed. Thermal treatment allowed decreasing particle size in nanodiamond. It would be possible because there were changes in electrical forces in the suspension. These electrical forces are the responsible for agglomeration process. DLC films with nanoparticles showed good friction coefficient (around 0.08), low hydrogen content (13-15%) and small total compressive stress of around 0.7 GPa.

*Corresponding author: jmgutierrezb@unal.edu.co

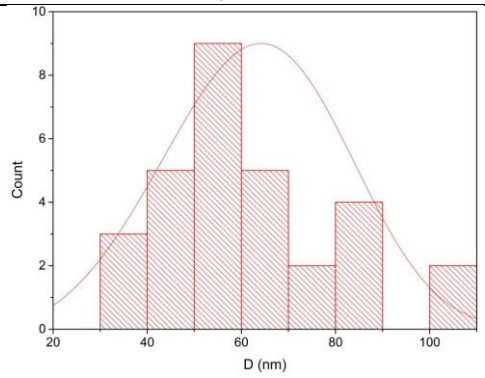

Fig. 1. *Histogram for nanodiamond after suspension process.*

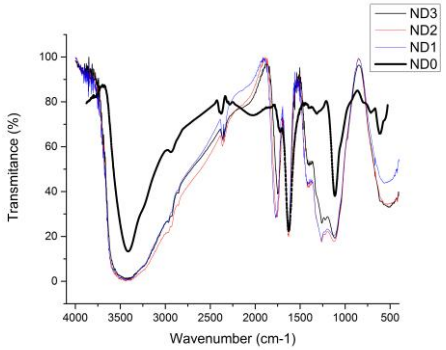

Fig. 2. *Infrared analysis before and after of thermal functionalization process.*

4. References

[1] G. Capote, E. J. Corat, and V. J. Trava-Airoldi, *Surf. Coatings Technol.*, 260, 133-138, (2014).

[2] F. R. Marciano, L. F. Bonetti, L. V. Santos, N. S. Da-Silva, E. J. Corat, and V. J. Trava-Airoldi, *Diam. Relat. Mater.*, 18, 1010–1014, (2009).

[3] F. R. Marciano, D. a Lima-Oliveira, N. S. Da-Silva, a V Diniz, E. J. Corat, and V. J. Trava-Airoldi, *J. Colloid Interface Sci.*, 340, 87–92, (2009).

[4] F. R. Marciano, L. F. Bonetti, D. a. Lima-Oliveira, C. B. Mello, M. Ueda, E. J. Corat, and V. J. Trava-Airoldi, *Diam. Relat. Mater.*, 19, 1139–1143, (2010).

[5] F. R. Marciano, L. F. Bonetti, R. S. Pessoa, J. S. Marcuzzo, M. Massi, L. V. Santos, and V. J. Trava-Airoldi, *Diam. Relat. Mater.*, 17, 1674–1679, (2008).

[6] M. Rai, A. Yadav, and A. Gade, *Biotechnol. Adv.*, 27, 76–83, (2009).

[7] T. Tamulevičius, A. Tamulevičienė, D. Virganavičius, A. Vasiliauskas, V. Kopustinskas, Š. Meškinis, and S. Tamulevičius, *Nucl. Instruments Methods Phys. Res. Sect. B Beam Interact. with Mater. Atoms*, 1-6, (2014).

[8] C. C. Wachesk, C. a. F. Pires, B. C. Ramos, V. J. Trava-Airoldi, A. O. Lobo, C. Pacheco-Soares, F. R. Marciano, and N. S. Da-Silva, *Appl. Surf. Sci.*, 266, 176–181, (2013).

[9] Y. Wu, J. Chen, H. Li, L. Ji, Y. Ye, and H. Zhou, *Appl. Surf. Sci.*, 284, 165–170, (2013).

[10] M. A. Ramírez R, P. C. Silva, E. J. Corat, and V. J. Trava-Airoldi, *Surf. Coatings Technol.*, 284, 235–239, (2015).

*Corresponding author: jmgutierrezb@unal.edu.co

ID 11: INFLUENCE OF ZIRCONIA NANOPARTICLES SUSPENSIONS ON TRIBOLOGICAL PROPERTIES OF DIAMOND LIKE CARBON FILMS PRODUCED BY DC-PECVD

Jesús Manuel Gutierrez Bernal[1]*, Thalita Sani Taiariol[2], Gil Capote Rodriguez[3], Vladimir Trava-Airoldi[4].

[1]Facultad de Ingeniería: Universidad Nacional de Colombia, Bogotá.
[2] Instituto de Ciência e Tecnologia. Universidade Federal de São Paulo (UNIFESP), São José Dos Campos, Brasil
[3]Facultad de Ciencias: Universidad Nacional de Colombia, Bogotá.
[4] Laboratorio Associado de sensores y Materiais (LAS), Instituto Nacional de Pesquisas Espaciais (INPE), Brasil.

1. Introduction

Research and development of Diamond Like Carbon films (DLC) with nanostructures is a new field for applications on different industries as automotive, aerospace, biomedical and electronic. DLC´s films have attracted attention due to their low friction coefficient, chemical inertness, high hardness and biocompatibility [1]. Zirconia is one of the most corrosion resistant and refractory oxides, having become a material used for thermal barrier coatings, gas sensors [2], [3] and also in applications for biocompatibility. Lastly, the use of nanoparticles for new applications has increased, especially in DLC films [3]–[6]. However, the use of zirconia nanoparticles in colloidal chemistry with dispersant is not very clear [5]. These nanoparticles are materials with very good properties which could help to improve the DLC films properties, not only decreasing the friction coefficient and stress but increasing the hardness, and biocompatibility [6]–[10]. In these research suspensions with zirconia nanoparticles and hexane and methanol as solvents were made. After DLC films by PECVD were obtained and characterized finding low hydrogen content and good tribological properties.

2. Experimental

Thermal functionalization for zirconia nanoparticles (Sigma-Aldrich, size particle <100 nm) was made in a closed oven at 420°C for oxidizing surface functional groups to carboxyl group (-COOH). Fourier Transform Infra-Red (FTIR) technique was employed to find superficial functional groups and analyzing their changes before and after of functionalization process. Suspensions made from zirconia nanoparticles in different solvents as hexane and methanol were obtained by agitation with ultrasound (Vibra-Cell 750®, amplitude 60%). Times from 15 to 60 minutes were used. Some films were deposited on a flat polish silicon (100) substrates from drops of the suspensions obtained and solvent evaporation in air. Particle sizes on the films were measured using a High Resolution Field Emission SEM (TESCAN) and image digital treatment with software (MIRA3®, TESCAN) for making histograms as show in figure 1. An amorphous silicon interlayer was synthesized using gas silane (SiH_4) as precursor in order to improve the film adhesion. DLC films doped with nanoparticles were deposited using a pulsed-DC Plasma Enhancement Chemical Vapor Deposition (PECVD) system with an active screen as additional cathode [1], [11] and zirconia nanoparticles suspensions. Hydrogen content and total compressive stress in the films were determined by Raman spectroscopy (LabRam HR evolution) and Stones equation (Optical perfilometer), respectively. Coefficient of friction (COF) in DLC films was determined employing a CETR UMT2 tribometer with the ball on disc technique in linear reciprocated mode with a ZrO_2 ball. A constant force of 10N was applied on the samples at room temperature and under 40% relative humidity. The adhesion test was made using a CETR UMT-2 tribometer with a Rockwell C indenter with a 200 μm which increased over time from 0 to 50N, while maintaining a constant displacement rate of 0.1 mm/s. The critical load was determined as the value of the applied load at which film began to be pulled from the substrate.

3. Results and Discussions

Ultrasound helped to improve the deagglomeration process in zirconia nanoparticles. There were no changes in the superficial organic groups, fact corroborated by the analysis of these nanoparticles with FTIR. Time suspension is important for obtaining DLC film with better properties. In this paper only 60 minutes as ultrasound time was found is able to deagglomerate and stabilize the suspension. Suspensions showed decrease in size particle after ultrasound treatment as it is observed in fig 2. There was a decreasing in particle size to 20 nm. It would be possible because there were changes in electrical forces in the suspension. These electrical forces are responsible for agglomeration process. DLC films obtained with nanoparticles showed good friction coefficient (around 0.07), low hydrogen content (15-17%), good adhesion (L_{c1}=22 N)

*Corresponding author: jmgutierrezb@unal.edu.co

and small total compressive stress around 0.6 GPa. These tribological properties, compared with a DLC film with crystalline diamond obtained by Marciano et al. [12], are better, despite their low hydrogen content. In contrast, total compressive stress was higher. The DLC film found show good adhesion compared with the result obtained by Ramirez et al [11]. This is the first research has been done with zirconia nanoparticles which showing interesting results compared with DLC films obtained with silver, and diamond nanoparticles [8], [10], [12].

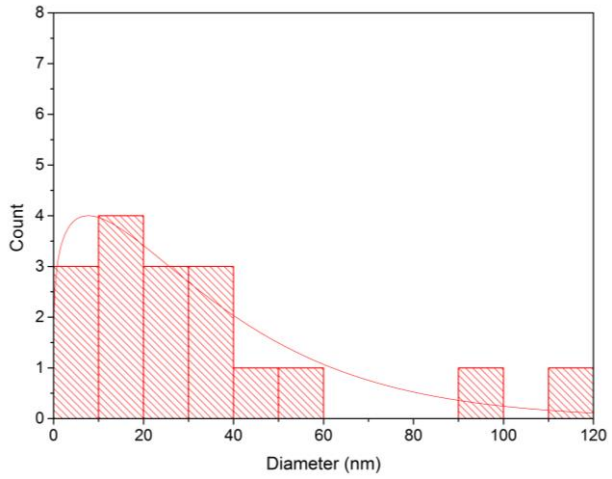

Fig. 1. *Histogram for zirconia nanoparticles after 60 minutes suspension process.*

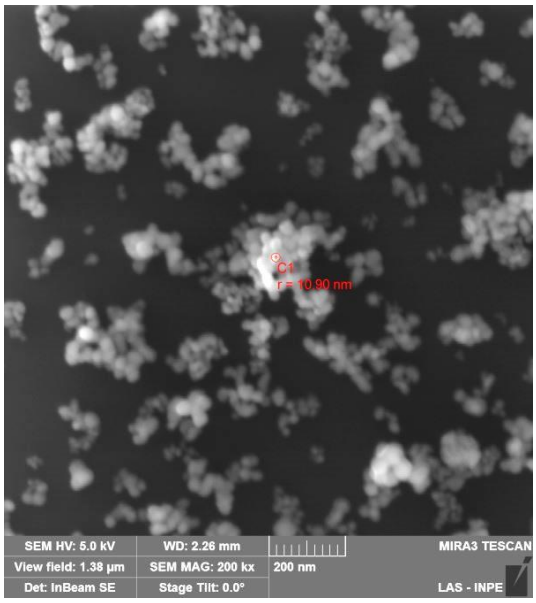

Fig. 2. *SEM image 200-Kx obtained after 60 minutes suspension process.*

4. References

[1] G. Capote, E. J. Corat, and V. J. Trava-Airoldi, *Surf. Coatings Technol.*, 260, 133-138, (2014).
[2] D. A. Zyuzin, S. V. Cherepanova, E. M. Moroz, E. B. Burgina, V. A. Sadykov, V. G. Kostrovskii, and V. A. Matyshak, *J. Solid State Chem.*, 179, 10, 2965–2971, (2006).
[3] M. L. A. Guel, L. D. Jiménez, and D. A. C. Hernández, *Ultrasonics chemistry*, 35, 514-517, (2017).
[4] M. Stoia, P. Barvinschi, L. Barbu-Tudoran, A. Negrea, and F. Barvinschi, *J. Cryst. Growth*, 381, 93–99, (2013).
[5] T. Fengqiu, H. Xiaoxian, Z. Yufeng, and G. Jingkun, *Ceram. Int.*, 26, 93–97, (2000).
[6] F. R. Marciano, L. F. Bonetti, R. S. Pessoa, J. S. Marcuzzo, M. Massi, L. V. Santos, and V. J. Trava-Airoldi, *Diam. Relat. Mater.*, 17, 1674–1679, (2008).
[7] M. Rai, A. Yadav, and A. Gade, *Biotechnol. Adv.*, 27, 76–83, (2009).
[8] T. Tamulevičius, A. Tamulevičienė, D. Virganavičius, A. Vasiliauskas, V. Kopustinskas, Š. Meškinis, and S. Tamulevičius, *Nucl. Instruments Methods Phys. Res. Sect. B Beam Interact. with Mater. Atoms*, 341, 1–6, (2014).
[9] C. C. Wachesk, C. a. F. Pires, B. C. Ramos, V. J. Trava-Airoldi, A. O. Lobo, C. Pacheco-Soares, F. R. Marciano, and N. S. Da-Silva, *Appl. Surf. Sci.*, 266, 176–181, (2013).
[10] Y. Wu, J. Chen, H. Li, L. Ji, Y. Ye, and H. Zhou, *Appl. Surf. Sci.*, 284, 165–170, (2013).
[11] M. A. Ramírez R, P. C. Silva, E. J. Corat, and V. J. Trava-Airoldi, *Surf. Coatings Technol.*, 284, 235–239, (2015).
[12] F. R. Marciano, L. F. Bonetti, D. a. Lima-Oliveira, C. B. Mello, M. Ueda, E. J. Corat, and V. J. Trava-Airoldi, *Diam. Relat. Mater.*, 19, 1139–1143, (2010).

*Corresponding author: jmgutierrezb@unal.edu.co

ID 13_1: THIN FILM THICKNESS MEASUREMENT USING TAPER SECTIONING METHOD

A. Barata[1]*, C. de Carvalho[1], L.C. Gontijo[1]
[1]*InstitutoFederal do Espírito Santo – Propemm – Campus Vitória*

1. Introduction

Thickness of thin films is an important characteristic and using the correct technique is crucial to guarantee an accurate measurement. In some cases of very thin film layers it is quit difficult to measure using optical microscopy. An alternative method for conventionals in using scanning electron microscopy (SEM) for thin films it is a simple techniques called sample taper sectioning developed by L. E. Samuels [1, 2]. In this technique, the sample is placed at an angle to the plane of examination where the layer width is enlarged when examined in an optical microscope. This work will demonstrate the use of taper sectioning used for a duplex treatment on AISI 1045 carbon steel which was treated with plasma physical vapor deposition (PVD) using a cathodic cage.

2. Experimental

A sample of AISI 1045 was mechanically ground, polished with alumina 0.3 µm and cleaned with acetone before treatment. Firstly, the sample was carbonitrided at 420º C during 5 h, vacuum pressure at 2 torr and gas flow with 80 cm3/min N2 e 200 cm3/min H2 and 4 cm3/min CH4 using a stainless steel cathodic cage. After that was deposited with a TiN coating at 240º C during 5h, a vacuum pressure of 0,98 torr and gas flow of 310 cm3/min H2 and 100 cm3/min N2 using a titanium cathodic cage. The sample was left into the reactor over vacuum after finishing deposition to room temperature. After this time, the sample was mounted using taper sectioning method as indicated in figure 1, resined, mechanically ground, polished with alumina 0.3 µm and 0.1µm and finally etched with Nital. The sample microstructure was observed using the confocal microscope in bright field.

3. Results and Discussions

According to figure 1(a), the true coating thickness (A) can be determined by calculating using the thickness measured (B) using an optical microscope. In figure 2(b) has shown the thickness tapered as mounted in figure 1(b). The average thickness coating values measured (B) obtained from figure 2 using confocal microscope is 7,05µm with 0,94µm standard deviation. The average calculated coating thickness (A) is 4,99µm with a standard deviation of 0,67µm in a taper angle of 45º according to figure 1(b). Figure 2(a) shows the sample microstructure without taper sectioning in which is not possible to identify the coating thickness with accuracy comparing with figure 2(b). Using taper sectioning amplify thickness visualization at optical microscope making easy the measuring. Another positive point of taper sectioning is that the sample preparation is quicker and with good edge retention than conventional sectioning method.

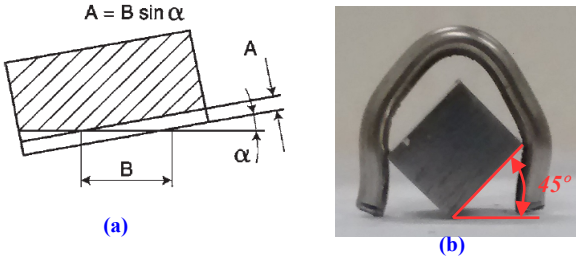

Fig. 1. *(a)Taper section with taper angle α in which the true coating thickness A can be calculated by measuring B in optical microscope [2]. (b) Sample taper section as mounted.*

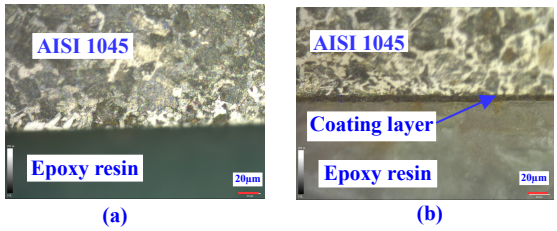

Fig. 2. *(a) sample micrography without taper mounting after etching and (b) sample micrography with taper mounting after etching (500x).*

4. References

[1] L. E. Samuels,, "*Metallographic Polishing by Mechanical Methods*", ASM International, Materials Park, Ohio, USA, (2003).
[2] K. Geels, Metallographic and materialographic specimen preparation, light microscopy, image analysis and hardness testing, ASTM International, West Conshohocken, PA, USA, (2007).

*aguinaldobarata15@gmail.com

ID 13: COMPARATIVE STUDY OF SHIELD MASK TECHNIQUES KAPTON® TAPE AND TIO2 FOR THIN FILM THICKNESS MEASUREMENT

A. Barata[1]*, C. de Carvalho[2], L.C. Gontijo[3]
[1,2,3]*InstitutoFederal do Espírito Santo – Propemm – Campus Vitória*

1. Introduction

The thin film thickness is an important characteristic and the accurate determination is required in research studies and also for coating quality control. Several techniques were already studied by thickness measurements of thin films[1]. The most commons techniques are using profilometer or optical devices to measure thin film deposited over substrates [1, 2, 3]. However, getting a sharp and clean coating edge plays an important role in reaching precision on thickness measurement [1]. Masking is a usual technique to produce a step between substrate and coating. The most usual devices used for masking is a metal sheet, thermal resistant tapes or solvent cast polymer [2]. For all those techniques the mask should be lifted off from the coating to get access to step and measure its height. Nevertheless, lifting off any device can damage by cracking or removing some parts of coating edge. Using tapes or polymers are temperature limited for depositions process over 400º C. According to DuPont Kapton® data sheet, the majority characteristics are available between 20 to 200º C and there are no complete data available extreme condition. Some studies at IFES Surface Treatment and Tribology Laboratory were performed using Kapton® tape for coating thickness measurement which. But, this tape was not suitably stable during a deposition over 250 ºC in which it had reacted and caused causing shadows and coating accumulation in most point in edge line. Some interference by Kapton tape on coating is observed due to minor gas bubbles present in deposition close edge line which should be investigated in near future.This study demonstrates that using TiO2 diluted with isopropanol [1] is a suitable device for masking deposition substrate avoiding Kapton® tape handicaps.

2. Experimental

Two samples of AISI 304 stainless were mechanically ground and polished with alumina 0.3 µm. A painting coat of TiO2 dilued in isopropanol was applied in one extremity of the samples and the other extremity was applied a piece of Kapton tape. A coating of TiN was deposited on one side of samples employing pulsed glow discharge (PGD) process using the cathodic cage in titanium with following regulations: 310 cm3/min H2 and 100 cm3/min N2 mass flow, a pressure of 0,92 torr, temperature of 250ºC. Cathodic cage is a device used in surface treatment to eliminate edge effect and overheating which occurs during PVD with plasma [9]. Samples were left into the reactor over vacuum after finishing deposition to room temperature. After this time, Kapton tape was removed by lift-off and tape glue was cleaned using acetone. The TiO2 painting was removed by dissolution with deionized water simply but, carefully, to avoid coating scratches. Thickness measurement and of coating edge conditions were analyzed with Leica DCM 3D confocal microscope.

3. Results and Discussions

Figure 1 shows coating using Kapton tape and figure 2 using TiO2 painting. Comparing both figures is evident that TiO2 painting mask gives a cleaning and straight edge line. Also, it is possible to observe at figure 1 fringes with different colors which indicate that Kapton tape reacts with TiN coating during deposition. Thickness were 107 nm average with 7,7 nn Std for TiO2 painting side and 243 nm average with 13,1 nm Std for Kapton tape side.

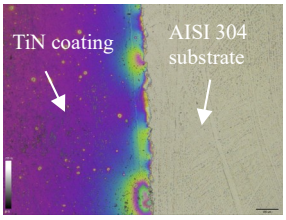

Fig. 1. *Sample extremity which used Kapton tape.*

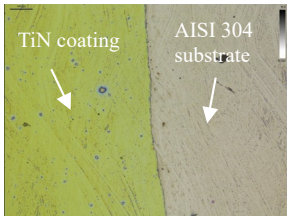

Fig. 2. *Sample extremity which used TiO2 painting.*

4. References

[1] A.Piegary and E.Masseti, Thin Solid Films, 124, 249-257, (1985).
[2] P. G. Hartley, H. Thissen, T. Vaithianathan, and H. J. Griesser, Plasmas and Polymers, Vol. 5, No. 1, (2000).
[3] S.Zhang, Journal of Materials Processing Technology, 39, 165-177, (1993).

*Corresponding author: aguinaldobarata15@gmail.com

ID 16: DEVELOPMENT OF A HYBRID CORONA-DIELECTRIC BARRIER DISCHARGE FOR SURFACE PROPERTIES MODIFICATION OF TEXTILES

Larissa Maciel do Nascimento[1]*, Gilberto Petraconi Filho[1], Fernando Gasi[2], Edson Bittencourt[3]
[1]*Instituto Tecnológico de Aeronáutica*
[2]*Universidade Federal do ABC*
[3]*Universidade Estadual de Campinas*

1. Introduction

A critical aspect in the development of polyamide textiles is the surface properties modification to enhance the dyes absorption processes, quality and functionality. The aim of this work is to develop a hybrid corona-dielectric barrier discharge for surface properties modification of textiles. Initially the raw material initially chosen for plasma treatment was the mesh fabric composed of 6.6 polyamide due to its physical and chemical properties, and variety of applications. In order to analyze the increment of functional groups for using in technical and medical textiles and optimize the beneficiation process by reducing the consumption of dyes, water and energy, the fabrics will be exposed to the plasma generated in a hybrid corona-dielectric barrier discharge operating at atmospheric pressure with a controlled environment using different gases, power, electrodes gaps and exposure times. Tests to determine static and dynamic contact angle will be performed to check the moisture absorption, dyeing kinetics and colorimetry to enhance the efficiency process and manufacturing costs. For characterizing the surface morphological properties and roughness will be used Atomic Force Microscopy and Scanning Electron Microscopy techniques. The FTIR (Fourier Transform Infrared spectroscopy) and XPS (X-ray Photoemission Spectroscopy) techniques will be used to evaluate the increment of functional groups on the plasma treated surfaces and mark out the development of a kinetic/chemical model for plasma/surface interaction.

Among the surface modification techniques applied in the industry to improve adhesion, plasma treatment is widely used. Several studies have been carried out, especially in the last decade, analyzing textile articles of different fibers regarding performance and applications. Today, so-called Technical Textiles have emerged considerably. The number of scientific papers and industrial application of these materials is in constant increasing [1]. Technical fabrics are defined as textile materials produced mainly for their technical applications due to its performance and functional properties, rather than their aesthetic or decorative features [2]. The technical textiles sector is generally segmented in several areas depending on the specific applications [3]:

- Indutech: filters and insulation for aviation;
- Clothtech: Functional components for footwear and clothing;
- Geotech: Geotextiles and civil engineering;
- Medtech: Hygiene and medicine;
- Sporttech: Components for sport and leisure.

With the use of plasmas generated by electric discharges operating at atmospheric pressure, the surface properties of textile substrates can be modified, increasing their hydrophilicity and ability to dye, reducing the temperature in the dyeing process, generating more intense colors, more solid and with different shades [4]. The raw material chosen initially for the surface treatment of plasma was Polyamide 6.6, a polymer with wide application versatility (aeronautical industry, medical textiles, and fabrics for high performance). In this scope, the main motivation of this work is to characterize the plasma treatment of mesh fabrics made from polyamide 6.6, in order to provide greater functionality in the surface properties (absorption, adhesion, protection against ultraviolet radiation, resistance and elongation), and to reduce the dye concentration and water consumption during the manufacturing process. The modification of surface properties creates unlimited possibilities for the development of new products for the textile industry, especially in the area of technical and medical textiles.

*chazfisica@gmail.com

2. Experimental model

The objective of this research was to develop a reactor of plasma, under the concept of corona discharge using a dielectric barrier operating in air at atmospheric pressure aiming the treatment of textile substrates - see figure 1. This equipment allows to modify the surface properties of textile substrates to provide improvements in the functional properties for application in technical and medical textiles. In addition, the reactor improves the tissue processing by reducing the consumption of dyes, water and energy. Furthermore, is intended to investigate the operating windows of the plasma reactor dedicated to the surface treatment process of textile substrates, mainly polyamide, which are characterized by to have high tensile strength, elasticity, toughness and abrasion resistance. Thus, is possible to evaluate the increase of functional groups on surfaces treated with plasma and the development of a kinetic-chemical interaction model for plasma / surface and surface / dye. The laboratory plasma system for surface treatment of polyamide fabric consists basically of a process chamber, a power system, a sample handling system and a gas injection system (see Figure 2).

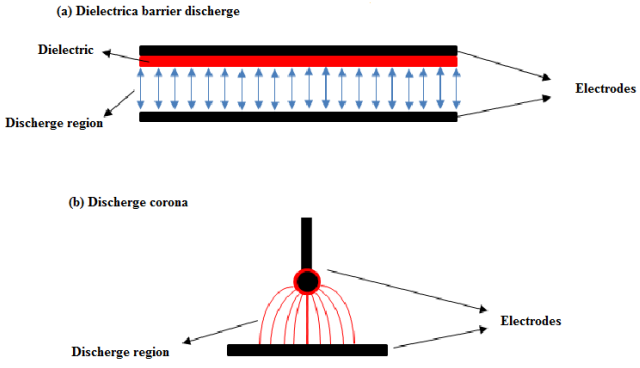

Figure 1. (a) Dielectric barrier discharge and (b) corona discharge.

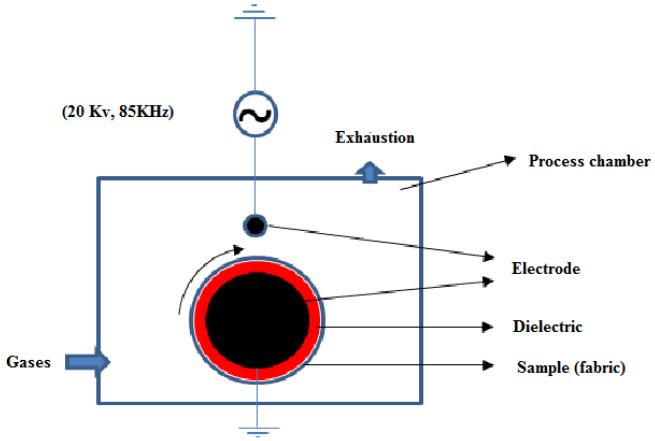

Figure 2. Schematic proposal of the plasma system.

The importance of this work lies in the study of the modification of the surfaces of textile substrates by plasma treatment, to replace the conventional processes of preparation of fabrics, which use chemical agents that attack the textile effluents and generate several substances harmful to the environment. Plasma is proposed as a pre-treatment of the material without action of such agents, being exclusively a physical treatment, reducing the water consumption. Also, this process is clean and faster than other used currently.

3. References

[1] M. ARAÚJO.; R. FANGUEIRO.; H. HONG. Têxteis Técnicos: Materiais do Novo Milénio. Williams, Lda. Braga, 2001.
[2] ARUP RAKSHIT, MANISHA HIRA & U. K. GANGOPADHYAY.Technical Textiles – What India need to do now, 2007.
[3] DAVID RIGBY. Technical textiles and nonwovens: world market forecasts to 2010 ;
[4] SOUTO, P.; OLIVEIRA, F.; CARNEIRO, N.. Polyamide 6.6 Modified by DBD Plasma Treatment for Anionic Dyeing Processes. Textile Dyeing, Edited by Prof. Peter Hauser, 2011.

Acknowledgments
Instituto Tecnológico de Aeronáutica, CAPES, INPE, FAPESP.

*chazfisica@gmail.com

ID 19: LANGMUIR PROBE DIAGNOSTICS OF A DC GLOW DISCHARGE USED AT INPE

Marcondes A.R.[1]*, Ueda M.[2], Bergamo E.C.[3]
[1,2,3]*Laboratório Associado de Plasma, Instituto Nacional de Pesquisas Espaciais*

1. Introduction

Langmuir probe is one of the simplest ways to measure plasma parameters. Basically, it consists of a thin wire that is inserted into the plasma. Once in contact with the plasma, the current in the wire is measured at different applied voltages. Based on current and voltage measurements, the I x V characteristic curve is obtained and the plasma parameters may be calculated from the coordinates and slopes from the curve. Plasma immersion ion implantation (PIII) is a relatively novel plasma treatment used at INPE to modify the surface of different types of materials and components. In our laboratory, the most common source of plasma for PIII is the DC glow discharge (GD). In this discharge, there is a fixed cathode and a fixed anode. Electrons are accelerated from the cathode to the anode acquiring more and more energy during their pathway. Collisions among electrons and ions and neutral particles occur and provide more ionized particles and electrons as the free electrons can transfer energy to bonded electrons during the collisions. If the electric field strength is high enough, the energy transfer can reach a certain level and an avalanche breakdown will happen in the gas inside the chamber. The avalanche breakdown multiplies de electrons and ions inside the chamber leading to a gas full of positive, negative ions and electrons. This state is called plasma where there is an assemblage of free positively and negatively charged particles and neutrals, and the negative and positive charges nearly balance each other at the macroscopic level. The plasma is usually characterized by the ions and electron densities and ions and electron energies or temperature. Other important parameters to be known are the plasma potential and the floating potential, that is respectively, the plasma potential relative to the walls of the chamber and the potential developed at a surface in contact with a plasma when electrically isolated from the ground.

2. Experimental

In this work, the Langmuir probe from *Impedans Ltd* was used to perform the diagnostic of a DC glow discharge formed in the 3IP-CE treatment system at INPE. The plasma conditions were those usually used during the PIII treatments. The DC voltage was 300 V and the current was 2.0 A. The gas used was Nitrogen with a working pressure of 4.3×10^{-3} mbar. The diagnostics of this GD were performed using simple and double Langmuir probes.

3. Results and Discussions

Diagnostic using simple probe has shown no good results as the plasma potential is relatively high due to the high DC voltage applied by the DC power supply. The diagnostic using double probe has shown better results. In this case, it was possible to determine some plasma parameters. Preliminary measurements have indicated that the glow discharge operating in the conditions above presents an electron temperature of around 12 eV, an ion density of 1.6×10^{9} cm^{-3} and a current density of 1.2 A/m^2. The setup of the new *Impedans* Langmuir probe is still going on and much work needs to be done to adapt the probe to the other PIII treatment systems of our laboratory.

*andre.marcondes@inpe.br

ID 25: EXPERIMENTS ON HIGH CURRENT, LOW VOLTAGE, HOLLOW CATHODE DISCHARGES FOR PLASMA IMMERSION ION IMPLANTATION (AND DEPOSITION) INSIDE TI6AL4V 1.1 CMØ TUBE

Mario Ueda [1]*, Carla da Silva[1,2], Gelson B. Souza[3], Rogério M. Oliveira[1]
[1]*Associated Laboratory of Plasma, National Institute for Space Research, São José dos Campos, SP, Brazil*
[2]*Associated Laboratory of Sensors and Materials, National Institute for Space research, S.J.Campos, SP*
[3]*State University of Ponta Grossa, Ponta Grossa, PR, Brazil*

1. Introduction

Hollow cathode discharges are receiving much attention recently because they are quite versatile and powerful plasma sources for diverse applications as in Plasma Immersion Ion Implantation and Deposition (PIII&D) inside metallic tubes, powerful light sources for spectroscopy and lasers, plasma propulsion, Atomic Layer Deposition (ALD), rocket nozzle, gun barrel, and so on. Titanium alloy tubes are important components for fuel transporting/feeding and also as refrigeration components in aerospace systems. In particular, ½ an inch tubes (1.3 cm OD tubes) are most suitable ones for those purposes given their convenient size, weight and ductility. The objective of this work was to improve the surface properties of the Titanium alloy tube internal wall for different space applications.

2. Experimental

Newly acquired high power high voltage pulser RUP-6 (maximum of 17 kV, 100 A and 13 kW) was utilized to drive a small diameter Ti6Al4V (TAV) tube of 1.5 cmØ OD and 15 cm length, with a thickness of 2mm. High density nitrogen plasma was produced (high light emission, large nitrogen uptake, reached temperature of the tube as high as 900ºC) and used as a source for the PIII and PIII&D treatments of the internal walls of the TAV tube and of the samples placed there as monitors. Used samples were SS304, Ti6Al4V and Si, all prepared and cleaned adequately for ion implantation, sputtering and deposition studies.

3. Results and Discussions

In one experiment, the PIII&D system was operated for 1 hour at 5.6 kV, 20 A, at a frequency of 500Hz, 30 µs pulse length and working nitrogen pressure of $7x10^{-2}$ mbar. A total of 1600W of power was distributed to the ballast resistors (250Ω) and the plasma (100Ω) as 1000W and 600W, respectively, with about 600V peak voltage applied to the tube. The tube temperature during the nitrogen PIII&D was limited to 900 ºC to avoid excessive heating of the viewing window. An entire Si wafer (4 inch diameter) was placed in front of the tube mouth to map the film deposition profile due to the plasma flowing out the tube. This measurement could assist us to confirm a simple model for PIII&D inside metallic tubes using hollow cathode plasmas. Large nitrogen implantation, followed by thermal diffusion, resulted in a thick TiN layer on the TAV sample, as seen by XRD pattern shown below (Fig.1). Other results of surface analysis of the samples used for post-mortem diagnostics (FEG, cof, nanoindentation, roughness) will be shown and a general discussion of the results on the obtained hollow cathode discharges will be given at the conference. When the nitrogen PIII&D treatment was finished, and the pulser was turned-off after 1 h of treatment, the TAV tube with 900ºC glowed intensely, as shown in Fig.2. Results of other treatments but different PIII&D conditions will also be presented for comparison purposes.

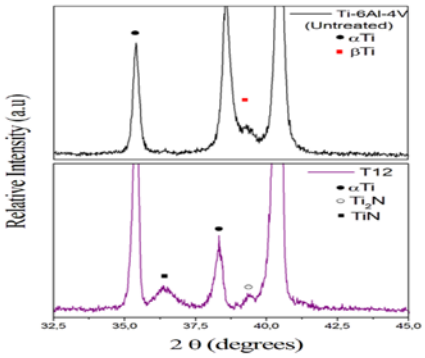

Fig. 1. *XRD patterns for untreated and PIII treated TAV samples inside the tube.*

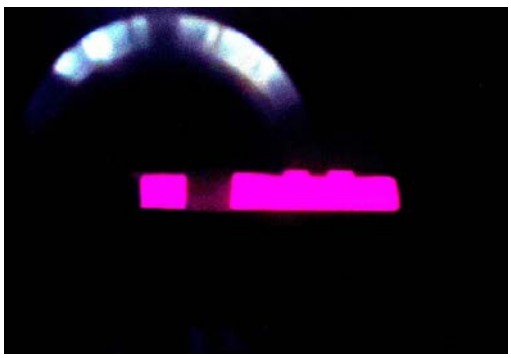

Fig. 2. *Picture of the glowing hollow cathode tube side view after plasma turn-off. Half circle behind is a reflection from a flange inside the chamber.*

Acknowledgments: Work supported by MCTIC, CNPq and CAPES

*Corresponding author: mario.ueda@inpe.br

ID 26: Permittivity and permeability measurement of the foam Electric characterization of the foam powder

Braulio H. K. Lopes [1]*, Roberto C. Portes[2], Alexsandra S. Monteiro[3], Aline C. Rodrigues[4] A. M., M. A. Amaral Junior [5], Jossano S. Marcusso[6], Gisele Amaral-Labat [7], Emersom S. Gonçalves[8], Mauricio R. Baldan[9], and Sandro F. Quirino[10],

[1]DCTA-INPE/LAS, [2]INPE/LAS, [3]INPE/LAS, [4]DCTA/AMR, [5]INPE/LAS, [6] INPE/LAS, [7]USP/DEMM/LABAT, [8]DCTA/AMR, [9]INPE/LAS, [10]ETEP/INPE/LAS

1. Introduction

Porous carbon materials are products that have a wide application in the market, as they are easily found in several items of our daily life as the waste generated in Kraft pulping of the pulp and paper industry. This residue is rich in lignin, which can be easily worked to generate porous materials [1]. In this work, the structural and morphological characterization of porous carbon foams of a sustainable origin was performed aiming at their use as an attenuating material for electromagnetic radiation in aeronautical and aerospace environments.

2. Experimental

The materials will be prepared via chemical synthesis by modifying the methodology described in the literature [2] aiming at the integral use of the pulp and paper industry waste with a "polymerized resin". The acrylic polymer PMMA will be used in the medium in different granulometries for the development of porosity. The materials produced will be crushed and characterized via Raman and scanning electron microscopy and the electric will be performed through the network vector analysis combined with a waveguide in the microwaves range.

3. Results and Discussions

Figure 1 shows the structure of the generated material. It is formed by hemispheres with different orientations. In Figure 2, Rama spectroscopy reveals the presence of carbon, with two bands at 1356 cm^{-1} and 1608 cm^{-1}. The second order does not show peaks that define a crystallinity, so it reveals that the structure is amorphous. This amorphism allied to the hemispheres of the order of micro-particles suggests that this material can be used as a microwave radiation attenuator.

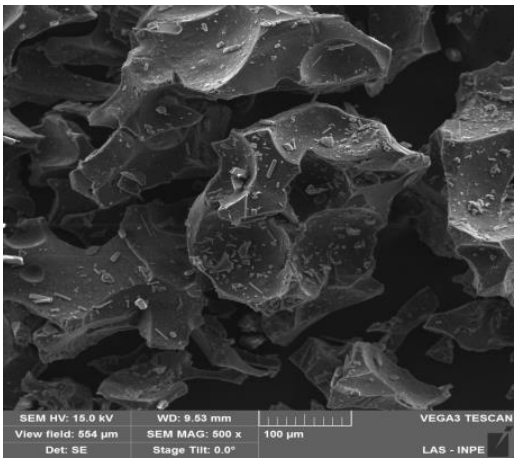

Fig. 1. *Electron microscopy of porous carbon.*

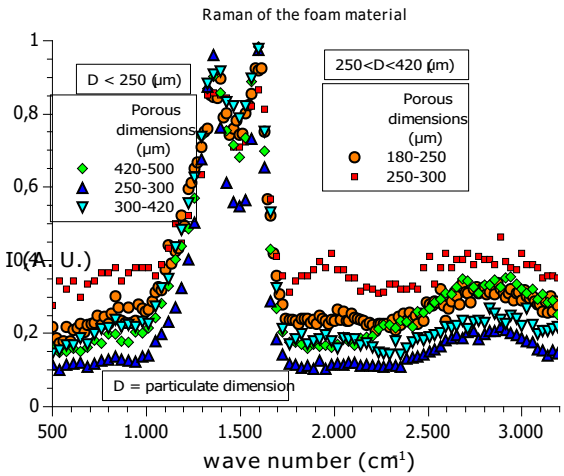

Fig. 2. *Raman porous carbon.*

4. References

[1] Grishechko LI, Amaral-Labat G, Szczurek A, Fierro V, Kuznetsov BN, Celzard A. Lignin – phenol – formaldehyde aerogels and cryogels. Microporous and Mesoporous Materials, 168, 2013b, 19-29.

[2] Seo J, Park H, Shin K, Baeck SH, Rhym Y, Shim SE. Lignin-derived macroporous carbon foams prepared by using poly(methyl methacrylate) particles as the template. Carbon, 76, 2014, 357-367.

*Corresponding author: place the email of the corresponding author here (bookman old style 9 pt)

ID 29: Scratch and tribocorrosion analysis of the NiTi60 alloy coated with DLC for use in urine processor at space station

Ana C Sene[1], Luciana O Paula[1], Angela A. Vieira[1], Polyana A. Radi[1,2], Lúcia Vieira*[1] [1]*Universidade do Vale do Vale do Paraíba – IP&D, São José dos Campos – SP* [2]*Instituto Tecnológico de Aeronáutica – LPP, São José dos Campos – SP*

1. Introduction

On Earth, the natural system provides everything we need, such as air, water and all other conditions that sustain life. In space, these functions must be done by artificial means. For this, there is a system called "Environmental Control and Life Support System" (ECLSS). One of the most important actions for support life in space is to provide potable water for consumption, food preparation and hygiene uses. Solutions to reduce friction, wear, and energy consumption and increase the life of the ECLSS equipment are relevant issue for the aerospace industry [1]. Nitinol (NiTi60) are widely used in space devices because it high wear and corrosion resistance [2-3]. Diamond-Like carbon (DLC) coatings are used in many industrial applications that requires low coefficient of friction, high wear resistance, adhesion and thermal stability [4]. In this work, DLC films were deposited by Plasma Enhanced Chemical Vapor Deposition System (PECVD) system according to the methodology previously described by Capote et al [5]. Their chemical properties were analyzed using Raman spectroscopy. These films were analyzed by scratching tests, the tribocorrosion was analyzed in synthetic urine. After tribocorrosion test, the corrosion morphology was analyzed by using Scanning Electron Microscopy (SEM). The samples studied were NiTi60 and NiTi60 thermal treated (NiTi60T).

2. Methodology

NiTi60 and NiTi60T were sanded with different sand paper grit sizes (80 to 2000) followed by a polishing with diamond paste. The samples were cleaned in an ultrasonic bath for 15 minutes: 99.5% acetone, 10% detergent in distilled water, distilled water and isopropyl alcohol, respectively. NiTi60 and NiTi60T samples were coated with DLC using the parameters described in Table 1.

Stages	Gas	Pressure (Torr)	Power (V)	Flow (sscm)	Time (min)
Cleaning	Argon	$2{,}5x10^{-3}$	400	5.5	30
Interlayer	Silane	$5x10^{-2}$ a $7x10^{-2}$	700	5.5	10
DLC Film	Acetylene	$5x10^{-3}$ a $7x10^{-3}$	700	15.4	120

Table 1. *Deposition parameters and their steps for obtaining a film*

After film deposition the films were analyzed by scratching test using progressive load from 0-50 N with a Rockwell C diamond tip, following the norm C1624-05 standard. The tribocorrosion tests were performed in synthetic urine using Al2O3 ball (ϕ= 4.76 mm) under 5N. The track distance was 2 mm under frequency of 2.5 Hz. The open circuit potential (OCP) was measured for 60 minutes in static mode, 30 minutes in dynamic mode and 60 minutes in static mode. All tests were performed in triplicate. The corrosion morphology images were obtained after tribocorrosion tests using SEM technique.

3. Results and Discussions

3.1 Scratching test

Table 2 presents the results of scratching test. The critical load (LcN) was evaluated according to the type of damage observed on scratch track, which were categorized according to ASTM C1624-05 [6]. The first critical normal load (Lc1), is related to the first damages or cracks on the films and are evidenced by the rise in the acoustic emission; The second critical load (Lc2), is related with the complete coating failure [7-8]. The treated NiTi60 sample showed no exposure to the substrate (Lc2), indicating a high resistance to scratch due thermal treatment. The imagens from scratching tracks are presented in Fig. 2, where we can identify the critical loads for each film/substrate.

Alloys	Lc1 first crack (N)	Lc2 full delamination (N)
NiTi60 Treated **load range (0-50N)**	19,5	-
NiTi60 **load range (0-50N)**	34	40

Table 2. *Scratching test results for DLC on NiTi60 and NiTi60T.*

[1]E-mail: anna.sene@hotmail.com
[2*]E-mail:lucia.vieira@univap.br

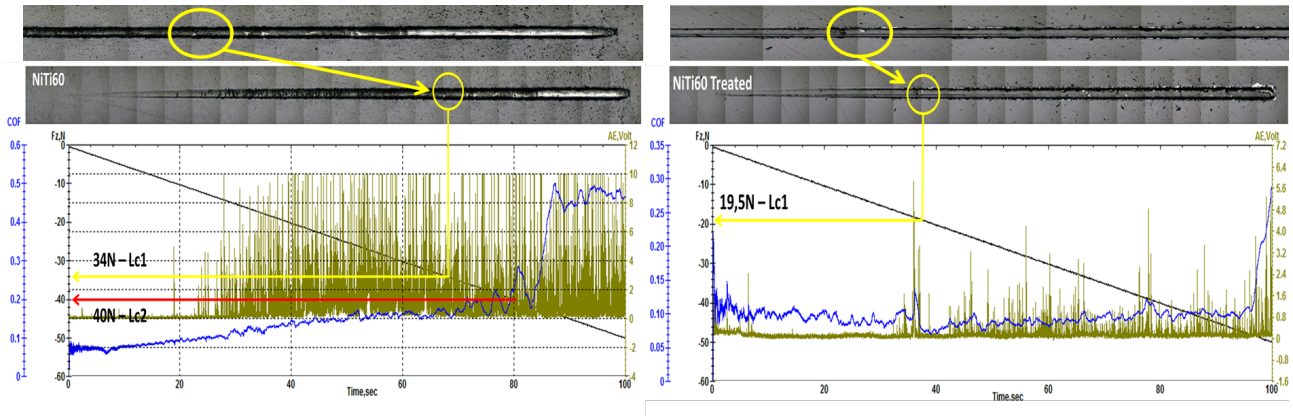

Figure 2. *Scratching test results for (a) NiTi60 and (b)NiTi60T showing Normal Load (Fz, N), friction coefficient (COF) versus time (s). The arrows and circles in yellow are indicating the places were critical loads occurred.*

3.2 Corrosion morphology analyses

The substrates with DLC film were submitted to a tribocorrosion test immersed in synthetic urine to simulate a urine processor environment. Fig. 3 (a) shows the friction coefficient from DLC over NiTi60T and bare NiTi60T, which demonstrates the effectiveness of the DLC film reducing the friction coefficient in 25.6%. Fig. 3 (b) shows the OCP of the NiTi60 alloy with and without DLC coating, showing that the DLC did not change the corrosion potential of the sample but reduced the friction coefficient. Fig. 3 (c) shows SEM images from tribocorrosion track where can be observed some cracks in the film and some corrosion pits. Fig. 3 (d) show a magnification from image 3 (c) up to 2.50k times, highlighting the pits morphology like plates. This king of corrosion is common in metal alloys.

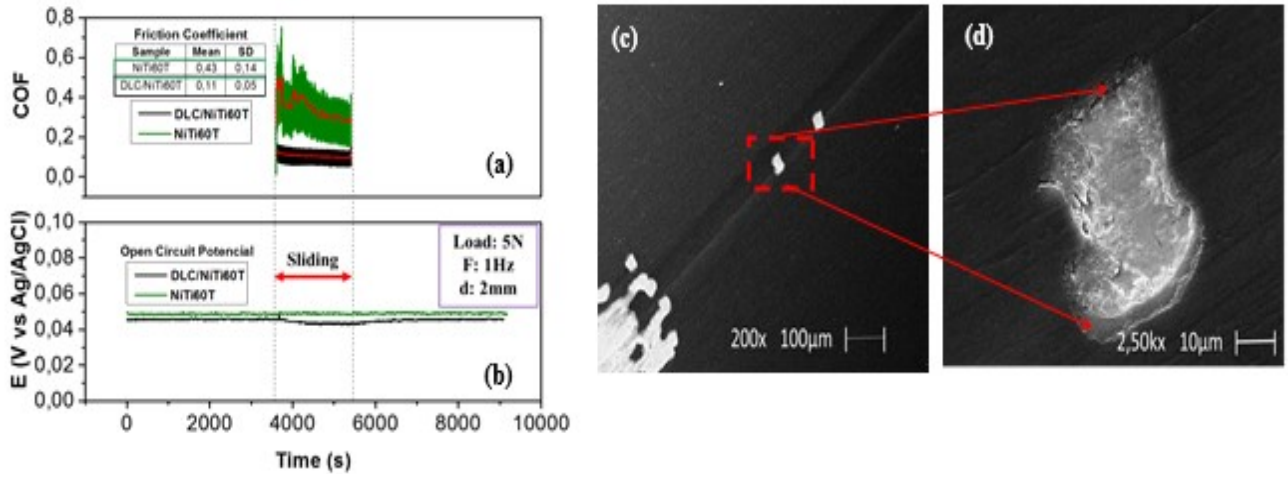

Figure 3. *Comparison of coefficients of friction coefficients (a) tribocorrosion test (b) the SEM imagens with 200 times magnification on the treated NiTi60 substrate (c) image magnification (c) up to 2.5 thousand times, and identification of the formed corrosion.*

Acknowledgments

The authors would like to thank Dr. Christopher Della Corte for NiTi60 samples supply.

References

[1] Control, T. E., & Support, L. (n.d.). NASA facts.

[2] J. Robertson, Materials Science and Engineering, p. 129-281

[3] Christopher Della Corte, Malcolm K. Stanford, Timothy R. Jett - Tribology Letters, p.1-10

[4] Abhay K. Jha, Satish Kumar Singh, M. Swathi Kiranmayee, K. Sreekumar, P.P. Sinha - Engineering Failure Analysis 17, p. 1457–146.

[5] Bonetti, L. F., Capote, G., Santos, L. V., Corat, E. J., & Trava-Airoldi, V. J. (2006). Adhesion studies of diamond like carbon films deposited on Ti6Al4V substrate with a silicon interlayer. Thin Solid Films, 515(1), 375–379. https://doi.org/10.1016/j.tsf.2005.12.154

[6] C1624-05 (2015) A. Standard Test Method for Adhesion Strength and Mechanical Failure Modes; ASTM Int. 2012;C1624-5:1–29. doi:10.1520/C1624-05R10.

[7] Nass KCF, Radi PA, Leite DMG, Massi M, da Silva, Sobrinho AS, Dutra RCL, et al. Tribomechanical and structural properties of a-SiC:H films deposited using liquid precursors on titanium;. Surf Coatings Technol. 2015;284:240–6. doi:10.1016/j.surfcoat.2015.06.080.

[8] Vieira L, Lucas FLC, Fisssmer SF, dos Santos LCD, Massi M, Leite PMSCM, et al. Scratch testing for micro- and nanoscale evaluation of tribocharging in DLC films containing silver nanoparticles using AFM and KPFM techniques;. Surf Coatings Technol. 2014;260:205–13. doi:10.1016/j.surfcoat.2014.06.065.

[1]E-mail: anna.sene@hotmail.com
[2*]E-mail:lucia.vieira@univap.br

ID 31: DEVELOPMENT OF COLD ATMOSPHERIC PRESSURE PLASMAS JETS FOR SURFACE MODIFICATION AND MEDICAL APPLICATIONS

K. G. Kostov[1]*, V. Prisyazhnyi[1], A. H. R. Castro[1], T. M. C. Nishime[1], C. Y. Koga-Ito[2], T. S. M. Mui[1], L. L. G. da Silva[3], R. P. Mota[1], A. C. Borges[2], M. Machida[4]

[1]*Faculty of Engineering – FEG, São Paulo State University – UNESP, Guaratinguetá, SP, Brazil*
[2]*Institute of Science & Techology – ICT, São Paulo State University – UNESP, São José dos Campos, SP, Brazil*
[3]*Technological Faculty in Pindamonhangaba – FATEC, Pindamonhangaba, SP, Brazil*
[4]*Insitute of Physics – IFGW, University of Campinas – UNICAMP, Campinas, SP, Brazil*

1. Introduction

The cold atmospheric pressure plasma jets (APPJs) were first reported in nineteen-nineties and since then they have been subject of intense research and development. For instance, over the last decade the number of publications on plasma jets in the literature has grown exponentially [1]. Also, various high impact journals published special issues and review papers dedicated on APPJs. A distinguishable feature of cold plasma jets is that they can be operated in air and provide enhanced chemistry via production of reactive species (radicals, photons and charged particles) while the gas temperature is maintained sufficiently low for processing of organic and biological components. Nowadays, plasma jets are routinely used in material processing for surface cleaning and deposition, etching, surface activation of polymers, decontamination of surfaces etc. [1]. Recently, application of non-thermal plasma jets in living tissues has been extensively studied giving the origin of so-called plasma medicine [1, 2].

2. Experimental

In most plasma jets barrier discharge is excited in a noble gas that flows through a thin dielectric tube and the resulting plasma is projected into the surrounding ambient forming a several cm-long plasma plume. An important issue for the operation of a plasma jet is its geometry, which together with dielectric properties of the substrate, strongly influences the shape and the extension of generated plasma plume. Therefore, depending on the intended application many different plasma jet configurations have been investigated. Here, we report several plasma jet devices developed in our laboratory for specific applications.

3. Results and Discussions

The exit geometry of a plasma jet device directly affects its gas flow dynamic and electric properties. Here we study the effect of a horn-like jet nozzle, which allows extending plasma over larger area of the sample. This jet configuration was used for adhesion improvement of Al alloys and also for treatment of seeds.

A three-electrode plasma jet configuration (one powered electrode and two grounded) was especially designed for deposition of polymer films at atmospheric pressure. Argon was employed as working gas for plasma generation. Mixtures of air with acetylene or hexamethyldisiloxane (HMDSO) were used as polymerizing agents. The films were deposited on glass substrates placed on an auxiliary grounded electrode and can be used as biocompatible coating or for corrosion protection.

A crucial question in plasma medicine is how to deliver active plasma species to tissues or organs inside human body. Most commercially available plasma sources are too big and rigid for this purpose. Here, we report a method that allows generation of cold plasma jet at the end of long (up to few meters), flexible, plastic tube. The tube can be held with hand without risk of electric shock and the plasma jet can be easily handled and directed to a target. Here, we will describe the method and present some results of surface modification of polymers. Also, *in-vitro* experiments for microbial inactivation using APPJs at the end of plastic tube will be presented. Special attention will be given to plasma treatment of biofilms that represent major infection risk for medical gear in hospitals.

Finally, we will report some results of *in-vivo* tests performed on the tongues of laboratory rats that were experimentally infected with *C. albicans.*

4. References

[1] J. Winter, R. Brandenburg, and K.-D. Weltmann, *Plasma Sources Sci. Technol*. **24,** 064001 (2015).
[2] H. Tanaka and M. Hori, *J. Clin. Biochem. Nutr*. **60,** 29 (2017).

Acknowledgments

This work was supported by FAPESP under research grant #2015/21989-6

*Corresponding author: kostov@feg.unesp.br

ID 33: AA7050-T7451 ALUMINUM ALLOY CHARACTERIZATION: MICROESTRUCTURE AND FATIGUE BEHAVIOR

Yara Coelho Bastos[1], Verônica Mara de Oliveira Velloso[1] and Herman Jacobus Cornellis Voorwald[1]
[1]*Group " Fatigue and Aeronautical Materials" Universidade Júlio de Mesquita Filho, Unesp, Campus de Guaratinguetá*

1. Introduction

When a material is developed in aerospace industry, mechanical properties evaluation is very important. Structural components, such as landing gear are subjected to cyclic loads during take-off, fligh and landing and, therefore, fatigue properties are taken into account. Aerospace industry applies the aluminum alloy 7000 series due to its high mechanical strength, high strength to weight ratio, and low cost. However, these alloys need surface treatments to withstand corrosion and work temperatures higher than room temperature. The microstructural characterization and statistical analyzes make possible the mechanical behavior understanding of this alloy. The AA7050-T7451 alloy is subjected to aging and surface treatments that can reach temperatures capable of modifying the original microstructure, typical of these alloys (with micro and nanometric precipitates). Therefore, the aim of this study was to characterize the AA7050-T7451 alloy microstructurally and to analyze its behavior under cyclic load. This work is part of a larger study that modifies aluminum alloy through surface treatments to increase structural components life. The previous characterization of the alloy without surface treatment will allow a real understanding of its contribution to the mechanical behavior of these alloys.[1 2]

2. Experimental or Theory

AA7050-T7451 aluminum alloy was prepared following the usual metallographic characterization. The rotating bending fatigue tests were performed using INSTRON ® R.R.Moore model. The fatigue tests were conducted until fracture, with loading ratio R= -1. Fifteen (15) test pieces were used to obtain the SxN curve. The aluminum alloy were characterized by Vickers microhardness; optical microscopy (grain size and coarse precipitates quantification); SEM and XRD. Fatigue results were analyzed with Log – Normal and Weibull models.

3. Results and Discussions (bold face Times New Roman 11 pt)

The results obtained will be correlated with fatigue behavior. Figures 1 and 2 presents double aged aluminum alloy. According to ANTUNES (2017) and MAZZER (2013) who studied the AA7050 microstructure, the dark points identified by red arrows are intermetallic particles and showed composition equal to Al7Cu2Fe and Mg2Si. After chemical attack, Figure 2 shows that the precipitates are located in the grain boundaries. The microstructure is homogeneous with a distribution of varied grain sizes that, through the ImageJ software, were found values of average grain size, fine and coarse particles percentage and particles per area (Table 1).

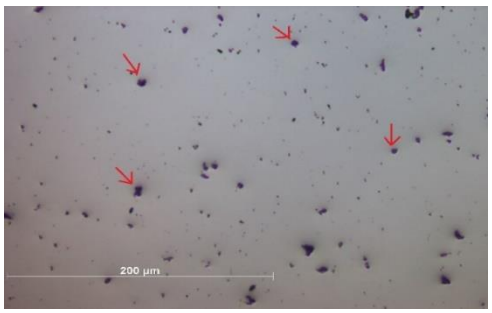

Fig. 1. *AA7050-T7451 alloy optical microscopy: grain morphology and the presence of intermetallic particles (20x). No chemical attack.*

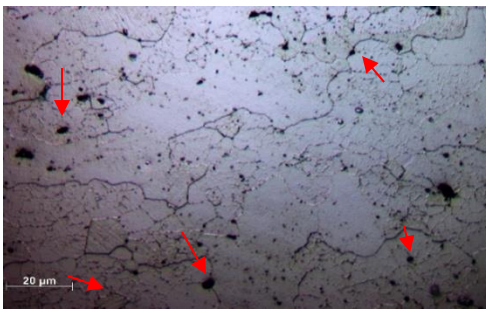

Fig. 2. *AA7050-T7451 alloy optical microscopy:grain morphology and the presence of intermetallic particles (50x). Chemical attack - Keller.*

The fine and coarse grains were circulated providing a good observation how the grains are arranged throughout the sample area (Figures 3 and 4). SEM analysis shows the intermetallic particles. XRD technique was used to identify the phases, corresponding to Al (FCC), which represents about 89.6% of the mass composition (MINTO, 2016).

*Corresponding author: place the email of the corresponding author here (bookman old style 9 pt)

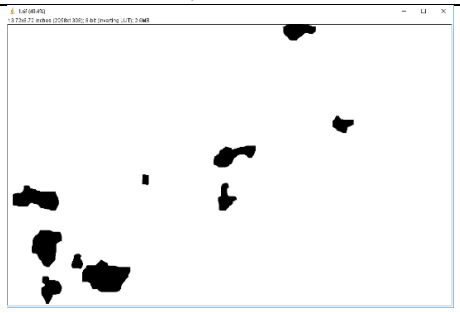

Fig. 3. *AA7050-T7451 alloy optical microscopy: fine grains distribution.*

Fig. 4. *AA7050-T7451 alloy optical microscopy: coarse grains distribution.*

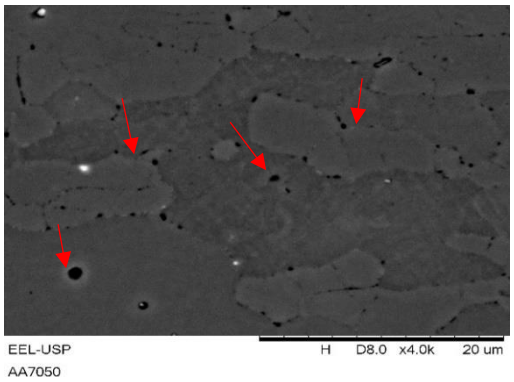

Fig. 5. *SEM of AA7050-T7451 alloy: distribution and morphology of intermetallic particles and grains. Chemical attack - Keller*

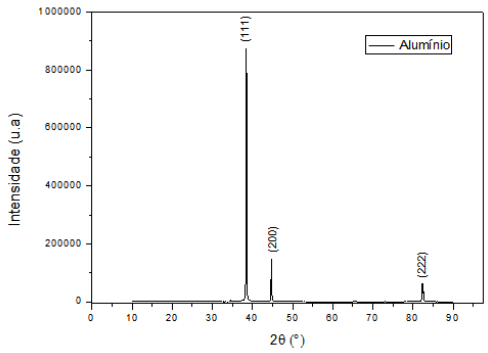

Fig. 6. *AA7050-T7451 alloy DRX: Al (FCC)..*

Fatigue tests performed at stresses ranging from 50% to 70% of yield strength.

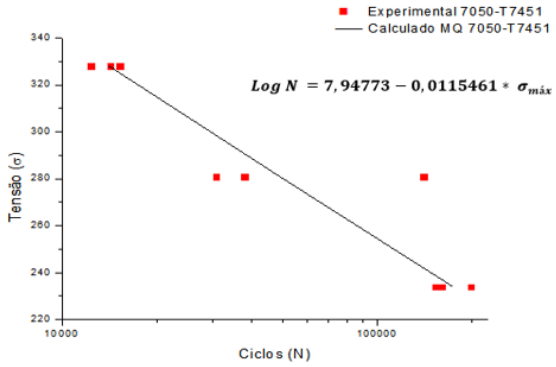

Fig. 7. *Fatigue test results: Alloy AA7050-T7451*

Aluminum Alloy AA 7050-T7451

Coarse Grains	31,09 ± 6,36
Fine Grains	68,91 ± 6,36
Coarse Particles	3,38 ± 0,39
Particles/Area	1133,5 ± 64,61

Table. 1. *Fine, coarse grains and intermetallic particles per area values.*

The formation of metallic particles observed in the micrographs shows a common feature of the aluminum alloys of the 7000 series in the condition T7451 observed in the work of ANTUNES (2017), which can increase the mechanical strength of the material.

4. References

[1] MAZZER, Eric Marchezini et al. Caracterização microestrutural e mecânica da liga AA7050-T7451 reciclada por conformação por spray e extrusão. 2013.
[2] ANTUNES, Ana Márcia Barbosa. Estudo do comportamento em fadiga de alto ciclo das ligas de alumínio AA6351 e AA7050 para aplicação aeronáutica. 2017. Tese de Doutorado. Universidade de São Paulo.
[3] MINTO, Thiago Alexandre. Influência do tratamento superficial 3IP na vida em fadiga da liga de alumínio AA7050-T7451 para aplicação aeronáutica. 2016.

Acknowledgments

Thanks to the Fatigue Group and Aeronautical Materials of UNESP.

*Corresponding author: place the email of the corresponding author here (bookman old style 9 pt)

ID 34: COMPARISON OF NITROGEN AND ARGON PLASMA IMMERSION ION IMPLANTATION (AND DEPOSITION) INSIDE AND OUTSIDE STAINLESS STEEL 304 TUBES

Carla da Silva[1,2]*, Mario Ueda[1], Carina B. Mello[1], Helfried Reuther[3].

[1]*Associated Laboratory of Plasma, National Institute for Space Research, São José dos Campos, SP, Brazil*

[2] *Associated Laboratory of Sensors and Materials, National Institute for Space Research, São José dos Campos, SP, Brazil*

[3] *Institute of Ion Beam Physics and Materials Research, Dresden, Germany*

1. Introduction

Hollow cathode discharge has been employed in a wide variety of applications: plasma immersion ion implantation in tubes, surface modification and deposition of thin film, space propulsion, basic plasma research, nitriding, among others [1]. Recently, surface treatments have been carried out using hollow cathode discharges as a plasma source due to the better plasma confinement and its higher density [2].

In this work, a comparison of nitrogen and argon plasma immersion ion implantation in tubes of stainless steel 304 was carried out, in order to investigate the influence of working gas in the treatment.

2. Experimental

For the present PIII processing, hollow cathode configurations were chosen for the experiments using stainless steel 304 tubes with 11.0 and 4.0 cm diameter and 20.0 cm of length. In these configurations, a sample support (ss) placed at 10.0 cm distance from the tube was used. Samples of stainless steel 304 and silicon wafer were placed inside and on the top of tube, as well as and on the ss.

Argon ion bombardment was used previous to the treatment of the samples surface for their cleaning, during 10 minutes and then, the nitrogen or argon implantation was carried out for up to 120 minutes.

3. Results and Discussions

The analyses of elemental depth profiles obtained after the treatment using the ss placed at 10.0 cm of distance from the tube (11.0 cm diameter) allowed to verify that the maximum depth of nitrogen ion implantation was 43.0 nm with nitrogen peak at 26.0 at.% in silicon sample placed at the ss, as shown in Fig. 1. However, residual oxygen can be observed in large amount on the surface of the Si sample. When there is such an elevated percentage of oxygen present on the surface of SS304 during the N-PIII, strong segregation of nickel should occur [3]. Indeed, that phenomenon can be verified in this case. In the standard stainless steel samples, the elements composing it show stoichiometric iron compared with other elements that are Cr, Ni, Mn, Si and C. Due to this fact, it was verified by a TRIM simulation code that the sputtering rate will also follow the stoichiometric ratio.

Figure 2 shows the depth profiles in silicon sample treated by Ar-PIII, and it can be observed a great percentage of iron (35.0 at.%) but the atomic percentage of chromium is around zero whereas that of nickel is 14.0 at.%. Using the argon as working gas, the nickel segregation was not observed any more, although a high oxygen concentration was measured on the surface of silicon sample. It was observed that chromium was present in low atomic percentage instead (chromium segregation).

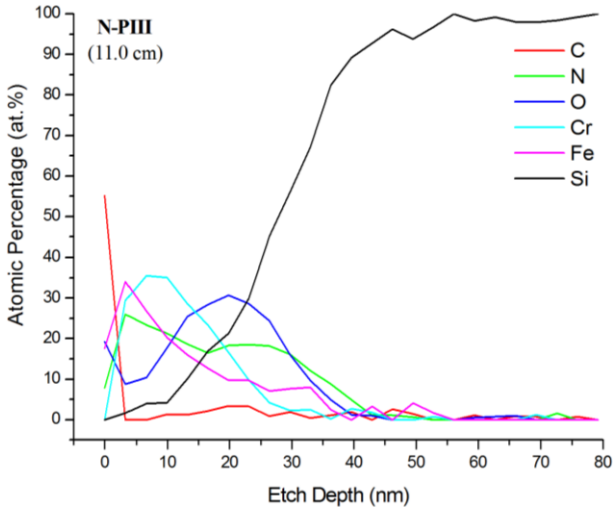

Fig. 1. *Elemental depth profile obtained by Auger Electron Spectroscopy (AES) of silicon sample treated with N-PIII.*

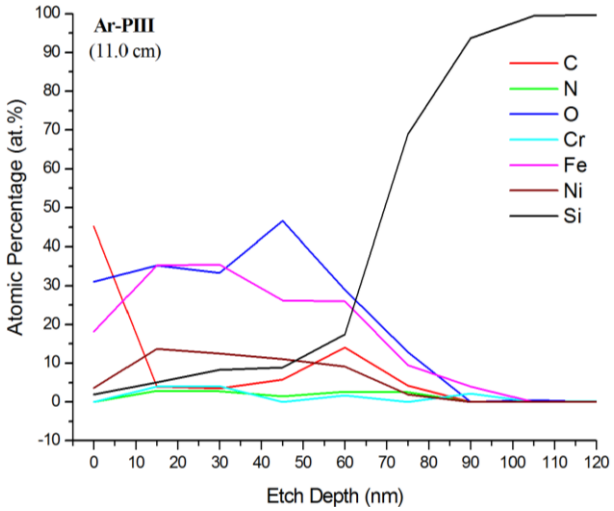

Fig. 2. *Elemental depth profile obtained by Auger Electron Spectroscopy (AES) of silicon sample treated with Ar-PIII.*

*Corresponding author: carla.sjc@gmail.com

The X-Ray Diffraction data obtained allow us to verify the formation of expanded austenite in sample treated with N-PIII. On the other hand, in the samples treated by Ar-PIII, it was observed the formation of FeO. These phase and compound formations were observed only in the samples placed inside the tube. In the samples placed on the top of the tube and at the ss no phase or compounds were formed.

Results obtained in other tube diameter, will be presented at the conference with results of XRD, FEG, EDS, among others.

4. References

[1] S. Muhl, A. Pérez. Thin Solid Films, **579**, 174-198, (2015).
[2] M. Ueda, A. R. Silva, E. J. D. M. Pillaca, S. F. M. Mariano, R. M. Oliveira, et. al. Rev. Sci. Instrm., **87**, 013902-013902-8, (2016).
[3] X. Tian, R. K. Y. Fu, L. Wang, P. K. Chu. Mater. Sci. Eng., A., **316**, 200-204, (2001).

Acknowledgments

This project is supported by CAPES and MCTI.

*Corresponding author: carla.sjc@gmail.com

ID 37: MICROSTRUCTURAL EVALUATION OF MARAGING 300 STEEL LASER TREATED

Adriano Gonçalves dos Reis[1,2]*, Danieli Aparecida Pereira Reis[3,4], Antônio Jorge Abdalla[4,5], Antônio Augusto Couto[2,6], Luciana Aparecida Narciso da Silva Briguente[3], Luiz Ricardo Olivetti Marchetto[3], Javier Oñoro Lopez[7]

[1]*Universidade Estadual Paulista (Unesp), Instituto de Ciência e Tecnologia, São José dos Campos.*
[2]*Instituto de Pesquisas Energéticas e Nucleares (IPEN), Ciência e Tecnologia de Materiais, São Paulo.*
[3]*Universidade Federal de São Paulo (UNIFESP), Instituto de Ciência e Tecnologia, São José dos Campos.*
[4]*Instituto Tecnológico de Aeronáutica (ITA), Materiais e Processos de Fabricação, São José dos Campos.*
[5]*Instituto de Estudos Avançados (IEAv), Fotônica, São José dos Campos.*
[6]*Universidade Presbiteriana Mackenzie (UPM), Engenharia de Materiais, São Paulo.*
[7]*Universidade Politécnica de Madrid (UPM), Engenharia e Ciência de Materiais, Madrid.*

1. Introduction

Maraging steels are Ni-Co-Mo-Ti alloys of ultra-high resistance and spread application, since defense and nuclear industry until aeronautic components, pressure vessels and sports industry. Maraging steels have been investigated by a number of steel producers, mainly for nuclear and aerospace applications, due to high mechanical resistance allied to an excellent tenacity, behavior that are required to reduce weight and increase safety [1]. These steels are part of the priority list of advanced materials to the Brazil's technological development and are proposed to replace the current 300M in some parts of Brazilian satellite launcher [2,3]. Maraging steels are composed by a metastable martensitic microstructure. Some research show that they revert to austenite when heated at intermediate temperatures, close to the aging temperature, becoming worst when increasing temperature and time of exposure [1]. This work aims to evaluate the microstructural behavior of a maraging 300 steel after superficial laser treatment to reduce the oxygen permeability in the structure, increasing the mechanical resistance at elevated temperatures. Microstructural characterization will be done by scanning electron microscopy (SEM), X-ray diffraction and roughness by profilometry.

2. Experimental

The maraging steel used in this study was a 300-grade solution treated at 820 °C— 1 h in a Brasimet Koe 40/25/65 furnace. Samples of 20 x 20 mm and 3 mm in thickness was grinded by using 200# and 600# SiC paper and then cleaned with acetone in a ultrasonic bath for 20 min. Laser surface treatment was carried out using a Rofin DY 033 Nd:YAG continuous laser, which was operated at a wavelength of 1064nm. The focus laser spot size had a diameter of 0.5 mm, and the treatment was performed under a nitrogen flow rate of 20 l/min. The energy and the sample speed were set at 675 W and 100 mm/s, respectively. The focal length of the lens used equaled 120 mm. Following laser surface treatment, the surface was characterized by scanning electron microscopy (SEM), X-ray diffraction and profilometry.

3. Results and Discussions

Fig. 1 is a SEM micrograph showing the surface of the laser treated maraging 300 steel. We clearly see the laser path, each track typically 500 µm wide.

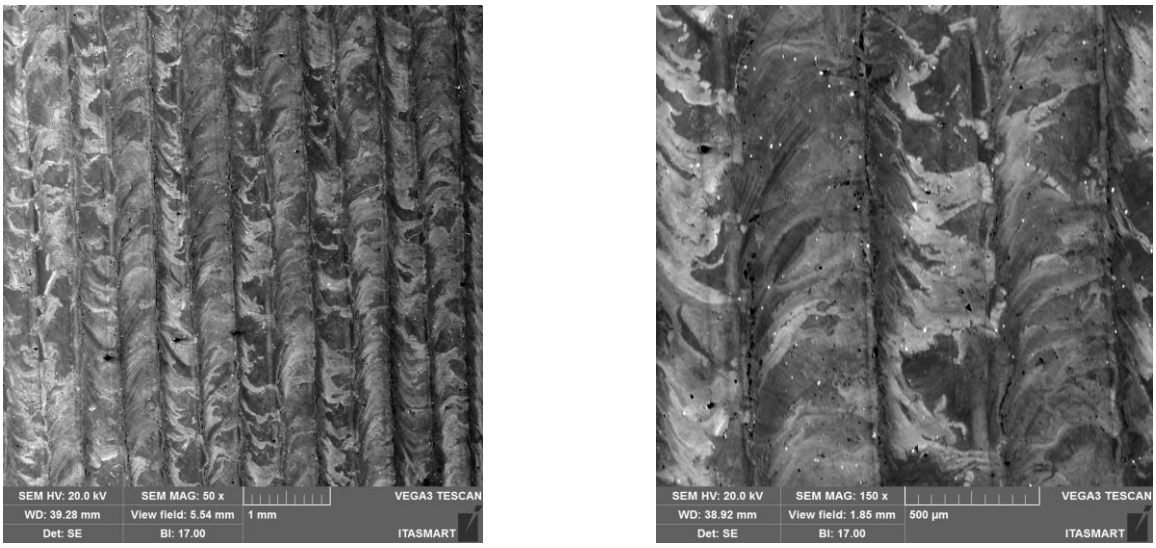

Fig. 1. *Micrograph maraging 300 steel surface treated with magnification of (a) 50x and (b) 150x.*

*Corresponding author: adriano.reis@ict.unesp.br

Fig. 2 is the 2D and 3D profilometry of the laser treated material. Surface roughness results: R_a = 634 ± 160 nm; R_q = 789 ± 185 nm and R_t = 8,2 ± 3,2 nm.

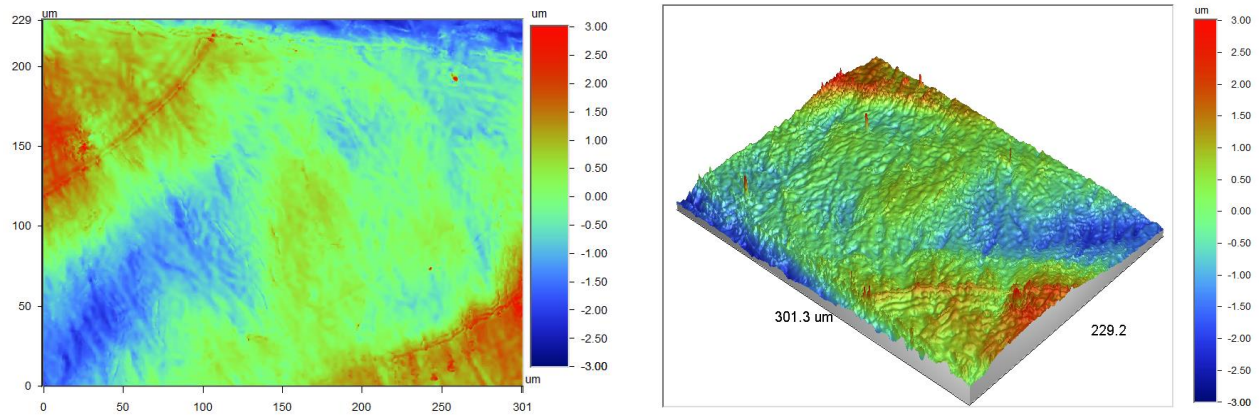

Fig. 2. *2D (a) and 3D (b) optical profilometry images of maraging 300 steel laser treated.*

The XRD pattern in the 2θ ranging from 30–100º of maraging 300 steel with and without laser treatment are shown in Figure 3. Both samples exhibit diffraction peaks due to the martensitic phase α'-Fe, but laser treated sample exhibit additional diffraction peaks related to austenite phase (γ-Fe) at 50.7° and related to Fe_2N/Fe_3N at 40.2°. Austenite phase formation can be associated to the overaging caused by laser heating [1,4], and the iron nitrides are probably associated to the nitrogen gas added during the laser treatment.

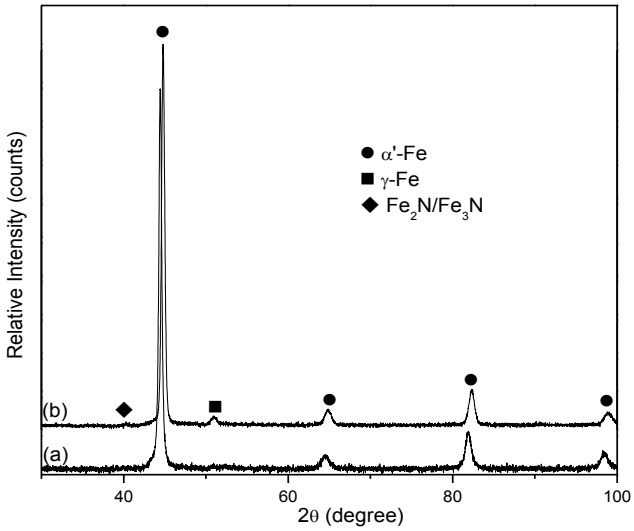

Fig. 3. *X-ray diffraction pattern of maraging 300 steel (a) without laser treatment and (b) laser treated.*

Creep tests will be performed to evaluate the effect of microstructural change by laser treatment in the mechanical resistance at elevated temperatures.

4. References

[1] W. Sha and Z. Guo, "*Maraging steels: modelling of microstructure, properties and applications*", Woodhead Publishing, USA, (2009).

[2] F. C. R. Assunção, "*Materiais avançados: 2010-2022*". Centro de Gestão e Estudos Estratégicos, Brasília, (2010).

[3] D. R. Santos, *Otimização dos parâmetros de tratamento térmico e soldagem do aço maraging 18Ni 300*. 2001. 118 f. Dissertação (Mestrado em Engenharia Mecânica) - Universidade Estadual Paulista Julio de Mesquita Filho, Faculdade de Engenharia de Guaratinguetá.

[4] A. G. Reis, D. A. P. Reis, A. J. Abdalla, J. Otubo, Mater. Charact., **107**, 350-357, (2015).

Acknowledgments

This work was supported by CNPq (Proc.nº 403070/2016-3) and FAPESP.

*Corresponding author: adriano.reis@ict.unesp.br

ID 38: STUDY OF THE RELATIONSHIP BETWEEN PLASTIC DEFORMATION AND CORROSION RESISTANCE

Mariana Cristina de Oliveira[1]*, Maximiliano Pressiani [2] Heloísa Andrea Acciari[1], Eduardo Norberto Codaro[1]
[1]*Universidade Estadual Júlio de Mesquita Filho, Guaratingueta, Brazil*
[2]*Universidad Tecnológica Nacional, Santa Fe, Argentina*

1. Introduction

The steel API 5L X65 is commonly used to manufacture pipelines for oil and gas transport and extraction. In order to improve the mechanical properties these pipeline are fabricated through TMCR processing [1]. The lower strength microalloyed steels are less susceptible to generate and propagate cracks under stress within sour environments (containing H_2S) [2].

The working environment is under high internal pressures [1]. Internal pressures cause hoop stress wich should be evaluated in order to keep the structural integrity of a dented pipeline containing a curvature change without a reduction in wall thickness [3]. Moreover these pipeline can be damaged by plastic deformation by outside forces such as ground subsidence, ground liquefaction, cold bending and mechanical damage. These damages modify the mechanical properties such as tensile strength, yield strength and fracture toughness [4]. Corrosion processes are responsible for 50% of the failures such as: fractures, ruptures, contaminations, explosions in pipelines These failures can present tragic and even fatal consequences. Thus understanding the principles of corrosion as well as avoiding it has been a major challenge in the engineering field. In addition to the environmental and social impacts caused by these failures, there are economic impacts because the damages caused by the corrosion generate extremely high costs to repair or replace the pipe in question [5]. Therfore the pipeline deformed should be evaluated about load bearing capacity and resistance corrosion in order to establish the integrity of pipeline.

2. Experimental

The specimens were cut from the tube in the transverse direction by oxyfuel in a weld-free region. A traction machine was used to deform the samples plastically by 2.5%. For the microscopic analyzes the samples were mechanically sanded in an electric polishing machine with sandpaper of 120 to 2500 granules, polished with cloth and alumina (particles of 1μm), rinsed in ultrasonic bath with propan-2-ol for 15 minutes. The chemical attack was done with Nital 2%. An optical microscope was used with 500-fold magnifications to analyze the microstructure of the specimens. The Icc3 Camera connected to the microscope and the AxionVision Release 4.9.1 SP3 software (08-2013) were used to capture the images of the microstructures.

To perform the electrochemical tests the samples were mechanically sanded (granules 120 to 2500), rinsed in a propan-2-ol ultrasonic bath and dried with a cold air jet. Five replicates were made for the deformation condition and the standard condition (0% deformation) for all electrochemical assays. At each repetition the surface was renewed to ensure that in all the experiments the specimens were in the same conditions. All electrochemical measurements were performed on an Autolab PGSTAT302 potentiostat, equipped with Autolab NOVA 1.10 software for data collection and analysis. The experimental arrangement were: an electrochemical cell for flat samples (PAR) containing a solution of 236.5 grams of water, 12.5 grams of sodium chloride and 1.25 grams of acetic acid (NACE 177A), an reference electrode of Ag / AgCl and a silver wire counter electrode. The electrochemical tests were done in depleted environment bubbling N2 gas for 30 minutes before starting the experiment and during the experiment time. Firstly, the open circuit potential (OCP) was monitored for 3 h, the value at the end of this period being recorded and taken as a reference to obtain the Tafel curves (at a rate of 0.166 mV s -1, starting the scan To -250 mV of the OCP and continuously following up to +250 mV of OCP).

3. Results and Discussions

The microstructures of the samples in the standard condition (Figure 1) and plastic deformation condition 2.5% (Figure 2) are shown below. It is possible to observe a ferritic matrix with perlite points.

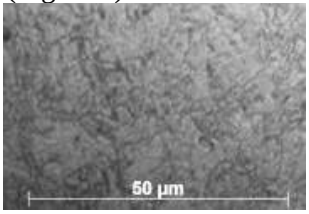

Fig. 1. *Image obtained by optical microscopy of API 5L X65 steel for standard condition.*

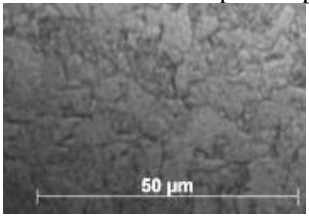

Fig. 2. *Image obtained by optical microscopy of API 5L X65 steel for 2,5% plastic deformation condition.*

*Corresponding author: marianaeng@uol.com.br

It is also possible to observe a gentle extension of the grains as the deformation of the steel increases.

All curves of the electrochemical tests were obtained for the first replicate of each deformation condition. The potential in open circuit (Figure 3) does not present significant variation, reaching in all conditions a near steady state. The relative stability of the open circuit potential indicates that there is no significant change in the anodic and cathodic reactions during corrosion. Figure 4 represents the Tafel polarization curves. It is possible to observe that the corrosive process is controlled by activation under all conditions, since there is a constant increase of the anodic and cathodic current with the increase of potential [6]. Under all conditions, the curves have similar profiles and velocities.

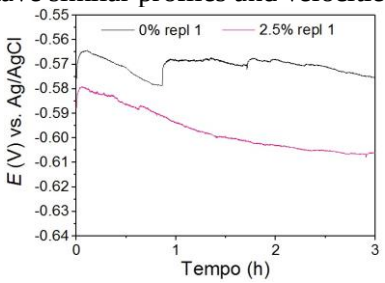

Fig. 3. *Open circuit curves of the API 5L X65 steel under different conditions of plastic deformation obtained in a standard acid medium (NACE 177).*

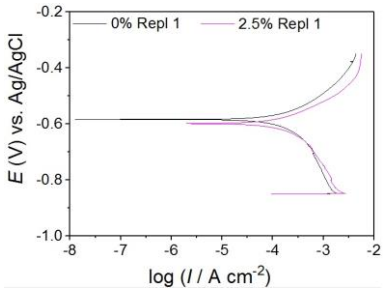

Fig. 4. *Tafel curves of the API 5L X65 steel under different conditions of plastic deformation obtained in a standard acid medium (NACE 177).*

The values of the polarization resistance (Rp) were calculated from the Tafel plots for all the replicates of each condition, it was verified that the standard condition showed less dispersion than deformed. As shown in the scatter diagram below:

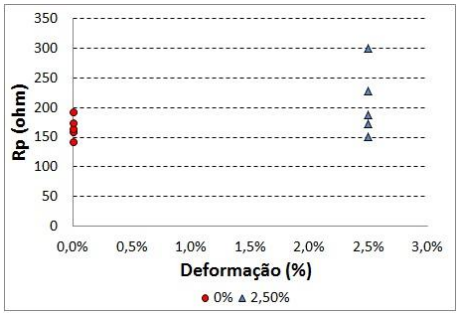

Fig. 5. *Dispersion diagrams of the Rp values calculated from the Tafel curves.*

Even though there is a dispersion between the values, it is not possible to observe a significant variation between Rp values and the increase in deformation.

The next step of the work is to analyze other deformation conditions (0.5%, 1.0%, 1.5% and 2.0%) and perform electrochemical impedance experiments for all conditions for a statistical and comparative analysis between The electrochemical methods.

4. References

[1] Sayyed H. Hashemi. "*Correction factors for safe performance of API X65 pipeline steel*", International Journal of Pressure Vessels and Piping, 86, 533-540 (2009).

[2] A. Fragiel, S. Serna, B. Campillo, L. Cota. "*Dissimilar mechanical properties—microstructures microalloyed pipeline steels cracking performance under sour environment*", Materials Science and Engineering A, 467, 1-7, (2007).

[3] Jong-hyun Baek∗, Young-pyo Kim, Woo-sik Kim, Jae-min Koo, Chang-sung Seok, "*Load bearing capacity of API X65 pipe with dent defect under internal pressureand in-plane bending*", Materials Science and Engineering A, 540, 70-82 (2012).

[4] Jong-hyun Baeka, Young-pyo Kim, Cheol-man Kim, Woo-sik Kim, Chang-sung Seok. "*Effects of pre-strain on the mechanical properties of API 5L X65 pipe*", Materials Science and Engineering A, 527, 1473-1479 (2010).

[5] Terzi R, Mainier FB. "*Monitoramento da corrosão interna em plataformas offshore*". TECNO-LÓGICA, 12, 14-21 (2008).

[6] TAIT W. S. "*An introduction to electrochemical corrosion testing for practicing engineers and scientists*", PairODocs Publications, 26, 138 (1994).

Acknowledgments

Leandro de Paula for the supply of API 5L X65 samples. UNESP / FEG and Capes for financial resources.

*Corresponding author: marianaeng@uol.com.br

ID 39: Treatment of reentrant niobium cavities via Plasma Immersion Ion Implantation and HiPIMS

Michel Felipe Lima de Araújo, Lilian Hoshida, Odylio Denys de Aguiar, Carina Barros Mello, Graziela da Silva Savonov, Elvis Camilo Ferreira, Vincenzo Liccardo, Rogério de Moraes de Oliveira
[1]National Institute for Space Research (INPE)

1. Introduction

Reentrant niobium cavities are used in the Mario Schenberg gravitational wave detector, operating in DAS / INPE, playing the role of parametric transducers. They are part of a system designed to convert mechanical vibrations from a solid Al-Cu sphere of the detector into electrical signals. Nitrogen plasma immersion ion implantation (PIII) and High Power Impulse Magnetron Sputtering (HiPIMS) have been evaluated to treat these cavities in order to increase its respective quality factors (Q).

The first method is devoted to implant nitrogen ions into the near surface of niobium, since it was reported recently [1] that the presence of interstitial nitrogen into the crystal lattice of Nb has the effect of increasing such Q-values. The second method is devoted to deposit stoichiometric niobium nitride (NbN), another successful method reported in the literature [2,3] to attain this goal.

There is a vast investigation [4,5,6,7] being carried out by the international community in order to increase the quality factor of niobium superconducting resonant cavities, which also have application in High Energy Physics, specifically in particle accelerators [8,9].

One of the most promising studies regarding the improvement of Q, makes use of thermal treatment for the insertion of nitrogen on the surface of niobium [10,11]. These results present good convergence with recent experimental data attained by the PIII / LAP group at INPE [1].

A set of characterization results will be presented for samples treated by both methods, including profilometry, X-ray diffraction, scanning electron microscopy (field emission gun), X-ray photoelectron spectroscopy and atomic force microscopy.

2. Description of Techniques

A variation of conventional PIII has been used herein in order to heat the substrate during nitrogen ion implantation. In the current experiments it has been performed High Temperature PIII (HTPIII). The heating of the substrates facilitates the diffusion of the nitrogen ions implanted into niobium and it is an efficient tool to control de depth of the implantation and respective atomic concentration.

This controlled process can lead to the formation of nitrides and also the implantation of nitrogen in interstitial spaces of the crystal lattice of niobium. Concerning HiPIMS, in the process, a niobium target of high purity is sputtered in reactive glow discharge, mixing argon and nitrogen. The aim is to partially ionize Nb particles due to the high peak power density applied to the targed; thus it is expected the implantation and deposition of niobium and nitrogen into/onto the surfaces of Nb samples.

3. Expected Results

After evaluating the set of characterization methods for Nb samples treated by HTPIII and HiPIMS, some experimental conditions previously used will be repeated for the treatment of the cavities in order to search for a correlation between the respective operation parameters of these processes and the Q-factors.

4. References

[1] Liccardo, V. ; França, E. K. ; Aguiar, O. D. ; Oliveira, R.M. ; Ribeiro, K. L. ; Silva, M. M. N. F. “Study of the effect of NbN on microwave Niobium cavities for gravitational wave detectors”. Journal of Instrumentation, v. 11, p. P07004-P07004, (2016).

[2] LUO, Quanshun; YANG, S.; COOKE, K. E. Hybrid HIPIMS and DC magnetron sputtering deposition of TiN coatings: Deposition rate, structure and tribological properties. Surface and Coatings Technology, v. 236, p. 13-21, 2013.

[3] HELMERSSON, Ulf et al. Ionized physical vapor deposition (IPVD): A review of technology and applications. Thin Solid Films, v. 513, n. 1, p. 1-24, 2006.

michellfisico@gmail.com

[4] FURTADO, Sérgio Ricardo. Desenvolvimento de transdutores paramétricos de alta sensibilidade para o detector de ondas gravitacionais Mario Schenberg. **Doctor Thesis, Inst. Nacional de Pesquisas Espaciais**, 2009.

[5] BARISH, Barry C. The detection of Gravitational Waves with LIGO. arXiv preprint gr-qc/9905026, 1999.

[6] GENG, R. L. et al. Testing the first 1300 MHz reentrant cavity. In: **Proceedings of the Workshop of Pushing the Limits of RF Superconductivity, Argonne National Laboratory**. 2004.

[7] KELLY, Michael. Superconducting radio-frequency cavities for low-beta particle accelerators. **Reviews of Accelerator Science and Technology**, v. 5, p. 185-203, 2012.

[8] WEINGARTEN, Wolfgang. Field-dependent surface resistance for superconducting niobium accelerating cavities. **Physical Review Special Topics-Accelerators and Beams**, v. 14, n. 10, p. 101002, 2011.

[9] CIOVATI, Gianluigi; DHAKAL, Pashupati; GUREVICH, A. Decrease of the surface resistance in superconducting niobium resonator cavities by the microwave field. **Applied Physics Letters**, v. 104, n. 9, p. 092601, 2014.

[10] GRASSELLINO, A. et al. Nitrogen and argon doping of niobium for superconducting radio frequency cavities: a pathway to highly efficient accelerating structures. **Superconductor Science and Technology**, v. 26, n. 10, p. 102001, 2013.

[11] ROMANENKO, A. et al. Proximity breakdown of hydrides in superconducting niobium cavities. Superconductor Science and Technology, v. 26, n. 3, p. 035003, 2013.

michellfisico@gmail.com

ID 40: INVESTIGATION OF WC-CO HARDMETAL SURFACES PREPARED FOR BORIDING PROCESSES

da Silva Neto, J. V.[1]*, Fraga, M. A.[1], Contin, A.[1], Campos, R. A.[2], Trava-Airoldi, V. J.[1], Corat, E.J.[1]
[1]*National Institute for Space Research, INPE, São José dos Campos*
[2]*Federal University of South and Southeastern Pará, Marabá*

1. Introduction

Regarding to industrial performance, tools having higher hardnesses and toughness are those that will deliver better results and longer lifespan, what made hard metal tools widely used. Looking for enhancing this properties chemical vapor deposition (CVD) diamond coatings are quite promising candidates [1]. However the most used type of hard metal, tungsten carbide (WC-Co) tools, have Cobalt as binder metal, this element has catalyst function on the formation of graphite, and causes poor film adhesion during CVD diamond deposition process [2]. This promoves intense search for methods to mitigate or neutralize its negative influence, one of them is the formation of a blocking boride barrier through controlled reactions between boron and the constituent elements of the substrate, such as Carbon, Tungsten and the process main target, Cobalt, previously achieved by reactive thermodiffusion [3]. This work aims the development of a boriding process through activation by hot filament assisted chemical vapor deposition (HFCVD). Finally samples were analyzed by Energy-dispersive X-Ray Spectrometry (EDS) and X-Ray Diffraction (XRD).

2. Experimental

Tungsten carbide samples with 9% Cobalt metal binder were introduced into the reaction chamber and exposed to a pretreatment with reagent gas mixtures of H_2 and H_2 as carrier gas for a heated solution of Boron trioxide (B_2O_3) in methanol with or without CH_4 as Carbon source. Gas mixtures, time and sample temperature of process were as described in Table 1:

Sample	H_2 (sccm)	H_2+boron solution (sccm)	CH_4 (sccm)	Temperature (°C)	Time (h)
I	99	1	0	720	5
II	98	1	1	830	5

3. Results and Discussions

EDS and DRX spectra of Sample I and II were closely the same and shown high Cobalt concentration if compared to sample's starting 9%, as a consequence of the long time period exposed to high themperature, Cobalt present in deeper levels of the samples tended to migrate to surface, increasing considerably its concentration at this point and low Boron element concentration. Little or none Boron compound was identified by XRD, since its formation could be impaired by low concentration at final gas mixture or preferential reaction with other gas specimens, such as the Oxigen present in its own source molecule.

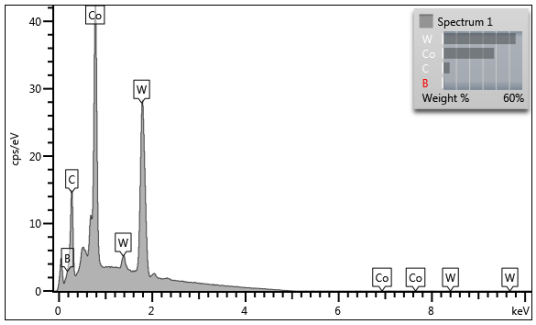

Fig. 1. *Sample I EDS spectra.*

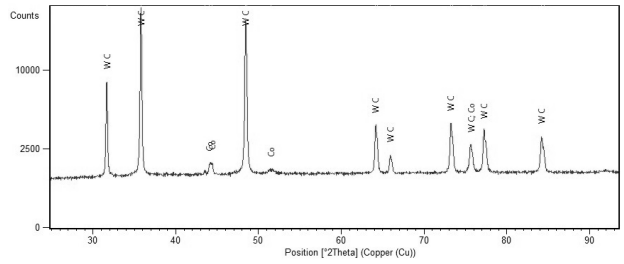

Fig. 2. *Sample I DRX Spectra.*

4. References (bold face Times New Roman 11 pt)

[1] T. Wang, L. Xiang, W. Shi, and X. Jiang, *"Deposition of diamond/β-SiC/cobalt silicide composite interlayers to improve adhesion of diamond coating on WC-Co substrates by DC-Plasma Assisted HFCVD,"* Surf. Coatings Technol., vol. 205, no. 8–9, pp. 3027–3034, 2011.

[2] R. Haubner, A. Köpf, and B. Lux, *"Diamond deposition on hardmetal substrates after pre-treatment with boron or sulfur compounds,"* Diam. Relat. Mater., vol. 11, no. 3–6, pp. 555–561, 2002).

*Corresponding author: place the email of the corresponding author here (bookman old style 9 pt)

[3] Campos, R. A., Contin, A., Trava-Airoldi, V. J., Barquete, D. M., Moro, J. R., and Corat, E. J. *"Influence of Boriding Process in Adhesion of CVD Diamond Films on Tungsten Carbide Substrates"*. Materials Research, 18(5),pp. 925-930, 2015

Acknowledgments
To FAPESP (processes number: 12/15857-1, 14/18139-8 and 13/25939-8) and CAPES for financial support.

*Corresponding author: place the email of the corresponding author here (bookman old style 9 pt)

ID 41: TIO_2 FILMS OBTAINED FROM HEAT TREATMENT OF TI FILMS DEPOSITED ON SODA-LIME GLASS SUBSTRATE

Philippsen, Maria Elisa[1,3*]; Tomiyama, Masahiro[2]; Irala, Dianclen do Rosario[3]; Stryhalski, Joel[4]; Soares, Paulo[5]; Fontana, Luis César[1]

[1]*Plasma Physics Laboratory, University of the State of Santa Catarina, Santa Catarina, Brazil*

[2]*Engenharia, University of the State of Santa Catarina, Santa Catarina , Brazil*

[3]*Fisica, University Center – Católica de Santa Catarina, Joinville , Brazil*

[4]*Fisica, Federal Institute of Santa Catarina - IFSC, Jaraguá do Sul , Brazil*

[5]*Engenharia, Pontificia Universidade – Católica do Paraná, Curitiba , Brazil*

1. Introduction (bold face Times New Roman 11 pt)

The increase in pollution results in increased dirt and degradation of materials such as glass, especially in building [1]. Self-cleaning materials have attracted interest due to the ease and reduction of maintenance costs, since they are great in applications that are difficult to access and that make cleaning difficult [2]. Self-cleaning glasses can be made through various types of surface coatings by improving or adding some characteristics of the glass.

2. Results and Discussions

Titanium and titanium oxide films were deposited on glass substrates, through triode magnetron sputtering technique. The influence of the working atmosphere (controlled proportions of argon and oxygen) during the thin films deposition and post annealing treatment on the transparency and the self-cleaning properties of films were studied. After the deposition of the films, a set of samples was heat treated, in atmosphere and ambient pressure, at temperatures of 500°C for one hour, with subsequent slow cooling in ambient atmosphere. Results indicate that the contact angle, between water drop and TiO_2 films, reduces after annealing treatment. It was also observed a decrease in the contact angle after UV irradiation on film surface, that is a well-known characteristic of TiO_2. Before the film oxidation through heat treatment, the contact angle was 40°. However, it reduces to around 10° after the heat treatment. Moreover, after UV radiation on the samples, during 24 hours, the contact angle diminished to less than 10° that is a characteristic of super hydrophilic material.

3. References

[1] PARAMÉS, J.; BRITO, J. Teoria e Prática na Engenharia Civil, n.15, p.55-62, Abril, 2010.

[2] YUANHAO, WANG; LU, LIN; YANG, HONGXING; CHE, QUANDE. Journal of Nanoparticle Research, 2013: 15:1384.

* lisa.ph10@gmail.com

ID 43: PLASMA TREATMENT OF MAIZE BIOMASS SURFACE FOR LIGNIN BREAKING

Lucas A. Manfroi[1]*, Polyana A. Radi[1,2], Lucia Vieira[1]
[1]*Universidade do Vale do Paraíba - IP&D, São José dos Campos – SP*
[2]*Instituto Tecnológico de Aeronáutica – LPP, São José dos Campos – SP*

1. Introduction

Brazilian's agricultural production is among the most prosperous of the planet, and maize is one of the most important products of this sector [1]. With the large maize production there is a large amount of waste, such as maize cob [2]. This maize cob posses high percentages of cellulose, hemicellulose and lignin in its composition [3]. Studies using plasma treatment in a DBD (Dielectric Barrier Discharge) reactor, can cause the lignin to detach from the lignocellulosic material [4]. This treatment can be used to remove lignin from lignocellulosic materials, which could be discarded, and with the removal of lignin the cellulose is free to be used to obtain various types of sugars. In this paper we are presenting the use of plasma treatment in liquids to treat maize and check the amount of lignin extracted.

2. Experimental

Maize lignocellulosic material was properly cleaned and separated in two groups which were immersed in an alkaline solution (pH ~12), for 40 minutes, one group was submitted to plasma treatment and the other group passed by the same temperature conditions, however, without the interaction of the plasma. After the treatment, the solutions were filtered under vacuum. They were separated in liquid and solid part, the liquid part was used for color analysis and UV-Vis, in the solid part the analysis of FTIR.

3. Results and Discussions

In Figure 1 presents a picture with two bottles of solution containing solubilized lignin from the extraction by plasma treatment (Figure 1-A) and the control (Figure 1-B). The control solution presented more soft and translucent coloration. This coloration is due to the solubilized lignin, which is darker in solution with more solubilized lignin, representing a higher extraction rate.

Fig. 1. *Image of solubilized lignin extracted from corn, A being treated with plasma and B with control treatment.*

The lignin absorbs in the UV region due to the π * ← π transition of its C = C bonds [5]. There are some differences in UV spectra of different lignins, with a maximum absorption between 280 nm and 350 nm, due to different structures [6-7]. Figure 2 shows the results of the UV-Vis spectroscopy performed on the solution after treatment, the plasma treated results are presented in the black curve from this curve it is possible to see a higher absorbance compared to the red curve and this difference in absorbance was 53% higher, indicating a higher concentration of extracted lignin in the plasma treated sample. In the region of 390 nm and 450 nm, there is a small absorption in the visible region of the violet, the yellow color being complementary to the violet, the yellow color is seen in the solution.

The phenolic compounds that constitute lignin are the guaiacyl and syringyl nuclei [8], which can be observed in Figure 3, which shows the results of the Raman spectra in 1121 cm^{-1} and 1263 cm^{-1} guaiacyl and 1215 cm^{-1} of syringyl on the red curve of the untreated sample, whereas the plasma-treated, black curve sample does not contain such lignin constituents.

*Lucas A. Manfroi: lucas.manfroi@univap.br

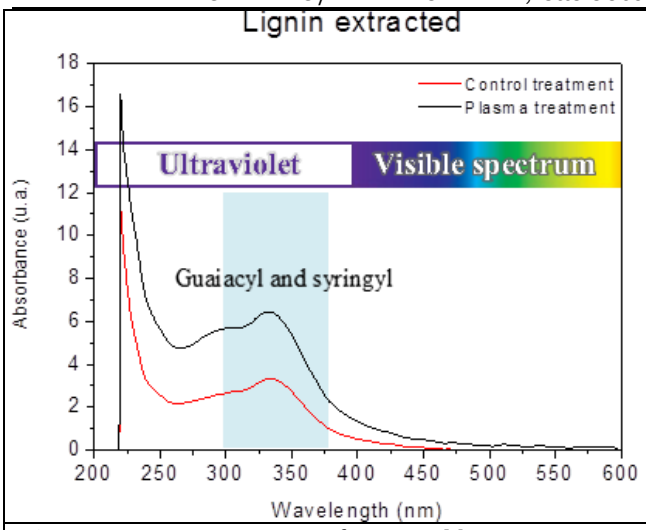

Fig. 2. *UV-Vis spectrogram of extracted lignin.*

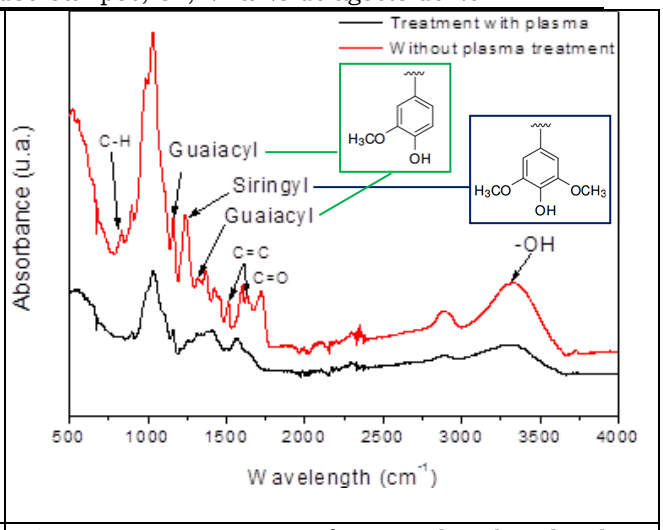

Fig. 3. *FTIR spectrogram of maize cob with and without treatment.*

4. Conclusions

Plasma treatment presents promising results, showing a extraction of lignin around 53%, this process improves the release of cellulose and consequently sugars production could be improved.

5. References

[1] P. e. A. d. M. G. Secretaria Estadual de Agricultura, "Secretaria Estadual de Agricultura, Pecuária e Abastecimento de Minas Gerais, " 22 10 2015. [Online]. Available: http://www.agricultura.mg.gov.br/component/gmg/story/2485-soja-e-milho-favorecem-possibilidade-de-recorde-da-safra-em-minas-gerais. [Acesso em 23 04 2016].

[2] F. Souza, "Síntese e Caracterização de Hemiceluloses Catiônicas a Partir do Reaproveitamento da Palha de Milho," Universidade Federal De Uberlândia - Instituto De Química - Programa De Pós-Graduação Em Química, Uberlândia - MG, 2012.

[3] R. Silveira, "Atividades Biológicas de Xilana de Sabugo de Milho," Universidade Federal do Rio Grande do Norte - Centro de Biociências - Departamento de Bioquímica, Natal-RN, 2010.

[4] M. Halttunen, "Study of Residual Lignin in Pulp by UV Resonance Raman Spectroscopy," Holzforschung, vol. 55, pp. 631-638, 2001.

[5] F. A. Gomes, "Avaliação dos Processos Kraft Convencional e Lo-Solids para Madeira de Pinus Taeda," Dissertação de Mestrado - Escola Superior de Agricultura Luiz de Queiroz - Universidade de São Paulo, Piracicaba, 2009.

[6] K. Marabezi, "Estudo sistemático das reações envolvidas na determinação dos teores de lignina e holocelulose em amostras de bagaço e palha de cana-de-açúcar.," Dissertação de Mestrado - Instituto de Química de São Carlos - Universidade de São Paulo, São Carlos, 2009.

[7] F. S. Miranda, "Estudo do Pré-Tratamento do Bagaço De Cana-De-Açúcar Utilizando Plasma em Líquidos," Dissertação de mestrado Universidade Do Vale Do Paraíba Programa De Pós-Graduação Em Processamento De Materiais E Catálise, São José dos Campos, 2013.

[8] R. S. Fukushima e R. D. Hatfield, "Um novo método analítico para a determinação do teor de lignina em produtos vegetais.," VIII Encontro Nacional sobre Métodos dos Laboratórios da Embrapa, Jaguáriuna - SP, 2003.

Acknowledgments

The authors thank the IP&D of UNIVAP for the use of the equipment and the realization of the experiments.

*Lucas A. Manfroi: lucas.manfroi@univap.br

ID 44: TRIBOLOGICAL BEHAVIOR OF NIOBIUM TREATED BY HIGH TEMPERATURE NITROGEN PLASMA BASED ION IMPLANTATION

Lilian Hoshida[1]*, Michel Felipe Lima de Araújo[1], Rogério de Moraes Oliveira[1]
INPE – National Institute for Space Research - São José dos Campos, SP, Brasil.

1. Introduction

Niobium is a refractory metal that exhibits excellent properties such as high melting point (2468ºC), high electrical conductivity, good corrosion resistance, malleability, high hardness and low density in comparison to other refractory metals and a wide variety of applications, such as in components of nuclear reactors, rockets, missiles, space systems engineering [1]. A major disadvantage of niobium is that in its pure state, it promptly oxidizes at high temperatures (above 400ºC) in the presence of oxygen. Nevertheless, the incorporation of nitrogen to its surface may have the effect of improving the oxidation resistance of the bulk and improve its mechanical and tribological properties [2]. In this work, niobium was treated by high temperature nitrogen plasma based ion implantation (HTPBII), in order to produce a thick niobium nitride layer on its surface. The modified surface layer was characterized in relation to its tribological properties.

2. Experimental

The niobium samples (99.4% purity) were cut in discs with 13 mm in diameter and 3mm in thickness. These samples were polished until a mirror like surface finish had been obtained. After polished the samples were cleaned by ultrasound bath with acetone for 10 minutes. Before treatment they were cleaned by argon sputtering for approximately 10 minutes. Nitrogen PBII was run at a working pressure of 6 x 10^{-3} mbar, and high voltage pulses of 7kV/30μs/500Hz were applied in two different conditions, for 4 and 8 hours. For both cases the samples were heated up to 1200ºC during treatments.

Dry friction coefficient measurements were accomplished in pin-on-disk tribometer using a 3mm diameter Al_2O_3 ball, which was loaded by the force of 2 N against the rotating flat niobium surface with 5 cm/s of linear speed and 2.06 mm of wear track radius. The worn tracks were examined by scanning electron microscopy (SEM) and the volume loss and wear rate were calculated according to ASTM G-99.

3. Results and Discussions

The pin-on-disc test revealed that the samples treated by HTPBII presented lower coefficients of friction (CoF) in relation to untreated sample, as shown in Figure 1. The measurements were monitored up to 8,000 revolutions and, for this case, slightly lower CoF values were attained for the sample treated during 4 hours. The worn tracks of all the samples were examined by SEM, as shown in Figure 2. The width of the tracks (*D*) was measured at five different points, revealing a significant reduction of respective mean values in favor of the treated samples. In fact, while $D \sim 1430$ μm for untreated sample, a tenfold reduction was measured for the sample treated during 4 h ($D \sim 171$ μm). For the sample treated during 8 h, $D \sim 95$ μm, almost half the value measured by the sample treated during 4 h. The respective volume loss (*V*) was calculated taking into account the mean width of worn tracks, sliding distance and number of revolutions. Once again, the longer treatment time led to very significant reduction of *V*. In fact, $V \sim 2{,}27$ mm^3 for untreated sample, $3{,}60E^{-3}$ mm^3 for 4 hours sample and $6{,}17E^{-4}$ mm^3 for 8 hours sample. It seems that thicker modified layers attained by the treatments performed for longer times are the main responsible for additional improvement of tribological behavior of untreated samples.

Further analysis will be carried out, as the comparative study of tribological performance by increasing the number of revolutions during pin-on-disk tests. Additionally, EDS analysis will be also performed to evaluate nitrogen peaks present on the worn tracks.

*Corresponding author: lilianhoshida@gmail.com

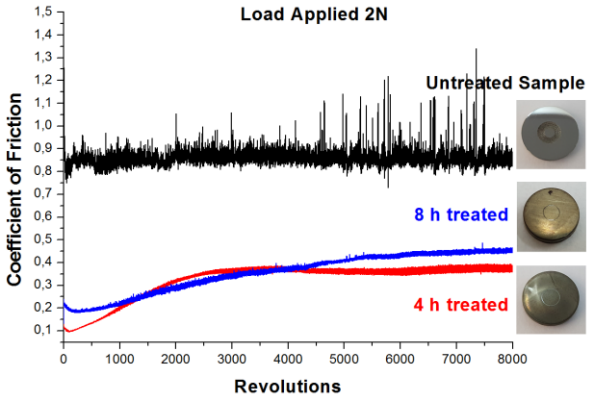

Fig. 1. *Coefficient of friction for untreated and treated samples.*

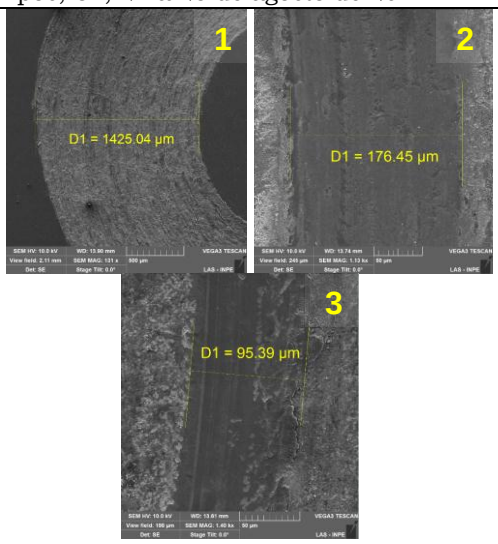

Fig. 2. *Worn tracks viewed by SEM for (1) untreated sample, (2) 4 hours treated and (3) 8 hours treated.*

4. References

[1] R. M. Oliveira, A. C. Oliveira, F. C. Carreri, G. F. Gomes, M. Ueda. App.Surf. Science, 283, 382-388, (2013).

[2] C. Borcz, C. M. Lepienski, S. F. Brunatto. Surf. and Coatings Technol., 224, 114-119, (2013).

*Corresponding author: lilianhoshida@gmail.com

ID 45: MECHANICAL CHARACTARIZATION OF NITRIDE LAYERS ON NITI SUBSTRATE

S. H. Gonsalves[1], G. B. De Souza[1], F. C. N. Borges[1], R. M. Oliveira[2] and J. Otubo[3]*

[1]Universidade Estadual de Ponta Grossa, Ponta Grossa, PR, Brazil
[2]Institudo Nacional de Pesquisas Espaciais, São José dos Campos, SP, Brazil
[3]Instituto Tecnológico de Aeronáutica, São José dos Campos, SP, Brazil

1. Introduction

The NiTi alloy is a typical shape memory material, which also demonstrate pseudo-elastic properties. These characteristics are result of a reversible martensite transformation when the material is deformed beyond its elastic limit, either by heating (SME) or by the applied load release (SE). In temperatures above the austenite starting point (As), the austenite phase (A - body centered cubic) is stable under low stresses and temperatures under the martensite starting point (Ms); under high stress conditions, the martensite phase (M - monoclinic or tetragonal) become stable. Despite the interesting features, as the low elastic modulus and high corrosion resistance, in situations where the Ni release by tribo-corrosion occurs make the NiTi alloy unsuitable for use in orthopedic devices [1-2].

The plasma immersion ion implantation (PIII) is a satisfactory technique for the NiTi surface modification, improving hardness and corrosion resistance, eventually reduction of nickel ions release in the biological environment [3].

Instrumented indentation and the analytical Oliver-Pharr methodology [4], are the most adopted methods to characterize the mechanical properties of modified surfaces . However, the phase transformations in the NiTi alloy during loading results in a coexistence of two phases with different moduli in the volume of deformation. Hence, the direct application of the Oliver-Pharr method is inadequate in such a situation. The proper study of the nitride layer formed over NiTi, ruling out the substrate influences, demands to consider the phase transition under loading, as well as the reverse transformation during unloading [5].

The objective of the work reported here was the study of mechanical properties of nitride layers formed on NiTi substrates by PIII, also considering the phase transformation induced in the bulk during indentation.

2. Experimental

The NiTi alloy was annealed at 1000 °C with subsequent water quenching at 0 ºC. The homogenized samples were submitted to PIII. The power supply applied a voltage of 8 kV with current of 10 A. The pulse width was 30 μs. The pressure of the N_2 atmosphere was kept constant at 7.3 kPa. The samples heating was attained with a hot filament adjusting the desired treatment temperatures to 600, 700 and 800 °C. To obtain substrates with similar features as those found in the nitrided samples, additional samples, not nitrided, were heat treated in a furnace, using argon atmosphere to simulate the PIII thermal conditions.

The structural changes were characterized by X-ray diffraction in the range 20°–60°, using Cu-Kα radiation. Additional grazing incidence XRD (GI-XRD) with fixed incidence angle of 2° were also carried out. The morphology of the modified surfaces was analyzed by scanning electron microscopy (SEM). The instrumented indentation was performed in two different batches:

- those samples submitted only to thermal treatment were indented using a spherical punch (R = 20 μm) under single loadings to estimate the elastic modulus; subsequently, a Berkovich indenter was employed for hardness.
- the nitrided samples were submitted to the quasi-continuous stiffness measurement (QCSM) method with a Berkovich indenter.

3. Results and Discussions

3.1 Heat Treatment

3.1.1 Structural Characterization

The diffractograms of the thermally treated samples indicated an M+A+precipitates bulk composition. There was an increase in the of $TiNi_3$ precipitate contribution as compared to the reference (only solubilized) substrate. The 600 ° C sample presented the most significant increase. In the 700-800 °C samples, there was a decrease in the $TiNi_3$ peaks in comparison with the 600 ºC case, indicating that a re-homogenization occurred at those temperatures. The Ti_2Ni compound was also identified on samples after heat treatment. It precipitated in the NiTi alloy due to stoichiometrically unbalanced Ni/Ti ratio caused by the $TiNi_3$ precipitation, which provided more available Ti atoms to nucleate new Ti-rich precipitates, as Ti_2Ni.

e-mail: silvio0rk@gmail.com

3.1.2 Mechanical Properties

In instrumented indentation tests, loads were applied individually to avoid that the induced martensite from the previous loading interfered in the next cycle. The A+M+precipitates elastic modulus (*E*) was obtained by adjusting the loading curve with the Hertz equation, provided that the maximum displacement / indenter radius where lower than 0.001 [5]. The calculated values for the NiTi bulks ranged from 50-70 GPa.

To determine hardness avoiding pile-up effects during loading, the Cheng-Cheng [6] method was employed. The reference sample (NiTi just solubilized) presented the highest value (5.4 GPa). In all the heat treated samples, there was an important hardness decrease with the increasing load due to the larger induction of martensite in the volume of interaction, since the M phase presents inferior hardness than the A phase [6].

3.2 Nitrided Samples

3.2.1 Structural Characterization

The nitride layer thicknesses were 240 nm, 340 nm, and 560 nm for the treatment temperatures 600, 700 and 800 °C, respectively. The TiN compound was produced in all the nitrided surfaces, most significantly in the 800 °C treatment. Regarding the bulk precipitates, the Ti_2Ni content notably increased, in accordance with [6]. It was concluded that the temperature-modified NiTi matrices reproduced quite well the thermal conditions found in the nitriding process, inducing the precipitation of compounds of the same stoichiometry ($TiNi_3$ and Ti_2Ni) with equivalent temperature dependence. Therefore, the mechanical properties measured in the thermal treated samples do represent the bulk properties of the nitride ones, as seen next.

3.2.2Mechanical characterization

The effective elastic modulus of the nitride layers produced on TiNi, discounting the substrate effects, were inferred through the model proposed by Hay-Crawford [8]. It demands the knowledge of the substrate and the layer elastic modulus *E* and the Poisson´s ratios, as well as the layer thickness. The nitride layers formed at the three nitriding temperatures presented elastic modulus between 110 and 130 GPa.

The effective hardness of the nitride layers on NiTi substrates were calculated through the method proposed by Bhattacharya and Nix [9], using the hard layers on soft substrates equation. It demands the knowledge of the effective elastic modulus, calculated above with the Hay-Crawford method. The nitrided layers promoted a surface hardening to NiTi up to 4 times higher than the values found for the corresponding thermally treated substrates.

Acknowledgements

The C-LABMU/UEPG for the analyses facilities. This work was partially founded by CNPq (grant nº 310819/2015-6).

4. References

[1] Otsuka, K; REN, X..Progress in Material Science.50, 511-678, 2005.
[2] OTUBO J., ANTUNES A. S. Materials Science Forum Vol. 643, 55-59. 2010.
[3] Yeung, K. W. K. et al. Surface and Coatings Technology.V 201, p 5607-5612. 2017.
[4] OLIVER, W.C.; PHARR, G.M.. Journal Material. Research. v. 19, n. 1, 2004.
[5] Yan, W. et al. Journal of the Mechanics and Physics of Solids. Vol 61. Pg2015-2033. 2013.
[6] Vecchio, K. S. Jiang, F. Adharapurapu, R. R. Materials Science and Engineering A. vol 527. 2010.
[7]Cheng, Y-T.; Cheng, C-M.. Applied physics Letters. V. 73 n. 5. Pg 614-616. 1998.
[8]Hay, J.; Crawford, B.. Journal Materials research. Vol. 26. N6. 2011.
[9] Bhattacharya, A. K.; Nix, W. D. International Journal of Solids and Structures. V. 24. 1998.

e-mail: silvio0rk@gmail.com

ID 46: INFLUENCES OF PLASMA JET PARAMETERS ON SEEDS TREATMENT

T. S. M. Mui, R. P. Mota, K. G. Kostov
Faculty of Engineering – FEG, Universidade Estadual Paulista – UNESP, Guaratinguetá, SP, Brazil

1. Introduction

In the last decade, atmospheric pressure plasmas have been attracting the researchers attention, due to their wide application range, especially in the field of biology and medicine [1]. One of the main advantages of plasma processing is that it does not generate hazardous by-products, thus it is environment friendly. Application of plasma in agriculture is considered as one of its newest applications. Due to vast differences between type of seeds and plasma setups, the effects of plasma on seeds are not fully comprehended, yet [2]. Therefore, in this work we present a study of the plasma jet parameters that influence on the power of the plasma to be used on seeds.

2. Experimental

A plasma jet terminating with a wide (horn-like) nozzle was employed in this study. Argon plasma was excited by an AC power supply generating an amplitude-modulated sinewave with 25 kHz frequency and 24.0 kVp-p amplitude. To verify the influence of the parameters on the applied power, the flow rate and number of cycles of voltage signal were varied. Afterwards, different types of seeds (eggplant and lentil) were treated to observe the surface modifications and differences in the seeds germination.

3. Results and Discussions

In Fig. 1 is shown the influence of the number of active voltage cycles on the power. As can be seen, when the number of cycles is incremented the applied power increases. In Fig. 2 is exhibited the power dependence on the gas flow. The discharge power scale up with both variables, showing how important each parameter is. Furthermore, after plasma treatment of seeds it was observed that high values of power and long exposure times could damage seeds and prevent their germination.

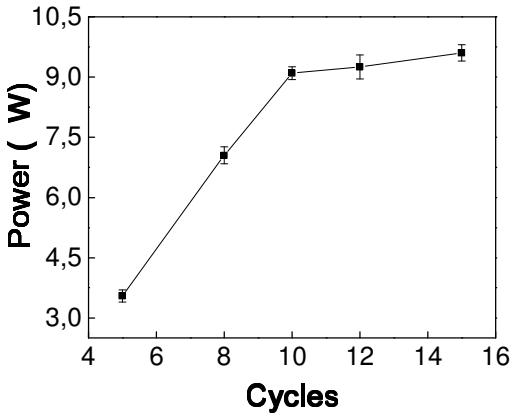

Fig. 1. *Discharge power versus number of voltage active cycles. (Flow Rate = 1.2 L/min).*

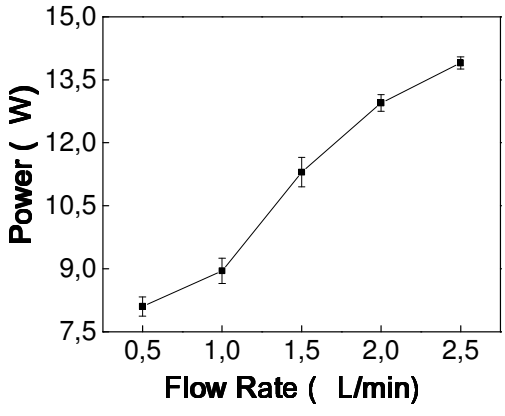

Fig. 2. *Power dependence on gas flow rate (Cycles = 12).*

4. References

[1] M. Keidar et al.. Cold atmospheric plasma in cancer therapy. Physics of Plasmas 20, 1–8 (2013).
[2] A. Zahoranová; M. Henselová; D. Hudecová et al. Effect of Cold Atmospheric Pressure Plasma on the Wheat Seedlings Vigor and on the Inactivation of Microorganisms on the Seeds Surface. Plasma Chemistry and Plasma Processing 36, 397–414 (2016).

Acknowledgments

This research was funded by CAPES.

*Corresponding author: taiana_mui@yahoo.com.br

ID 49: REAL AND VIRTUAL LEAKS IN VACUUM SYSTEMS

L. Delarion[1]*, N.H. Medina[1], V.A.P. Aguiar[1], and L. M. F. Fagundes[1]
[1]*Instituto de Física da Universidade de São Paulo*

1. Introduction

In order to achieve low pressures in high vacuum or ultra-high vacuum regimes, several molecules sources must be taking into account such as molecules from the volume, molecules adsorbed in the surface of the material, water vapors and residual oils from the diffusion or mechanical pumps, for example. Other important factor to reach very low pressure is the selection of the materials used in the construction of the vacuum system. Although the previous information are important for achieving low pressures, special attention should be given to sealing techniques in order to avoid general leaks. The most important leaks found in vacuum systems are real and virtual leaks. Real leaks are easier to find, since they can be located using helium leak detectors, on the other hand virtual leaks cannot be detected with these devices [1]. Virtual leaks are created when small volumes of gas, inside vacuum systems, are connect to the main volume by very high impedance connections. In this situation, the air inside this small volume is evacuated following an exponential law depending on the cavity volume, the connection impedance and the pump speed. This kind of leak must be avoided in any case in vacuum systems, since it can result in very long times to reach the working pressure. In this work, it was studied the pressure decay as a function of time in a standard vacuum chamber with a real leak, no leak and with a virtual leak. Also, as part of this work, a procedure to measure metal outgassing is being developed [2].

2. Theory and Experimental setup

The pressure decay as a function of time, in a normal vacuum system, is well known and is given by equation (1) [3], where P_o is the initial pressure, S the pump speed, V the volume of the system and P_{res} the residual pressure due mainly by the material outgassing.

$$P(t) = P_o\, e^{-\left(\frac{S}{V}\right)t} + P_{res} \quad (1)$$

Real leak in vacuum systems is represented by the following equation [3]:

$$P_r = \frac{C_r\, P_{atm}}{S} \quad (2)$$

where P_{atm} is the Atmospheric pressure and C_r the hole conductance, responsible for the leak.

On the other hand, the residual pressure as a function of time, in a system with virtual leaks, is described by equation (3) [3].

$$P_r = \frac{C_v P_0}{S}\, e^{-\left(\frac{C_v}{V_c}\right)t} \quad (3)$$

where V_c is the volume of a very small cavity, connected to the main vacuum system by a very low conductance, represented by C_v.

The leak experiments were performed using a vacuum system composed of a standard chamber, a 130 l/s diffusion pump, a Bayard-Alpert gauge, and a system composed of a needle valve and two Hoke valves used to simulate the leaks. In Figure 1, the experimental setup is shown. Initially, the vacuum system was pumped down to a pressure around 2.0 x 10^{-6} Torr. The needle valve was opened to simulate a real leak, then the pressure achieved a higher pressure value. At this point, the Hoke valve was suddenly closed. While the valve was being closed, the Bayard-Alpert gauge controller was recorded at a 30 fps rate creating a movie from which was taken the pressures and times used to study pressure variation.

In order to study the virtual leak decay, the same experimental setup was used. In this case, after the pressure reach the residual pressure, around 2.0 x 10^{-6} Torr. The Hoke valve was opened in order to fill the cavity with Atmospheric pressure. The Hoke valve was closed and the needle valve as gently opened, in order to create a hole with very high impedance. At this point, the other Hoke valve, placed on the other side of the vacuum chamber, was open to allow the rising of the pressure to around 10^{-3} Torr and then this valve was suddenly closed. The same procedure was adopted to record the pressure variation.

*luan.babetto@usp.br

3. Results and Discussions

The obtained results for real leaks, as shown in Figure 2, suggest that special attention should be given to sealing techniques in order to avoid general leaks and, specially, to avoid the occurrence of virtual leaks. This procedures together with a careful selection of materials *e.g*: a vacuum chamber made of a low degasification rate metal [2], should allow a faster achievement of high vacuum.

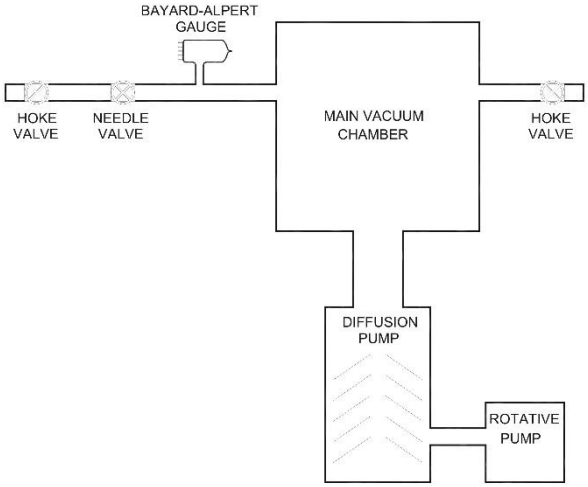

Fig. 1. *Schematic drawing of the vacuum system used for the analysis of the pressure as a function of time for simulated real and virtual leaks. The vacuum system is composed by a main vacuum chamber, a diffusion pump, a needle valve and two Hoke valves and a Bayard-Alpert gauge.*

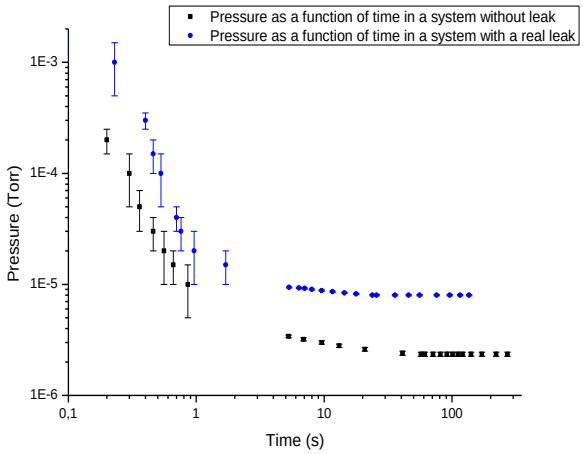

Fig. 2. *Example of pressure values as a function of time in two different situations: with no leak and with a real leak. The discontinuity in the dada points is due to the need of changing manually the scale of the Bayard-Alpert gauge.*

Another very important issue to obtain very low pressures in vacuum system is the choice of the materials, since the outgassing is the major source of molecules in low-pressure regimes [2]. To study outgassing of several materials, small boards of aluminum, brass, copper, stainless steel, and other metals and non-metal materials are being prepared. All these materials will be placed in a high vacuum chamber of the new beam line of the São Paulo Pelletron accelerator [4]. The high vacuum in the main chamber of this beam line is achieved with a 400 l/s turbo-molecular pump. With this system it will be possible to study the outgassing of several materials as a function of time and also as a function of the temperature.

4. References

[1] ROTH, A., *Vacuum Technology*. 3rd edition. Amsterdam, Netherlands: Elsevier Science, 1990. Chapter 7.
[2] STRAUSSER, Y., Varian Reports VR-51, *"Review of Outgassing Results"*.
[3] ONUSIC, H., FAGUNDES, L. M. *Vazamentos em Sistemas de Vácuo: Modelos e Detecção*. Anais do 1º Seminário Sul Americano de Controle de Qualidade (ABCQ) Novembro-1980.
[4] MEDINA, N. H., et al., *Experimental Setups for Single Event Effect Studies*. Journal of Nuclear Physics, Material Sciences, Radiation and Applications, v. 4, p. 13-23, 2016.

Acknowledgments

The authors would like to thank the São Paulo Pelletron accelerator staff and to acknowledge financial support by the Brazilian funding agency CNPq, and São Paulo University.

*luan.babetto@usp.br

ID 54: SO_3 FORMATION FROM THE IRRADIATION OF SO_2 ICE BY X-RAYS: EXPERIMENTS AND INVESTIGATIONS IN THEORETICAL CHEMISTRY

Víctor S. Bonfim[1]*, Patricia Barreto[2], Leonardo Baptista[3], Sergio Pilling[1,4]
[1]*Universidade do Vale do Paraíba – UNIVAP – São José dos Campos (SP) – Brazil*
[2]*Intituto Nacional de Pesquisas Espaciais (INPE) – São José dos Campos (SP) – Brazil*
[3]*Universidade do Estado do Rio de Janeiro (UERJ) – Resende (RJ) – Brazil*
[4]*Instituto Tecnológico de Aeronáutica, ITA - DCTA – São José dos Campos (SP) – Brazil*

1. Introduction

Sulfur dioxide (SO_2) and its related ions, radicals and fragmentation products are important reagents to prebiotic synthesis, since they can lead to the production of sulfur-containing amino acids. SO_2 is also an important constituent of Jupiter moon Io and is also present at other astrophysical environments. This work presents an experimental and theoretical research on the formation of SO_3 molecule during the photolysis of a pure SO_2 ice sample by synchrotron radiation (mainly soft X-rays) at 12 K.

2. Experimental / Theory

Experiments have been performed at the National Synchrotron Light Laboratory (LNLS), in Campinas, Brazil, under ultra-high vacuum conditions (Pressure below 3 x 10^{-8} mbar). In situ analysis was performed using an infrared Fourier transform spectrometer (FTIR) at different fluences, just as described in details in the experimental work of Pilling and Bergantini [1]. The experimental results led to studies in Theoretical Chemistry. Calculations were performed at MP2 theory level with cc-pVTZ basis set, which is consistent with the studied systems size [2]. All chemical species had the equilibrium geometry confirmed and the enthalpy value obtained at 12 K by applying standard statistical thermodynamics equations. Computations were carried out initially in the gaseous phase and then the solid (SO_2 ice). For calculations in the solid phase, the Polarized Continuum Model (PCM) has been chosen [3].

3. Results and Discussions

FTIR spectra of the irradiated SO_2 sample have presented formation of SO_3, a new chemical species. Consequently, it is important to gather information about the SO_2 molecule fragmentation pattern and the SO_3 formation channels at the experimental conditions. Through the calculation of reaction enthalpies with or without the solvent influence, one may infer that the presence of the solid SO_2, as described by its dielectric constant, decreases the reactivity of the O^+ species regarding the formation of SO_3. However, it should be noted that all the intermediate species assumed to take place in the SO_3 production, as SO, O^+, O_2, and O are products from a previous SO_2 dissociation, and therefore their participation as intermediates is coupled to this first step. In order to give an overview of the calculations results, it was produced an illustrative scheme with the most favorable chemical reactions for the combined process of SO_2 photolysis and SO_3 formation (Fig. 1). From this schematic network, it is clear the channel involving oxygen atom has the advantage of requiring only one photodissociation process, totalizing two elementary reactions for the trioxide formation. Additionally, activation barriers calculations for the most important reactions are in progress. The theoretically identified reaction channels in this study may provide a better understanding for the chemical evolution of SO_2-rich ices, which is relevant to both Astrochemistry and Astrobiology.

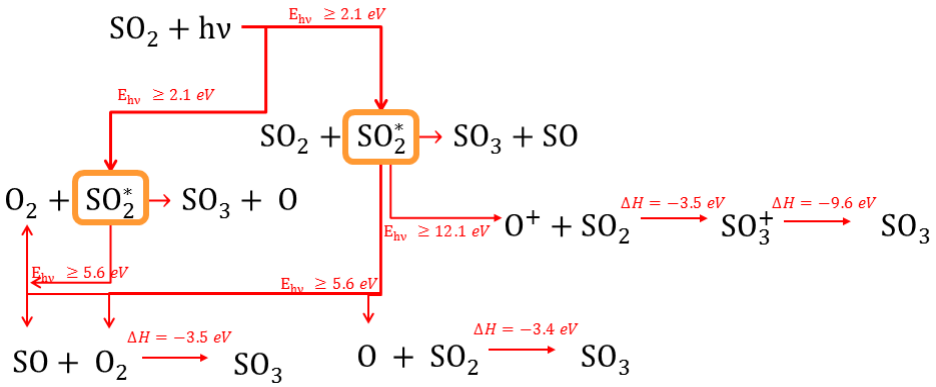

Fig. 1. *Diagram for thermochemically favored SO_3 formation routes (in SO_2 ice), as indicated from this work calculations. The asterisks in SO_2* indicate the chemical species participates as an excited state at the referred chemical reaction [4], as emphasized by the orange squares.*

*Corresponding author: victordsb@gmail.com

4. References

[1] S. Pilling and A. Bergantini, Astrophys. J., **811**, 151, (2015).
[2] S. Dobrin et al., J. Phys. Chem. A, **104**, 10695-10700, (2000).
[3] S. Miertuš, E. Scrocco, J Tomasi, Chem. Phys., **55**, 117-129, (1981).
[4] A. R. Whitehill et al., Proc. Natl. Acad. Sci., **110**, 17697-17702, (2013).

Acknowledgments

The authors would like to thank FAPESP (JP2009/18304-0) and CAPES agencies, as well as the LNLS staff.

*Corresponding author: victordsb@gmail.com

ID 55: TRIBOCORROSION PROPERTIES OF SIC FILM DEPOSITED ON AISI 316L

A. A. Vieira[1], L. A. Manfroi[1], A. Sene[1], L. O. de Paula[1], T. B. Santos[1], P. A. Radi[1,2], S. A. Silva[3], G. de Vasconcelos[3], L. Vieira[1]

[1]Universidade do Vale do Paraíba, São José dos Campos – SP, Brasil
[2]Instituto Tecnológico de Aeronáutica, São José dos Campos – SP, Brasil
[3]Instituto de Estudos Avançados, São José dos Campos – SP, Brasil

1. Introduction

AISI 316L is one of the most popular materials used as a raw material for orthopedic prosthesis due to its low cost, manufacturability and reasonable corrosion resistance [1]. Prosthesis in dynamic contact with body fluids induces bio- and tribo-corrosion process. AISI 316L contains cobalt, chromium and nickel, which are carcinogenic elements. These chemical elements produces a processes of inhibition and repair of damaged DNA [2]. These elements are also aggressive for biological environment when applied for a long time releasing harmful particles, that can increase wear and metallosis as observed by Waterhouse and Lamb [3]. Coatings with high hardness and biocompatibility are essential for steel wear and corrosion protection [4]. SiC films have been studied in biomedical applications, due to its properties, such as high hardness, biocompatibility, corrosion resistance and others physicochemical properties [5]. These films can be obtained several methods as Physical Vapor Deposition (PVD), Chemical Vapor Deposition (CVD) [6] and laser cladding [7]. The laser cladding process has been a promising technique, due to having a faster, automated and versatile process in comparison with conventional techniques and could be carried out in an atmospheric environment [7]. Furthermore, the addition of TiO_2 in SiC films can increase the protection of the steel. In this work, we examined the tribocorrosion behavior of AISI 316 L stainless steel with SiC coating, also with and without TiO_2 nanoparticles in comparison with uncoated steel.

2. Experimental

Prior films deposition, the AISI 316L samples with dimensions of 20.0x20.0x4.5 mm were polished with different sandpaper grit size (280, 400 and 600, respectively). Then they were cleaned using an ultrasonic bath for 15 minutes using: water with 10% detergent, distilled water and acetone, respectively. Carbon Dioxide laser was used as a radiation source for laser cladding under output power of 125 W and laser beam diameter of 180 μm. Nitrogen flow (5L/min) was used to provide environmental purging to avoid surface oxidation. The SiC or SiC + TiO_2 powder was sprayed on the AISI 316L substrate surface using a pneumatic gun in order to prepare the samples for laser irradiation. The samples were then irradiated with four steps: on first step the laser parameters was 30 % of laser power and 500 mm/s; following three steps 100 % of laser power and 500 mm/s. After step 3, the samples were sanded with sandpaper number 600 to remove loose powder. The powder was again pulverized and a further laser irradiation was carried out again. The irradiation by laser in each step takes about 0.8 seconds for the whole sample.

The films were analyzed by confocal Raman microscope Horiba model Lab Ram HR evolution with ionic argon laser wavelength (λ = 514nm) under backscattering geometry. Tribocorrosion analyses were performed in Ringer's solution, to simulate extracellular fluids, on static and dynamic modes and the corrosion protection effect of SiC and SiC + TiO_2 films were evaluated. For these tests, the samples were placed in an electrochemical cell according to ASTM G119, using a silver/silver chloride reference electrode (Ag/AgCl), and a platinum counter electrode. The working electrode was the sample.

The tribocorrosion tests were performed using an Al_2O_3 ball (ϕ= 4.76 mm) under 1.5N. The track distance was 2 mm under frequency of 2.5 Hz. The open circuit potential (OCP) was measured for 30 minutes in static mode, 30 minutes in dynamic mode and finally for a further 30 minutes in static mode. All tests were performed in triplicate.

3. Results and Discussions

Fig.1. shows the Raman spectra of films: SiC film was presented in (green line) and SiC+TiO_2 (blue line) and SiC powder in (red line), and TiO_2 powder in (black line). Is it possible to see that TiO_2 in anatase phase presented 4 peaks centered in 144 cm^{-1} (E_g), 398 cm^{-1} (b_{1g}), 519 cm^{-1} (a_{1g}), 639 cm^{-1} (E_g) these peaks are according just the characteristics peak centered in 788 cm^{-1} was not observed according to the literature [8]. The SiC film presented characteristic peaks of amorphous silicon in the regions of 200-600 cm^{-1} for Si-Si vibration mode and 1300-1600 cm^{-1} for C-C vibration mode according to the literature [9]. Peaks centered at 1368 cm^{-1} and 1590 cm^{-1} also indicate the formation of microcrystalline graphite according to the literature [10]. From SiC films also is possible to observe the peaks 778 cm^{-1}, 978 cm^{-1}, the intensity of these peaks decreased after the laser irradiation when compared with SiC powder (in red line), which was already observed in literature after thermal treatment effects [11]. From the SiC+TiO_2 film was observed SiC peaks

*lucia.vieira@univap.br
*angela.vieira@univap.br

(in blue line) remained in the same position after irradiation when compared with SiC powder (in red line). In addition, TiO_2 powder peaks were observed in black line, the plot with SiC+TiO_2 (in blue line) also indicated that this mixture avoids SiC amorphization. Fig. 2 shows the Open Circuit Potential (OCP) curves before, during and after the tribocorrosion test. In the static mode, the AISI 316L presented OCP higher than SiC and SiC+TiO_2. These results indicate a lower corrosion potential for the sample without film. After 1800s the sliding starts and the OCP of AISI 316L shows an abrupt drop for around -0.3 V due to the removal of the passive layer from its surface [12]. For the samples coated with SiC + TiO_2 film mixture, the OCP was -0.1 V during the static period. The OCP decreased slightly to -0.2 V in the sliding region (from 1800 to 3600 seconds) and then stabilized around -0.13 V. When sliding test finished the OCP increased to -0.11 V. For the sample covered with SiC film the OCP started with -0.15V in the static phase and decreased in the sliding region slightly stabilizing around -0.17 V. The OCP increased and stabilized region around -0.16V, after sliding movement. The oscillations in the potential values in red line are attributed to the mechanical and electrochemical repassivation [13]. The tribocorrosion tests showed that both coatings improved the tribocorrosion behavior of the surfaces. The protection provided by SiC + TiO_2 films can contribute to increase the life time of manufactured prosthesis for knee, shoulder and hip implants avoiding early replacement surgeries. Thus, SiC and SiC + TiO_2 films, can be produced rapidly and inexpensively by laser cladding. The films show to be promising as a coating protection of prosthesis due to improving prosthesis material tribocorrosion resistance.

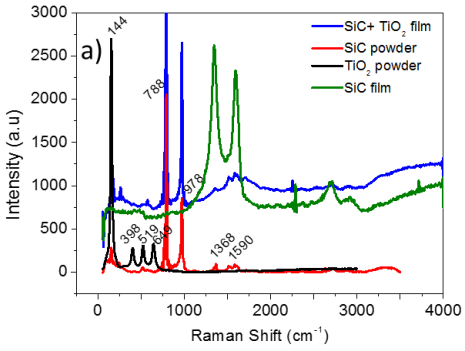

Fig. 1. *Raman spectra of obtained films from SiC and SiC + TiO_2 and of SiC and TiO_2 anatase powders.*

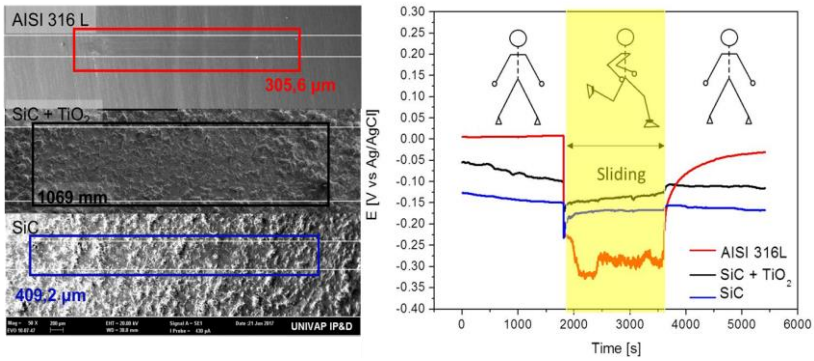

Fig.2. *Open circuit potential (OCP vs Ag/AgCl) values before, during and after tribocorrosion tests and wear.*

4. References

[1] S. A. Naghibi, K. Raeissi, and M. H. Fathi, *Mater. Chem. Phys.*, vol. 148, no. 3, pp. 614–623, 2014.

[2] A. Sargeant and T. Goswami, *Mater. Des.*, vol. 28, pp. 155–171, 2007.

[3] R. B. Waterhouse and M. Lamb, *Wear*, vol. 60, pp. 357–368, 1980.

[4] A. S. Sayed-noor and G. O. Sjödén, *Am. Assoc. Hand Surg.*, pp. 86–89, 2009.

[5] C. R. Wronski, E. Materials, and H. A. Silicon, *Sol. Energy*, pp. 373–379, 1994.

[6] T. B. Santos, A. A. Vieira, L. O. Paula, E. D. Santos, and P. A. Radi, *J. Mech. Behav. Biomed. Mater.*, vol. 68, no. May 2016, pp. 239–246, 2017.

[7] A. Contin, G. De Vasconcelos, D. Maciel, R. Alves, V. J. Trava-airoldi, and E. José, *Diam. Relat. Mater.*, vol. 65, pp. 105–114, 2016.

[8] I. R. Beattie and T. R. Gilson, pp. 407–429, 1968.

[9] C. G. Jin, X. M. Wu, and L. J. Zhuge, vol. 2008, 2008.

[10] A. C. Ferrari, J. C. Meyer, V. Scardaci, C. Casiraghi, M. Lazzeri, F. Mauri, S. Piscanec, D. Jiang, K. S. Novoselov, S. Roth, and A. K. Geim, vol. 187401, no. NOVEMBER, pp. 1–4, 2006.

[11] T. Ohsaka, F. Izumi, and Y. Fujiki, vol. 7, no. 6, pp. 321–324, 1978.

[12] N. Diomidis, J. Celis, P. Ponthiaux, and F. Wenger, pp. 53–67, 2009.

[13] P. Ponthiaux, F. Wenger, D. Drees, and J. P. Celis, vol. 256, pp. 459–468, 2004.

Acknowledgments

The authors thank INPE for the use of the Raman and CAPES for the financial support of this work.

*lucia.vieira@univap.br
*angela.vieira@univap.br

ID 56: DEVELOPMENT OF A NOVEL THERMAL PLASMA PROCESS FOR THE DEPOSITION OF HIGH PERFORMANCE OVERLAY COATINGS

F. R. Caliari[1], F. S. Miranda[1], D. A. P. Reis[2], A. M. Essiptchouk[3], G. P. Filho[1]

[1]*Centro de Ciência e Tecnologia de Plasmas e Materiais - PlasMat, Instituto Tecnológico de Aeronáutica - ITA, São José dos Campos, SP 12228-900, Brasil*
[2]*Instituto de Ciência e Tecnologia, Universidade Federal de São Paulo – UNIFESP, São José dos Campos, SP 12231-280, Brasil*
[3]*Instituto de Ciência e Tecnologia, Univ. Estadual Paulista – UNESP, São José dos Campos, SP 12247-004, Brasil*

1. Introduction

Thermal Spray (TS) is a key technology used on several industrial sectors such as transport, energy, materials processing, biomedical and electronic application, with a global market estimated of USD 8 billion [1,2]. To meet the increased market requirements and expand the TS application, innovative approach needs to be developed. In this sense, a novel TS process called High Velocity Plasma Spray (HVPS) is herein described. The core of HVPS process is a plasma torch with a novel design [3].

2. Experimental Procedures

The HVPS process is based on a novel plasma torch that operates with a low arc voltage fluctuation, axial injection of feedstock and operation under supersonic regime. According to the Figure 1, this process is composed of the plasma torch, a powder feeder that injects the feedstock into the rear part of the plasma torch, and a sample holder that controls the rotational speed of the samples along with on-line monitoring of the sample temperature. In-flight particle characteristics, such as particle velocity (v_p) and temperature (T_p), was monitored using an infrared pyrometer (DPV-2000), and at least 3000 particles data were gathered.

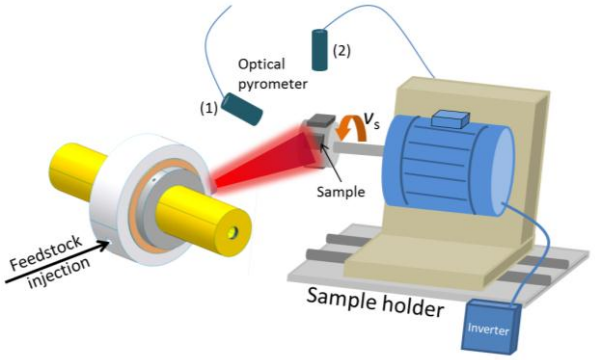

Fig.1. *Experimental setup of HVPS process for coating depositions*

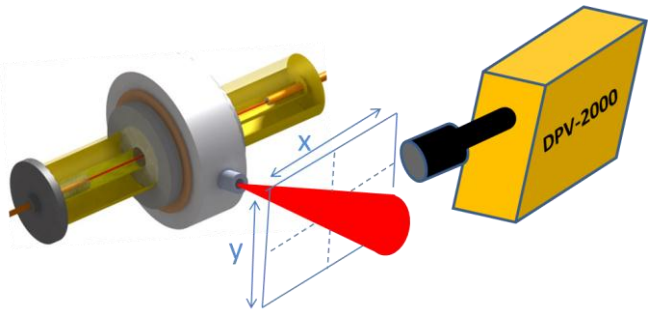

Fig.2. *In-flight particle analysis of HVPS process*

A Thermal Barrier Coating (TBC) coating was deposited using a bond coat of CoNiCralY (22-45 μm) and a top coat made of 7%YSZ (5-22 μm). The metallic and ceramic coatings were analyzed using SEM, XRD, mechanical profilometry and instrumented indentation test.

3. Results and Discussions

The results of DPV-2000 showed that the HVPS process sprayed the metallic powder at a v_p of 500 m/s and a T_p of 2440°C. The range of particle velocity and temperatures for the ceramic powder 7% YSZ is 491-683 m/s and 2535-2636°C, respectively. Following the Nusselt (*Nu*) number (Equation 1) calculated from the thermal and kinetic characteristics of the plasma jet, the estimated calculation showed that, on the HVPS process, the heat transfer coefficient (*h*) can be up to 270% higher than the conventional plasma spray process [4].

$$Nu = \frac{hd_p}{\lambda_g} = 2 + 0{,}66Re^{0{,}5}Pr^{0{,}33} \qquad \text{Equation 1}$$

where λ_g is the thermal conductivity, Re is the Reynolds number and Pr is the Prandtl number of the plasma jet.

*Corresponding author: felipercaliari@yahoo.com.br

Due to the particular v_p and T_p characteristics provided by the HVPS process, it was observed that both metallic and ceramic coatings possess low roughness and defects, elevated hardness and modulus of elasticity, and deposition of high temperature stable phases, i.e., close to nanostructured coatings reported in the literature [5]. Therefore, it was demonstrated that the HVPS is a new cost-saving process that promotes the deposition of low defect coatings, with superior mechanical properties using 1/3 of total input power in comparison to coatings produced by APS [6].

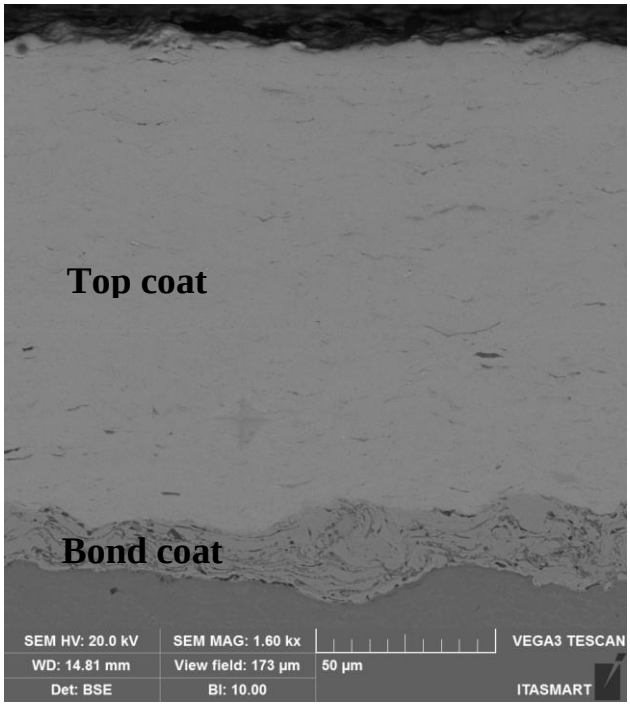

Fig.3. *SEM cross section image of the TBC coating*

Properties	Bond coat CoNiCrAlY	Top coat 7%YSZ
Surface Roughness (Ra, µm)	5.8 ± 0.2	2.8 ± 0.4
Coating thickness (µm)	50	130
Porosity (%)	0.8 ± 0.3	0.25 ± 0.09
Oxide content (%)	3.8 ± 0.7	-
Main phases	γ, Co-Ni-Cr β, (Co,Ni)Al	t', c
Hardness (GPa)	6.1 ± 1.6	14.3 ± 1.1
Elastic Modulus (GPa)	155 ± 21	208 ± 9
Interface Toughness ($MPa.m^{1/2}$)	2.4	-

Table.1. *Main properties of bond coat and top coat deposited by HVPS process*

4. References

[1] Espallargas, Nuria. 2015. Introduction to Thermal Spray Coatings. In Future Development of Thermal Spray Coatings, edited by Nuria Espallargas, 1–15, ed. Elsevier.

[2] Vaßen, Robert, Maria Ophelia Jarligo, Tanja Steinke, Daniel Emil Mack, and Detlev Stöver. 2010. Overview on Advanced Thermal Barrier Coatings. Surface and Coatings Technology 205 (4). Elsevier B.V.: 938–942.

[3] Caliari, F.R., F.S. Miranda, D.A.P. Reis, G.P. Filho, L.I. Charakhovski, and A. Essiptchouk. 2016. Plasma Torch for Supersonic Plasma Spray at Atmospheric Pressure. Journal of Materials Processing Technology 237, 351-360.

[4] Xiong, Hong Bing, Li Li Zheng, Li Li, and Anirudha Vaidya. 2005. ―Melting and Oxidation Behavior of in-Flight Particles in Plasma Spray Process. International Journal of Heat and Mass Transfer, 48 (25–26): 5121–5133.

[5] Fauchais, P, G Montavon, R S Lima, and B R Marple. 2011. ―Engineering a New Class of Thermal Spray NanoBased Microstructures from Agglomerated Nanostructured Particles, Suspensions and Solutions: An Invited Review. Journal of Physics D: Applied Physics 44 (9), 53p.

[6] G. Mauer, D. Sebold, R. Vaßen, E. Hejrani, D. Naumenko, W.J. Quadakkers. Impact of Processing Conditions and Feedstock Characteristics on Thermally Sprayed MCrAlY Bondcoat Properties. Surface and Coatings Technology, 318, 114-121.

Acknowledgments

The authors acknowledge financial support from FAPESP (Grant No. 2012/24851-7), CNPq, and CAPES.

*Corresponding author: felipercaliari@yahoo.com.br

ID 57: EFFECT OF NITROGEN PLASMA IMMERSION ION IMPLANTATION ON SURFACE DISCHARGE BREAKDOWN VOLTAGE OF ALUMINIZED POLYIMIDE

Marcondes A.R.*, Rossi J.O., Ueda M.
Laboratório Associado de Plasma, Instituto Nacional de Pesquisas Espaciais

1. Introduction

Kapton™ (trademark from DuPont) is the most known polyimide film. Kapton is a polymer that has been used for many years in a great variety of applications due to its outstanding and unique properties. The combination of its properties makes Kapton ideal for use in harsh environments, especially in space. In space technology, thermal blankets are vital for regulating the temperature of most of the spacecrafts. The blankets usually consist of many layers of thin sheets with aluminized Kapton as the outer layer. Aluminized Kapton film is used to absorb/reflect the solar energy in order to avoid overheating and overcooling in the interior of the spacecraft. Kapton is a material widely used in thermal blankets due to its high strength-to-weight ratio, good mechanical properties, excellent thermal stability, chemical inertness and suitable thermal optical properties [1]. However, in space, Kapton is subject to several aggressive agents, including atomic oxygen, UV radiation, outgassing, energetic particle radiation, and meteoroids and debris. Prolonged exposure of the Kapton surface to those agents can significantly degrade Kapton, affecting the thermal control performance and resulting in premature failure of the mission. The multiple aggressive agents in space environment affect Kapton in different ways. Energetic charged particles are present throughout the Earth magnetosphere [2]. Energetic particles, particularly from the radiation belts and from solar particle events, cause radiation damage to spacecrafts. Many satellites have been lost and others have had significant operational anomalies due to spacecraft charging caused by the charge accumulation provided by the impact of energetic charged particles [3]. The energetic charged particles that impact the surface of Kapton cause both surface charging and internal charging in the bulk of the material. The charge accumulation can be damaging to the Kapton and compromises the thermal blanket function. Potential differences appear on the surface of the Kapton due to energetic charged particle impacts. When the potential difference exceeds a certain threshold, surface discharge happens [4]. The breakdown discharge on the surface of the Kapton causes damages in its structure and can affect other components of the spacecraft as antennas and on-board electronics. So, it is desirable to improve the flashover characteristic of the aluminized Kapton to turn the polymer less susceptible to surface breakdown discharges. It is well known that the polyimides can be strongly modified by ion implantation [5]. Plasma immersion ion implantation (PIII) is an evolving technique that has been used for a long time to promote surface modification in a wide variety of materials. In the last decades, several researchers have concentrated their attention on the surface modification of polymers using PIII. This technique has been used to improve different properties of many kinds of polymers [6,7], including Kapton [8]. In this work, we use PIII technique to improve the flashover characteristic of aluminized polyimide, that is, to increase the polymer surface breakdown voltage.

2. Experimental

Kapton used in this study was produced by DuPont as a thin film. The film was 25μm in thickness and metallized with a very thin layer (around 70nm) of aluminum in one side. The DuPont film sheet was cut in samples of two sizes (80mm x 130mm and 50mm x 360mm) which were then treated by nitrogen PIII using the same processing parameters. The samples were put inside the plasma using two sample holders. One sample holder was an aluminum cylinder in which the Kapton samples were wrapped around it, and the other one was a 4-inches diameter stainless steel tube in which the Kapton samples were put on its inner side. In both cases, the samples were treated with and without a stainless steel metallic grid placed over the samples. The use of the metallic grid is a well-known technique used to avoid charge accumulation when dielectric samples are treated by PIII. Some samples placed inside the tube were treated with the use of magnetic field which was applied to create a denser plasma around the sample. The surface breakdown voltages of the untreated and treated samples were measured using the experimental apparatus depicted in Figure 1. The apparatus is composed by a DC power supply to charge a high-voltage capacitor and two ignition coils used to elevate the discharge capacitor voltage. The samples were placed between two electrodes separated by a distance previously known. The voltage in the DC power supply was step by step increased up to the electric breakdown on the Kapton surface. After the capacitor charging at a value set previously, the closure of a manual switch allowed that pulsed voltages were applied to the samples to cause the dielectric breakdown discharge. The voltages across the two coils were measured by means of a digital

*andre.marcondes@inpe.br

oscilloscope as shown in Figure 2. The breakdown voltage is given by the peak to peak differential measurement on the voltage waveforms.

3. Results and Discussions

The dielectric strengths were obtained dividing the breakdown voltages by the linear distance between the electrodes. As a probability distribution of failure for each sample test was used, a minimum of five measurements was required for the statistic method The obtained data were treated using the Weibull distribution and failure analysis. The results indicate that nitrogen PIII of aluminized Kapton can be advantageous to improve its dielectric strength, especially when the sample is treated without the use of the metallic grid and inside the tube. In this case, the increase in the dielectric strength reached circa of 59% compared to the untreated sample. A significant increase of 42% was also obtained in the same case when Kapton samples were treated with cylindrical sample holder. The treatments using metallic grid have shown no good results, regardless the type of holder. The treatments using magnetic field have provided an increase in the dielectric strengths, but not as relevant as in the case without the magnetic field.

Fig. 1. *Experimental apparatus used for the measurement of the surface dielectric strength of the untreated and treated samples.*

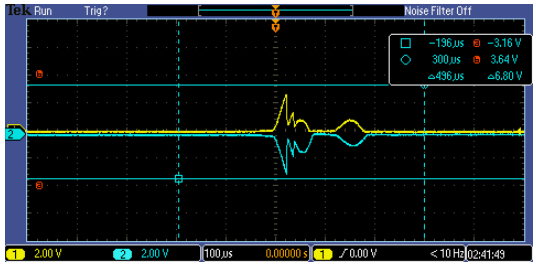

Fig. 2. *Waveform of the pulsed voltage applied to the Kapton sample. The abrupt fall on the waveform indicates the dielectric breakdown and the peak-to-peak value gives the surface breakdown voltage.*

4. References

[1] KIM, Jooheon; IM, Hyungu; CHO, M. H. Tribological performance of fluorinated polyimide-based nanocomposite coatings reinforced with PMMA-grafted-MWCNT. Wear, v. 271, n. 7, p. 1029-1038, 2011.
[2] ECSS-E-ST-10-04C Space engineering – Space environment
[3] GARRETT, Henry Berry. The charging of spacecraft surfaces. Reviews of Geophysics, v. 19, n. 4, p. 577-616, 1981.
[4] WANG, Song et al. A New Charging Model for Spacecraft Exposed Dielectric (SICCE). IEEE Transactions on Plasma Science, v. 44, n. 3, p. 289-295, 2016.
[5] PIVIN, J. C. Hardening and embrittlement of polyimides by ion implantation. Nuclear Instruments and Methods in Physics Research Section B: Beam Interactions with Materials and Atoms, v. 84, n. 4, p. 484-490, 1994.
[6] FU, Ricky KY et al. Surface modification of polymeric materials by plasma immersion ion implantation. Nuclear Instruments and Methods in Physics Research Section B: Beam Interactions with Materials and Atoms, v. 237, n. 1, p. 417-421, 2005.
[7] MARCONDES, A. R. et al. Improvements of ultra-high molecular weight polyethylene mechanical properties by nitrogen plasma immersion ion implantation. Brazilian journal of physics, v. 34, n. 4B, p. 1667-1672, 2004.
[8] TAN, I. H. et al. Treatment of polymers by plasma immersion ion implantation for space applications. Surface and Coatings Technology, v. 186, n. 1, p. 234-238, 2004.

*andre.marcondes@inpe.br

ID 58: HOLLOW CATHODE DESIGN FOR A BRAZILIAN ION THRUSTER

José Américo Neves Gonçalves[1 *], Gilberto Marrega Sandonato[2], Ricardo T. Irita[3]
[1]*Associated Plasma Laboratory, National Institute for Space Research*
[2]*Associated Plasma Laboratory, National Institute for Space Research*
[3]*Associated Plasma Laboratory, National Institute for Space Research*

1. Introduction

The INPE Associated Plasma Laboratory is carrying out the development of ion thrusters to be used in the attitude control of geostacionary satellites. Current research activities includes the performance tests of an electron bombardment ion thruster of a 5mN thrust with employs xenon as propellant. This constraint is posed by the low power capability of the remote sensing sattelite. Two hollow cathodes will be used in the present thruster to generate the plasma and to neutralized ion beam. A great deal of attention has been devoted to the need for a thermal and mechanical design, aimed at minimising the total power input for startint and for steady state operation. At the cathodes, the requiriments is to attain the operation tip temperature rapidly and then to maintain it after discharge initiation. With sufficiently low heat loss from the cathode, the energy dissipated in the cathode discharge is sufficient to maintain the tip temperature, and hence the discharge, without operation of the heater. It is important to ensure that the tip temperature by electron bombardment is not excessive (~ 900 ^{o} C), minimizing loss of barium. A (Ba, Sr, Ca)CO_3 suspension was used for coating of tantalum spiral inserts wich after breakdown thermal process is ready for used in hollow cathodes. We report on the performance of a hollow cathode emission parameters. Measures have been taken of the emission current as function of cathode temperature and anode voltage. Good capability of this cathode has been demonstrated and forthcoming data will be used to stablish life endurance models relevant to ion thrusters applications.

2. Experimental

In the Associated Plasma Laboratory (LAP), ion thrusters started running with tungsten filaments, which were replaced by oxide cathodes, and presently they are equipped with rolled-tantalum-oxide-foil hollow cathodes. All these cathodes were entirely developed and built at LAP. The present hollow cathode consists of a 5-mm diameter by 40-mm long, 0.3-mm-wall thickness tantalum tube, with a cold-pressed 1-mm diameter orifice tungsten tip. The insert consists of a 5-turns rolled tantalum foil painted with a thin layer of mixed carbonates, (Ca, Ba, Sr)CO_3, which are converted to oxides by heating the insert up to 900 ^{o}C. The cathode heater comprises a boron nitride body machined in the shape of a revolver cylinder, in which holes a coiled tungsten filament is passed through. This heater expends 90 W to heat the cathode up the carbonate to oxide conversion temperature. As there are no commercial standard pipe fittings for 5 mm-diameter tubes, both the connector and the ferrules must be developed and machined specially for sealing the cathode body. The present hollow cathode full assembly is shown in Fig.1.

3. Results and Discussions

The preliminary experimental tests have revealed that this hollow cathode can operate at currents in the range of 3 to 10 A for long time periods, and at 18 A for short time periods. This cathode is still under investigation aiming both at its complete performance characterization and performance enhancement.

Figure 1. *Rolled-tantalum-oxide-foil hollow cathode: heater cartridge fully assembled.*

ID 59: ELECTRICAL PROPERTIES OF TiO_x THIN FILMS DEPOSITED BY TRIODE MAGNETRON SPUTTERING FOR APPLICATION AS TRANSPARENT AND CONDUCTIVE OXIDE

R. S. Santiago, D. A. Duarte[*]

Federal University of Santa Catarina, Joinville Center of Technology, Laboratory of Surface Treatments, Joinville, SC, Brazil.

1. Introduction

The development of transparent and conductive oxides (TCOs) enabled the description of a new optoelectronic scenario by means of touchscreen displays and light-emitting diodes. In the solar industry, it was possible to improve the general properties of dye sensitized solar cells [1, 2]. The most used TCOs are ITO ($Sn:In_2O_3$) and FTO ($F:SnO_2$), where ITO has the highest conductivity. However, due to its higher cost, other materials are under research. Among many candidates, titanium dioxide (TiO_2) is the promising one. Although this material present optical transmittance near to glass, its electrical resistivity is near to an insulator. To improve the electrical conductivity, several methods have been suggested, where the most simple is the deposition of TiO_x (with $x < 2$) [3, 4]. This structure is a transparent semiconductor with electrical resistivity below to 10^{-2} Ω.cm [5, 6]. For application of the TiO_x as TCO in solar cells, it is important to know the influence of the solar radiation in the sheet resistance. The most energetic part of the solar spectrum is composed by UV and it represents about 7% of the total radiation reaching the earth's surface. Thus, this paper investigates the sheet resistance of TiO_x under UV exposition for films deposited in several experimental methods. For data comparison and evaluation, the sheet resistances of commercial TCOs were also measured.

2. Experimental

Ti_xO_y thin films were deposited on microscope slides (cleaned with Extran MA 02) by triode magnetron sputtering technique. The chamber was evacuated to a base pressure of 1×10^{-4} Torr (~ 1.3×10^{-2} Pa) by a pumping system composed by mechanical (Edwards E25) and turbo molecular (Pfeiffer HICUBE 80 eco) pumps. Films were deposited with a DC Pinnacle Plus power supply at several powers (340, 370, 400, 430 and 460 W) where the deposition time was kept in 10 minutes. Before each deposition, the hysteresis curve was taken to know the target poisoning point. All depositions were made before this point, where were possible to deposit suboxides. The deposition pressure was maintained between 3 and 3.5 mTorr with the argon flow rate kept in 1.7 sccm. The oxygen flow rates ranged from 3.4 to 4.8 sccm, according to the power applied in the target. The temperature of the substrate remained between 49 and 56°C for all depositions. All films produced have colorations between blue and green. The electrical properties of the samples were analyzed by 4-point probe (feed by a Keithley source meter model 2400) under UV exposition with 254.7 nm wavelength [7, 8].

3. Results and Discussions

Figure 1 shows the sheet resistance of the films as function of the exposition time of UV light for the commercial TCOs and deposited films. Results show that UV light does not have any influence in electrical properties of the commercial TCOs; on the other hand, the sheet resistance of the deposited films decreases as the exposition time increases. Note that films deposited with 400, 430 and 460 W present sheet resistances of only one order higher than that presented by the commercial TCOs.

The decrease of the resistivity of the nonstoichiometric film may be explained through Fermi level [9]. For a stoichiometric TiO_2 the Fermi level is located near the valence band, where the electrons have low mobility, explaining why this material presents high sheet resistance. When the film is doped with a metal, as in the case of the commercial TCOs, the Fermi level is shifted into the conduction band (phenomenon known as Burstein-Moss effect) and, then, the sheet resistance is poorly affected by UV. For a nonstoichiometric TiO_2, the Fermi level is located near the bottom of the conduction band; thus, the electron mobility is affected under UV/Vis/NIR exposition due to the existence of mid-gap states.

* Corresponding author: diego.duarte@ufsc.br

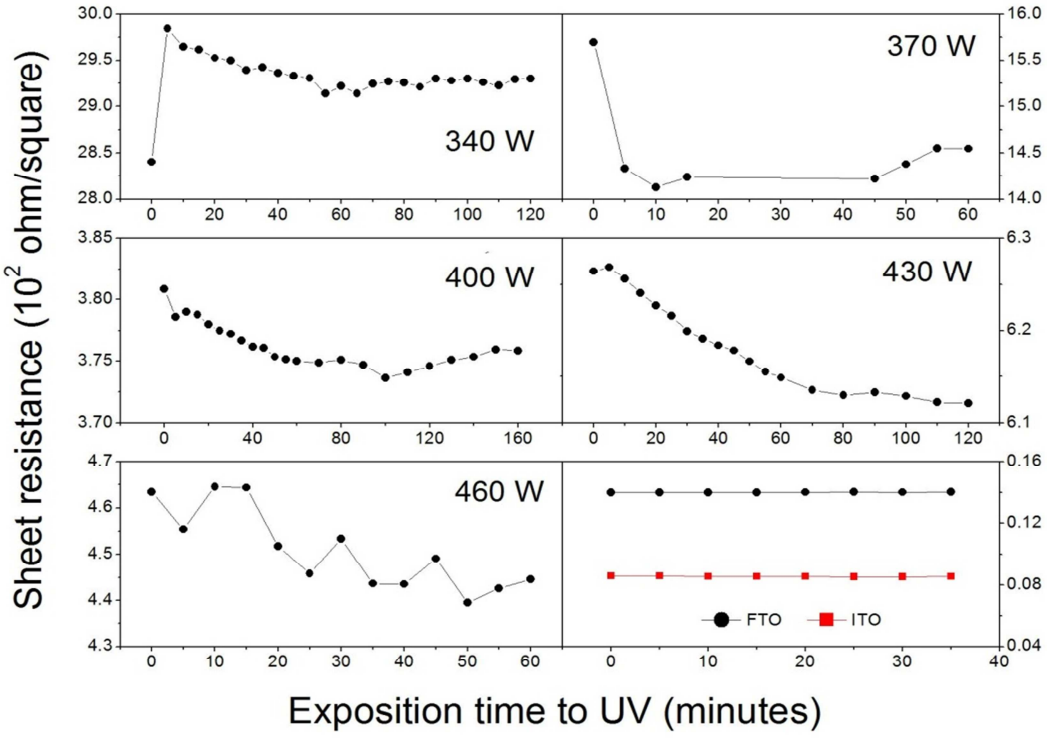

Fig. 1. Sheet resistance of the films as function of the exposition time to UV.

4. References

[1] J. Müller, B. Rech, J. Springer and M. Vanecek, "TCO and light trapping in silicon thin film solar cells", Solar Energy, vol. 77, 2004, pp. 917-930.

[2] B. O'Regan and M. Grätzel, "A low-cost, high-efficiency solar cell based on dye-sensitized colloidal TiO 2 films", Nature, vol. 353, 1991, pp. 737-740.

[3] C. G. Granqvist, "Transparent conductors as solar energy materials: A panoramic review", Solar Energy Materials and Solar Cells, vol. 91, 2007, pp. 1529-1598.

[4] T. Minami, "Transparent conducting oxide semiconductors for transparent electrodes", Semiconductor Science and Technology, vol. 20, 2005, pp. S35-S44.

[5] R.S. Santiago, D.A. Duarte, R.G. Delatorre, F. D. Origo, J. C. Sagas, "Deposition of titanium oxide thin films by triode magnetron sputtering for application as transparent and conductive oxide", Congresso Regional de Iniciação Científica e Tecnológica em Engenharia, 2016, Joinville. Anais do Congresso Regional de Iniciação Científica e Tecnológica em Engenharia, 2016.

[6] R.S. Santiago, D.A. Duarte, R.G. Delatorre, "Estudo das propriedades elétricas de filmes finos de TixOy em função da temperatura e do tempo de exposição em radiação ultravioleta para aplicação no setor solar", X Foro Científico Estudantil da UNISOCIESC, 2016, Joinville, 2016.

[7] E. M. Girotto and I. A. Santos, "Medidas de resistividade elétrica DC em sólidos: como efetuá-las corretamente", Quim. Nova, vol. 25, 2002, pp. 639-647.

[8] H. Liang, J. Xu, D. Zho, X. Sun, S. Chu and Y. Bai, "Thickness dependent microstructural and electrical properties of TiN thin films prepared by DC reactive magnetron sputtering", Ceram. Int, vol. 42, 2016, pp. 2642-2647.

[9] S. M. Rezende, "Materiais e Dispositivos Eletrônicos", Editora Livraria da Física, 2nd edition, pp. 145-149, 2004.

Acknowledgments

Authors thank the Laboratory of Plasma, Thin Films and Surfaces of the Santa Catarina State University for the films deposition. The first author thanks CNPq for the financial support.

* Corresponding author: diego.duarte@ufsc.br

ID 60: FRICCION AND WEAR BEHAVIOR OF TI-W PVD COATING ON STEEL AISI 316L

Oscar Gordillo[1]*, Williams Steve Hincapie Campos[1], Oscar Piamba[1], Jhon Olaya[1], Gil Capote[1], Edgar Alfonzo[2], Vladimir Trava-Airoldi[3]

[1]Universidad Nacional de Colombia, Facultad de Ingenierías, Carrera 45, N. 26-85; Edificio Uriel Gutiérrez, Bogotá D.C., Colombia
[2]Universidad Nacional de Colombia, Facultad de Ciencias, Carrera 45, N. 26-85; Edificio Uriel Gutiérrez, Bogotá D.C., Colombia
[3]Instituto Nacional de Pesquisas Espaciais (INPE), Laboratório Associado de Sensores e Materiais (LAS), Av. dos Astronautas, 1758-São José dos Campos, 12227-010, SP, Brazil

1. Introduction

With the most effective balance of carbon, chromium, nickel and molybdenum for corrosion resistance, AISI 316L austenitic stainless steel is widely used for high temperature, aggressively corrosive conditions and nuclear reactor applications. However, with a low hardness (200 HV) and an austenitic structure which cannot be hardened by heat treatment, there is no easy way to improve its wear resistance [1].

The PVD has aroused considerable interest in recent years since it permits the deposition of dense and compact coatings, leading to improved chemical and mechanical properties. This technique produces a wide range of coatings with high wear and chemical resistance at relatively low cost and through easy coating procedures [2]. In order to improve their surface properties, different types of coatings such as oxides, nitrides, carbides and "Diamond Like Carbon" (DLC) can be deposited trough this technique in order to improve wear properties [3], [4].

The aim of this study was to investigate Ti-W coating on AISI 316L by PVD in order to improve the sliding wear resistance of stainless steel 316L.

2. Experimental

Sample of AISI 316L stainless steel (0.03 C wt%, 16.7 Cr wt%, 9.5 Ni wt%, 2.9 Mo wt%, and Fe balance) with sizes 1.5 cm x 1.5 cm x 0.6 cm was used as substrate. The substrate was prepared metallographically and cleaned ultrasonically in an acetone bath for 15 minutes before of deposition. A R.F. magnetron sputtering system (13.56 MHz) and target Ti10W90 (99.99% pure) were employed to TiW interlayer deposition. The coating was synthesized using a pressure in the chamber of 0.19 Pa and applying power of 200 W, while Ar was used as precursor gas for plasma with flow of 20 sccm. The deposition times was selected in order to obtain a thickness of 300 nm.

The crystal structure was determined by X-ray diffraction (XRD) using an X-pert Pro Panalytical device operating in beam mode at 5°, with monochromatic line Kα of copper (1.540998 Å) working at 45 kV and 40 mA. The chemical composition of the interlayer was determined via energy-dispersive X-ray spectroscopy (EDX) with energy of 4 kV to 6 kV using a SEM MIRA3. Tribological studies were carried out using ball on disc method on the CSM instrument tribometer at a load of 1N, linear speed of 16 cm/s and sliding distance of 3m. Prior to wearing test, the coating and ball were ultrasonically cleaned in isopropyl alcohol for 3 min and then dried in the air. Stainless steel AISI 316 ball of 4 mm in diameter was chosen as the counterpart. Tribology experiment were conducted in ambient atmospheric condition at room temperature.

After the wear test, the 2D profile, 3D profile and wear loss of track on sample was measured by a Bruker Contour GT-K vertical scanning interferometer. The surface morphology of the coating was analyzed using a scanning electron microscope (SEM, Tescan/mira 3), operating at a voltage of 15 kV. Energy dispersive X-ray spectroscopy (EDS, X-MAX 50/Oxford Instruments) was used for elemental analysis of wear track.

3. Results and Discussions

The evolution of coefficient of friction (COF) on Ti-W coating and 316L substrate during the ball on disc tribological test at room temperature is summarized in Fig. 1. The COF of the Ti-W coating was lower than of the 316L substrate. Friction coefficient of the sliding system Ti-W/316 is 0,16 which increases to 0,4 while de sliding system of substrate has a significantly higher value in the range 0,5-1,5. The friction curve is unstable in case of substrate sliding system. This instability appears due to the large deformation occurring during sliding according to Fig. 6. The Ti-W coating presented a better anti wear properties with lower COF

oagordilloh@unal.edu.co

value than 316L substrate, however, it increased during wear stage, which could be attributed to an accumulation of wear products (debris) in the contact zone.

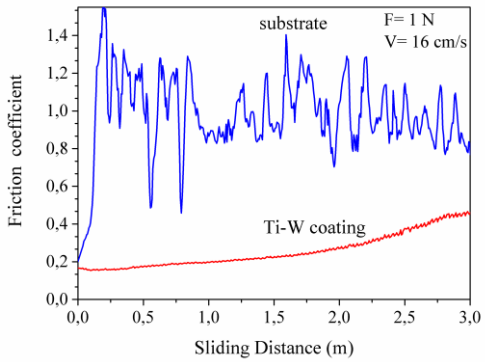

Fig. 1. *Friction coefficient of the Ti-W coating and 316L substrate*

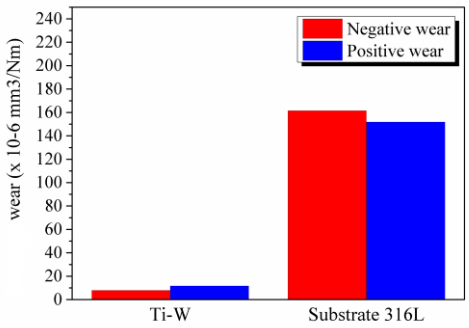

Fig. 2. *Wear rate of the Ti-W coating and 316L substrate*

The wear rate (mm^3/Nm) of the coating and substrate against sliding distance was calculated by the formulae used in literature [5],[6]. The results shown in Fig. 2. indicated that the wear rate of the Ti-W coating was higher than substrate. 2D wear profiles cross the sliding direction were obtained on the wear scars of the substrate and coating, under normal load of 1N the maximum wear depth of the Ti-W coating was approximately 0,03µm, much smaller than that of the 316L substrate approximately 5µm. This suggesting that the substrate under this normal load suffered a much severe wear. The drx shows the presence of two phases Ti y W, there is not formation of new peak indicating the absence of a new phase. The calculated network parameter for Ti and W was 0.28954 nm and 0.31137 nm respectively.

4. References

[1] C. Tassin, F. Laroudie, M. Pons, L. Lelait. Surface and Coatings Technology., 80, 207-210, (1996).
[2] S.A. Naghibi, K. Raeissi, M.H. Fathi. Materials Chemistry and Physics.,148, 614-623, (2014).
[3] E.L. Dalibon, D. Heim, Ch. Forsich, S.P. Brühl. Procedia Materials Science., 9, 163-170, (2015).
[4] P.N. Silva, J.P. Dias, A. Cavaleiro. Surface and Coatings Technology., 202, 2338-2343 (2008).
[5] Lei Shan, Yongxin Wang, Jinlong Li, He Li, Xuedong Wu, Jianmin Chen. Surface and Coatings Technology., 226, 40-50, (2013).
[6] Jiri Nohava, Pascal Dessarzin, Pavla Karvankova, Marcus Morstein. Tribology International., 81, 231-239, (2015).

oagordilloh@unal.edu.co

ID 60_1: INFLUENCE OF TiW INTERLAYER IN ADHESION OF THE DLC COATINGS ONTO AISI 316L STAINLESS STEEL

Williams Steve Hincapie Campos[1]*, Gil Capote[2], Jhon Olaya[1], Edgar Alfonzo[2], Vladimir Trava-Airoldi[3]

[1]Universidad Nacional de Colombia, Facultad de Ingenierías, Carrera 45, N. 26-85; Edificio Uriel Gutiérrez, Bogotá D.C., Colombia
[2]Universidad Nacional de Colombia, Facultad de Ciencias, Carrera 45, N. 26-85; Edificio Uriel Gutiérrez, Bogotá D.C., Colombia
[3]Instituto Nacional de Pesquisas Espaciais (INPE), Laboratório Associado de Sensores e Materiais (LAS), Av. dos Astronautas, 1758-São José dos Campos, 12227-010, SP, Brazil

1. Introduction

Diamond-like carbon (DLC) films have attracted attention in the last years because of their properties, such as low friction coefficient, high hardness, high elastic modulus, chemical inertness, biocompatibility, and high degree of wear resistance [1]. Nevertheless, the DLC coatings not have good adherence on metallic substrates. This behavior is basically due to difference of the coefficients of thermal expansion between the coatings and the substrates ($0.8x10^{-6} < \alpha < 4.5x10^{-6}$ K^{-1}, for $293,15 < T < 1073,15$ K for diamond, and approximately $11x10^{-6}$ K^{-1} for steels) [2]. On the other hands, carbon presents a very large solubility in most ferrous materials and the Fe vapour pressure affects the plasma [3]. Due to this fact, several researches have been made to increase the adherence of DLC coatings onto metallic surfaces. The most common process is to place an interlayer between the substrate and the DLC film [1, 2, 4-7].

Another authors have studied as influenced the diffusion in the adhesion [8], [9]. They calculated the diffusion of diverse materials in the Fe and it was suggested that the interlayer should serve as a diffusive barrier between carbon and iron with a mutual diffusion with the substrate. Spinnewyn et al. [8] concluded that is better to use W, Ta, and Cr as interlayer due to their excellent diffusion barriers for the iron from the steel substrates. They obtained that Si and Ti would require very thick layers and they decided to use W and Mo as interlayers, but low adhesion was observed. On the other hands, another authors [9] ensured that Fe has a low diffusion in Cr, Ta, and W; average in Cu, Au, and Ag; and high in Ti. Therefore, a good adhesion was expected between the steel substrate and the titanium interlayer. From that point of view, the interlayer of Ti does not seem to be adequate in comparison to W interlayer. However, at the beginning of diamond growth the formation of TiC and diamond nucleation can form quickly and if the deposition temperature is low, the carbon diffusion may be reduced. Thus, they selected titanium as an interlayer material getting good adhesion.

In order to reduce the coefficient of thermal expansion gradually multi-layers were deposited by several authors [10], [11], but the use of the interlayers made with alloys are not been reported. For this reason, in this work an alloy of TiW was used as interlayer in order to improve adhesion of the DLC coatings onto AISI 316L stainless steel substrates. The influence of the interlayer thickness was studied, using 100, 200, and 300 nm. The TiW interlayers were deposited via R.F. magnetron sputtering, while the DLC coatings using a modified pulsed-DC PECVD system with an additional cathode.

2. Experimental

Samples of AISI 316L stainless steel (0.03 C wt%, 16.7 Cr wt%, 9.5 Ni wt%, 2.9 Mo wt%, and Fe balance) with sizes 1.5 cm x 1.5 cm x 0.6 cm was used as substrate. The substrates were prepared metallographically and cleaned ultrasonically in an acetone bath for 15 minutes before of deposition. A R.F. magnetron sputtering system (13.56 MHz) and $Ti_{10}W_{90}$ target (99.99% pure) were employed to TiW interlayer deposition. The interlayers were synthesized using a pressure in the chamber of 0.19 Pa ($1,9X10^{-3}$ mbar) and applying power of 200 W, while Ar was used as precursor gas for plasma with flow of 20 sccm. The deposition times were selected in order to obtain thicknesses of 100 nm, 200 nm, and 300 nm, respectively (see figure 1). After the interlayer deposition, the substrates were put into a pulsed-DC PECVD reactor with an asymmetrical bipolar pulsed-DC power supply and an active screen for the DLC coating depositions. Before DLC film deposition, the substrates were sputter cleaned in an argon atmosphere for 15 minutes in order to remove any contamination on the surface. DLC films were deposited using methane as precursor gas, a pressure of 5 Pa (gas flow of 5 sccm), and applying a negative voltage of -700 V for 3 hours.

The crystal structure was determined by X-ray diffraction (XRD) using an X-pert Pro Panalytical device operating in beam mode at 5°, with monochromatic line Kα of copper (1.540998 Å) working at 45 kV and 40 mA. The surface morphology was observed using a high-vacuum FEI QUANTA 200 scanning

wshincapiec@unal.edu.co

electron microscope (SEM), operating at a voltage of 30 kV. The chemical composition of the interlayer was determined via energy-dispersive X-ray spectroscopy (EDX) with energy of 4 kV to 6 kV using a SEM MIRA3. Raman spectroscopy allowed determining the microstructure of the DLC films using a HR Evolution spectrometer and a laser of 514 nm. Scratch test was employed to calculate the critical load using a Rockwell C indenter and varying the applied force, also test of indentation was used.

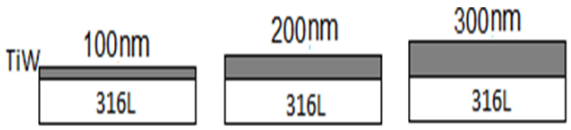

Fig. 1. *Interlayer scheme.*

3. Results and Discussions

A TixWy interlayer was deposited on AISI 316L substrates in order to improve DLC coating adhesion. The composition of the interlayer's were 56 W wt% and 44 Ti wt% for the film with 300 nm of thinness, while in the film with 100 nm 49.7 W wt%, 41.7 Ti wt%, and 8.6 Fe wt% were determined. Surface morphology showed that the coatings did not grow homogeneously, observing zones with high content of W and Ti. X-ray diffractograms are shown in figure 2, presenting of two phases Ti y W, there is not formation of new peak indicating the absence of a new phase. The calculated network parameter for Ti and W was 0.28954 nm and 0.31137 nm respectively. A change of the preferential direction for the different thicknesses was detected. Raman spectra showed that DLC coatings with a content of hydrogen between 20 and 30% were deposited. The adhesion strength did not change significantly when different interlayer thicknesses were used, showing a critical load of about 30 N. This preliminary work allowed the deposition of DLC films with good adhesion on surfaces of AISI 316L substrates. Other investigations are being carried out in order to grow these coatings using lower pressures (less than 1 Pa) and other interlayer's.

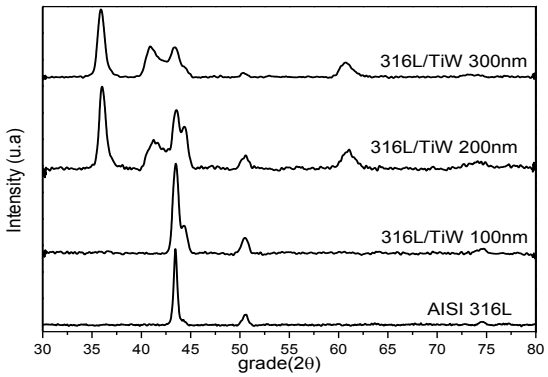

Fig. 2. *X-ray diffractograms.*

4. References

[1] G. Capote, E. J. Corat, and V. J. Trava-airoldi, *Surf. Coat. Technol.*, 260, 133-138, (2014).
[2] F. J. G. Silva, J. S. Fernandes, F. M. Costa, P. M. Baptista, and E. Pereira, *Diam. Relat. Mater.*,13, 828-833, (2004).
[3] F. J. G. Silva, P. M. Baptista, E. Pereira, V. Teixeira, Q. H. Fan, J. S. Fernandes, and F. M. Costa, *Diam. Relat. Mater.*, 11, 1617-1622, (2002).
[4] U. Helmersson, B. O. Johansson, J. E. Sundgren, H. T. G. Hentzell, and P. Billgren, *J. Vac. Sci. Technol. A3*., 3, 308, (1985).
[5] M. Y. Al-Jaroudi, H. T. G. Hentzell, S. E. Hörnström, and A. Bengtson, *Thin Solid Films*., 182, 153-166, (1989).
[6] S. J. Bull, P. R. Chalker, C. F. Ayres, and D. S. Rickerby, *Mater. Sci. Eng. A*, vol. 139, 71-78, (1991).
[7] Y. Xu, L. Li, X. Cai, and P. K. Chu, *Surf. Coat. Technol.*, 201, 6824-6827, (2007).
[8] J. Spinnewyn, M. Nesládek, and C. Asinari, *Diam. Relat. Mater.*, 2, 361-364, (1993).
[9] Q. Hua Fan, A. Fernandes, and J. Grácio, *Diam. Relat. Mater.*, 7, 603-606, (1998).
[10] J. Deng and M. Braun, *Diam. Relat. Mater.*, 4, 936-943, (1995).
[11] A. A. Voevodin, J. M. Schneider, C. Rebholz, and A. Matthews, *Tribol. Int.*, 29, pp. 559-570, (1996.)

wshincapiec@unal.edu.co

ID 62: SURFACE CHARACTERIZATION OF HMDSO FILMS DEPOSITED BY ATMOSPHERIC PRESSURE PLASMA JET ON SAE 1020 STEEL

Pedro V. M. Fagundes[1]*, Nilson A. Ferraz[1], V. Prysiazhnyi[2], Konstantin G. Kostov[2] and Leide L. G. Silva[1,2]
[1] *Faculdade de Tecnologia de Pindamonhangaba – FATEC, Pindamonhangaba, SP, Brazil*
[2] *Faculdade de Engenharia de Guaratinguetá – FEG, Universidade Estadual Paulista – UNESP, Guaratinguetá, SP, Brazil*

1. Introduction

Deposition of polymer films by plasma has emerged as an alternative approach because it is environmentally friendly, promoting enhancement of adhesion to metallic substrates and protection from corrosion [1, 2]. The most studies of plasma polymers are performed at low pressure, which requires expensive vacuum systems [1]. In contrast, plasma processing at atmospheric pressure for obtaining polymer films is economically favorable because does not require such apparatus. The aim of this work is to study the surface properties of polymer films obtained by Atmospheric Pressure Plasma Jet (APPJ) on SAE 1020 steel.

2. Experimental

The substrates used in this work were SAE 1020 steel discs. The plasma jet system consists of a 18.0-mm-diam Pyrex tube terminating with a horn-like nozzle, a HV electrode placed inside it and a grounded electrode covered by glass table that is placed beneath the tube. Plasma was excited by an AC power supply operating at 19.0 kHz and voltage amplitude of 15.0 kVp-p. The device was flushed with 1.0 L/min argon flow resulting in an approximately 10-mm-long plasma plume, which was extracted from the tube exit. In order to deposit polymer film a mixture of air/monomer at flow rate of 0.1 and 0.05 L/min was introduced into the discharge. Samples were exposed to the plasma jet for 10 and 20 min. using a nozzle-to-sample distance of 2.0 to 6.0 mm. First, open circuit potential curves were obtained to optimize the experimental conditions and after this, the polarization analyses, contact angle, and scanning electron microscopy were carried out in the best condition for obtaining the HMDSO films.

3. Results and Discussions

A decrease of the water contact angle from 98° up to 28° was observed for the samples without and with deposited film, respectively. As evidenced by SEM, the HMDSO films exhibited non homogeneous surface morphology as evidenced by two different regions in the figure 1, a rougher (R1) and a smoother (R2). Figure 2 presents a magnification of the R2 region. The cauliflower structure can also influence the surface wettability. The results of electrochemical measurements presented a slight improvement of the corrosion potential and corrosion current density of SAE 1020 steel after the HMDSO film deposition.

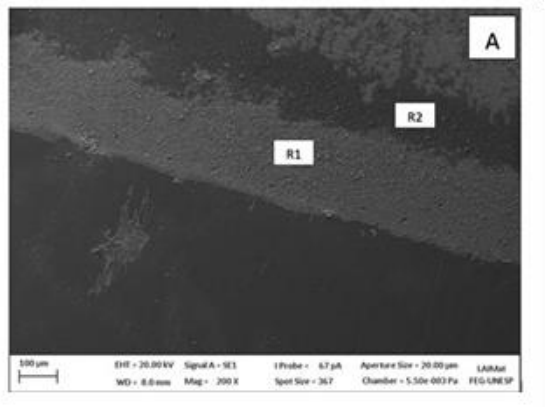

Fig. 1. *SEM images of HMDSO films (t=10 min, gap=6mm): 200X.*

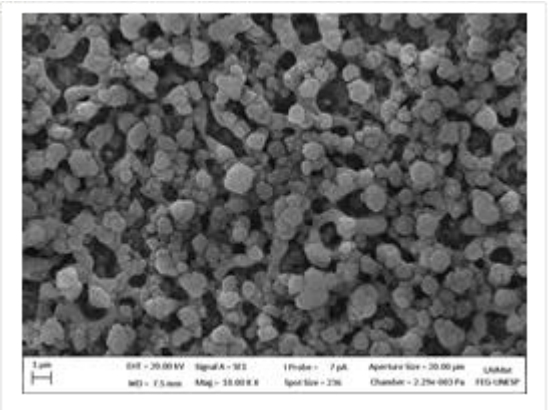

Fig. 2. *SEM images of HMDSO films (t=10 min, gap=6mm): 10,000X*

Acknowledgments

The author thanks to the Plasma and Applications group, DFQ-UNESP by the polymer films depositions.

4. References

[1] U. Lommatzsch and J. Ihde, Plasma Processes and Polymers. **6**, 642, (2009).
[2] A. Vogelsang, A. Ohl, R. Foest and K-D Weltmann. Plasma Processes and Polymers, **10**, 364-371, (2013).

*pedro.fagundes@fatec.sp.gov.br

ID 63: H-IMPLANTATION CHANGES STOICHIOMETRY AND HYDROXYLATION STATES OF NITRIDED TITANIUM SURFACES

G. B. de Souza[1]*, S. H. Gonsalves[1], K. C. Ribeiro[1], D. G. Ditzel[1], M. Ueda[2] and W. H. Schreiner[3]
[1]*Departmento de Física, Universidade Estadual de Ponta Grossa - UEPG*
[2]*Laboratório Associado de Plasma, Instituto Nacional de Pesquisas Espaciais – INPE*
[1]*Departmento de Física, Universidade Federal do Paraná - UFPR*

1. Introduction

As versatile materials, titanium and titanium-based devices are often exposed to challenging situations, which can compromise their mechanical integrity. In super-hydrophilic films, fuel cells, fusion reactor walls or tritium storage targets, the surface interacts with hydrogen in varied degrees of severity, which can eventually lead the material to undergo embrittlement mediated by the precipitation of hydrides [1]. A nitride layer produced, e.g., by plasma-based methods, operate as a barrier for the hydrogen diffusion into the bulk [2]. On the one hand, the hydrogen interaction with nitrides at near surface is not yet completely understood; on the other hand, the controlled irradiation of TiN and the native surface oxides can lead to interesting modifications due to the charge balance in the surface. These issues were investigated here.

2. Experimental

Titanium samples were plasma nitrided in a conventional glow discharge chamber at 600 ºC, and subsequently hydrogen-implanted through plasma immersion ion implantation, using ion energies from 1.2 keV to 5.0 keV. The surfaces were analyzed by scanning electron microscopy, instrumented indentation, X-ray diffraction, micro-Raman spectroscopy, X-ray photoelectron spectroscopy (XPS) and Fourier-transform infrared spectroscopy (FTIR).

3. Results and Discussions

The plasma nitrided surfaces consisted in hardened (40% higher hardness than substrate) and stiffer (200% higher elastic modulus) layers constituted of Ti_2N and TiN. Differently from the intense plasma-based hydrogenation, described elsewhere [3], the H-implantation were restricted to very shallow depths on the nitrided surfaces, producing no assessable changes in the crystalline structure, mechanical properties or morphology. Such features corroborated with the *H-barrier effect* provided by the nitrides layer.

The Ti2p doublet, N1s and O1s XPS analyses disclosed that the TiN amount reduced with the rising H-implantation, as the TiO_2 contribution to the spectra increased. From the photoelectron detection theory [4], and assuming a stratified TiO_2 + TiN_xO_y + TiN layer on the top surface, it was demonstrated that

$$\ln\frac{I_{ox}}{I_{lay}} = \ln\frac{I_{0,ox}}{I_{0,lay}} + \ln\left[1-\exp\left(-\frac{d}{\lambda\sin\theta}\right)\right] \quad (1)$$

is directly proportional to the increase of the oxide layer and decrease of the TiN one, which correlated in a linear-like fashion with the H-implantation energy, as shown in Fig. 1. In the equation above, *I* are integrated intensities of Ti2p XPS peaks ascribed to the layer (*lay*) and the oxide (*ox*), where the index *0* denotes values calculated for photoelectron beams emerging from "infinitely thick" materials. θ is the take-off angle from the surface, *d* the layer thickness, and λ the inelastic mean free path.

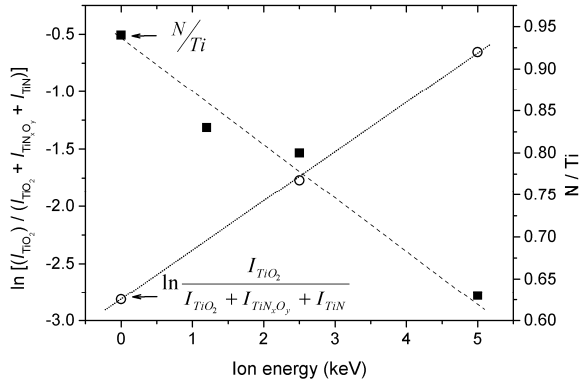

Fig. 1. *Correlations of the H-implanted ion energies with features of the nitrided surfaces. Open symbols are ascribed to Equation 1 and addressed to the left side axis. The close symbols address to the right side axis, which were calculated through Equation 2. Lines are only guides for the eyes.*

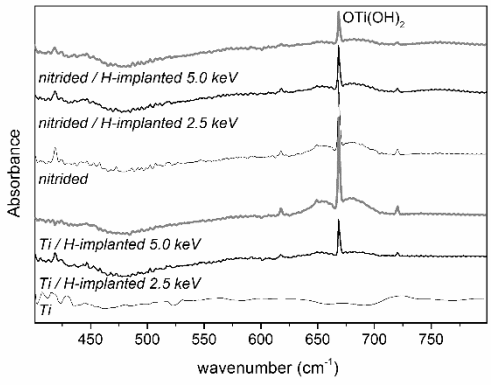

Fig. 2. *FTIR spectra of titanium and nitrided titanium surfaces, prior and after the H-implantation with ion energies 2.5 keV and 5.0 keV.*

*Corresponding author: gelsonbs@uepg.br

Also linear with the H-implantation energies were the N/Ti atomic ratio, inferred for the TiN compound from Raman spectra by [5]

$$\frac{N}{Ti} \propto \frac{I_{TO}+I_{LO}}{I_{TA}+I_{LA}}. \quad (2)$$

In this relation, the integrated peak intensities *I* stands for first-order transversal and longitudinal optic (TO, LO) and acoustical (TA, LA) scattering modes. Differently from equation (1), the N/Ti ratio was nearly inversely proportional to the H-implantation energy, as also shown in Fig. 1. The evolutions of equations (1) and (2) with respect to the H-implantation energy were indicatives of the *surface denitriding*. This phenomenon is probably a conjunction of physical and chemical effects, promoted by momentum transfer from the energetic ions and the environmental chemical conditions.

Fig. 2 presents FTIR spectra of titanium and nitrided titanium, prior and after the H-implantation. A strong and narrow line at 668 cm^{-1} was produced on the H-implanted titanium. It was also observed in the plasma nitrided samples, which persisted after hydrogenation, although with lower absorbance intensities. These peaks are ascribed to Ti-OH stretching in the $OTi(OH)_2$ molecule bonded in the surface [6]. It was produced on titanium through changes in the *hydroxylation states* of native oxides by the energetic H-bombardment. On nitrided titanium surfaces, the formation mechanism possibly involved photocatalysis in air atmosphere, enhanced by the presence of oxinitrides. The subsequent H-implantation changed the oxinitrides stoichiometry, as seen in Fig. 1, with consequences to the hydroxylation states of the nitrided surface. Perhaps, some photocatalysis controlling can be attained by the H-irradiation on titanium and nitrided titanium.

4. References

[1] G. B. de Souza et al., Surf. & Coat. Tech., **312**, 91-100, (2017).
[2] M. Soltani-Farshi et al., Surf. & Coat. Tech., **104**, 299-303, (1998).
[3] G. B. de Souza et al., Mater. Chem. Phys., **124**, 443-452 (2010).
[4] D. P. Woodruff and T. A. Delchar *"Electron Spectroscopies"*, 2nd ed., Cambridge Univ. Press, UK, (1999).
[5] Y. H. Cheng et al., J. Appl. Phys., **92**, 1845 (2002).
[6] L. Shao et al., Chem. Phys. Lett., **343**, 178-184 (2001).

Acknowledgments

The Brazilian Funding Agencies CNPq (grants no. 477973/2011-6 and 310819/2015-6) and Fundação Araucária (grants no. 363/2012 and 608/2014) for the financial support.

*Corresponding author: gelsonbs@uepg.br

ID 65: EVALUATION OF THE PHYSICAL-MECHANICAL PROPERTIES OF CEMENT-BASED COMPOSITES REINFORCED WITH SURFACE-MODIFIED CELLULOSE PULP

Sara Aparecida Alexandre[1*], Bianca Paula de Almeida[1], Alexandre Fassini Michels[2], Rafael Farinassi Mendes[1], Lívia Elisabeth Vasconcellos de Siqueira Brandão Vaz[1]

[1]Universidade Federal de Lavras
[2]Universidade de Caxias do Sul

1. Introduction

Cement matrices, without addition of fibers, tend to crack when subjected to mechanical tensile testing. Fibers can be introduced into these matrices aiming at improvements in their traction resistance. Asbestos fibers were widely used for this purpose, but because of problems related to the health of those who manipulated them and because of legislation of several countries converged to prohibit and ban the use of this mineral, this kind of fibers have been replaced [1, 2]. Synthetic fibers as wood, sisal, jute and hemp were first tested and, in spite of their good results, its use entails a high cost final product [3,4]. The use of reinforcements of vegetable origin appears as an interesting alternative because it is economically viable, ecologically correct and it is possible to modify the surface of them to avoid any obstacles that limit its use into cement-based composites [5].

2. Experimental

In this work, the physical-mechanical properties of extruded cement-based composites produced with cellulose pulps superficially modified with silicone was evaluated. The experimental design for the superficial chemical modification of the cellulose was based on the evaluation of silicone in concentrations of 0, 5, 10, 15, 20 and 25% in relation to the dry mass of pulp. The treatments that presented satisfactory surface modification were used to produce cement-based composites, by the extrusion method. The formulation used in the production of the composites was 5% cellulose, 60% Portland cement CPV-ARI, 33% ground agricultural limestone, 1% HPMC (Hydroxypropylene Methylcellulose) and 1% ADVA (Polyether carboxylic additive), with final water / cement ratio of 0.4.

3. Results and Discussions

The cement-based composites had their physical-mechanical properties analyzed by physical tests of apparent density, water absorption and apparent porosity and by mechanical tests of static bending for determination of proportionality limit, modulus of rupture, modulus of elasticity and toughness. The composites that presented satisfactory results for the analyzes to verify the efficiency of adhesion between pulp and cement were those elaborated with increment of pulp cellulosic with concentrations of silicone varying between 10 and 20% in relation to the dry mass of pulp.

4. References

[1] H. Castro; F. Gianassi; C. Novello. Ciência e Saúde Coletiva, **8**, 903-911(2003).
[2] R. S. P. Coutts. Cement and Concrete Composites, **27**, 518-526 (2006).
[3]M. J. John; S. Thomas. Carbohydrate Polymers ,**71** , 343-364 (2008).
[4]A. K. Mohanty; L. T. Drzal et al., Journal of Adhesion Science and Technology ,**16** ,999-1015 (2002).
[5] L. J. Silva et al., 65° Congresso Internacional da ABM (2010).

Acknowledgments

Empresa Brasileira de Pesquisa Agropecuária (Embrapa), Universidade Federal de Lavras (UFLA), Universidade de Caxias do Sul (UCS), Coordenação de Aperfeiçoamento de Pessoal de Nível Superior (Capes), Conselho Nacional de Desenvolvimento Científico e Tecnológico (CNPq) and Fundação de Amparo à Pesquisa do Estado de Minas Gerais (Fapemig).

*Corresponding author: salexandre.eng.amb@gmail.com

ID 67_1: POSSIBLE PATHWAYS IN THE FORMATION OF FORMYL RADICAL HCO

Washington Barbosa da Silva[1], Patrícia R. P. Barreto[2], Alessandra F. Albernaz[3], Eberth Correa[4]*
[1]Instituto Federal de Brasília, Campus Ceilândia, Ceilândia, DF, CEP 72220-260
[2]Laboratório Associado de Plasma, Instituto Nacional de Pesquisas Espaciais, CP515, São José dos Campos, SP, CEP 12247-970
[3]Instituto de Física, Universidade Brasília, CP04455, Brasília, DF, CEP 70919-970
[4]Universidade de Brasília, Campus do Gama, Gama, DF, CEP 72444-240, Brasil

1. Introduction

The interest in the reaction between the CO molecule and the H atom comes from its relevant processes in atmospheric chemistry [1, 2]. In particular, one of the products of this reaction, formyl radical HCO, is a very important molecule in many fields as atmospheric chemistry [2], combustion science [3] and interstellar space [4]. The nature of the interaction between H atoms and CO has been investigated through studies of collisions between these species [5]. As the second most abundant molecule in the universe, carbon monoxide, CO, is observed in star-forming regions and protoplanetary disks, and in external galaxies. It is commonly used as an indicator of the physical conditions in the regions where CO infrared emission is observed [6]. To extract astrophysical parameters from the observed spectral lines, it is not appropriate to assume local thermodynamic equilibrium in the dilute gas of astronomical sources [6].

In this work we investigate the possible pathways for the reaction of the carbon monoxide with hydrogen. Initial equilibrium geometries of the reactions, intermediate reactions, transition states, and product were optimized at G3 method for all species involved in the reaction. The rate constants were calculated using transition state theory and master equation software package MESMER [7], at low pressure written in the Arrhenius and alternatives forms. The first pathway is the well studied HCO addition and the respective dissociation in the reverse pathway as one can see bellow

$$\mathrm{H} + \mathrm{CO} \underset{k_{-1}}{\overset{k_1}{\rightleftarrows}} PRC_1 \overset{M}{\underset{k_2}{\leftrightarrow}} \mathrm{HCO} \qquad \text{(R1)}$$

The second one is the alternative pathway pointed out by our intrinsic reaction coordinate (IRC) calculations visualized as the following:

$$\mathrm{H} + \mathrm{CO} \underset{k_{-3}}{\overset{k_3}{\rightleftarrows}} PRC_2 \underset{k_{-4}}{\overset{k_4}{\rightleftarrows}} \mathrm{HOC} \overset{M}{\underset{k_5}{\leftrightarrow}} \mathrm{HCO} \qquad \text{(R2)}$$

R2 is basically composed by a reversible reaction towards the complex PRC_2, which in turns with the aid of a "third body M" collision is stabilized towards HOC, and finally (by means of an isomerization) produces HCO. Our findings in the determination of the rate constant for the addition showed that this pathway is very unlikely. However, we found more likely the HCO dissociation along this pathway. For this reason, we calculate the rate constant for the HCO dissociation along this pathway. Assuming quasistationary concentrations for the highly unstable complexes, the rate constants for the reactions are given by:

$$k_{PW1} = \frac{k_1 k_2 [M]}{k_{-1} + k_2 [M]} \qquad (1)$$

$$k_{PW2} = \frac{k_3 k_4 k_5 [M]}{k_{-3} k_{-4} + k_{-3} k_5 [M] + k_4 k_5 [M]^2} \qquad (2)$$

2. Computational Methods

The G3 Method, in Gaussian 09 program, was employed to optimize the geometries, vibrational frequencies and energies of the reactant, intermediate complexes, transition states, and products of the H + CO reactive process. To confirm that the transition state really connects to designated intermediates along the reaction path, the intrinsic reaction coordinate (IRC) calculations were performed. Also the IRC calculations were used to confirm the connection between the designated transition states and the reactants or products.

The rate constants were calculated taking into account the potential energy surface (PES) with the aid of the Master Equation Solver for Multi Energy Well Reactions (MESMER) open source program [7]. The MESMER approach uses a stochastic energy grained master equation (EGME) to model phenomenological kinetics, for which the energy transfer due to an external bath is relevant. The bath gas M used during all the calculations is the non-reacting He gas. As mentioned elsewhere, our IRC calculations showed energy barriers in the formation of the several products for the addition and dissociation (reverse pathway) reactions displayed in Figure 1 represented by R1 and R2.

*patricia.barreto@inpe.br

3. Results and Discussions

Along the pathway on the reactive potential energy surface, first the H-atom attacks the CO molecule, forming the HCO molecule H+CO ⇆ *PRC₁* → *TS₁* → HCO (R1). The second pathway is *PRC₂* →*TS₂* → HOC → *TS₃* → HCO (R2). The energies (relative to the reactant total energy set zero) of all species involved are summarized in Figure 1. In particular, the formation of HOC has been little investigated theoretically, and, no experimental data are available about this radical. The geometry parameters, energies ΔE, relative to H + CO, and the imaginary frequencies of the saddle points (in parentheses) are calculated using the G3 method and are visualized in Figure 1. Our results are in relative good agreement with other studies.

In Figure 2, we display our simple RRKM result for the addition reaction R1 for a range of temperatures 298 – 1000 K. For comparison with well known results we chose $\langle \Delta E \rangle_d$ = 160 cm^{-1} and 40 cm^{-1} for the grain size. In order to solve the master equation for this bimolecular reaction, MESMER models the pseudo-first order bimolecular source defining an excess of reactant and a deficient reactant. In this case the concentration of the excess of reactant is due to the CO molecule and we set 5.8 × 10^{16} mol cm^3. The first part of reaction occurs without any barrier and the MesmerILT was used with A_∞ = 0.2 × 10^{-14} cm^3 $molecule^{-1}$ s^{-1}, n_∞ = 0.6, T_∞ = 300 K and E_∞ = 0. For a fixed temperature, the resulting second order rate constant k_{PW1} can be calculated using Eq. (1), which in turn is divided by the bath concentration, [He], to obtain the respective rate constant. In Figure 3, is shown the dissociation path, equation (2) in the range of temperatures 600 – 2500 K. For the alternative pathway R2 the reaction takes place through the *TS₂* and *TS₃* barriers as indicated in Figure 1. For this reaction we used a value of $\langle \Delta E \rangle_d$ = 180 (T = 300 K) 0.25 cm^{-1} and 95 cm^{-1} for the grain size. In this case we used the MesmerILT ag with A_∞ = 3.5 ×10^{-14} cm^3 $molecule^{-1}$ s^{-1}, n_∞ = 1.0, T_∞ = 300 K and E_∞ = 3.7 kJ mol^{-1}. In addition, we used the Eckart tunneling correction for both barriers due to the fact that there is a low mass (H) atom transfer involved, and resulted very important to calculate the overall rate constant in this case.

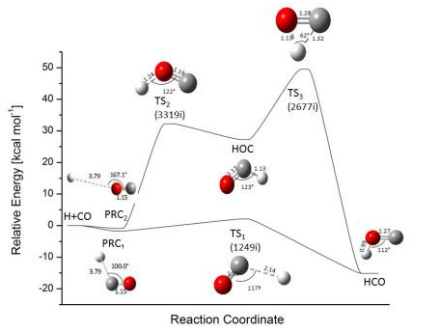

Fig 1: *Potential energy diagram for H + CO → HCO reaction using G3 Method.*

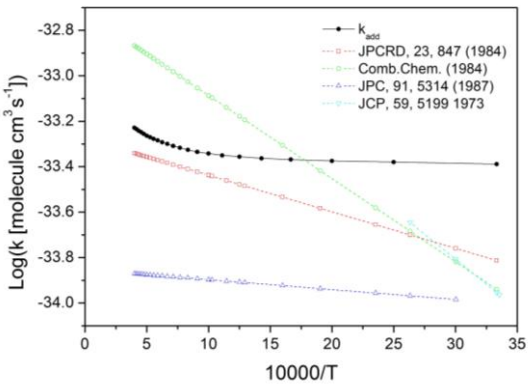

Fig 2: *Association rate*

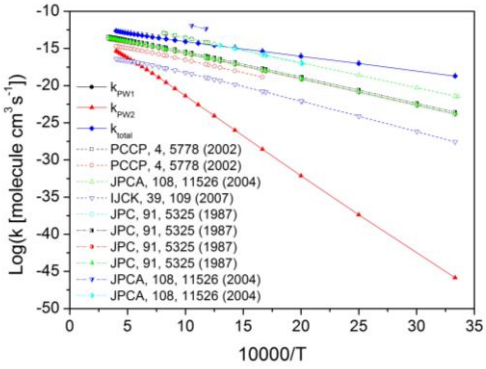

Fig 3: *Dissociation rate*

4. References

[1] P. S. Peters, D. Duot, L. Wiesenfeld, C. Toubin, J. Chem. Phys. 139, 164310, (2013)
[2] P. V. Hobbs, Introduction to Atmosphere Chemistry, Cambridge University Press, Cambridge, (2000).
[3] J. A. Miller, R. J. Kee, C. K. Westbrook, Annu. Rev. Phys. Chem. 41, 345, (1990).
[4] S. Chu, A. Dalgarno, Proc. Roy. Soc. A 342, 194, (1975).
[5] C. A. Wight, S. R. Leone, J. Chem. Phys. 78, 4875, (1983).
[6] L. Song, A. van der Avoird, G. C. Groenenboom, J. Phys. Chem. A 117, 7571, (2013)
[7] D. R. Glowacki, C.-H. Liang, C. Morley, M. J. Pilling, S. H. Robertson, J. Phys. Chem. A 116, 9545, (2012).

*patricia.barreto@inpe.br

ID 67: HYPERSPHERICAL COORDINATE POTENTIAL ENERGY SURFACE FOR THE Rg_3 COMPLEX, WITH Rg=Ne, Ar, Kr AND Xe

Patrícia R. P. Barreto[1], Alessandra F. Albernaz[2]
[1]*Laboratório Associado de Plasma, Instituto Nacional de Pesquisas Espaciais, CP515, São José dos Campos, SP, CEP 12247-970,*
[2]*Instituto de Física, Universidade Brasília, CP04455, Brasília, DF, CEP 70919-970*

1. Introduction

Since the appearing of first work on He_3 in 1972[1], several theoretical papers have been published using different methods: Monte Carlo [2, 3], specific functions [4] and hyperspherical coordinates [5]. Nevertheless, unfortunately, an analytic form of the PES simple enough to be used for all the purposes were missing. On a previous paper [6], we had fill out the above gap by furnishing a very simple and accurate analytical expression of the PES for the He_3 and now we apply it for all the rare gas series. In the hyperspherical coordinate system, we define the hyperradial coordinate ρ that provides a measure of the size of the system, in addition to a set of hyperangle, Θ and Φ. In the literature we can find different approach to different systems, as variational approach, which uses atom pair coordinates and a distributed Gaussian function (DGF) basis set. For the heavier rare gases as Krypton and Xenon littler information about the PES is found in the literature.

2. Theoretical and Computational Details

The coordinate system is made by three variable, the hyperradius ($\rho > 0$) and two hyperangles ($0 \leq \Theta \leq \pi/4$) and $0 \leq \Phi \leq \pi/3$). The hyperangle Θ represents the area of the triangle and the hyperangle Φ is related with the shape of it, the hyperradius, ρ, is the vector pointed out from the center-of-mass (CM) of the system, see Fig.1.

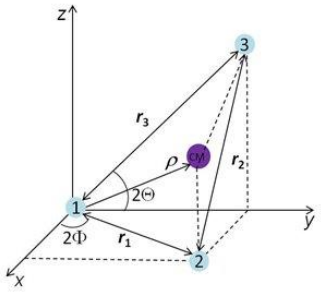

Fig. 1 *Definition of the hyperspherical coordinates (ρ,Θ,Φ). The vector r_i (x_i; y_i; z_i) (i = 1; 2 and 3) representing the internuclear distances of the rare gas atoms, ρ is the vector with representing the distance between the center-of-mass of the molecule system.*

In this figure, the vectors $\boldsymbol{r}_i$ (x_i; y_i; z_i) (i = 1; 2 and 3) representing the interatomic distances in space. We have obtained the PES using the mass unscaled hyperspherical coordinates. Note that the ranges of Θ and Φ are lower than their standard values. Symmetry restrictions are, indeed, needed to account for the exchange of identical particles. The definition of the hyperradius and hyperangles can be find in our previous work [6].

Using the coordinates system, presented in Fig.1, the PES can be expanded into a series of angular functions multiplied by radial coefficients (expansion moments):

$$V(\rho,\Theta,\Phi) = \sum_m \upsilon_m(\rho) F_m(\Theta,\Phi) \quad (1)$$

where the $\upsilon_m(\rho)$ coefficients are the expansion moments depending on the ρ coordinate and $F_m(\Theta,\Phi)$ are angular functions which can be written as the real Wigner D-functions [7] with the γ angle equal to zero, where the D-function is given by: $D^l_{m,n}(\Theta,\Phi,\gamma) = e^{-im\Theta} d^l_{m,n}(\Phi) e^{-im\gamma}$, and $d^l_{m,n}(\Phi)$ is tabulated function. In that, way the term $F_m(\Theta,\Phi)$ can be written as:

$$F^l_{m,n}(\Theta,\Phi,\gamma) = \sqrt{\frac{8\pi^2}{2(2l+1)}}\left(D^l_{m,n}(\Theta,\Phi,\gamma) + \epsilon D^l_{-m,-n}(\Theta,\Phi,\gamma)\right) \quad (2)$$

Truncating equation (1) at $m = 1$, which is enough to represent a three-body system, we have:

$$V(\rho,\Theta,\Phi) = \sqrt{2}\{\upsilon_{0,0}(\rho) d^0_{0,0}(4\Phi) + \upsilon_{0,1}(\rho)\left[d^1_{0,0}(4\Phi) + d^1_{0,1}(4\Phi)\right] + \upsilon_{1,1}(\rho)\cos(6\Theta)\left[d^1_{1,0}(4\Phi) + d^1_{1,1}(4\Phi)\right]\} \quad (3)$$

This shows that three not dependent radial functions are needed for $V(\rho,\Theta,\Phi)$, thus we considered three different arrangements (leading configurations) of the Rg_3 complex: the linear disposition, the equilateral triangle and a scalene triangle. The expansion moments are, then, obtained by a linear combination of the potential profiles calculated for the leading configurations. The moments $\upsilon_{m,n}(\rho)$ are related to the potentials of the leading configurations by:

$$\begin{aligned} V_{eq}(\rho) &= \sqrt{2}\left(\upsilon_{0,0}(\rho) - \upsilon_{0,1}(\rho)\right) \\ V_{sc}(\rho) &= \sqrt{2}\upsilon_{0,0}(\rho) + \tfrac{1}{2}\left(\sqrt{3} - \sqrt{2}\right)\upsilon_{0,1}(\rho) \\ V_{lin}(\rho) &= \sqrt{2}\left(\upsilon_{0,0}(\rho) + \upsilon_{0,1}(\rho) + \upsilon_{1,1}(\rho)\right) \end{aligned} \quad (4)$$

* patricia.barreto@inpe.br

Solving the above system of equations for $v_{0,0}(\rho)$, $v_{0,1}(\rho)$ and $v_{1,1}(\rho)$, gives:

$$v_{0,0}(\rho) = \left(\sqrt{\frac{3}{2}} - 1\right)\left((\sqrt{3} - \sqrt{2})V_{eq}(\rho) + 2\sqrt{2}V_{sc}(\rho)\right)$$
$$v_{0,q}(\rho) = -\sqrt{2}(\sqrt{6} - 2)\left(V_{eq}(\rho) + V_{sc}(\rho)\right) \quad (5)$$
$$v_{1,1}(\rho) = \left(4\sqrt{3} - \frac{9\sqrt{2}}{2}\right)V_{eq}(\rho) + 4(\sqrt{2} - \sqrt{3})V_{sc}(\rho) + \frac{\sqrt{2}}{2}V_{lin}(\rho)$$

Therefore, by substituting eq. (5) into eq. (4), the full potential is obtained provided analytical expressions for $V_{lin}(\rho)$, $V_{eq}(\rho)$ and $V_{sc}(\rho)$ are available. To get U(ρ), where $U(\rho) = V_{sc}(\rho), V_{sc}(\rho), V_{sc}(\rho)$; we have computed the energies of 151 points having different values of ρ for each of the three leading configurations, then we have fitted the energies vs ρ by means of a nonlinear least-square procedure, using a fifth degree generalized Rydberg potential as the fitting function. The complex energy is expressed as: $E_{int} = E_{Rg_3} - 3E_{Rg}$.

3. Results and Discussions

The ab initio calculations were carried out by using the Molpro2010 program. The CCSD(T)/aug-cc-pVQZ for all Rg_3 system, except for Xe_3 where the basis set aug-cc-pvQZ-PP was used. First, a simple optimization and frequency calculation for all dimers and trimers were carried out to determine the equilibrium configuration. It will be used as a guide for the PES calculation. For all trimers, we have computed 151 energies to different values of distance, while for the dimers we calculated 101 energies. A nonlinear least-squares procedure was used to obtain the values of the adjustable parameters that minimize the differences between the analytical energies obtained with the fifth degree generalized Rydberg function.

Fig.2 compared the PES for the dimers. The optimized data are, also, included in this figure, with the reference data. It is possible to observe that our optimized data are in good agreement with the reference data. The biggest error in the ab initio fitting is for the Xenon dimer, with a rms of 0.033252 cm^{-1}.

Fig.3 present the ab initio and the Rydberg fitting for leading configuration of each rare gas trimer. The smallest and biggest rms among all the fittings are 0.006707 and 0.158722 cm^{-1} for the scalene Xe_3 and equilateral Kr_3, respectively.

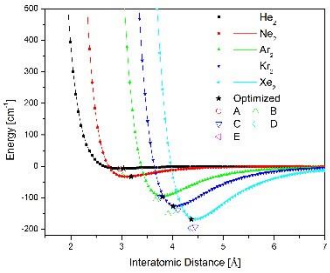

Fig. 2: *Dimers potential energy surface, [A] J. Chem. Phys. 1972, 56, 5801, [B] J. Chem. Phys. 1976, 65, 3242, [C] J. Mol. Spectr. 1973, 46, 454, [D] J. Chem. Phys. 1974, 61, 3081, [E] J. Chem. Phys. 1974, 61, 4880*

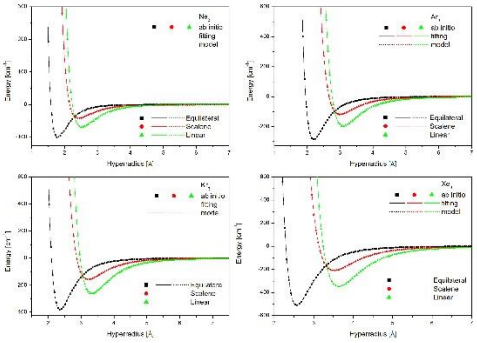

Fig. 3 *Rg_3 leading configurations*

4. References

[1] O. A. Navarro, V. Beltran-Lopez, J. Chem. Phys., 56, 815, 1972.
[2] D. Blume, C. H. Greene, J. Chem. Phys., 112, 8053, 2000.
[3] T. Gonzlez-Lezana, J. Rubayo-Soneira, S. Miret-Artés, F. A. Gianturco, G. Delgado-Barrio, P. Villarreal, J. Chem. Phys., 110, 9000, 1999.
[4] M. J. M. Cohen, Chem. Phys. Lett., 260, 371, 1996.
[5] D. Blume, C. H. Greene, B. D. Esry, J. Chem. Phys., 113, 2145, 2000
[6] A. F. Albernaz, P. R. P. Barreto, Rev. Virtual Quim., 8, 338, 2016.
[7] Varshalovich, D. A.; Moskalev, A. N.; Khersonskii, V. K.; *Quantum Theory of Angular Momentum*, World Scientific: Singapore, 1988.

Acknowledgements
This work was supported by a MCTI-PCI grant, Institutional Process Number 454779/2015-1, Individual Process Number 170134/2016-4.

* patricia.barreto@inpe.br

ID 69: EVALUATION OF CR-N THIN FILMS DEPOSITED BY REACTIVE PLASMA IMMERSION ION IMPLANTATION AND DEPOSITION (PIII&D) AND HOLLOW CATHODE DISCHARGE

Fabricio Iusuti de Medeiros[1]*, Carina Barros Mello[1], Nazir Monteiro dos Santos[1]
[1]*Instituto Nacional de Pesquisas Espaciais - INPE*

1. Introduction

The magnetron sputtering (MS) deposition of thin films allows depositing different materials on various substrates. Nevertheless, the small fraction of ions and the great variety of directions in the sputtered particles trajectory turns the deposition difficult to control [1]. The iPVD processes are alternatives to increase the ions fraction and control particles direction during film's growth. In this work, chromium nitride deposition was performed by the association of the DC reactive magnetron sputtering, hollow cathode secondary discharge and plasma immersion ion implantation and deposition. Chromium nitride coatings have high hardness and good wear, corrosion and oxidation resistances at high temperature. Studies show that its composition is generally dominated by two phases: CrN and Cr2N with different mechanical properties, as well as hardness, elastic modulus, wear resistance and coefficient of friction [2]. The CrN and Cr2N phases' formation in the chromium nitride coatings are associated to the used nitrogen flow in the precursor gas mixture [2]. Each coating was deposited with a different nitrogen ratio in order to evaluate its influence on chemical composition, surface defect density, morphology and wear resistance.

2. Experimental

A high purity chromium target was used as the metallic source in MS. Negative high voltage pulses were applied in a metal tube positioned between the target and the substrate, generating a high density plasma inside it. Part of the sputtered particles that pass through the high-density plasma are ionized. The high voltage pulses were applied simultaneously to the carbon steel substrate, resulting in ion implantation. Voltage, frequency and width of the pulses were kept constant for all experiments. For comparison, two experiments were performed without the secondary discharge. The amount of nitrogen in the gas mixture was 33, 50, 66, 75 and 100%, with argon in balance. The substrate and target surfaces were cleaned with argon bombardment for 10 minutes before the film growth. The growth process took 60 minutes and the working pressure during the experiments was maintained at $3{,}5\times10^{-2}$mbar.

3. Results and Discussions

In comparison to the deposited films by reactive magnetron sputtering without secondary discharge, the proposed system with DCMS, IIIP and hollow cathode discharge resulted in coatings with better adhesion to the substrate, higher wear resistance and lower surface defect density. The low stress between coating and substrate, caused by ion implantation during the deposition may be one of the reasons for the better quality presented by these films. Both CrN and Cr2N phases were identified in the coatings by XPS analysis, but the presence of CrN phase was affected by the amount of nitrogen into the chamber until a certain extent. The grown film with 66% of nitrogen in the gas mixture presented lower friction coefficient, although the grown film with 33% of nitrogen presented higher wear resistance. The complete results obtained by characterizations in these coatings deposited with and without secondary discharge and variation of nitrogen flow will be presented at the conference.

4. References

[1] U. Helmersson, M. Lattemann, J. Bohlmark, *Thin Solid Films* 513, 1–24, (2006).
[2] Z. Han, J. Tian, Q. Lai, X. Yu, G. Li, *Surf. & Coat. Tech*., 162, 189-193, (2003).

Acknowledgments

This project is supported by CAPES and MCTIC.

*Corresponding author: fiusuti@gmail.com

ID 72_1: GROWTH AND CHARACTERIZATION OF BDD/CF1000 AND BDD/CF2000 MODIFIED WITH TIO_2 TO IMPROVE THEIR PHOTOCATALYTIC RESPONSES

Couto A.B.*, Pereira, L.A., Ferreira N.G.

National Institute for Space Research INPE, Av. dos Astronautas, 1758, Jd. Granja, 12227-010 São José dos Campos, SP, Brazil

1. Introduction

Titanium dioxide (TiO_2) has been focused on its photocatalyst properties associated with its strong oxidizing power [1]. Boron doped diamond (BDD) also presents singular electrochemical properties such as low and stable background current and wide potential window, which allow it to reach a high anode potential to generate the hydroxyl radical (OH•) [2]. Thus, the deposition of TiO_2 associated with the BDD deposition has been used in investigation of improvements in electrodes applied for organic compounds degradation, due to their electrochemical properties [3]. In this context, carbon fiber (CF) also appears as an interesting substrate to grow BDD films to obtain a three-dimensional material by exhibiting high surface area as well as high active site density in a homogeneous porosity distribution. Thus, this work shows the production and characterization of ternary TiO_2/BDD/CF composites using CF substrates obtained at two different temperatures of 1000 and 2000 °C pointing out the CF structural organization effects on the composite photoelectrochemical responses.

2. Experimental

CF substrates were obtained from polyacrylonitrile (PAN) precursor heat treated at two different temperatures of 1000 and 2000 °C at nitrogen atmosphere and were cut 10 x 10 mm^2. BDD films were grown on CF1000 and CF2000 substrates by hot filament chemical vapor deposition the following growth parameters: 750 °C, 30 Torr, 8h and gas mixture of 2/198 % CH_4/H_2. Boron source was obtained by an additional hydrogen line passing through a bubbler containing B_2O_3 dissolved in methanol with B/C ratio of 15000 ppm in solution. TiO_2 depositions on BDD/CF1000 and BDD/CF2000 substrates was obtained by anodic hydrolysis of $TiCl_3$ under potentiostatic mode, at a fixed potential of 0.75 V for 60 min in a 5 $mmol.L^{-1}$ $TiCl_3$ + 0.1 $mol.L^{-1}$ KCl (pH = 2) aqueous solution. All the electrochemical experiments were performed in a conventional three-electrode glass cell, using a platinum wire as a counter electrode and $Ag/AgCl/KCl_{(sat)}$ as the reference electrode. Both composite materials were characterized by field emission gun-scanning electron microscopy (FEG-SEM) images, Raman spectroscopy analyses, and photoelectrochemical responses, using a mercury/xenon lamp model 69920-450 W Tectraphysics in 0.1 mol L^{-1} KCl at scan rate of 20 mV s^{-1}.

3. Results and Discussions

Fig. 1 shows FEG-SEM images for TiO_2/BDD/CF1000. Images demonstrate that CF1000 were completely covered by a diamond polycrystalline film and the rougher TiO_2 film texture is dominant and homogenous covering all diamond grains. The morphology of TiO_2 deposits in BDD/CF2000 were similar the TiO_2/BDD/CF1000 composite. The photoelectrochemical activities of all electrodes were measured by linear sweep voltammetry, under intermittent UV irradiation. As an example, the TiO_2/BDD/CF1000 electrode photoelectrochemical response considering the dark current (I_d) and the photocurrent (I_{ph}) densities are shown in the Fig 2 for TiO_2 deposition time of 60 min. No significant photoanodic current was verified for BDD/CF1000 sample in the same experimental conditions. Therefore, this photoanodic current density is certainly associated to the TiO_2 presence on the electrode surface. The results showed that anodic hydrolysis of $TiCl_3$ under potentiostatic mode was a suitable procedure to produce ternary composites on both BDD/CF samples. As expected, both ternary composites depicted similar photoelectrochemical responses. Slight differences in photocurrent values may be related to CF conductivity as well as to electrode surface area which are directly related to CF structural organization.

In summary, we have obtained preliminary results with success. The relationship among CF properties, BDD quality and morphology not to mention TiO_2 deposition on BDD surface are complex parameters and this work is exploring a systematic study also correlating the TiO_2 photocatalytic responses with all of them.

*Corresponding author: abcouto@yahoo.com.br

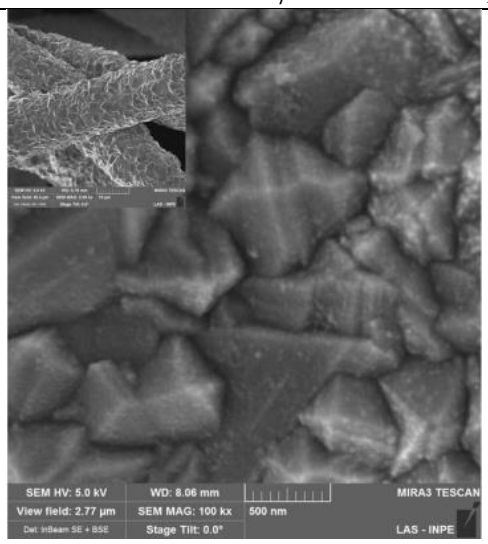

Fig. 1. *FEG-SEM images of TiO_2/BDD/CF1000 composite.*

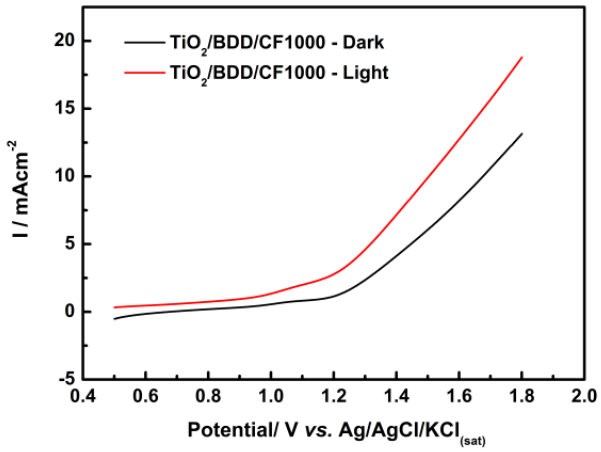

Fig. 2. *Photoelectrochemical responses of TiO_2/BDD/CF1000 in 0.1 mol L^{-1} KCl solution at scan rate of 20 mV s^{-1}.*

4. References

[1] Y. Zhang, X. Xiong, Y. Han, X. Zhang, F. Shen, S. Deng, H. Xiao, X. Yang, G. Yang, H. Peng, Chemosphere, 88, 145-154, (2012).
[2] C. Zhang, L. Gu, Y. Lin, Y. Wang, D. Fu, Z. Gu, J. Photochem. Photobiol., A, 207, 66-72, (2009).
[3] J. Qu, X. Zhao, Environ. Sci. Technol., 42, 4934-4939, (2008).

Acknowledgments

FAPESP, CAPES and CNPq

*Corresponding author: abcouto@yahoo.com.br

ID 72: PRODUCTION OF CARBON FIBER/REDUCED GRAPHENE OXIDE/NICKEL OXIDE COMPOSITE FOR ELECTROCHEMICAL APPLICATIONS

André Ferreira Sardinha, Andrea Boldarini Couto*, Neidenêi Gomes Ferreira

Instituto Nacional de Pesquisas Espaciais, Av. dos Astronautas 1758, São José dos Campos, SP, Brazil

1. Introduction

The increasing demand for sustainable energy has driven intensive research efforts on the development of energy storage systems such as supercapacitors, which have a greater power density and longer cycle life than batteries [1]. Graphene Oxide (GO) / Metal Oxide composites have been extensively studied as electrodes for supercapacitores [2-6]. Thus, this work is focused in the production and characterization of nickel oxide (NiO)/reduced graphene oxide (RGO)/ carbon fiber (CF) ternary composite aiming its electrochemical application for supercapacitors. CF substrate was chosen due to its high surface area in addition to its RGO synergism .The constituent materials as well as the composite were characterized by field emission gun-scanning electron microscopy (FEG-SEM), Raman spectroscopy and cyclic voltammetry (CV).

2. Experimental

GO was obtained following the modified Hummers method according to the synthesis described by X. Li [7]. Graphite (3 g) was mixed with 120 mL of sulfuric acid (95%) in a 1000 mL flask. The mixture was stirred for 30 min in an ice bath. In the continuous vigorous stirring for 4 h, potassium permanganate (15 g) was added to the suspension, controlling the reaction temperature lower than 20 °C. Afterwards, the mixture was stirred for 12 h at room temperature. Then, 400 mL of deionized water was slowly added to the mixture with vigorous agitation and the color of the suspension changed to brown. The diluted suspension was stirred for more 30 min. Then, 10 mL of 30% hydrogen peroxide was added to the mixture and the color turned into bright yellow. For purification, the mixture was washed by 5% hydrochloric acid followed by deionized water for several times. GO was obtained after drying this mixture at 120 °C under vacuum. The binary electrodes were firstly prepared by electrochemical GO reduction (RGO) on CF using cronoamperometry technique at -1.25 V vs Ag/AgCl for 300 s using a conventional electrochemical cell. Finally, the ternary composite was also obtained by electrochemical method using 30 mL of 0.1 M de $Ni(NO_3)_2$ solution at -1.25 V vs Ag/AgCl for 300 s on the binary RGO/CF electrode.

3. Results and Discussions

Raman spectra for CF, RGO/CF, and NiO/RGO/CF are shown in the figure 1, which depict two major peaks of 1350 cm^{-1} (the D-band) and 1580 cm^{-1} (the G-band) in all of them. These peaks are characteristic of carbon materials as CF and/or RGO. Nonetheless, RGO/CF binary composite also show a second order peaks, related to carbon material improvement with the appearance of the 2700 cm^{-1} peak. For the ternary composite, characteristic peaks of NiO, at around 730, 1000 e 1100 cm^{-1}, confirmed the success in the NiO deposition. Figure 2 shows VC curves for CF, RGO/CF, and NiO/RGO/CF in 0.5 M de H_2SO_4 at scan rate of 100 mV/s. The results showed the current intensity increase for binary and ternary composites. Besides, mainly for NiO/RGO/CF, this square curve shape is typical for supercapacitor response and is directly related with the charge/discharge capability of this electrode [8].

In summary, the production and characterization of binary and ternary composites using carbon fiber as substrate were obtained with success from electrochemical methods demonstrating the synergism among these constituent materials. While the Raman spectra confirmed the composite structures, the CV curves results showed that the combination of NiO/RGO presented the best performance for supercapacitor electrode.

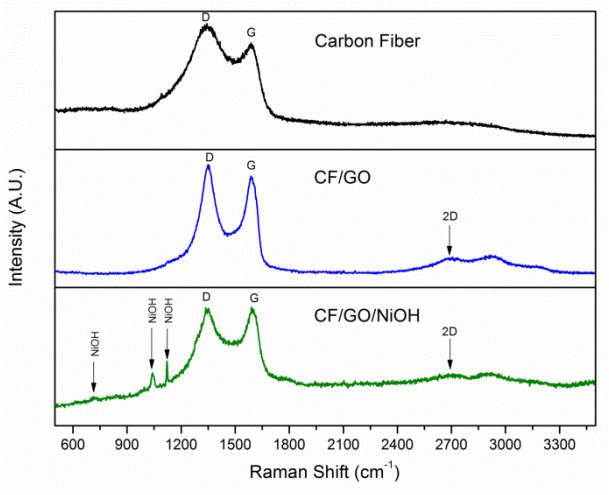

Figure 1. Raman spectra of the materials used in the different steps of this study.

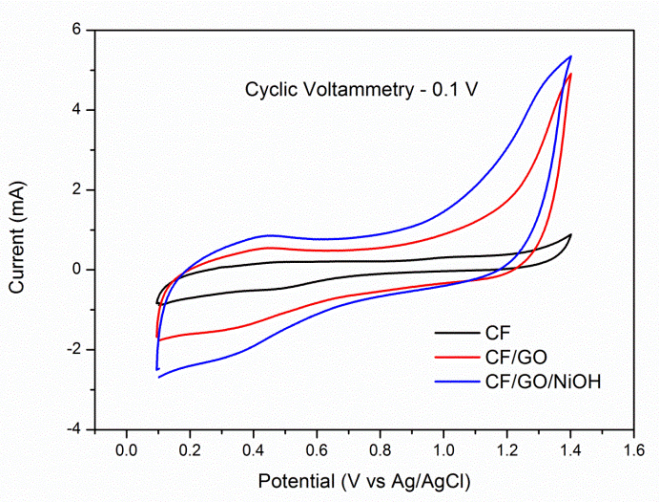

Figure 2. CV curves of the materials used in the different steps of this study.

4. References

[1] B.E. Conway, "*Electrochemical Supercapacitors, Scientific Fundamentals and Technological Application.*" Plenum Press, New York, USA (1999).
[2] Y.B. Tan, J.-M. Lee, J. Mater. Chem. A, 2013, 1, 14814–14843.
[3] I.R.M. Kottegoda, N.H. Idris, L. Lu, J.-Z. Wang, H.-K. Liu, Electrochimica Acta 56 (2011) 5815–5822
[4] M. Pumera, Chemical Society Reviews 39 (2010) 4146-4157.
[5] A. Cormiea, A. Crossa, A.F. Hollenkamp, S.W. Donne, Electrochim. Acta 55 (2010) 7470–7478.
[6] J.P. Zheng, P.J. Cygan, T.R. Jow, J. Electrochem. Soc. 142 (1995) 2699–2703.
[7] Z.A. Hu, Y.L. Xie, Y.X. Wang, L.J. Xie, G.R. Fu, X.Q. Jin, Z.Y. Zhang, Y.Y. Yang, H.Y. Wu, J. Phys. Chem. C 113 (2009) 12502– 12508.
[8] X. Li, Q. Zhong, X. Zhang, T. Li, J. Huang, Thin Solid Films584 (2015) 348-352.
[9] J. Yang, L. Zou, Electrochimica Acta 130 (2014) 791–799.

Acknowledgments

FAPESP, CAPES and CNPQ,

ID 73: DEPOSITION OF MICRO AND ULTRANANOCRYSTALLINE DIAMOND ON RETICULATED VITREOUS CARBON FOR USE IN THE NITRATE ELECTROREDUCTION

Silvia Sizuka Oishi[1]*, Andrea Boldarini Couto[1], Edson Cocchieri Botelho[2], Neidenêi Gomes Ferreira[1]
[1]*LAS, Instituto Nacional de Pesquisas Espaciais, São José dos Campos, São Paulo 12227-010, Brasil*
[2]*Departamento de Materiais e Tecnologia, UNESP-Univ Estadual Paulista, Guaratinguetá, São Paulo 12516-410, Brasil*

1. Introduction

Boron doped diamond (BDD) electrodes have been extensively used due to their higher electrochemical performance compared to vitreous carbon, graphite and platinum. The diamond growth by chemical vapor deposition (CVD) allows obtaining micro, nano and ultrananocrystalline films on various substrates depending on the gas mixture [1]. Currently, studies on nano and ultrananodiamond started to be more explored since they have been highlighted because of their excellent electrical, mechanical, thermal and biocompatible properties [2-4]. The combination of diamond and carbon substrate may produce a particular composite with good electrical conductivity depending on the carbon heat treatment temperature (HTT) as well as the diamond doping process. In this work, reticulated vitreous carbon (RVC) heat treated at 1000 and 2000 °C were used as carbon substrate for micro and ultrananocrystalline diamond growth and the nitrate electroreduction ability of these composites were demonstrated.

2. Experimental

RVC was processed using polyurethane foams with 70 pores per inch as a matrix for the poly(furfuryl alcohol) (PFA) resin impregnation. The impregnated foams were cured in an oven until 130 °C and then were heat treated at 1000 °C and 2000 °C (named RVC1000 and RVC2000). Micro and ultrananocrystalline diamond films were grown by hot filament chemical vapor deposition (HFCVD) technique for 18h under the pressure of 4 kPa, using 5 filaments of tungsten with 125 µm diameter and placed at 6 mm of sample top. Before diamond deposition, the RVC samples were prepared using seeding pretreatment to improve the diamond growth process. The substrates were immersed in a solution containing 0.25 µm of diamond particles dispersed in hexane solvent, followed by ultrasonic agitation for 2 h. Microcrystalline diamond films were grown on RVC1000 and RVC2000 with a gas mixture composed by 99.0 % H_2 and 1 % CH_4 and substrate temperature of about 800 °C. Ultrananocrystalline diamond were also grown on RVC1000 and RVC2000 with a gas mixture composed by 70.8% Ar, 28.3% H_2 and 0.88% CH_4 and substrate temperature kept at 680 °C. The boron doping was performed by an additional hydrogen line passing through a bubbler containing B_2O_3 dissolved in CH_3OH. The solution was prepared with a concentration of B_2O_3 dissolved in CH_3OH that correspond to B/C ratio of 30,000 ppm. The films were characterized by field emission scanning electron microscopy (FESEM), Raman spectroscopy and X-ray diffraction. All electrochemical experiments were performed in a conventional three-electrode cell, using the BDD/RVC and BDUND/RVC as working electrode, a Pt screen as the counter electrode and Ag/AgCl electrode as reference.

3. Results and Discussions

Micro and ultrananocrystalline diamond were grown with success on RVC stems. Figure 1 shows the XRD patterns of BDD and BDUND films grown on RVC heat treated at 1000 and 2000 °C. All samples present the carbon band (002) and diamond peaks (111), (220) and (311). The diamond peak (111) is more evident in BDD films due to its higher crystallite size while for BDUND film this peak is much broader. Figure 2 presents the Raman spectra of BDD and BDUND films which depict similar features to those obtained on the literature [2,5]. The characteristic bands for BDD films are the diamond peak at 1332 cm^{-1} in addition to the 500 and 1200 cm^{-1} bands related to the boron doping. The characteristic bands for BDUND films are the diamond peak shifted to lower wavenumbers (at around 1320 cm^{-1}) overlapped by the D band at 1350 cm^{-1}; the bands at 1150 and 1490 cm^{-1} related to the transpolyacetylene segments at the grain boundaries of the ultrananocrystalline diamond surface; the band at 1550 cm^{-1} assigned to G band; and the bands at 500 and 1220 cm^{-1}, related to the boron doping.

The electrochemical response of RVC, BDD/RVC and BDUND/RVC to nitrate was studied by cyclic voltammetry (CV) in 0.1 mol L^{-1} K_2SO_4 solution containing 0.01 mol L^{-1} KNO_3 as shown in Figure 3 and 4.

*Corresponding author: silviaoishi@uol.com.br

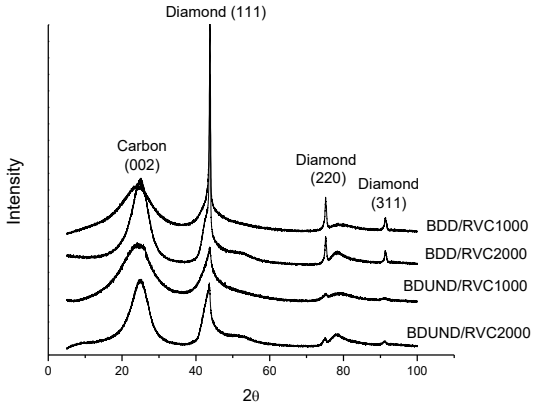

Fig. 1. *XRD patterns of BDD/RVC and BDUND/RVC composites*

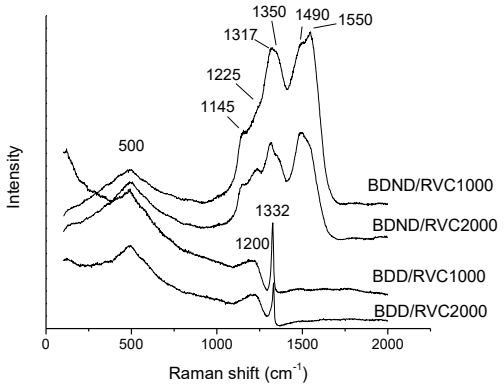

Fig. 2. *Raman spectra of BDD/RVC and BDUND/RVC composites.*

A comparison among RVC1000, BDD/RVC1000 and BDUND/RVC1000 electrodes for nitrate reduction (Figure 3) shows that in the presence of 0.01 mol L^{-1} KNO_3, the nitrate reduction clearly appears from -1.0 V for RVC1000, -0.65 V for BDD/RVC1000 and -0.75 V for BDUND/RVC1000 and they follow increasing the current when compared to the blank solution. Figure 4 presents the nitrate reduction for RVC2000, BDD/RVC2000 and BDUND/RVC2000 electrodes. The onset of the cathodic current in the presence of 0.01 mol L^{-1} KNO_3 appears at -0.85 V for RVC2000, -0.65 V for BDD/RVC2000 and -0.8 V for BDUND/RVC2000. These results indicate that both BDD and BDUND films improve the nitrate electroredution in comparison to RVC electrode, however, the BDD films are slightly better than BDUND films.

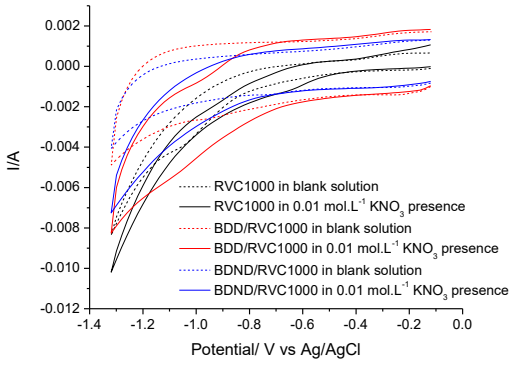

Fig. 3. *Cyclic voltammetries of RVC1000, BDD/RVC1000 and BDUND/RVC1000 in 0.1 mol L^{-1} K_2SO_4 (dotted line) and in presence of 0.01 mol L^{-1} KNO_3 (full line).*

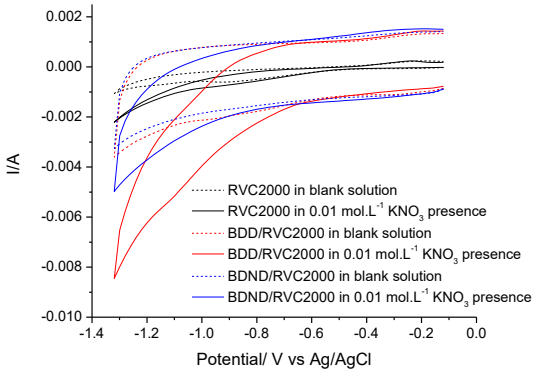

Fig. 4. *Cyclic voltammetries of RVC2000, BDD/RVC2000 and BDUND/RVC2000 in 0.1 mol L^{-1} K_2SO_4 (dotted line) and in presence of 0.01 mol L^{-1} KNO_3 (full line).*

4. References

[1] M. Marton, M. Vojs, M. Kotlár, P. Michniak, Ľ. Vančo, M. Veselý, and R. Redhammer, Appl. Surf. Sci. **312**, 139-144, (2014).
[2] A. F. Azevedo, M. R. Baldan and N. G. Ferreira, Int. J. Electrochem., **2012**, 1-16, (2012).
[3] O. A. Williams, M. Nesladek, M. Daenen, S. Michaelson, A. Hoffman, E. Osawa, K. Haenen and R. B. Jackman, Diam. Relat. Mater., **17**, 1080-1088, (2008).
[4] O. A. Williams, Diam. Relat. Mater., **20**, 621-640, (2011).
[5] F.L. Migliorini, M.D. Alegre, M.R. Baldan, M.R. V Lanza, and N.G. Ferreira, Thin Solid Films **564**, 97-103 (2014).

Acknowledgments

The authors acknowledge the financial support from São Paulo Research Foundation (FAPESP) grant #2014/27164-6 and CAPES.

*Corresponding author: silviaoishi@uol.com.br

ID 74: DEVELOPMENT OF A REACTOR FOR MEASUREMENTS OF PHOTOCATALYTIC ACTIVITY OF THIN FILMS

Aliny Nayara Pereira Souza [1]; Stryhalski, Joel[2*];Fontana, Luis César[3]
[1]*Electrical engineering student, Federal Institute of Santa Catarina - IFSC, Jaraguá do Sul , Brazil*
[2]*Federal Institute of Santa Catarina - IFSC, Jaraguá do Sul , Brazil*
[3]*Plasma Physics Laboratory, University of the State of Santa Catarina, Santa Catarina, Brazil*

1. Introduction

Self-cleaning materials have attracted interest due to the ease and reduction of maintenance costs, since they are great in applications that are difficult to access and that make cleaning difficult [1]. Some materials act as catalysts in the presence of light, presenting what we call photocatalytic activity. This property can be used for the decomposition of organic matter [2]. The photocatalytic activity presented by materials such as titanium dioxide (TiO_2) is due to its semiconductor character. When radiation with energy equal to or greater than the bandwidth energy is incident on the material, there is the promotion of electrons from the valence band (BV) to the conduction band (BC) forming an electron-gap pair. The gap can promote reactions with H_2O and OH molecules that can react with organic matter mineralizing (degrading) it.

2. Experimental

Among the variables that generate interference on photocatalysis, the following are highlighted: [1]: the temperature, the pH of the solution, the molecular oxygen dissolved in the solution and the concentration of the organic matter. In this work a photocatalytic activity reactor was developed [3]. The objective is to determine how these variables affect the photocatalytic activity, to propose an assembly that presents greater sensitivity and easiness to perform such measurements

3. References

[1] YUANHAO, WANG; LU, LIN; YANG, HONGXING; CHE, QUANDE. Journal of Nanoparticle Research, 2013: 15:1384.
[2] TEIXEIRA, Cláudia Poli de Almeida Barêa; JARDIM, Wilson Figueiredo. Processos Oxidativos Avançados: Conceitos Teóricos. Campinas, 2004. 3 v.
[3] IRALA, Dianclen do Rosário. Obtenção de Filmes de TiO_2 com propriedades fotoinduzidas sobre aço AISI 1015 utilizando tecnologias de plasma. 2010. ITA, São Paulo, 2013.

* joel@ifsc.edu.br

ID 76: MORPHOLOGICAL CHARACTERIZATION OF S-DOPED TiO_2 THIN FILMS

Rodrigo Teixeira Bento[1]*, Margarida Szurkalo[1], Olandir Vercino Correa[1], Marina Fuser Pillis[1]
[1]*Nuclear and Energy Research Institute, IPEN–CNEN/SP.*

1. Introduction

Heterogeneous photocatalysis is an oxidative process that uses the radiant energy (visible or ultraviolet) absorbed by a catalyst to mineralize organic compounds [1,2]. Titanium dioxide (TiO_2) is a semiconductor capable of acting as a photocatalyst, producing hydroxyl radicals in order to degrade pollutants released into the water and effluents [3,4]. However, the TiO_2 band gap energy corresponds to 3.2 eV and the photocatalytic activity is observed only for UV light with $\lambda < 380$ nm [5]. Sulfur doping reduces the band gap, making the material active in the region of the spectrum of light visible. The objective of this research consists on the growth of TiO_2 thin films, their sulfur doping and morphological analysis of the grown films, by means of the Atomic Force Microscopy (AFM) technique, for the purpose of showing the preliminary results of the present study.

2. Experimental

The TiO_2 thin films were deposited on borosilicate substrates, by means of the technique of metal-organic chemical vapor deposition (MOCVD), in a conventional horizontal reactor. The growth of the films was carried out using Titanium Tetraisopropoxide (TTiP) as precursor of titanium and oxygen, under pressure of 50 mbar at 400°C, with a growth time of 31 minutes. The films obtained were doped with sulfur through a thermochemical treatment realized in a tubular furnace under H_2 / 2 wt.% H_2S atmosphere at temperatures of 100ºC and 150ºC, for 1h. The AFM Tapping Mode technique was used to characterize the roughness and mean grain size, employing a *SPM Bruker* equipment, model *NanoScope IIIA*.

3. Results and Discussions

The morphology and grain size influence the TiO_2 films photocatalytic efficiency [6,7]. Through the images obtained by AFM (Fig. 1), it can be observed that the surface of the titanium dioxide films presents defined grains and of rounded morphology, distributed on the substrate surface in a homogeneous way.

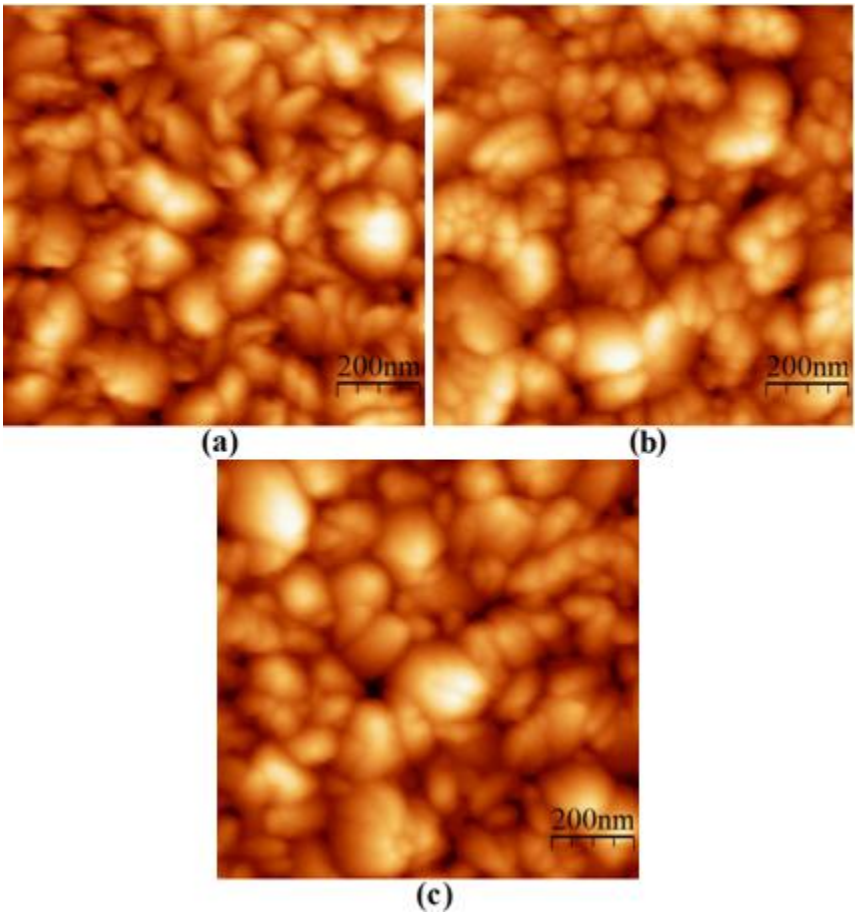

Fig. 1. *AFM images of thin films grown at 400°C: (a) non-doped TiO_2; Sulfur doped TiO_2 at (b) 100°C and (c) 150°C.*

*rodrigo.bento@ipen.br

The RMS (*Root Mean Square*) roughness expresses the values of a roughness profile that moves away from the midline, in other words, it is the standard deviation of the mean height Z [8,9], being mathematically expressed as:

$$RMS = \sqrt{\frac{\sum_{N=1}^{N}(Z_N - Z)^2}{N-1}} \quad (1)$$

where *N* is the number of peaks; *Zn* is the height of each peaks; and *Z* is the mean height of the N peaks. The RMS values of TiO_2 thin films varied around 19 nm, roughness considered favorable for photocatalytic applications [10]. A high value of roughness facilitates the contact of the adsorbed substances with the film, increasing its photocatalytic efficiency [11].

The mean grain size values, presented in Table 1, were obtained from the adjustment of the Gaussian curve generated by the equipment software.

Table 1 – Mean grain size and RMS (Root Mean Square) roughness for TiO_2 thin films doped at different temperatures.

Doped temperature	***Mean Grain Size (nm)***	***RMS roughness (nm)***
-	*96.5*	*19.1*
100ºC	*119.2*	*19.3*
150ºC	*110.8*	*19.2*

Analyzing the results, it is possible to note the MOCVD technique efficiency, reproducing TiO_2 thin films with high homogeneity, without cracks or pores. No evidences were observed about influence of the doping process on the morphology of TiO_2 thin films.

4. References

[1] Athalathil, S.; Erjavec, B.; Kaplan, R.; Stüber, F.; Bengoa, C.; Font, J.; Fortuny, A.; Pintar, A.; Fabregat, A. Journal of Hazardous Materials, **300**, 406-414, (2015).
[2] Gomes Júnior, O.; Borges Neto, W.; Machado, A.E.H.; Daniel, D.; Trovó, A.G. Water Research, **110**, 133-140, (2017).
[3] Khayyat, S. A.; Selvin R.; Roselin, L. S.; Umar, A. J. Nano. Nanotech. **14**, 7345-7350, (2014).
[4] Parkin, I. P. and Palgrave R. G. Journal of Materials Chemistry. **15**, 1689-1695, (2005).
[5] Dhayal, M.; Kapoor, R.; Sistla, P.G.; Pandey, R.R.; Kar, S.; Saini, K.K.; Pande, G. Materials Science and Engineering. C **37**, 99-107, (2014).
[6] Ao, Y.; Xu, J.; Fu, D.; Yuan, C. Applied Surface Science, **255**, 3137–3140, (2008).
[7] Guan, S.; Hao, L.; Yoshida, H.; Asanuma, H.; Pan, F.; Lu, Y. Journal of Materials Science: Materials in Electronics, **27(4)**, 3873-3879, (2016).
[8] Whitehouse, D.J. *Handbook of Surface Metrology*. IOP Publishing Ltd, London, 1994. 988 p.
[9] Dobrzanski, P. and Pawlus, P. Precision Engineering, **34**, 647-650, (2010).
[10] Carp, O.; Huisman, C.L.; Reller, A. Progress in Solid State Chemistry, **32**, 33, (2004).
[11] Zhou, M.; Yu, J.; Liu, S.; Zhai, P.; Jiang, L. Journal of Hazardous Materials, **154**, 1141–1148 (2008).

Acknowledgments

We are grateful to the "Laboratório de Filmes Finos do Instituto de Física da Universidade de São Paulo", Brazil, for the SPM facility.

*rodrigo.bento@ipen.br

ID 77: MORPHOLOGY OF THE PLASMA NITROCARBURIZED LAYER ON DIN 100Cr6 STEEL

M.A. Fontes[1, 2*], V.H.B. Scheid[3], D.S. Machado[4], L.C. Casteletti[4], P.A.P. Nascente[1, 5]
[1]*Universidade Federal de São Carlos, Programa de Pós-Graduação em Ciência e Engenharia de Materiais, 13565-905, São Carlos, SP, Brasil.*
[2]*Instituto Federal de Educação, Ciência e Tecnologia de São Paulo, Departamento da Mecânica, 14169-263, Sertãozinho, SP, Brasil*
[3]*Centro Técnico Aeroespacial, Instituto de Estudos Avançados,12228-001, São José dos Campos, SP, Brasil.*
[4]*Universidade de São Paulo, Escola de Engenharia de São Carlos, Departamento de Engenharia de Materiais, 13563-120, São Carlos, SP, Brasil.*
[5]*Universidade Federal de São Carlos, Departamento de Engenharia de Materiais, 13565-905, São Carlos, SP, Brasil*

1. Introduction

The surface treatments of metal alloys improve the surface properties by the deposition of another material or by surface modification, producing coatings. The nitrocarburizing, considered one of the most important thermochemical treatments, involves the simultaneous diffusion of N and C into the surface.

Understanding and controlling the formation of the nitrocarburized layer, as well as understanding the formation of the micro-porosity layer, have considerable industrial interest due to the improvements regarding wear, fatigue, and corrosion resistances on the metals and their alloys.

2. Experimental

In this work, it was performed the surface modification on DIN 100Cr6 steel by plasma nitrocarburizing process with pulsed dc luminescent discharge using a MP-250 equipment, where the chemical composition of the samples was: C in the range of 0.98 to 1.10; Cr in the range of 1.30 to 1.60; Mn in the range of 0.25 to 0.45; Si in the range of 0.15 to 0.35; balance Fe.

It was investigated the treatment temperature (550°C and 600°C) and the CH_4 concentration in the gas mixture composition, whereas for the only nitrided samples an atmosphere containing H_2-75% N_2 was used, and for nitrocarburized samples, an atmosphere containing H_2-74% N_2 and concentrations of CH_4 of 1, 1.5, and 2.0%. The treatment time was 2h. Scanning electron microscopy and energy dispersive spectroscopy (SEM/EDS) were used to evaluate the chemical composition, compound layer and diffusion zone thicknesses, as well the micro-porosity layer.

3. Results and Discussions

The chemical composition profile of the elements C and N (figure 1 and figure 2) shows that there is a small amount of carbon and a large amount of nitrogen at the compound layer, indicating the presence of the ε-Fe_3N and γ'-Fe_4N phases, for samples nitrocarburizing at both temperatures. The low amount of carbon is a consequence of a high nitrogen concentration, due to the higher thermodynamic stability of the nitrites in relation to the carbides [1]. At the diffusion zone, there is a greater amount of carbon and a smaller amount of nitrogen, but both contents decrease along the chemical composition line until reaching the chemical composition of the sample core.

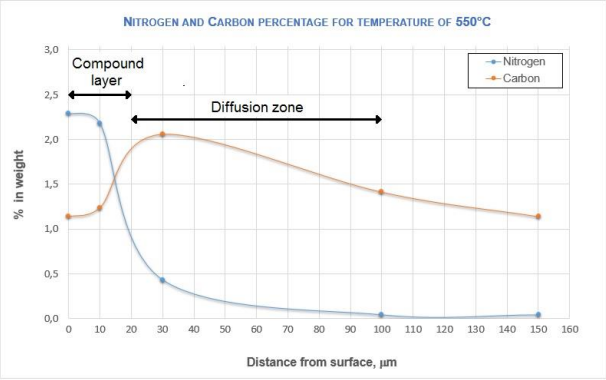

Figure 1. *Chemical composition line for 550°C.*

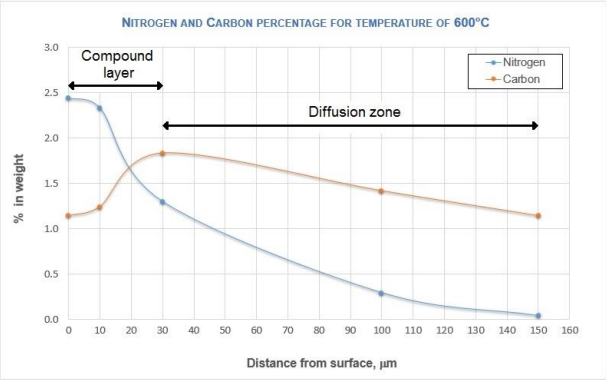

Figure 2. *Chemical composition line for 600°C.*

*fontesma@hotmail.com

From the results shown in figures 1 and 2 yet, it is evident that the increase of the temperature nitrocarburizing increases the compound layer and diffusion zone thicknesses. According to the *Arrhenius* equation (equation 1), the diffusion coefficient of the elements increases exponentially with increasing temperature, therefore, for higher temperatures, higher diffusion and consequently thicker the layer formed.

$$D = D_o . e^{-\frac{Q}{R.T}} \qquad \text{Equation 1}$$

All the nitrocarburized samples showed the formation of a porous surface layer (figure 3 and figure 4). For atmospheres with 0% CH_4, the micro-porosity layers were larger, as well as for nitrocarburized samples at higher temperatures. The high nitrogen concentrations, as well as the high process temperatures, promotes the higher absorption of nitrogen in the surface layer [2, 3], favoring consequently the production of the micro-porosity layer.

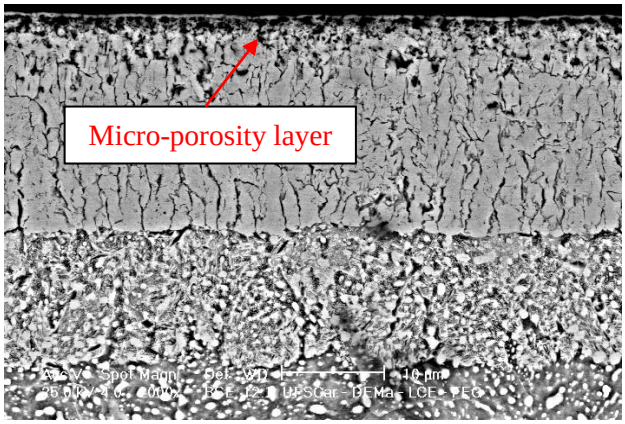

Figure 3. *Micro-porosity layer formed.*

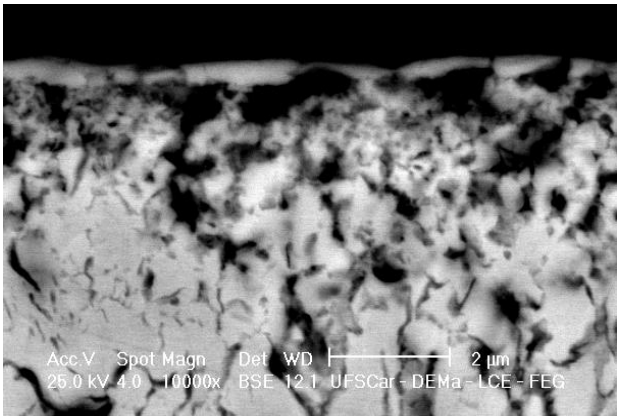

Figure 4. *Detail of the micro-porosity layer.*

4. References

[1] MITTEMEIJER, E. J. Steel Heat Treating Fundamentals and Processes. **ASM Handbook A**, v.4, 2013.
[2] MITTEMEIJER, E. J.; SOMERS, M. A. J. Thermochemical surface engineering of steels. **Woodhead Publishing Series in Metals and Surface Engineering**, n.62, 2015.
[3] LI, S.; MANORY, R. R. Surface morphology and compound layer pores of plasma nitrocarburized low carbon steel. **Metallurgical and Materials Transactions A**, v.27, n.1, p.135-143, 1996.

Acknowledgments

The authors would like to thank Fernando Nawate from UFSCar/DEMa, for his assistance in the SEM/EDS measurements. CNPq is acknowledged for support.

*fontesma@hotmail.com

ID 78: CONSTRUCTION OF A PHOTOELECTRON BEAM FOR CALIBRATION OF SPACE PLASMA ELECTROSTATIC ANALYZERS

Ing Hwie Tan*, Julio Guimarães Ferreira
Laboratório Associado de Plasmas
Instituto Nacional de Pesquisas Espaciais
São José dos Campos SP Brasil

1. Introduction

Space plasmas differ in many aspects from plasmas created in laboratories. Typical spatial lengths are obviously much larger, background pressures, plasma densities and beam fluxes are much lower than in typical plasma reactors. For this reason electrostatic energy analyzers in space operate with channel electron multiplier detectors (channeltrons) in counting mode, giving the number of electrons (or ions) per detection period instead of measuring an electrical current. The entrance aperture dimensions of these analyzers are also designed according to the fluxes to be measured and can be up to 1-2 cm^2 in area. The electron energies involved are typically from 0.1 eV to 50 keV.

The calibration of these analyzers therefore requires their exposure to an electron beam of very low intensity with diameters sufficiently large to illuminate the whole entrance area. This can be achieved using a cathode made of a thin gold film deposited over a fused silica substrate that is illuminated from the back with ultra-violet radiation. The UV photon energies are sufficient to produce photoelectrons in a large area of the thin film which are then accelerated to the desired energy.

In this work an electron beam system constructed for the calibration of a cylindrical electrostatic energy analyzer (project ELISA) to be launched in a scientific satellite (EQUARS mission) will be described.

2. Experimental

The electron beam was constructed with a photocathode comprised of a 21cm diameter gold thin film in a fused silica disk. Several UV radiation sources were tested and the HG2 Cathodeon mercury vapor lamp was selected. For controlling the radiation intensity, and consequently the beam intensity, thin metallic film filters, a radiation diffusing scheme and a third control grid were tested and will be described. The beam intensity is measured with a special picoampmeter set up, since the photocathode is kept in negative high voltages, and stray currents must be avoided.

The beam profile is measured using a channeltron detector scanned through its cross sectional area, and the measurements are integrated to be compared to the total current measured by the picoampmeter.

A two axis rotation structure (gimbal) supports the ELISA analyzer to vary the incidence angles between the beam and the entrance aperture axis. The detector´s response (number of counts) is measured for varying incidence angles and beam energies and is stored together with all parameters in a computer controlled data acquisition system.

3. Results

The beam intensity can be controlled by the three methods mentioned, but the diffusing system is not reproducible and the control grid presents difficulties in the picoampmeter electronic circuit. So thin metallic filters will be used.

The beam profile characterization was made using the gimbal system and a linear actuator system for radial displacement of the channeltron detector. The electrostatic analyzer was also used to certify that the electrons detected are the ones accelerated to the beam´s nominal energy and not secondary or reflected electrons that can be produced at the beam´s operating energy range.

The geometric factor (GF) of the electrostatic analyzer, determined by dividing the counting rates measured by the incident electron flux, will be presented. Counting rates are integrated over all angles of incidence and energies for each one of the 16 energy bands (from 1 to 27 keV) of the analyzer. Although the GF should depend only on the geometry of the device, the efficiency of the channeltron detector depends on energy.

The results are compared with numerical simulations made in an earlier work [1].

4. References

[1] P. D. G. de Melo, I. H. Tan, J. J. Barroso and R.S. Dallaqua, IEEE Trans. Plasma Sci. **44**(6), 1009-1017 (2016)

*Corresponding author: ing.tan@inpe.br

ID 79: APPROACH TO DEPOSITION OF FILMS OBTAINED FROM HYDROCARBONS AND HEXAMETHYLDISILOXANE BY PLASMA

R. P. Mota, K. G. Kostov, M. A. Algatti, M. E. Kayama, R. Y. Honda, F. V. P. Kodaira, P. W. P. Moreira Junior, A. R. Castro, D. A. Souza.
UNESP – Univ. Estadual Paulista ,Av. Dr. Ariberto Pereira da Cunha, 333 – Guaratinguetá, SP ,Brazil

1. Introduction

Low energy and temperature plasmas from gases and/or organic vapors were widely used for the production of low-thickness materials at atmospheric and low pressure discharges. These materials, usually in the form of thin films and/or powders, present chemical and physical characteristics that make them attractive to the optical, electro-electronic, biomaterial coating industries and others [1-3].

2. Experimental

For the deposition of the films we have used metallic and pyrex glass reactors with cylindrical configurations excited by radiofrequency in the inductive and capacitive modes operating in powers from 0 to 300 W and pressure between 0.1 and 20.0 Pa. For depositions at atmospheric pressure we used reactors in the jet configuration and/or dielectric barrier excited by high voltage and frequency that can be variable from a few Hz to hundreds of Hz. The characterization of the samples passed mainly through the molecular structure (FTIR) and surface characteristics by measurements of contact angle and profilometric microscopy.

3. Results and Discussions

Thin films deposited at low pressure from 1.3 to 15.0 Pa, at different radiofrequency applied powers between 1.0 and 50.0 W obtained from hydrocarbon monomers preserved their main absorption bands for whatever the deposition parameters, power or pressure. However the densities of chemical bonds observed by infrared spectroscopy showed changes in molecular structures of the samples. Moreover, non-existent vibrational modes in the monomers were observed in the films. Similar result also occurred for the depositions made with the hexamethyldisiloxane monomer. The energies involved in the process and the fact that the growth mechanism of the films is governed by free radicals contributed to this. The depositions of the films at atmospheric pressure using the same monomers produced similar materials to the previous ones, but with deposition rates very different. Normally, by increasing the power during deposition, the deposition rate of the films also increases for both low pressures and atmospheric pressure. Independently of the pressure, the molecular structures of the films tend to be more similar to the structures of the monomers for depositions at very low powers. This fact can be credited with fewer collisions in the plasma state and consequently fewer monomer fragments, preserving more molecular structure of the monomer in the film. In both methods of deposition, the films from hydrocarbons are hydrophilic and those obtained from hexamethyldisiloxane presented hydrophobic character. The surfaces of the samples did not preserve the topography of the substrates surfaces in both methods.

4. References

[1] Kodaira F.V.P., Ricci Castro A.H., Prysiazhnyi V., Mota R.P., Quade A., Kostov K.G., Surface & Coatings Technology, **312**, 117-122, (2017).
[2] Friedrich, J., Plasma Processes Polym., **8**: 783–802, (2011)
[3] H. Biederman "*Plasma Polymer Films",* 1st edition, World Scientific, USA, (2004)

Acknowledgments
The authors would like to acknowledge CAPES, FAPESP and CNPq for the financial support.

*Corresponding author: rmota@feg.unesp.br

ID 81: USE OF LOW COST SENSORS ARRAY AND SMALL DEVICES NOT ONLY ON RESEARCH BUT ALSO FOR TEACHING

Walter Pichi Jr. [1,2], Daniel C. Gatti[1] and Maria Lúcia P. da Silva[2,3]*
[1]*Pontifical Catholic University of S. Paulo, São Paulo, Brazil*
[2]*Faculty of Technology of São Paulo, CPS, São Paulo, Brazil*
[3]*School of Engineering, University of São Paulo, São Paulo, Brazil*

1. Introduction

In Brazil, the use of research equipment on laboratorial classes is common on graduation courses but not with high school student. Moreover, development of low cost equipment that could help on research and teaching simultaneously is rare. Nonetheless, with the new development tools available on the market several new approaches should be tested [1]. An iconic example could be environment issues that usually require an interdisciplinary viewpoint. Therefore this work aimed the development of low cost sensors and respective miniaturized device for volatile organic compounds (VOC) concentration and detection

2. Experimental

A team, formed by professors, PhD, undergraduate and high school students, was settled. This group makes use of a geographical advantage since both, the high school and the faculty, were at the same campus. Whereas PhD students took care of electronic equipment, materials professor and undergraduate students watched the development of miniaturized devices; finally high school pupils used it on tests of VOCs. This work used methodology for electronic development and testing, chemical characterization and environmental correct reactants.

3. Results and Discussions

Regarding electronic equipment (see Figure 1), it comprises 10 sensors (TGS 2620, Figaro, Japan), individually maintained in a mini holder, power supply and one ADC with proprietary software installed. The system was designed to be highly flexible; therefore, the distance between sensors and ADC can achieve up to 5 m. Moreover, due to the simple electronic involved on sensors power and signal connection, the sample holder has reduced dimensions, in order of 3 cm x 2 cm x 2 cm. the obtained answer is am excel table with the main information: sensors response, time of measurement , etc. After the electronic equipment was certified by the PhD. student, it was used by undergraduate during reactor development.

Fixed bed mini reactor were developed using PAN fibers [2] and medical suppliers´ connections; reactors manufacturing required only few steps: the cut of felt fibers, impregnation with tetraethoxysilane, on neutral, acid or basic environment, which provided surface modification able to concentrate polar or non polar VOCs species, respectively, and sealing using caps. However, impregnation step has some tricks since the organic silicon compound can be dropped directly on felt surface but the change on pH environment required volatile acid and basic reactants, i.e., hydrochloric acid and ammonium hydroxide. In this way, the polymerization is catalyzed but the velocity is low enough to permit the formation of small particles, as shown by optical microscopy, on the fiber surface. Raman analysis proved Si-O-C bonds were hydrolyzed since it was observed not but carbon - from fiber felt - after treatment (Figure 2).

The mini reactor is placed in a small holder in order to fix collinearly sensor, reactor and a three way valve. Thus, if needed, reactants/samples can be inserted using in a carrier gas; another possibility is the use of one miniaturized oven, to heat the reactor up to 80ºC, which means desorption can be accelerated from the felt (Figures 3 A an B, respectively).

Tests were primarily developed by graduate students to certify that the reactors could be used for concentration and/or analysis of VOCs (Figure 3C). After that, high school students were invited to test the same setup and explain the results. Although they are no able to fully understanding such proposal they were capable of operate it and also explained properly the most important phenomena observed.

Therefore, there is plenty of room to develop small, low cost equipment involving such heterogeneous group and this work showed some roadmaps in order to do so.

4. References

[1] J. West, N. Vadiee, A. McMahon, K. Lake, B. Ray, T. Billie, IEEE Integrated STEM Education Conference, 88-95, (2017).

[2] J. S. Marcuzzo, A. Cuña, N. Tancredi, E. Mendez, H. H. Bernardi, M. R. Baldan, Rev. Bras. Apl. Vac., **35** (2), 58-63 (2016)

*Corresponding author: malu@lsi.usp.br

Acknowledgments
Jossano Marcuzzo for PAN fibers, FAPESP and CNPq for financial support.

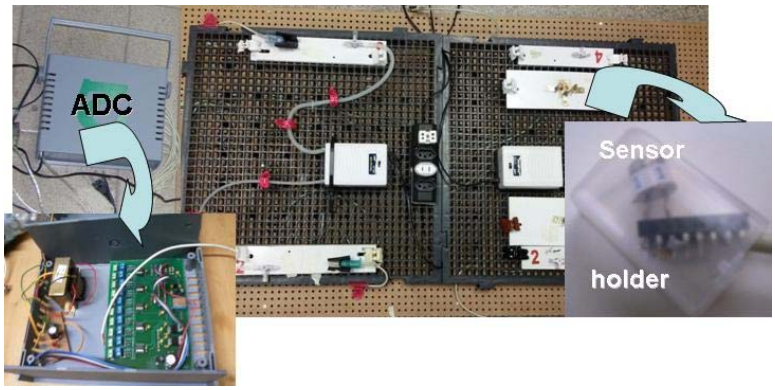

Fig. 1. *Electronic equipment.*

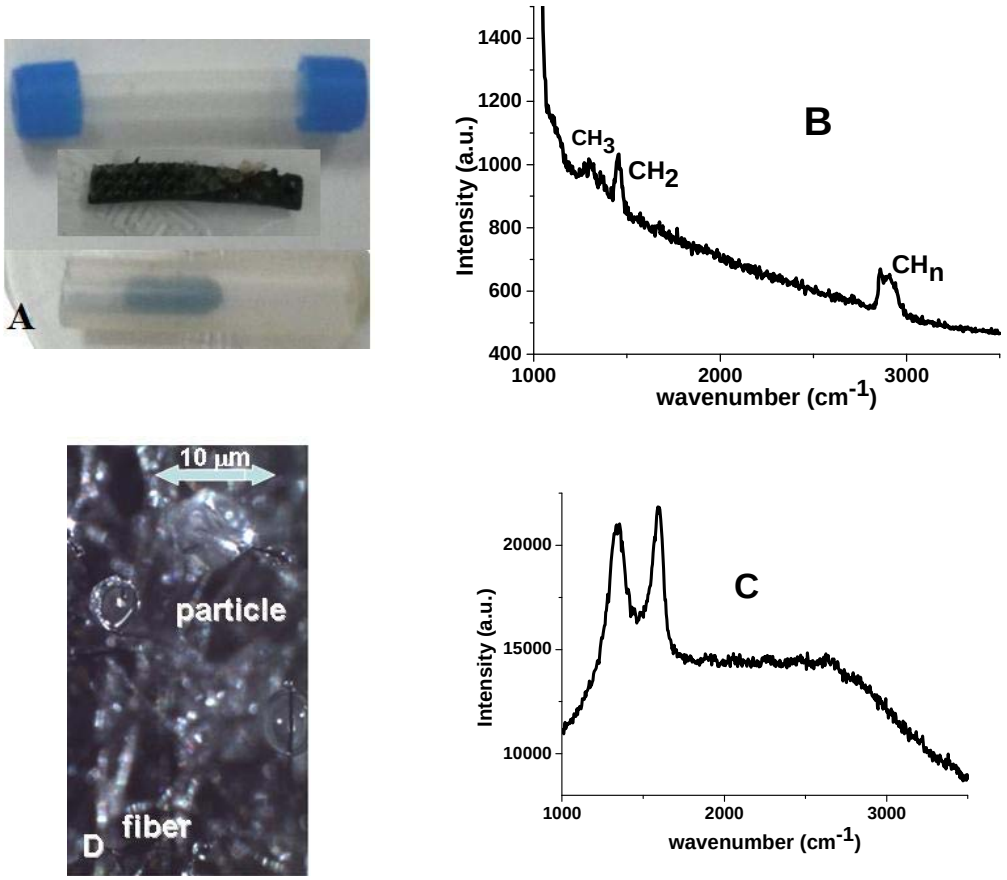

Fig. 2. *Fixed bed mini reactor: (A) parts and pieces;(B) Raman before and (C) after polymerization and (D) particles on fiber*

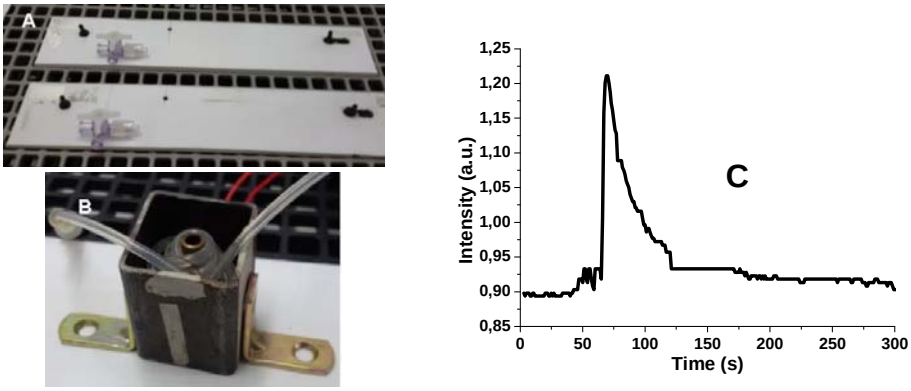

Fig. 3. *Mini reactor: (A) holders and (B) oven. Electronic equipment: (C) typical result.*

*Corresponding author: malu@lsi.usp.br

ID82: ACTIVE SCREEN PLASMA SYSTEM: FLOATING POTENTIAL AS A FUNCTION OF SCREEN OPEN AREA.

Felipe Corrêa*, Daniela Becker, Luis C Fontana
Universidade do Estado de Santa Catarina, Centro de Ciências Tecnológicas, UDESC, Joinville-SC, Brazil

1. Introduction

Active Screen Plasma System (ASPS) was primarily used for plasma nitriding, then named Active Screen Plasma Nitriding (ASPN). The active screen plasma method has been applied for treatment of a wide variety of materials, mainly, different kinds of steel. In recent years, it has been also used for treatment of polymeric materials and even functionalization of carbon fibers [1-4]. The main advantage of ASPS is that the workpiece is not the cathode of discharge, that is, the plasma is not produced directly on their surfaces, therefore it is not subjected to a high cathodic potential [5-6]. As a result, the "edge effect" on the pieces do not occur, the treatment is more homogeneous even though the workpieces have complicated geometry. The workpiece is placed into the cage and the cathode is the metal screen that surrounds the workpiece, therefore, the component to be treated stays under floating potential. In this work it was investigated the effect of the screen's open area ratio on the floating potential inside the cage.

2. Experimental

A schematic diagram of experimental setup used in the current study is shown in Fig. 1, which consists of a stainless steel grounded base with a glass chamber on top. The gas entry is also grounded and, as so, acts as anode, along with the base. The cage acts as cathode and a probe inside it is connected to an oscilloscope for measurement of the floating potential.

Four ~ 11 cm diameter ~ 11 cm high screen cages were made from four different mesh sizes, as indicated in Table 1. For each screen type, it was carried out experiments in Ar plasma. The pressure ranged from 0,3 Torr to 1,5 Torr, whilst the mean potential applied was between -100V and -200V, voltage pulse frequency of 100 kHz with an off pulse time of 4.0 μs.

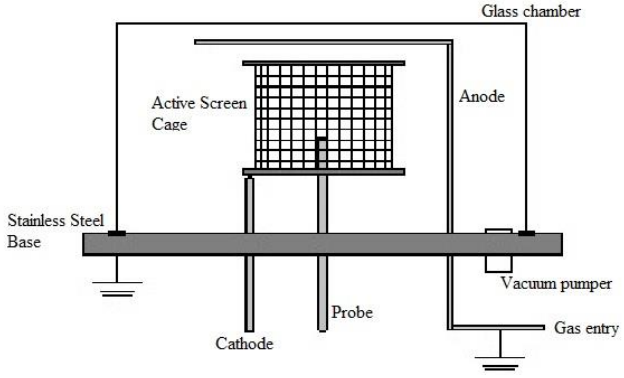

Fig. 1. *Schematic diagram of experimental setup*

Mesh Size	Open Area (%)	Sample
5	74	C5
10	60	C10
16	55	C16
35	42	C35

Table 1. *Open area of each mesh size used*

3. Results and Discussions

Fig. 2 and Fig. 3 show the negative mean floating potential inside the cage for different pressures and negative plasma voltage, respectively, for each cage geometry. The cage C5 shows a less intense negative floating potential for every condition, which is expected in an active screen setup. On the other hand, the cage with the smallest open area, C35, shows a different behavior, and, for every condition, it was observed very intense negative floating potential. A hypothesis for this phenomenon is the confinement of the electrons inside the cage due to the great electrical barrier produced on the cage walls. Secondary electrons generated on the wire of the cathode (screen) are accelerated away from the negative screen surface and are trapped inside the cage, where the probe was placed.

Depending on the value of the working gas pressure or the cathodic voltage in the screen, the floating potential may be similar to those of the luminescent region of the plasma (order of tens of volts) or very

*Corresponding author: felipehcorrea@yahoo.com.br

negative values of the order of hundreds of volts. This transition occurs abruptly as soon as the barrier between the plasma glow and the floating potential inside the cage is broken up. This "break up" occurs commonly through formation of hollow cathode in the holes of the grid.

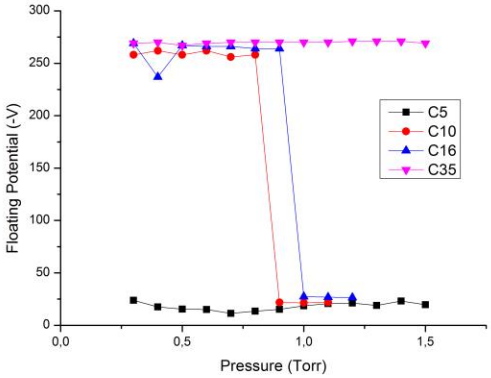

Fig. 2. *Floating potential inside the cages as a function of argon pressure.*

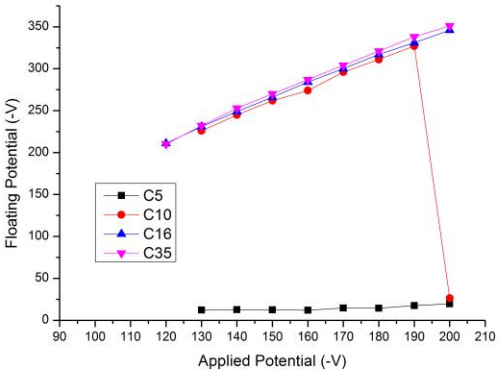

Fig. 3. *Floating potential as a function of plasma discharge voltage. .*

4. References

[1] S. Ahangarani, F. Mahboubi, and A. R. Sabour, "Effects of various nitriding parameters on active screen plasma nitriding behavior of a low-alloy steel," *Vacuum*, vol. 80, no. 9, pp. 1032–1037, 2006.

[2] C. X. Li, T. Bell, and H. Dong, "A Study of Active Screen Plasma Nitriding," *Surf. Eng.*, vol. 18, no. 3, pp. 174–181, 2002.

[3] C. X. Li, "Active screen plasma nitriding – an overview," *Surf. Eng.*, vol. 26, no. 1–2, pp. 135–141, 2010.

[4] S. Corujeira and G. Charitidishanshan, "Surface functionalization of carbon fibers with active screen plasma," *J. Vac. Sci. Technol. A Vacuum, Surfaces, Film.*, vol. 21404, no. 35, 2017.

[5] C. A. Jr, E. F. Silva, and A. E. Martinelli, "Effect of workpiece geometry on the uniformity of nitrided layers," *Surf. Coatings Technol.*, vol. 139, pp. 2–6, 2001.

[6] A. Nishimoto, T. Matsukawa, and H. Nii, "Effect of Screen Open Area on Active Screen Plasma Nitriding of Austenitic Stainless Steel," *ISIJ Int.*, vol. 54, no. 4, pp. 916–919, 2014.

Acknowledgments

This work was sponsored by FAPESC, CAPES scholarship and CNPq by project Universal/445242/2014-0.

*Corresponding author: felipehcorrea@yahoo.com.br

ID 83: MODELING AND EXPERIMENTAL ANALYSIS OF THE SUBSTRATE TEMPERATURE INFLUENCE ON THE REACTIVE MAGNETRON SPUTTER DEPOSITION

Júlia Karnopp*, Julio César Sagás

Laboratory of Plasmas, Films and Surfaces, Universidade do Estado de Santa Catarina, Joinville - SC

1. Introduction

The reactive magnetron sputter deposition is one of the most used methods for compound film deposition. In this process, a reactive gas is inserted into the chamber and reacts with deposited metal atoms. These reactions occur also in cathode surface (target), causing the poisoning. The reactive gas consumption dependence on surface compound fraction leads to the hysteresis in process curves (pressure, voltage, etc.) as a function of reactive gas flow and making the process unstable. The hysteresis curves are characterized by two critical points: the first, corresponding to target poisoning (increasing the gas flow) and the second corresponding to de-poisoning (decreasing the gas flow).

The compound formation on substrate occurs through gas chemisorption. This process can be described by Langmuir [1] and Kisliuk [1,2] models. The chemisorption rate is calculated by the product of reactive gas flux to the surface and the sticking coefficient. For Langmuir model, the sticking coefficient is an increasing function of temperature

$$\alpha^{L}(T_s, \theta_c) = \alpha_{00} \exp\left(\frac{-E_{ads}}{kT_s}\right)(1-\theta_c) \quad (1)$$

where k is the Boltzmann constant, T_s the substrate (collecting area) temperature, θ_c the compound fraction of collecting area (substrate and chamber walls), E_{ads} the activation energy of adsorption and α_{00} is the pre-exponential factor.

For the Kisliuk model, the sticking coefficient is

$$\alpha^{K}(T_s, \theta_c) = \frac{1}{1+\frac{K_{des}}{K_{ads}}\exp\left(\frac{E_{ads}-E_{des}}{kT_s}\right)} \frac{1}{\left(1+\frac{\theta_c}{1-\theta_c}K\right)} \quad (2)$$

where K_{des} and K_{ads} are the frequency factor of desorption and adsorption, respectively, E_{des} the activation energy of desorption and K is the Kisliuk factor.

The non-dissociative Langmuir model considers only molecular chemisorption on surface. On the other hand, in Kisliuk model the molecules physisorb in a precursor state and can move to another site. From this precursor state, the molecules can chemisorb or desorb.

Several parameters affect the hysteresis curves, the most part being included in the so-called Berg model [3]. This model simulates qualitatively the reactive sputter deposition process in the steady state using balance equations for reactive gas atoms on substrate and target surface. However, this model does not include explicitly the substrate temperature, parameter usually varied in experiments. The substrate temperature drives the surface diffusion of deposited atoms. Therefore, the main goal of the work is include the substrate temperature in Berg model and analyze qualitatively the effects caused by this parameter in reactive deposition, comparing the simulated results with experimental curves.

2. Methodology

To verify the effects caused by substrate temperature, the equations of Berg model was rewritten using the Langmuir model and, after, the Kisliuk model for adsorption. In these models, the substrate temperature dependence appears on sticking coefficient. The sticking coefficient for each model has been replaced in balance equation of substrate and in reactive gas flow equation of Berg model [3]. For Kisliuk model, the factor K was kept constant equal 1, keeping the same compound fraction dependence of sticking coefficient presented by Langmuir model.

After the modifications, hysteresis curves were simulated for different substrate temperatures. In these simulations, it was also varied the ratio between frequency factor of desorption and adsorption present on Kisliuk model (equation 2). The simulations results were compared with experimental hysteresis curves. The experiments were carried out in a triode magnetron sputtering with titanium target (99.5%) in argon and nitrogen atmosphere. The argon pressure was 0.40 Pa and the current was maintained constant at 1.00 A.

*julia_karnopp@outlook.com

3. Results and Discussions

Experimentally, it is observed that increasing the substrate temperature the first critical point is shifted for lower values of reactive gas flow, while the second critical point is not affected. Including the sticking coefficient of Langmuir model in Berg equations is not possible to obtain the experimental behavior. The hysteresis curve moves to the opposite side, i.e, for higher values of gas flow. This is due to the increase in sticking coefficient with temperature (equation 1). Increasing the temperature, the gas consumption in collecting area grows, thus the first critical point is shifted for higher gas flow rates, once that the first critical point corresponds to the maximum consumption of reactive gas by collection area.

Once that the Langmuir model is not adequate to describe the temperature dependence, it was also used the Kisliuk model. The hysteresis curves for this model are compatible with experimental curves. The first critical point is moved to lower flow rates when the temperature is increased. This occurs because increasing the temperature the sticking coefficient decreases (equation 2), reducing the gas consumption on substrate, due to the growing desorption. The second critical point is not affected by the temperature, because it depends mainly of sputtering yield.

Figure 1 shows the compound fraction on collecting area as a function of temperature and reactive gas partial pressure using the Kisliuk model. The frequency factor represents the probability of a molecule adsorbs or desorbs. The greater the ratio between frequency factors of desorption and adsorption, higher is the desorption probability, decreasing the chemisorption rate. Therefore, for a same pressure and temperature, the compound fraction decreases with increased ratio. For higher ratio values and high substrate temperature (Fig. 1b), it is needed a higher partial pressure to cover all surface with compound.

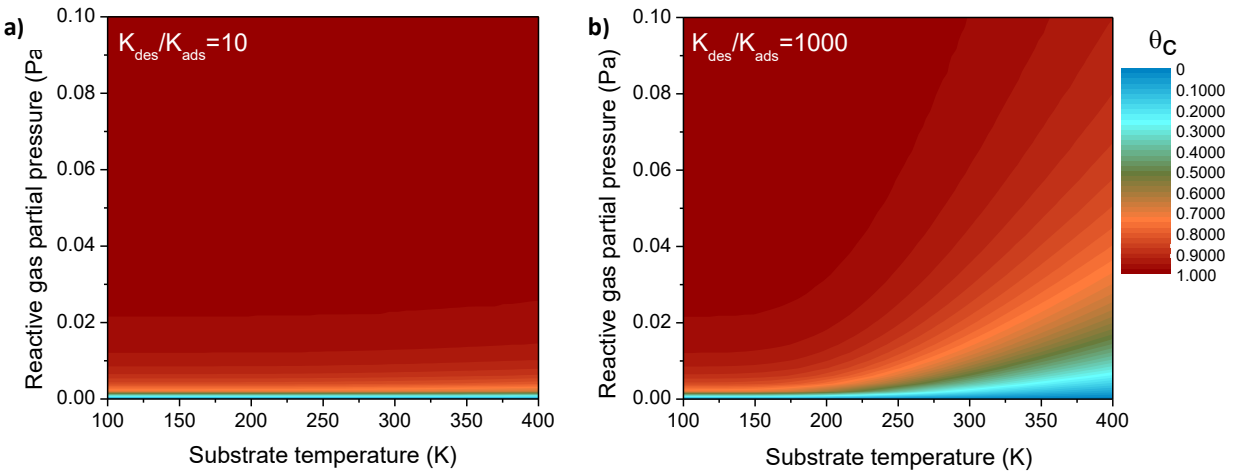

Fig. 1. *Compound fraction as a function of temperature and partial pressure. Ratio between frequency factor of desorption and adsorption equal 10 (a) and 1000 (b).*

It is noted that raising the substrate temperature the compound fraction is reduced due to the lowered chemisorption rate. For temperatures lower than 200 K, the ratio between frequency factors and the temperature have a little effect in compound formation. For these temperatures, the sticking coefficient is practically constant and near one, making the surface be covered with compound even at low reactive gas pressure.

4. References

[1] W. Ranke, Y. Joseph. Phys. Chem. Chem. Phys, 4, **2483–2498**, (2002)
[2] P. Kisliuk, J. Phys. Chem. Solids, 3, **95-101,** (1957)
[3] S. Berg, E. Särhammar, Thin Solid Films, 565, **186–192**, (2014)

*julia_karnopp@outlook.com

ID 84: STUDY OF THE REDISTRIBUTION OF SOLUTE IN EUTECTIC LEAD-TIN ALLOYS SOLIDIFIED UNDER HIGH ACCELERATION

TENÓRIO, P. I. G.*; TOLEDO, R. C.; AN, C. Y.; BANDEIRA, I. N.
Instituto Nacional de Pesquisas Espaciais – INPE, Associate Laboratory of Sensors and Materials – LAS

1. Introduction

The study of materials processed in centrifuges improves the understanding on influence of acceleration and convection in materials processing. Large centrifuges are expensive and rarely available for crystal growth and solidification experiments. To overcome this difficulty, a small centrifuge with an electric tubular furnace was designed and built at LAS/INPE, which provides an acceleration ranging from 1 to 10 times the earth gravity [1,2]. The scope of this work is to study the influence of the high gravity in the redistribution of solute due to effects of the buoyancy-driven convection and sedimentation. The samples were analyzed by densitometry and energy dispersive spectrometry (EDS). The PbSn eutectic alloy is a material that provides convenient physical properties such as low melting point (183°C), low vapor pressure, and does not react with the surface of the quartz ampoule, making it an ideal material for solidification studies of regular eutectic alloys [3].

2. Experimental

The solidification experiments were carried out in a furnace attached to the centrifuge (Figure 1). A mass of 20g of the $Pb_{38.1}Sn_{61.9}$ (wt%) eutectic alloy was prepared from 99.9999% purity elements and sealed under vacuum (5.10^{-6} Torr) in an 8 mm diameter and 100 mm length quartz ampoule (Figure 2). Solidification experiments were perfomed with both the furnace standing at 1g and rotating at 6g with the same thermal parameters, where g is the gravity acceleration on earth (9.81 m/s^2). In the second experiment, after heating the furnace up to a temperature of 200°C for 1 hour, the temperature controller was disconnected and the motor turned on at 92 rpm and kept running at constant speed during the whole solidification process.

Fig. 1. *Centrifuge (with furnace at the right side) of LAS/INPE*.

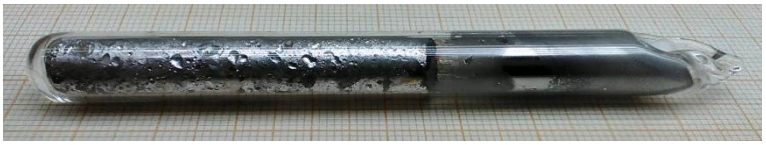

Fig. 2. *PbSn eutectic alloy sealed in a quartz ampoule.*

3. Results and Discussions

Figure 3(a) shows the average lead composition profile along axial direction measured by density measurements. It is observed that at the beginning of the both samples (at the tip of the quartz ampoule) there is a solute (Pb) accumulation caused by both convection and sedimentation due to density differences between Pb ($11.34 g/cm^3$) and Sn ($7.31 g/cm^3$). On the other hand, the samples analyzed by EDS, Figure 3(b), shows a smaller difference between both profiles because that in this case only the surface composition of each sliced

*Corresponding author: plinio.tenorio@inpe.br

sample was took into account. It was expected that higher gravity levels would cause a larger composition gradient along sample axial direction.

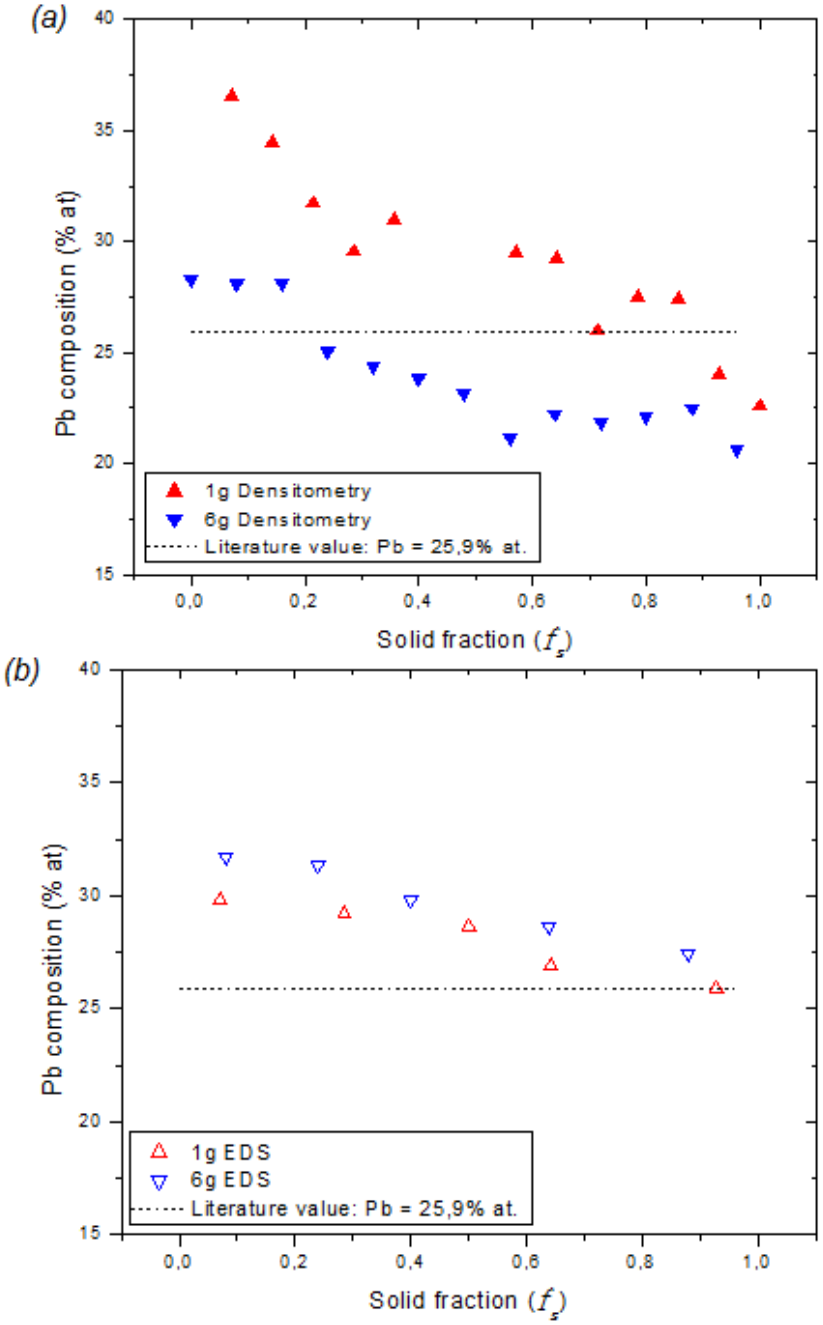

Fig. 3. *Lead composition profile for 1g and 6g PbSn eutectic alloy analyzed by densitometry (a); energy dispersive spectrometry (EDS) (b).*

4. Conclusion

PbSn eutectic alloys were solidified by centrifuge under high acceleration, and the average composition profile obtained at 6g level presents a smaller axial density gradient than that obtained under 1g earth gravity. The centrifuge can be used to control the solute redistribution by the effects of the buoyancy-driven convection and sedimentation.

5. References

[1]- Freitas, F.E. *et al*, Materials Science Forum, **869**, 631-636, (2016).
[2]- Tenório, P.I.G. *et al*, 6° Workshop em Engenharia e Tecnologia Espaciais, **Proceedings...**, 7, (2015).
[3]- An,C.Y. *et al*, Microgravity Science and Technology, **25**, 267-273, (2014).

Acknowledgments

The authors P. I. G. Tenório and R. C. Toledo are grateful to CAPES for the financial support.

*Corresponding author: plinio.tenorio@inpe.br

ID 85: EXPERIMENTAL DETERMINATION OF THE PERMITTIVITY AND PERMEABILITY OF AN ARRAY OF SPLIT-RING RESONANTORS IN A X-BAND WAVEGUIDE

Joaquim P. Leite Neto[1], Joaquim J. Barroso[2] , Pedro José de Castro, and Antonio Tomaz[2]
[1]*Instituto Nacional de Pesquisas Espaciais INPE- São José dos Campos- S.P*
[2]Instituto Tecnológico de Aeronáutica (ITA)
12228-900 São José dos Campos, S.P

1 Introduction

Experiments on the propagation and transmission of electromagnetic waves in waveguides loaded with anisotropic magnetic metamaterials (as for example, periodic arrangements of split-ring resonators, called SRRs) have enabled the development of waveguides of subwavelength, resonators, filters, etc. [1-5]. In this work, we use magnetic probes to excite the loaded waveguide and to study the effects of weak and strong coupling between the SRR array and the probe through a retrieval procedure of constitutive parameters ε and μ, as well as the transmission parameters, namely, the refractive index and the wave impedance. Detailed knowledge of the constitutive properties of such artificial materials becomes relevant for microwave applications, as for instance, antennas, dephasers, and absorbers. All experiments were implemented by loading a rectangular waveguide with a periodic arrangement of six SRRs, with dimensions and physical features detailed in [6]. The array is placed in the plane of symmetry of a X-band waveguide (WR90) having a cross-sectional area 2.29 x 1.02 cm^2 and cutoff frequency 6.55 GHz (Fig. 1).

Fig. 1. (a) *WR90 waveguide loaded with six SRRs. (b) Set-up to measure scattering parameters in the X-band waveguide loaded with the SRR array using waveguide coaxial adapters.*

2. Experimental Results and Discussion

First the waveguide loaded with the SRR array is symmetrically connected on both ends to identical X-band waveguide-to-coaxial adapters, by means of which the input and output signals have been injected and detected by an Agilent N5230C vector network analyzer [6]. The results presented in Fig. 2(a) show that the first passband is left-handed in nature and occurs around f ~ 3.45 GHz, but the transmission is very weak (S_{21}~ − 45 dB).

Fig. 2 **(a)** *The transmission band for the waveguide loaded with a periodic array of six SRRs measured with coaxial-waveguide adapters.**(b)** Magnitudes of reflection (S_{11}) and transmission (S_{21}) scattering parameters. Measurements were made by using magnetic probes.*

To enhance the transmission band resulting from the effect of magnetic resonance, a pair of magnetic probes is used to excite and detect the propagating signal, as described in [6]. The magnitudes and phases of reflection and transmission coefficients, respectively, S_{11} and $S_{21,}$ are obtained for two cases: a) weak coupling between the probe and the SRRs; b) strong coupling between the probe and the SRRs, as displayed in Fig. 2(b).

It is observed that in the case of weak coupling, the maximum transmission intensity (S_{21} ~ 0,22) is obtained at f ~ 3.32 GHz, while in the case of strong coupling the resonant frequency is slightly reduced (f ~ 3.28 GHz) and the transmission band is wider, with S_{21} reaching ~ 0.56.The refractive index retrieved, according to a method described in [7], is shown in Fig. 3(a). In the case of strong coupling the real part of the index is negative in all the range studied (f ~ 3.0 − 3.8 GHz), indicating negative refraction, with values varying in the range $-1.3 \lesssim n_r \lesssim -0.25$, whereas in the weak-coupling case the real part of the refractive index is negative only for frequencies $f \lesssim 3.32$ GHz and takes values in the range $-1.25 \lesssim n_r \lesssim 0.67$. The imaginary parts of the refractive index show that the strong coupling leads to a much lower energy dissipation level. In Fig. 3(b) the retrieved magnetic permeability shows a real part which is negative in almost all the range of frequencies, in both cases of weak and strong couplings. Although in the case of weak coupling, Re{μ} has larger negative values in the frequency range between 3.0 and 3.2 GHz, in practice it means nothing since the transmission in this frequency range is negligible (see fig. 2(b)). Note that in the region of stronger transmission, between 3.2 and 3.4 GHz, both permeabilities are approximately the same, indicating that the permeability nearly independent of the incident magnetic field. The electric permittivity ε_r of the SRR periodic array is negative only in the region around the magnetic resonance frequency ($f \sim 3.2 - 3.3$) GHz and is larger in the case of weak coupling, as shown in Fig. 3(c). In the frequency range $3.3 \leq f \leq 3.65$ GHz we have obtained $\varepsilon_r > 0$ for both the strong and weak coupling cases.

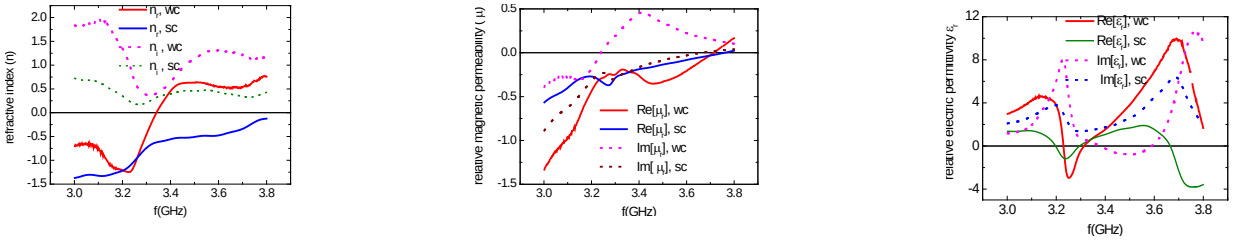

Fig. 3. *(a)Refractive index extracted from scattering parameters S measured in loaded waveguide. The solid lines refer to the real part n_r and the dotted lines to imaginary part n_i. The minima of n_i spectrum correspond to largest transmission, as would be hoped. (b) Magnetic permeability extracted from measured S -parameters. The solid lines refer to the real part and the dotted lines to imaginary part. (c) Relative Electric permittivity extracted from scattering parameters (S) measured. (sc=strong coupling, wc= weak coupling)*

The permeability and permittivity of an arrangement of resonant rings inserted in a X-band rectangular waveguide have been experimentally determined in the range of frequencies 3.0 ~ 3.8 GHz, which exhibits magnetic resonance below the cutoff frequency of the empty waveguide (6.55 GHz). It was noted that the excitation by using magnetic probe has intensified the transmission LH (left-handed) and that, depending on the intensity of the coupling, transmission can be equivalent to that of a balanced CRLH line (weak coupling) or a purely LH line (strong coupling). We also observed a negative refraction even in the range of frequencies over which the electric permittivity is positive. A reverse procedure (not explained in the text), retrieves all the original parameters (S parameters) using the permeability and permittivity extracted, fully validating the accuracy of the retrieved constitutive parameters.

REFERENCES

[1] R. Marques, J. Martel, F. Mesa, and F. Medina, “Left handed media simulation and transmission of EM waves in sub-wavelength split-ring- resonator-loaded metallic waveguides”, Phys. Rev. Lett, vol. 89, nº 18, art. ID, 183901,2002

[2] J.B.Pendry, A. J. Holden, D. J. Hobbins e W. J. Stewart, “Magnetism from conductors and enhance nonlinear phenomena, IEEE Trans. Theory Tech, vol. 47, pp. 2075, Nov 1999”

[3] S. Hrabar, J. Bartolic, Sipus, Z., “Waveguide miniaturization using uniaxial negative permeability metamaterial”, IEEE Trans. Antennas Propag., vol. *53*, nº1, pp. 110-119, 2005

[4] J.Carbonell, L. J. Roglá, V.Boria e D Lippens, “Design and experimental verification of backward-wave propagation in periodic waveguide structures”, IEEE Trans. On Microwave Theory and Techniques, vol. 54, no 4, Abril, 2006.

[5] X.Chen, T. M. Grzegorczyk, B I Wu, J. Pacheco e J. A. Kong, “Robust method to retrieve the constitutive effective parameters of metamaterials”, Phys. Rev. E *70*,016608, 2004.

[6] P. J. Castro, J. J. Baroso, J. P. Leite Neto, A. Tomaz, and U. C. Hasar, “ Experimental study of transmission and reflection characteristics of a gradient array of metamaterial split-ring resonators”, Journal of Microwaves, Optoelectronics and Electromagnetic Applications, v. 15, p. 380-389, December 2016.

[7] U.C. Hasar, A.Muratoglu, M. Bute, J. J. Barroso, e M. Ertugrul, “Retrieval method for effective constitutive parameters of bi-anisotropic metamaterials using waveguide measurements”, a publicar IEEE Trans. On Microwave Theory and Techniques

ID 86: CARBON FIBER PREPARATION FOR METAL MATRIX COMPOSITE APPLICATION

Glaucy Barbosa Barreto[1]*, Luryan Lara Caressato[1], Herman Jacobus Cornelis Voorwald[1], Durval Rodrigues Junior[2], Pérsio Mozart Pinto[2], Verônica Mara de Oliveira Velloso[1]
[1]*Fatigue and Aeronautical materials group, Materials Department, FEG - UNESP*
[2]*Materials Engineering Department, EEL - USP*

1. Introduction

Metal matrix composites (MMC's) have been used, especially in the aerospace industry, because of its high resistance and work temperature. In general, these composites are manufactured using as reinforcement fibers, such as carbon fibers [1, 2].

Carbon fibers are more expensive than other fibers used as reinforcement in composites, however they present better performance in structural applications. Fiber distribution influences uniformity or homogeneity of the composite: the more uniform it is, the more homogeneous is the reinforcement and the lower the chances of failure [3, 4].

Even et. al. (2008) prepared a metallic matrix metal composite based on carbon fiber reinforced titanium. The authors developed a technique that involves powder metallurgy and techniques used to process ceramic and polymer composites. They conclude that this method allows to process titanium (reactive at high temperatures) at lower temperatures, reducing their interaction and subsequent degradation of the reinforcement (carbon fibers). However, tensile tests showed that the presence of the reinforcement in different volumetric fractions caused a reduction in the stiffness and mechanical strength of the composite material [5].

The global demand for carbon fiber composites can reach 140.000 ton per year by 2020. As a result, waste generation during processing also grows [6]. Thinking about that, this research is being made using residual carbon fiber in a way to contribute with the environment, focused in the carbon fiber characterization for posterior application in metal matrix composite.

2. Experimental

The plain weave manufactured with 3000 filaments is being used. Carbon fibers Hexcel® AS4 GP were used. This is a continuous fiber, classified as high strength and high strain.

The fibers were separated and cut into smaller pieces to help with the grind. Milling was performed with 95% isopropyl alcohol for 1 hours. Scanning electron microscopy (SEM), X-ray diffraction (XRD) and energy dispersive X-ray spectroscopy (EDS) analyses were carried out to verify contamination during the milling, phases and morphology of carbon fibers.

3. Results and Discussions

Before milling process and after carbon fibers have been cut, they were analyzed by light microscopy to determine the mean fibers diameter. The mean diameter was calculated using ImageJ software, the result was 6.24 μm.

In the first attempt, dry milling was performed for 2 hours, and the fiber was not ground, only agglomerated. Thus, it was decided to perform wet milling with 95% isopropyl alcohol for 2 hours. The fiber was ground excessively and became powder, as can be seen in Figure 1. Finally, the milling last for 1 hour. Figure 2 shows carbon fiber after wet milling for 1 hour, which kept the fiber aspect (did not turn it into powder).

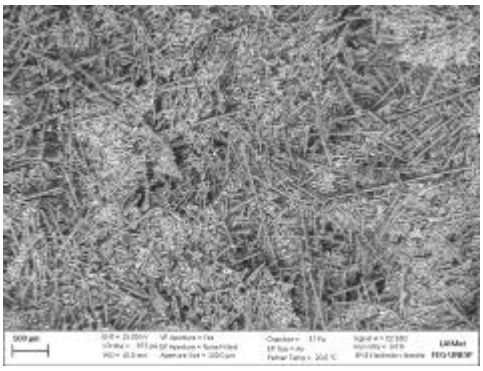

Fig. 1. *Carbon fiber after wet milling for 2 hours.*

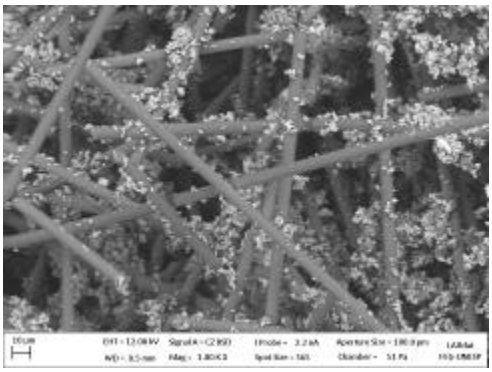

Fig. 2. *Carbon fiber after wet milling for 1 hour*

*Corresponding author: glau.glaucy@gmail.com

Analyzes by SEM, XRD and EDS showed a contamination due to the balls in the grinding jar. Figure 3 shows the fiber after sieving to reduce contamination. Even after drying, the alcohol, used in the grinding, agglomerated the fibers, making it difficult to separate them.

Therefore, the fibers were manually separated and cut with scissors without going through milling process (Figure 4).

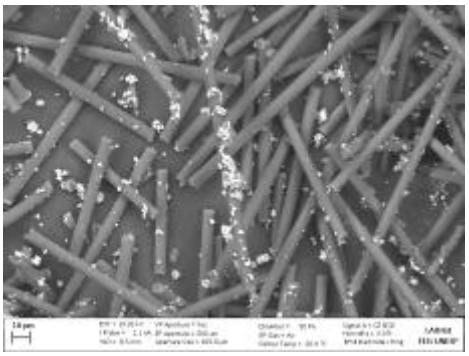

Fig. 3. *Carbon fiber after sieving.*

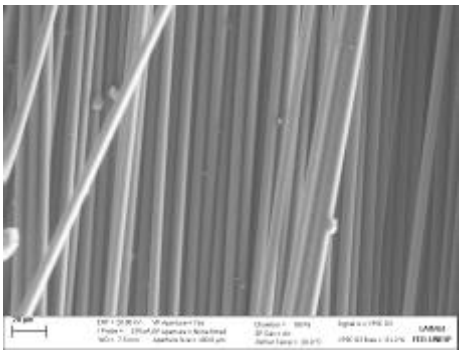

Fig. 4. *Carbon fiber without passing through milling process.*

At first, it was believed that, due to the high hardness of the carbon fiber, it would be necessary to seek a means to facilitate its separation for insertion into the metal matrix. The option found was the milling, in an attempt to obtain a smaller size of fiber, to provide a homogeneous distribution through the matrix, and avoid strain concentration, damaging the mechanical properties of the material [7]. Manual separation results in relatively larger sizes compared to the obtained one by milling. It demands special attention, since reinforcement size and fiber distribution influence mechanical properties [8].

There is a lack of detailed information on how to process carbon fiber. Carbon fiber grinding requires to be wet, due to its hardness, and keeps fiber morphology if it is done in a controlled way. However, the use of this technique is not efficient for the purposes of this research, because the resulting material agglomerates. Due to the use of mills and spheres already used in other processes, contamination can occur, and sifting can help minimize this situation.

4. References

[1] C. A. I. Merino, J. E. L. Sillas, J. M. Meza and J. M. H. Ramirez, Journal of Alloys and Compounds, **707**, 257-263, (2017).
[2] N. Meek, D. Penumadu, O. Hosseinaei, D. Harper, S. Young, T. Rials, Composites Science and Technology, **137**, 60-68, 2016.
[3] K. Shirvanimoghaddam, S. U. Hamim, M. K. Akbari, S. M. Fakhrhoseini, H. Khayyam, A. H. Pakseresht, E. Ghasali, M. Zabet, K. S. Munir, S. Jia, J. P. Davim, M. Naebe, Composites Part A: Applied Science and Manufacturing, **92**, 70-96, 2017.
[4] Y. Xie, L. Lu, Y. Tang, F. Zhang, C. Shen, X. Zang, X. Ding, W. Cai, L. Lin, Materials Letters, **186**, 70-73, 2017.
[5] C. Even, C. Arvieur, J. M. Quenisset, Composites Science and Technology, **68**, 1273-1281, 2008.
[6] C. S. R. Souza, J. M. F. Marlet, A. M. Cardoso and M. C. Rezende, Polímeros, **26**, 8-15, (2016).
[7] J. J. Lewandowski and C. Liu, Materials Science and Engineering, 241-255, (1989).
[8] J. Llorca and C. González, Journal of the Mechanics and Physics of Solids, **46**, 1-28, (1998).

Acknowledgments

Thanks to FAPESP (process number 2016/07603-0) and CNPQ (process number 122494/2016-4) for the financial support.

*Corresponding author: glau.glaucy@gmail.com

ID 87: CREEP BEHAVIOR OF THERMAL BARRIER COATING LASER REMELTED TREATMENT ON Ti-6Al-4V ALLOY

Filipe Estevão de Freitas[1]*, Flávio Perpétuo Briguente[2], Adriano Gonçalves dos Reis[3], Getúlio de Vasconcelos[4], Danieli Aparecida Pereira Reis[1]

[1]*Universidade Federal de São Paulo (UNIFESP), São José dos Campos, Brazil*

[2]*Instituto Tecnológico de Aeronáutica (ITA), São José dos Campos, Brazil*

[3]*Universidade Estadual Paulista (Unesp), Instituto de Ciência e Tecnologia, São José dos Campos, Brazil*

[4]*Instituto de Estudos Avançados (IEAv), São José dos Campos, Brazil*

1. Introduction

Thermal barrier coating (TBC) processed by air plasma spray (APS) has been widely used in components operating at high temperatures, such as gas turbine blades [1]. The TBC laser remelted is a technique that have been studied to improve the coating quality by increasing the isothermal and cyclic oxidation resistance, a higher hardness by the densification of the surface, a reduction of oxidation and corrosion phenomena and thermal shock resistance were enhanced around fourfold [2-5]. A comparative study of creep resistance was carried out of the Ti-6Al-4V alloy without treatment, as-sprayed TBC and the laser remelted TBC.

2. Experimental

The Ti-6Al-4V specimens used and the TBC deposition is described in [6]. The specimens were prepared in Rolls-Royce Company (São Bernardo do Campo, Brazil) using the same procedure for turbine blade coating. For TBC laser remelted was used a continuous CO_2 laser with beam diameter of 0.2 mm. The treatment was conducted with two different steps with their respective electric power (P) and scanning velocity (V): 1) P = 37.5 W and V = 800 mm/s; 2) P = 50 W and V = 500 mm/s. It was performed in the air with laser beam overlapping of 50%.

Constant load creep tests were conducted on a standard creep machine following the same procedure and equipment used in [6]. A comparison of creep behavior of the specimens was made for Ti-6Al-4V without treatment, as-sprayed TBC and laser remelted TBC at a temperature of 600 ºC and at stress levels of 125, 250 and 319 MPa.

3. Results and Discussions

Figures 1 to 3 show the creep curves at 600 °C and 125 to 319 MPa. A typical creep curves are observed in all conditions with most of the creep life dominated by a constant creep rate, that can be associated with a stable dislocation configuration due to recovery and hardening process.

Fig. 4 shows the stress dependence of the steady-state creep rate. By standard regression techniques, the results can be described in terms of power-law creep equation:

$$\dot{\varepsilon}_s = B\,\sigma^n \quad (1)$$

where $\dot{\varepsilon}_s$ is steady-state creep rate; B is structure-dependent constant, σ is the applied stress and n is the stress exponent from secondary creep.

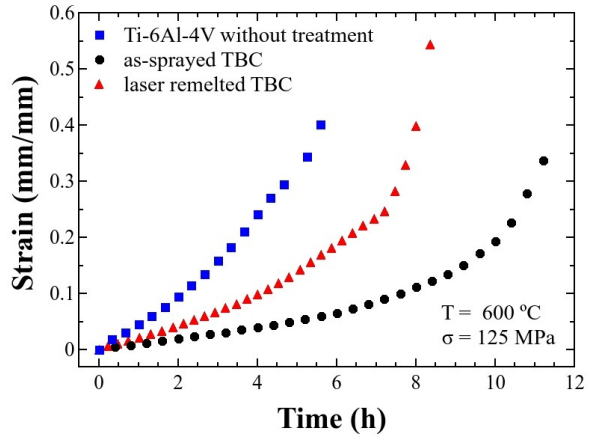

Fig. 1. *Creep curves at 600 ºC and 125 MPa.*

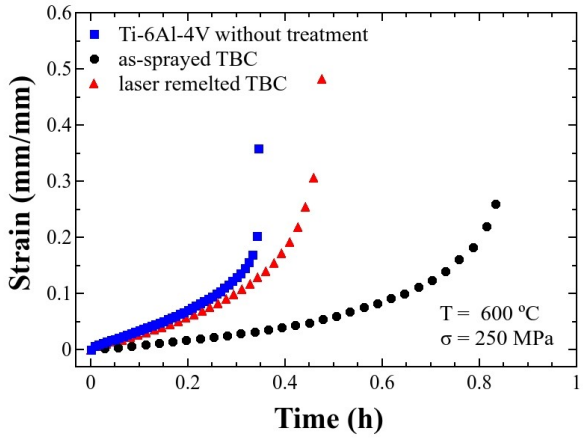

Fig. 2. *Creep curves at 600 ºC and 250 MPa.*

*filipe.estevao@gmail.com

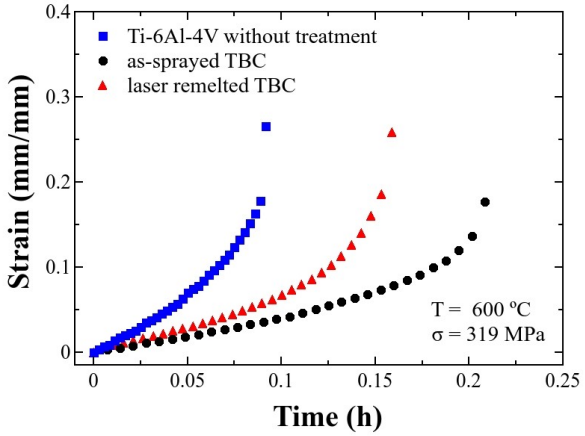

Fig. 3. *Creep curves at 600 ºC and 319 MPa.*

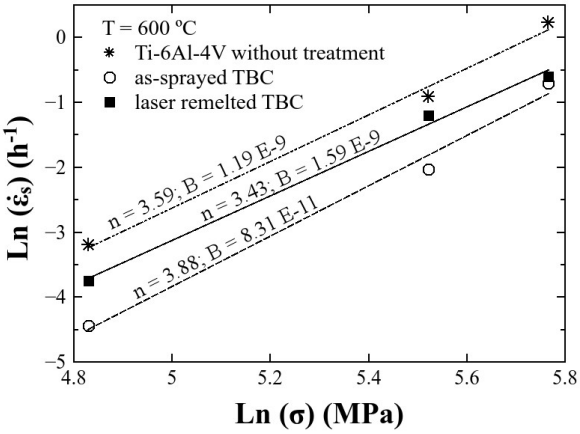

Fig. 4. *Stress dependence of the steady-state creep rate of Ti-6Al-4V without treatment, as-sprayed and laser remelted TBC at 600 ºC.*

The creep mechanism can be estimated based on the stress exponent from secondary creep rate (n), that are very similar for each treatment (3.43 to 3.88), which suggests the dislocation climb as dominant mechanism in all cases.

Results from the creep tests at 600 ºC are summarized in Tab. 1, where t_r is the time to rupture. The reduction of $\dot{\varepsilon}_s$ and higher values of t_r demonstrate a higher creep resistance in the laser remelted TBC compared to the Ti-6Al-4V without treatment. This occurred due to an improvement in the thermal barrier provided by the coating. However, comparing with the as-sprayed TBC, the creep behavior was worse in the laser treated. This fact can be related to the coating embrittlement and delamination of the top layer during creep elongation, as can be seen in Fig. 5.

The TBC increased the Ti-6Al-4V creep resistance because it acts as a thermal insulation and a barrier for inward oxygen diffusion into the alloy. The conditions used for the laser remelted treatment of TBC were not effective in improving creep behavior at 600 °C and 125 to 319 MPa compared to as-sprayed coating probably because of the TBC delamination during creep elongation.

Tab. 1. *Creep data at 600 ºC.*

Treatment	σ (MPa)	$\dot{\varepsilon}_s$ (h^{-1})	t_r (h)
Ti-6Al-4V without treatment	125	0.0410	5.58
	250	0.4030	0.35
	319	1.2703	0.09
As-sprayed TBC	125	0.0118	11.20
	250	0.1317	0.83
	319	0.4966	0.21
Laser remelted TBC	125	0.0237	8.37
	250	0.3023	0.48
	319	0.5507	0.16

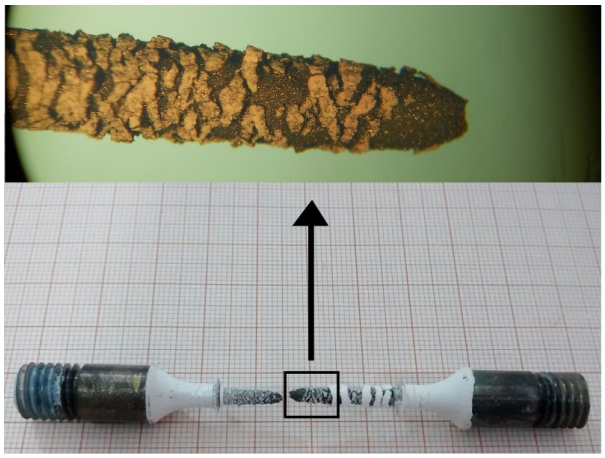

Fig. 5. *Photo of the fractured specimen after creep test.*

4. References

[1] R. Rajendran, Eng. Fail. Anal., **26**, 355-369, (2012).
[2] G. Antou *et al.*, J. Eur. Ceram. Soc., **26**, 3583-3597, (2006).
[3] C. Zhu *et al.*, Surf. & Coat. Tech., **206**, 3739-3746, (2012).
[4] R. Ahmadi-Pidani *et al.*, Opt. Laser. Eng., **50**, 780-786, (2012).
[5] M. Morks *et al.*, Appl. Surf. Sci., **256**, 6213-6218, (2010).
[6] F. P. Briguente *et al.*, Mater. Sci. Forum., **802**, 472-476, (2014).

Acknowledgments

The author is grateful to the CAPES and FAPESP for the financial support and Rolls Royce for plasma spray deposition.

*filipe.estevao@gmail.com

ID 89: WETTABILITY AND SURFACE ENERGY OF TiO_x FILMS DEPOSITED BY REACTIVE MAGNETRON SPUTTERING

Thais Macedo Vieira*, Julio César Sagás

Laboratory of Plasmas, Films and Surfaces, Universidade do Estado de Santa Catarina, Joinville-SC

1. Introduction

Titanium oxide films have a wide range of applications, specially the titanium dioxide (TiO_2) due to its photocatalytic properties [1]. However, many titanium suboxides (TiO_x) are also of technological relevance due to their higher electrical conductivity when compared to TiO_2 [2]. Among the interesting properties of TiO_2 is the photoinduced hydrophilicity. When exposed to UV radiation, the formation of electron-hole pairs in the material promotes a reduction of water contact angle, *i.e*. an increase in wettability [3]. The increased wettability implies in a higher surface energy. The photoinduced hydrophilicity is an important property for applications like photocatalysis and self-cleaning windows. The deposition temperature is a crucial parameter to cristallinity and phase formation in sputter deposition, thus it is a way to tune the wettability of the films by controlling their structure. In this work, TiO_x films deposited by reactive magnetron sputtering at different substrate temperatures are analyzed for their wettability and surface energy by contact angle measurements.

2. Experimental

The films were deposited onto glass substrates in a triode magnetron sputtering system in five different conditions of substrate heating: no heating, 100°C, 200°C, 300°C and 400°C. Even without external heating, the sample reaches a temperature of 94 ºC at the end of deposition. All depositions were performed at a total pressure of 0.40 Pa in an atmosphere of argon (Ar) and oxygen (O_2) during 30 min. The O_2 flow rate was adjusted to avoid target poisoning, *i.e*. the O_2 partial pressure is close to zero. The titanium target (99.5 %) has 100 mm in diameter. The grid-to-target and the target-to-substrate distances were fixed to 2.0 cm and 6.0 cm, respectively. The discharge power was set up to 470 W. The samples were biased by a bipolar asymmetrical power supply at – 200 V, frequency of 5 kHz and reverse time of 4.0 μs. In an earlier work [4], the films were characterized by X-ray diffraction, indicating a mixture of TiO_2 and suboxides, where Ti_2O_3 is the principal phase. Increasing the temperature there is an improvement in cristallinity and in the formation of Ti_2O_3. The contact angles were measured using an automated goniometer Ramé- Hart, model 590. The drop volume was set up to 0.83 μL and the measurements were made with deionized water, diiodomethane and glycerol, before and after UV exposure. The measurements were made in several different points of each sample, being ten measurements in each point with a time step of 1.0 s. The UV radiation source is a mercury lamp with 4 W and maximum intensity in the wavelength of 253.7 nm. The samples were irradiated during 24 h in a dark box before the measurements. The surface energy was determined using the multi-liquids method [5] from the linearization of equation (1)

$$(1+\cos\theta)\frac{\gamma_L}{2(\gamma_L{}^d)^{1/2}} = (\gamma_S{}^d)^{1/2} + (\gamma_S{}^p)^{1/2}\left(\frac{\gamma_L{}^p}{\gamma_L{}^d}\right)^{1/2} \quad (1)$$

where θ is the contact angle, γ_L is the surface free energy of the liquids and γ_S is the surface energy of the film. The indices *p* and *d* refer to the polar and dispersive components of the surface energy.

3. Results and Discussions

The contact angle has the same behavior as a function of deposition temperature for all the liquids, but the UV effect is more pronounced for deionized water. In figure 1, the water contact angle is shown, before and after UV exposure. It is observed that the photoinduced hydrophilicity is enhanced when the substrate temperature is raised, *i.e.* when the film cristallinity (and suboxide formation) is improved. It must be noted that the behavior of contact angle as a function of deposition temperature is changed after the UV exposure. The contact angle increases with temperature before UV, but decreases after UV. This result indicates a possible modification of surface chemistry with UV. In fact, the model for photoinduced hydrophilicity of TiO_2 [3] is based on the creation of oxygen vacancies in TiO_2 surface due to the break of chemical bonds between oxygen and titanium atoms after the generation of electron-hole pairs by UV absorption. It is expected that the suboxide films already have some oxygen vacancies.

*Corresponding author: vieira.thaism@gmail.com

The multi-liquids analysis shows a great uncertainty in the absolute values of surface energy. This is caused by a deviation from equation (1) due to the small number of liquids tested. The multi-liquids method is as good as higher the number of different liquids used. This is also the reason why the "standard" two-liquid method be strongly dependent of the liquid pair used.

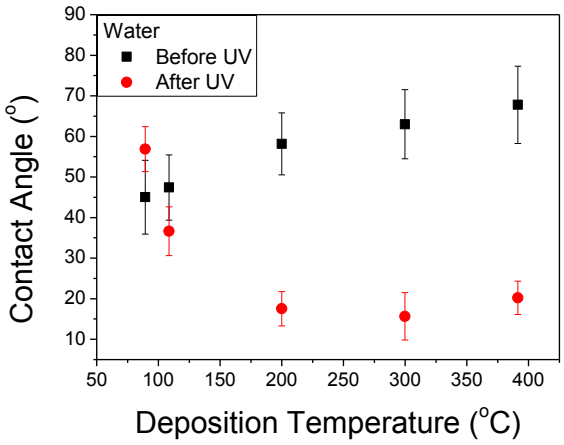

Fig. 1. *Water contact angle as a function of substrate radiation before and after UV exposure.*

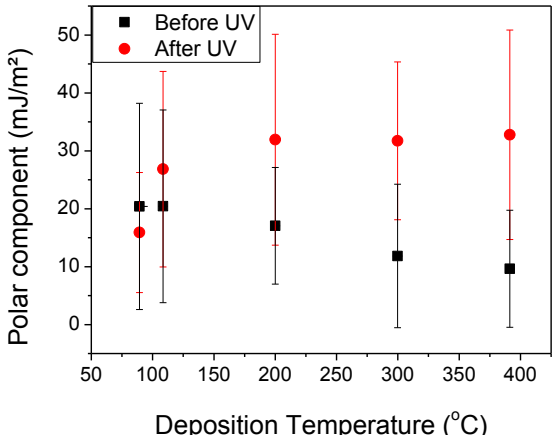

Fig. 2. *Polar component of surface energy as a function of deposition temperature before and after UV exposure.*

Despite this, the analysis shows that the reduction in contact angle caused by UV radiation is due to the raising of the polar component of surface energy, which explains the higher contact angle variation for water than for the other liquids, once that water is the most polar of the test liquids. The dispersive component also increases with UV, but the raise is not as strong as for the polar component. The growing of both components obviously implies in an increase of total surface energy as expected from the contact angle measurements.

It can be noted that the polar component drops with increased temperature before UV exposure, but it grows after UV exposure, the same behavior of contact angle. This behavior can be related to the formation of oxygen vacancies in film surface, but more detailed analyses are necessary to confirm this hypothesis.

4. References

[1] U. Diebold. Surface Science Reports, 48, **53–229**, (2003).
[2] M. Niu et al. Journal of Chemical Physics, 143(5). 054701, (2015).
[3] P. A. Fujishima, T. N. Rao, J. D. A. Tryk. Photochemistry and Photobiology. C: Photochemistry Reviews, 1, **1-21**, (2000).
[4] T. M. Vieira, J. C. Sagás, L. C. Fontana. "Temperature effect on the formation of Ti_2O_3 in magnetron sputter deposition", International Symposium on Non-Thermal/Thermal Plasma Pollution Control Technology and Sustainable Energy, (2016).
[5] S. Siboni et al. Journal of Colloid and Interface Science, 271(2), **454-472**, (2004).

Acknowledgments

T. M. Vieira thanks to UDESC by the financial support through PROBIC grant.

*Corresponding author: vieira.thaism@gmail.com

ID 90: INFLUENCE OF THE SYNTHESIS METHOD ON THE MORPHOLOGICAL AND ELECTROCHEMICAL PROPERTIES OF PANI / CARBON FIBER COMPOSITE

Dalva A. de Lima. Almeida[1]*, Lilian Mieko da Silva[1], Andréa Boldarini Couto[1], Neidenei Gomes Ferreira[1]
[1] *Instituto Nacional de Pesquisas Espaciais - INPE*

1. Introduction

Conducting polymers represent an interesting class of electrode materials for supercapacitors, due to their high kinetics of the electrochemical charge-discharge processes. Among them, polyaniline (PAni) has been the subject of intense research as flexible electrode for solid-state because of its, low cost, electrical conductivity, mechanical properties and high capacitance [1]. The charge is stored throughout the volume of the polymer material. Other material that has singular properties is the carbon fiber (CF) like large surface area, high conductivity, temperature stability and percolated pore structure [2]. Hence, CF is an excellent substrate, which acts as a template for PAni synthesis. In this context, the aim of this work was to evaluate the influence of two different synthesis methods to obtain PAni on the CF substrate. Emphasis was given in the morphological and electrochemical properties of the PAni/CF composites obtained.

2. Experimental

PAni chemical synthesis was performed using CF (1x1 cm) fixed in a platinum wire and placed in reaction medium containing distilled aniline (12.6 mmol L^{-1}) and 1.0 mol L^{-1} HCl, 3.0 mol L^{-1} NaCl. Then, the oxidizing agent solution (ammonium persulfate) was slowly dripped in the reaction medium, with 30 min of the deposition times at -10 ^{o}C with vigorous stirring. For electrochemical synthesis, the PAni was electrodeposited on CF electrode under galvanostatic mode using 5 mA cm^{-2} current density for 10 min in 0.5 mol L^{-1} H_2SO_4 aqueous containing 0.1 mol L^{-1} aniline. It was denominated PAni/CF_C the composite obtained for chemical synthesis and PAni /CF_E for prepared by the electrochemical synthesis.

3. Results and Discussions

The SEM images (Fig. 1(a) and (b)) showed heterogeneous PAni layer with small sponge-like agglomerates in the PAni/CF_C, while the PAni/CF_E presented homogeneous PAni layer. The cyclic voltammetry (CV) curves were carried out from −0.2 to 0.8 V at scan rate 25 mV s^{-1}. It was observed a pair of peaks well defined, which are attributed to the transition between leucoesmeraldina and emeraldine phase, besides a capacitive profile for both composites obtained. Based on the initial observations, both electrodes have potential of charge storage. However, the electrochemical synthesis appear as an interesting route to PAni/CF production because it spends less time, with a lower cost not to mention the minimum sludge. In this preliminary study, the electrochemical synthesis was the most suitable, but a more careful analysis will be required to test the efficiency of these electrodes, whose purpose will be to test them on devices energy storage.

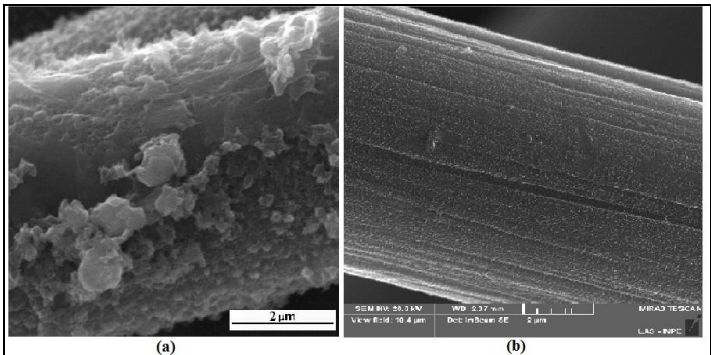

Fig. 1. *PAni/CF images: (a) PAni/CF_C obtained for chemical synthesis and (b) PAni/CF_E by electrochemical synthesis*

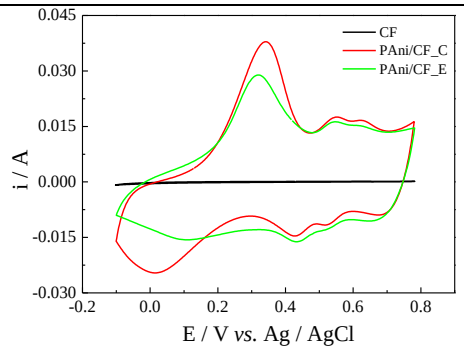

Fig. 2. *CV curves of PAni/CF obtained by both methods at a scan rate 25 mV s^{-1}.*

4. Reference

[1] P. Zhang et al., Electrochim. Acta, **184**, 1-7, (2015).
[2] S. Jiang et al., J. Power Sources, **272**, 16-23, (2014).

Acknowledgments

This work was supported by FAPESP 2016/13393-9, CAPES 086/2013 e CNPq.

*Corresponding author: dalva.dri@gmail.com

ID 91: EFFECT OF STRESS CONCENTRATIONS ON THE FATIGUE STRENGTH OF AISI 4140 STEEL USED IN OIL AND GAS COMPANY

Martin F. Fernandes[1]*, Verônica M. O. Velloso[1], Jefferson R. M. Santos[1], and Herman J. C. Voorwald[1]
[1]*Department of Mechanics, Sao Paulo State University, Guaratingueta, Brazil*

1. Introduction

The Oil and Gas companies use studs to join flanges or equipment connector in a marine environment, where fluctuations in the tensile stress occur in the studs due to the variation of the internal pressure in oil wells or due to the movement of sea waves. Cyclic loads of constant or variable amplitude may be responsible for the fracture mechanism known as fatigue of materials. An important characteristic of this mechanism is that fatigue failures occur at stresses below the yield strength of the material. Although fatigue occurs within the elastic regime, localized microscopic plastic deformations generate intrusions and extrusions, which act as microscopic scale stress concentrators.

The factors that may influence the fatigue life of the studs for petrochemical industries applications are the corrosive environment, anticorrosive coatings, and the stress concentrations in the screw threads. To prevent the material from corrosion, frequently the studs undergo an electrodeposition process with cadmium, which may reduce the fatigue life due to hydrogen embrittlement [1]. The existence of irregularities or discontinuities, such as the threads of the studs, increases the theoretical stresses near of this discontinuity, which decreases the fatigue life of the component [2, 3]. Since fatigue failures generally initiate at notches or discontinuities, the study of stress concentrations influence in the studs made of AISI 4140 steel is very significant to Oil and Gas industries.

2. Experimental

Table 1 shows the chemical composition of AISI 4140 steel used. The mechanical properties of the material are: (28-32) HRC, yield strength of 860 MPa, ultimate tensile of 978 MPa, and modulus of elasticity of 202 GPa. These properties were obtained by means of quenching (900°C for 3 hours, cooling in oil to 81°C) and double tempering (620°C for 3 hours, cooling in calm air). The thread was manufactured by rolling process. The specimens were tested in axial fatigue tests with fatigue ratio R=0.1 at frequency of 10 Hz and room temperature. Specimens without thread according to ASTM E466 (Fig. 1) and the studs were tested. Fig. 2 shows the device used to perform the axial fatigue tests in the studs, where the sleeves were fixed to the testing rig.

Table 1. *Chemical composition of AISI 4140 steel (wt. %)*

C	Mn	P	S	Si	Cr	Mo	V	B	Fe
0.38	0.75/1.00	<0.035	<0,04	0.15/0.35	0.8/1.10	0.15/0.25	<0.05	0.0005	Base

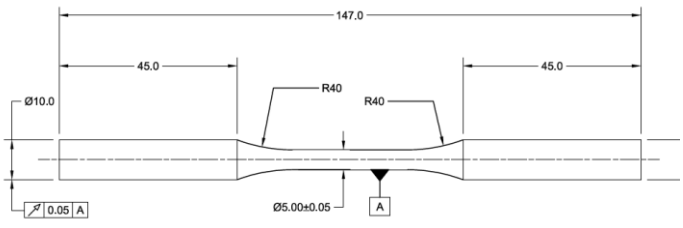

Fig. 1. *Specimen according to ASTM E466 (Dimensions in millimeters).*

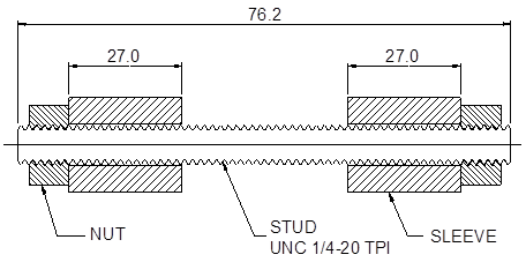

Fig. 2. *Testing Device (dimensions in millimeters, except thread).*

3. Results and Discussions

Fig. 3 shows the S-N curves for the specimens according to ASTM E466 standard and to the studs. The significant decrease in fatigue life of studs compared to the standard specimens is due to stress concentration that occurs near the threads, where the nucleation of the cracks occurs. For example, for a maximum stress of 700 MPa, while the specimens without threads would withstand 10^6 fatigue cycles, the studs would fracture after about 2×10^4 cycles.

Fig. 3 displays the stress concentrations effects for a larger number of cycles. The explanation for this behavior is that although the stress concentrations reduce significantly the number of cycles during the nucleation stage, they do not have a big influence on the number of cycles during the fatigue crack propagation. Therefore, at lower stress levels, when the fatigue life during the crack initiation stage is longer,

*Corresponding author: martin.ff@hotmail.com

the influence of the effect of stress concentrations in the threads is more significant than at higher stress levels, when the number of cycles for the crack to initiate is smaller.

Considering the applications of the AISI 4140 steel in the Oil and Gas industries, the studs are pre-loaded by torque application to withstand an internal pressure of up to about 155 MPa (22,500 psi) and avoid leakage on nuts. The pre-load provides tensile stresses of about 362 MPa that may reach up to 600 MPa in operation. At a stress level of 600 MPa, while for the specimens according to ASTM E466 the stress is lower than the fatigue limit, for the studs, the fatigue life would be about 6×10^4 cycles.

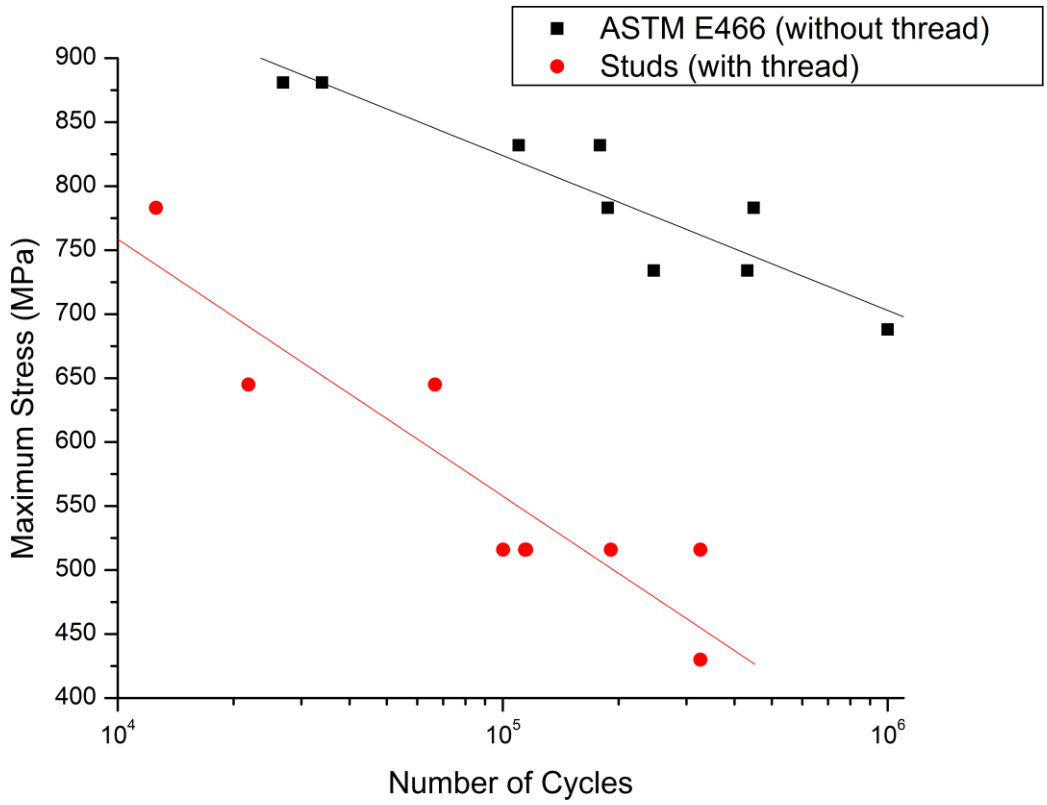

Fig. 3. *S-N curves for specimens according to ASTM E466 and studs*

The effect of the stress concentrations in the studs made of AISI 4140 steel is very important to Oil and Gas industries since the stresses in operation could overcome the fatigue limit of the studs depending on the variation of the internal pressure of the oil wells or due to other influences such as the movement of sea waves. Stress concentrations significantly reduced the fatigue life of the thread, an effect that is even more relevant for high cycle fatigue.

4. References

[1] H. J. C. Voorwald, I. M. Miguel, M. P. Peres, and M. O. H. J. Cioffi. Journal of Materials Engineering and Performance, 14, 249-257, (2005).
[2] C. P. Siqueira, C. P. M. Pereira, M. P. Nascimento, H. J. C. Voorwald, and R. C. Souza, SAE Technical Paper Series, 1, 177-182, (2001).
[3] V. Chaves, C. Madrigal, A. Navarro, Theoretical and Applied Fracture Mechanics, 87, 11-20, (2017).

Acknowledgments

The authors gratefully acknowledge all support from São Paulo State University (FEG/UNESP), and Onesubsea, Prec-Tech and CPF companies for the donated specimens.

*Corresponding author: martin.ff@hotmail.com

ID 95: CARBON FIBERS FUNCTIONALIZATION THROUGH N_2-H_2 PLASMA AS A PRETREATMENT FOR POLYANILINE POLYMERIZATION

Thayara Ceregatti[1]*, Carla Dalmolin[1], Luis Cesar Fontana[1], Daniela Becker[1]
[1]*Universidade do Estado de Santa Catarina, Centro de Ciências Tecnológicas, UDESC, Joinville-SC, Brazil*

1. Introduction

Carbon fibers (CFs) are used for reinforcements in polymer matrix composites. It exhibits high specific strength and stiffness, thermal stability, and corrosion resistance [1]. When combined with conductive polymers, they can be attractive materials for many applications, for example for supercapacitor. Polyaniline (Pani) is a representative conductive polymer for supercapacitance research because the entire volume of Pani can conduct the redox reaction and energy storage to obtain high capacitance [2]. Some researchers proposed a combination of carbon materials, such as porous carbon, carbon nanotubes (CNTs), carbon nanofibers (CNFs) and graphene, to improve the capacitance performance of Polyaniline (Pani)[3]. A large number of techniques have been reported to modify the surface of carbon fiber in order to improve its electrochemical characteristics and Pani deposition [1]. In the last years, non-thermal plasma has emerged as a method of surface modification, convenient for the incorporation of functional groups on the substrate surface. Recently, a successful method of Pani polymerization has been reported through the pretreatment of FCs by plasma [3]. The interaction between the active species generated in the plasma and the carbon surface indicates the type of functionalization. Active Screen Plasma System (ASPS) is a technology that may produce surfaces activation, with minimum damage due to ion bombardment [1]. By choosing the gas composition, functional groups can be selectively introduced onto the substrate surface. In recent years, the ASPS technique was used to functionalize with N_2, H_2 plasmas [4]. Since the plasma mechanism involves atomic processes a variety of species including free radicals or reactive sites may be present on the surface of the substrate, which in turn, in contact with the aniline monomer, can initiates polymerization thereof.

2. Experimental

The clean and dry carbon fibers mesh (PWB-3/Stackpole – USA) were cut into short segments (2 x 2 centimeters) and used as received. The plasma treatments were conducted inside of a plasma reactor, which consists of a stainless steel grounded base with a glass chamber on top. The cathodic mesh of the ASPS setup was made of stainless steel, with 74% open area. The samples were fixed on one of glass disk and were placed on an insulated work table, which was left at floating potential during the plasma treatment. The vacuum chamber was evacuated to a base pressure below 0,1 Torr, at which point a gas mixture consisting of 75% H_2 and 25% N_2 was fed into the chamber. The glow discharge was ignited between the mesh of the ASPS set-up, which acts as cathode, and the gas entry, which was also grounded, acts as anode. The gas pressure selected for the treatments was 0,22 Torr, the applied potential was 200 V, the current was varied between 0.5 and 0.3 A, and the treatment time ranged from 5 to 20 min. For comparison, it was treated samples in the glow discharge plasma at floating potential. After plasma treatment, the plasma treated samples were sent to contact angle analysis.

3. Results and Discussions

Contact angle measurements were obtained in an automated goniometer, using the sessile droplet method with deionized (DI) water. Figure 1 shows the water droplets on carbon fiber mesh treated under different conditions. The untreated carbon fiber exhibited a high contact angle with deionized water, which is characteristic of hydrophobic surfaces. After the ASPS plasma treatment (200V for 5 min, 10 min e 20 min), the contact angle decreased as shown in Table 1. Increased wettability was obtained in all cases, but the most significant changes were observed on those samples which were plasma treated for 20 minutes, indicating that a large number of radicals were generated on the surface of the fiber by breaking the C-C bonds, and to the introduction of several N and N-H groups in the surface, which turned the samples more hydrophilic.

Samples	Time of treatment (minutes)	Mean Contact angle
A	0	131,8º
B	5	98,9 º
C	10	93,3 º
d	20	75,4º

Table 1. *Summary of goniometer results obtained from carbon fibers*

*Corresponding author: thay.ceregatti@gmail.com

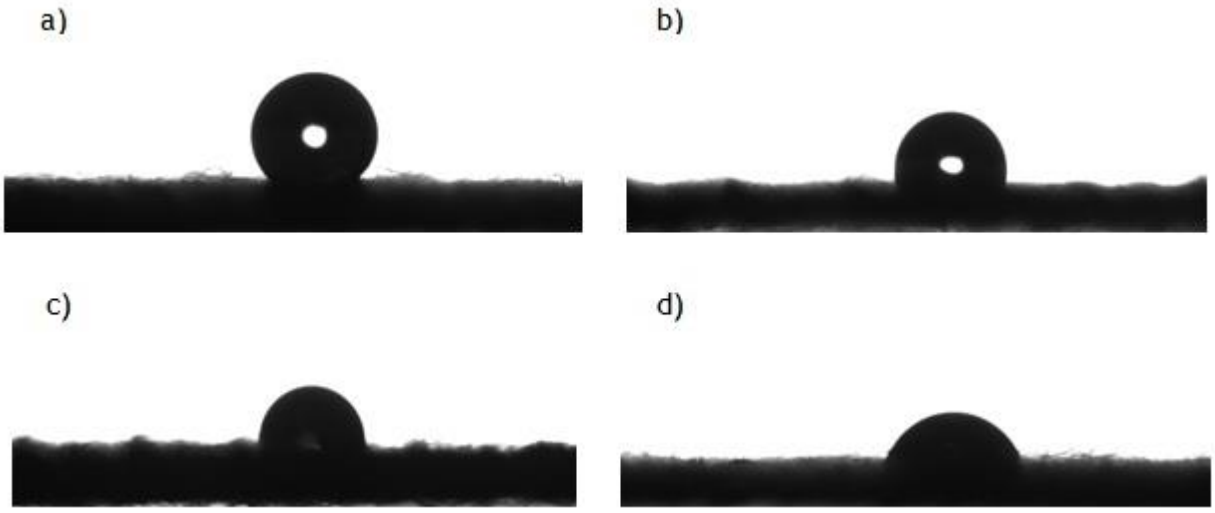

Fig. 1. *Droplets on carbon fiber without plasma treatment and after ASPS plasma treatments.*

Functionalization of carbon fibers with the active screen plasma technology is promising. The active screen plasma treatment also produced reduction in the contact angle of the carbon surfaces, indicating a possible presence of functional groups and increasing the hydrophilicity of the carbon fiber. Therefore, knowing the pre-existence of these groups, it is possible to expand the studies for the polymerization of polyaniline using plasma-treated carbon fiber.

4. References

[1] CORUJEIRA, S.; CHARITIDISHANSHAN, G. Surface functionalization of carbon fibers with active screen plasma. **Vacuum, Surfaces, and Films**, v. 35, p. 021404, 2017.
[2] KOTAL, M.; THAKUR, A. K.; BHOWMICK, A. K. Polyaniline-carbon nanofiber composite by a chemical grafting approach and its supercapacitor application. **ACS Applied Materials and Interfaces**, v. 5, n. 17, p. 8374–8386, 2013.
[3] CHANG, W. M.; WANG, C. C.; CHEN, C. Y. Plasma-Induced Polyaniline Grafted on Carbon Nanotube-embedded Carbon Nanofibers for High-Performance Supercapacitors. **Electrochimica Acta**, v. 212, p. 130–140, 2016a.
[4] X. Fu, M. J. Jenkins, G. Sun, I. Bertoti, and H. Dong, Surf. Coat. Technol. v 206, p 4799, 2012.

Acknowledgments

Authors would like to thank LaPE-UFSCar for CF supply, and FAPESC, CAPES and CNPq for scholarships and grants that made this work possible. T. Ceregatti is grateful to UDESC/PROAP for her scholarship.

*Corresponding author: thay.ceregatti@gmail.com

ID 96: DESIGN, MODELING AND CONSTRUCTION OF VACUUM OVEN WITH CONTROLLED TEMPERATURE

André G. Lima Caetano*, Viviane M. de Lima, Luciana Reyes Pires Kassab, Francisco Tadeu Degasperi
Faculty of Technology of Sao Paulo - FATEC-SP - CEETEPS - São Paulo - SP - Brazil

1. Introduction

This scientific work aims at the construction of a vacuum oven with controlled temperature for the treatment of thin carbon films. We present the project, modeling and development of the thermal control system. The process of propagation of heat in controlled vacuum environment will be obtained by applying current to the resistance of the oven. Through this oven it will be possible to reach temperatures of ~ 1273 K in a small time intervals. It will be used mainly for the treatment of carbon films, produced by the sputtering technique [1], in order to provide adequate crystallinity that guarantees the production of graphite and/or graphene.

2. Theory

The mechanical assembly of the oven consists of stainless steel 304L machined parts, standard DIN 912 bolts, dimensioned ceramic tubes and a tungsten helical resistor. The assembly can be seen in ***figure 1***.

The oven itself is also composed of other components such as: temperature control components and vacuum chamber, with the heat exchanges inherent to the vacuum oven.

Through electromagnetic waves released by the resistance, the heating of the sample door part occurs, since these waves propagate in the perfect vacuum (radiation). The phenomenon of radiation in the system is described by the next mathematical model[2].

$$\rho_{inox}.V_{even}c_{inox}.\frac{dT_C(t)}{dt} = P_{elé} - \sigma.\varepsilon.A_s^i\left\{T_C(t)^4 - T_{amb}^4\right\}$$

3. Results and Discussions

Electrical circuit tests proved to be effective, with heating occurring. From the results obtained is possible to corroborate the physico-mathematical model and perform the first temperature measurements at time $T = T_C(t)$.

The results indicate that the system is capable of operating. It is necessary to test the model obtained in the vacuum chamber under the working conditions for the treatment of thin films of carbon.

The high vacuum system shown in ***figure 2*** is operational and reaching the pressure of 10^{-5} mbar [3].

Heating tests performed. Applying power of 7 W it was found that the heating was commensurate with the model, getting 463K in 15 minutes. The model proposes the application of 35 W to obtain 1273 K in 2 min. For the final test, a thermal insulation is being constructed to avoid damage to the turbo drag vacuum pump with high radiated power.

Fig. 1. *Vacuum electric oven mechanical assembly.*

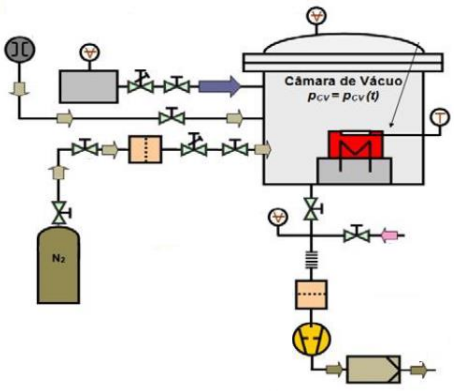

Fig. 2. *Vacuum set-up diagram.*

4. References

[1] Silva, Danilo L. Costa; Filmes finos depositados por técnica de Magnetron Sputtering usando Co, Cu e Ni como Buffer-Layers. 2015. Dissertação de Mestrado acadêmico–IPEN - (USP), São Paulo- SP, 2015.

[2]Inclopera, Frank P.; Dewitt, David P.: Fundamentos de Transferência de Calor e Massa, 4ª Edição, p. 320-321, 1998, LTC Editora.

[3] Degasperi, F.T., Modelagem e Análise Detalhadas de Sistemas de Vácuo. Dissertação de Mestrado. Universidade Estadual de Campinas – UNICAMP, Campinas - SP. 2002.

Acknowledgments

To *CNPq* for the concession of the two scholarship *PIBIC* - A. G. L. Caetano and V. M. de Lima.

andre_gustav@hotmail.com, andre.lima@mar.mil.br

ID 101: INFLUENCE OF THE SILICON INTERLAYER DEPOSITION PROCESS IN THE ADHESION OF THE DLC COATINGS DEPOSITED ON NITRIDED MARTESNITIC STAINLESS STEEL

Eugenia L. Dalibon[1]*, Dubrazkha C. Lugo[2], Marco A. Ramírez[2], Vladimir J. Trava-Airoldi[2], and Sonia P. Brühl[1]

[1]*Universidad Tecnológica Nacional, Facultad Regional Concepción del Uruguay, Argentina.*
[2]*Instituto Nacional de Pesquisas Espaciáis, Brasil.*

1. Introduction

The DLC coatings are characterized by good wear resistance, low friction coefficient and chemical inertness [1]. However, they have adhesion problems when they are deposited on metallic substrates. For this reason, a thin interlayer of different materials, such as silicon, is deposited previous to the coating in order to improve the adhesion. There are a few studies about the influence of the conditions of the silicon interlayer deposition on adhesion or properties of the coatings [2,3]. In this work, the adhesion of DLC coatings deposited on nitrided and non-nitrided martensitic stainless steel, modifying the silicon interlayer bias potential deposition, is studied.

2. Experimental

AISI 420 martensitic stainless steel was used as base material. The samples were nitrided in a DC pulsed discharge for 10 h at a temperature of 390°C using a gas mixture composed of 20% N_2 and 80% H_2. The DLC (Diamond Like Carbon) coatings were deposited by means of a modified PACVD (Plasma Assisted Chemical Vapor Deposition) process at INPE (Brazil) [4], using acetylene as precursor gas at 150 °C for 50 minutes. The total gas pressure was 6.10^{-4} Torr. Prior to the coating deposition, an amorphous silicon layer was deposited using silane gas for 10 minutes and different bias voltages: –5 kV, –8 kV and –10 kV. The coatings and interlayers were deposited on nitrided and non-nitrided stainless steel (named Duplex and Coated samples, respectively). The DLC coatings were characterized by means of EDS and Raman spectroscopy. The microstructure was analyzed by OM, SEM-FIB, and XRD. Adhesion was evaluated by means Scratch test using 10 N, 15 N and 20 N loads and Indentation Rockwell C.

3. Results and Discussion

The Raman spectra for DLC films presented two overlapping bands known as the D and G bands. The positions and intensity ratio of the D and G bands (I_D/I_G), FWHM G band for different samples are shown in table 1. Taking I_D/I_G ratio and the G band position into account, the percentage C–C sp^3 bonds should be about 20% according to the three stage model proposed by Ferrari [5]. The hydrogen content was about 20%, which was calculated from the slope of the fitted line to the base of the original Raman spectrum. It can be indicated that the growth voltage variations of the silicon interlayer did not affect the D and G bands position, FWHM or I_D/I_G ratio (Table 1).

Table 1. Summary of Raman results for different samples

Samples	Bias Voltage (-kV)	D Band (cm^{-1})	G Band (cm^{-1})	FWHM (G) (cm^{-1})	I_D/I_G
Coated	5	1388.70	1545.38	171.50	0.69
	8	1387.66	1541.20	176.26	0.66
	10	1385.96	1550.36	169.67	0.74
Duplex	5	1382.59	1548.17	174.92	0.69
	8	1389.34	1547.49	176.88	0.65
	10	1392.00	1551.76	166.84	0.75

The DLC coatings thickness was of about 1 µm with a well-defined interphase with the substrate. The nitrided layer thickness of 10 µm. The expanded martensite peaks, i.e. nitrogen expanded martensite, were detected by XRD in the duplex sample because the film is amorphous, transparent to x-ray radiation.
With respect to the adhesion, the duplex sample had better adhesion than the only coated sample as it could be observed in SEM image indentation Rockwell C (Figure 1, 2, 3 and 4).

*dalibone@frcu.utn.edu.ar

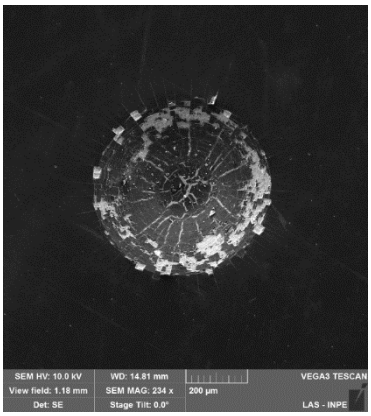

Fig. 1. SEM image of Indentation Rockwell C in duplex sample for -10 kV bias potential silicon interlayer.

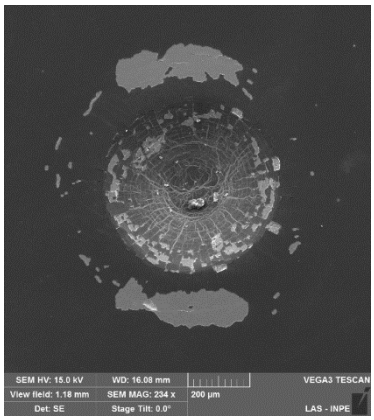

Fig. 2. SEM image of Indentation Rockwell C in coated sample for -10 kV bias potential silicon interlayer.

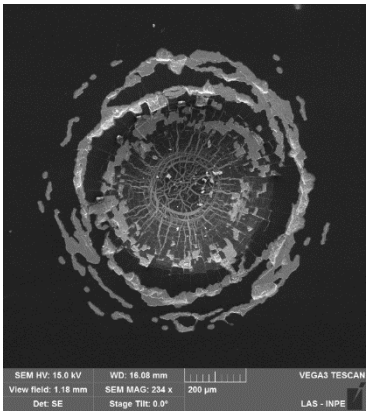

Fig. 3. SEM image of Indentation Rockwell C in coated sample for -5 kV bias potential silicon interlayer.

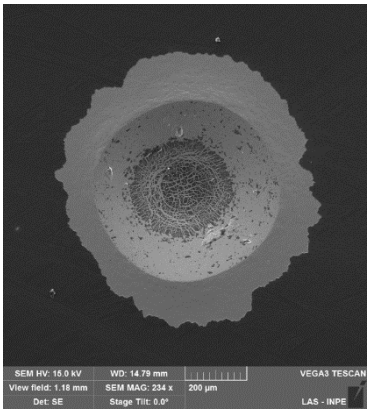

Fig. 4. SEM image of Indentation Rockwell C in coated sample for -5 kV bias potential silicon interlayer.

The same results were obtained in the Scratch Test where the coating detached with 10 N load in the coated sample. However, the coating is broken with 20 N load in the duplex sample. The improved adhesion for the duplex sample is attributed not only to the gradual transition interface between the coating and the substrate provided by the nitrided layer, but also to the affinity chemical between silicon of the interlayer and the nitrogen of the nitrided layer which can produces a chemical bonding Si-N as it was reported by some of the authors [6].

Moreover, the adhesion improved when the interlayer was deposited with higher bias voltage. The best adhesion was reached when the interlayer was deposited using −10 kV as it can be seen in Figure 1. With the bias voltage increase during silicon interlayer deposition, the ion bombardment energy increases and the adhesion improves as it was reported by some of the authors [4].

4. References

[1] J. Robertson, Mater. Sci. Eng. R Reports, **37**, 129–281, (2002).
[2] F. Cemin, L.T. Bim, C.M. Menezes, M.E.H. Maia, I.J.R. Baumvol, F. A. Figueroa, Surf. & Coat. Tech., **283**, 115–121, (2015).
[3] L.F. Bonetti, G. Capote, L. V Santos, E.J. Corat, V. J. Trava Airoldi, Thin Solid Films, **515**, 375–379 (2006).
[4] P. C. Santana Da Silva, M. Antonio Ramirez Ramos, E. J. Corat, V.J. Trava-Airoldi, Mat. Res., **19**, 882–888, (2016).
[5] C. Casiraghi, A.C. Ferrari, J. Robertson, Phys. Rev. B. **72**, 1–13, (2005).
[6] E.L. Dalibon, S.P. Brühl, V.J. Trava-airoldi, L. Escalada, S.N. Simison, J. Mater. Res., **31**, 3549–3556, (2016).

Acknowledgments

The authors are very grateful to UTN for financial support and to students from GIS–FRCU for their collaboration with the preparation of the samples.

*dalibone@frcu.utn.edu.ar

ID 102: POROSITY AND MORPHOLOGY OF HVOF SPRAYED WC-12CO-4CR COATINGS USING DIGITAL IMAGE PROCESSING

Celso Diniz[1], André Fernandes Martins[1], Rogério Pinto Mota[1], Emerson Ferreira de Lucena[2] and Elson de Campos[1,2]*
[1]UNESP – Faculdade de Engenharia – Campus de Guaratinguetá – SP
[2]EEAR – Escola de Especialistas de Aeronáutica – Guaratinguetá – SP

1. Introduction

The high-velocity oxygen-fuel (HVOF) process efficiently uses high kinetic energy and controlled thermal output to produce low porosity coatings that are homogeneous in structure. The coatings can operate under harsh service conditions, because they are characterized by higher durability and higher wear and corrosion resistance [1]. In this work, the ImageJ Macro language (IJM) was used to performed spray coating porosity values by digital image processing [2].

2. Experimental

Martensitic stainless steel (ASTM A743 CA-6NM) samples were machined, blasted, preheated and WC-12Co-4Cr coated (0.1 mm – sample S1 and 0.2 mm – S2 and S3) using by HVOF technique. The samples were sectioned using diamond cutting disc with 3 mm/s and 4000 rpm rotation. A solution made of OPU, diluted with water in ratio 1:2, was used as final polishing. Images were obtained by using light microscope NIKON EPIPHOT Model 200, coupled to a digital camera Spot Insight QE. The pore segmentation was performed by histogram analysis according to steps shown in figures 1-4 and applied to S1, S2 and S3 samples. The porous segmentation was performed by histogram analysis. The total sampled field of view was determined by statistical stability of porous fraction value average.

3. Results and Discussions

Table 1 shows the digital image processing results. According to standard deviation values, the sprayed layers analyzed (0.1 or 0.2 mm) not showed statistically significant differences on porosity values. The usual samples porous morphology was showed in Figure 4.

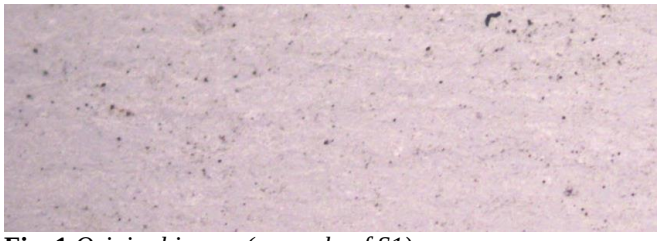

Fig. 1 *Original image (example of S1)*

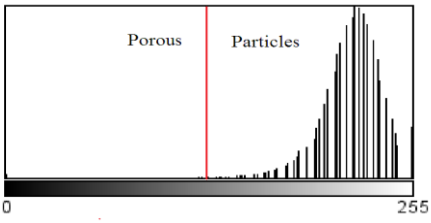

Fig. 3 *brightness distribution*

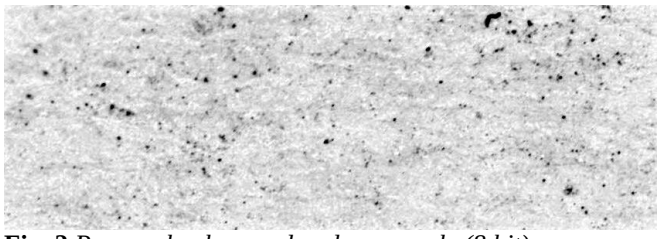

Fig. 2 *Remove background and gray scale (8 bit)*

Fig. 4 *Image after threshold*

Tab. 1 *results after digital image processing*

Sample	Porosity (%)	Porous number (average)	Circularity	Feret's diameter (μm)
S1	1.06 ± 0.83	619 ± 368	0.80 ± 0.05	0.59 ± 0.15
S2	1.92 ± 0.64	520 ± 116	0.77 ± 0.06	1.41 ± 0.83
S3	1.91 ± 0.53	677 ± 270	0.78 ± 0.06	1.64 ± 0.33

4. References

[1] Ozimina D, Madej M, Kałdoński T, Tribology Letters. **41**, Issue 1, pp 103-111, (2011).
[2] Schneider, CA; Rasband, WS & Eliceiri, KW, Nature methods **9(7)**, pp 671-675, (2012).

*elson@feg.unesp.br

ID 103: THEORETICAL STUDIES OF THE REACTIONS OF H_2 + CN: COMPETITION BETWEEN H-ABSTRACTION IN H + HCN/HNC CHANNELS.

Alessandra F. Albernaz[1], Patrícia R. P. Barreto[2]
[1]Instituto de Física, Universidade Brasília, CP04455, Brasília, DF, CEP 70919-970
[2]Laboratório Associado de Plasma, Instituto Nacional de Pesquisas Espaciais, CP515, São José dos Campos, SP, CEP 12247-970

1. Introduction

Reactions involving [H,C,N] systems are of wide interest in several chemical processes that occur in flames, comets, lasers and planetary atmospheres. Hydrogen cyanide (HCN) and its isomer, hydrogen isocyanide (HNC), have been detected in such diverse molecular astrophysical environments as diffuse interstellar clouds, prestellar disks, outflowing circumstellar envelopes, Titan's atmosphere and planetary nebulae. There are studies that show the importance of the nitriles/isonitriles compounds in prebiotic chemistry as possible precursors of molecules of biological interest. There is a variety of theoretical studies on the mechanisms of reactions that lead to the formation of the HCN/HNC radicals. In most of these studies, the HNC formation mechanism occur via $HCNH^+ + e$, $H_2CN^+ + e^-$,$H_2C + N$, $H_2N + C$, $CH + NH$ and $H + HCN$[1].

Thus a complete understanding of the HNC/HCN abundance ratio requires, in addition to some explanation for the low temperature enhanced abundance of the metastable HNC, a further explanation for the disappearance of this species with increasing temperature. Like, at present moment, there is no record of the location of any transition structure for hydrogen abstraction converting H_2 + CN to H + HNC; in this work, we propose investigate the production of HCN/HNC via neutral H_2 + CN reaction, with a linear configurations, leading to the formation of the H + HCN

$$H_2 + CN \rightarrow H + HCN \qquad \Delta H_f = -21.58\ kcal/mol$$

and H + HNC

$$H_2 + CN \rightarrow H + HNC \qquad \Delta H_f = -6.68\ kcal/mol$$

channels.

2. Theory Methods

The G3 Method were employed in our work to determine the potential energy surface (PES), geometries, vibrational frequencies and energies of the reactants, transition states and products of the H_2+CN reactive process. Vibrational frequencies were used to characterize the stationary points as minimum or transition states, the number of imaginary frequencies (0 or 1) indicate whether a minimum or a transition state has been located. To confirm that the transition state really connects reactants and products, the intrinsic reaction coordinate (IRC) calculations were performed. All calculations were performed with Gaussian 09 program. The rate constants for the present simple reactions have been calculated by conventional transition state theory (TST) and canonical variational transition state theory (CVT) with the APUAMA program [2]. The quantum effect corrections for the CVT rate constants have been made by zero-curvature tunneling (ZCT) and small-curvature tunneling (SCT) calculations. The results of these calculations will be compared later with experimental data and theoretical results.

3. Results and Discussions

For the H_2 + CN reaction system, the two product channels, as alluded to in the introduction, have been considered: H-atom abstraction processes by the carbon of the CN molecule $H_2 + CN \rightarrow H + HCN$ and H-atom abstraction processes by the nitrogen of the CN molecule $H_2 + CN \rightarrow H + HNC$. The optimized geometries of the reactants, transition states, products and relative energies, ΔE, (in parentheses) are calculated using G3 method can be seen in Fig. 1.

The schematic potential energy surfaces for the reaction between H_2 and CN are plotted in Fig. 1 with the following products: H + HCN and H + HNC. Note that energy of reactants is set to be zero as reference. To H + HCN channel, we found a barrier among the transition state TS_1 of the 3.40 kcal mol^{-1} that is close to the value found by Horst et al. of the 3.2 kcal mol^{-1} [3]. To H + HNC channel, the barrier height of the transition state TS_2 is 13.37 kcal mol^{-1}. At present moment, there is no record of the location of any transition structure for hydrogen abstraction converting H_2 + CN to H + HNC. The product energy goes from –22.83 kcal mol^{-1}, for H + HCN channel to –8.18 kcal mol^{-1} for H + HNC channel. The rate constants, calculated as conventional, Wigner correction tunneling and CVT to $H_2 + CN \rightarrow H + HCN$ and $H_2 + CN \rightarrow$ H + HNC reactions, are presented in Fig. 2 and 3, respectively. The branching ratios as a function of

* alessandra@fis.unb.br

temperature for channel 1 and 2 are displayed in Fig. 4. These results show that H+HCN product is the most important in range of temperature of 300–1700 K, with a probability of 100% of the total reaction, at 300 K. While, the H+HNC product is more favorable to high temperatures (T > 1700 K), with a probability of 100% of the total reaction, at 3000 K.

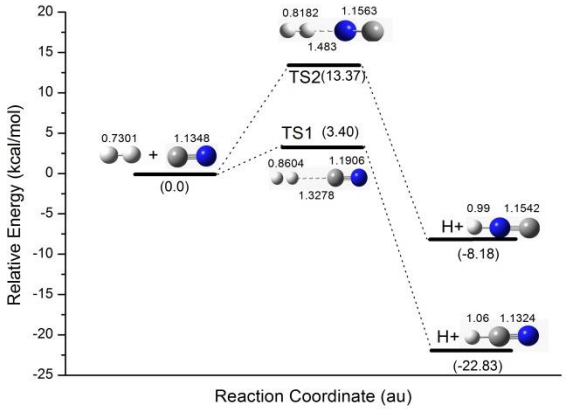

Fig. 1: *The profile of the doublet Potential Energy Surface of the H_2+CN→ H+HCN/HNC reactions with optimized geometries calculated at G3 Method, with ZPE correction.*

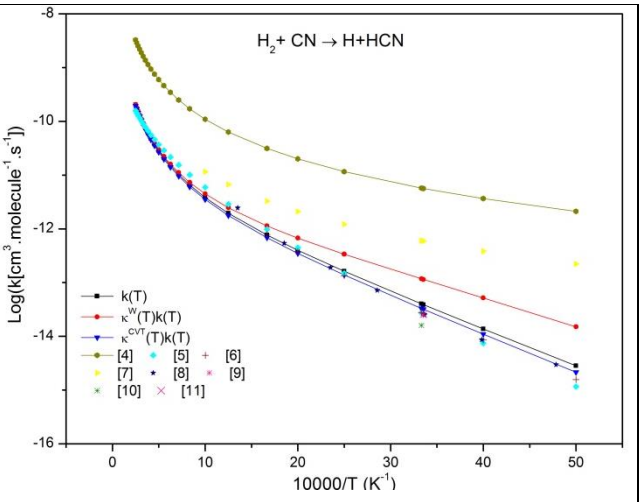

Fig. 2: *Comparison of the present thermal rate constants for the H_2+CN→ H+HCN reaction as a function of temperature (solid lines with symbols) are reported together with the corresponding values of references (symbols only).*

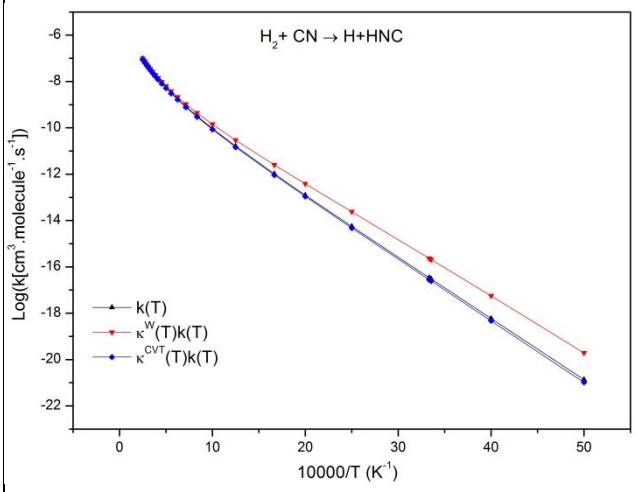

Fig. 3: T*hermal rate constants for the H_2+CN→ H+HNC reaction as a function of temperature.*

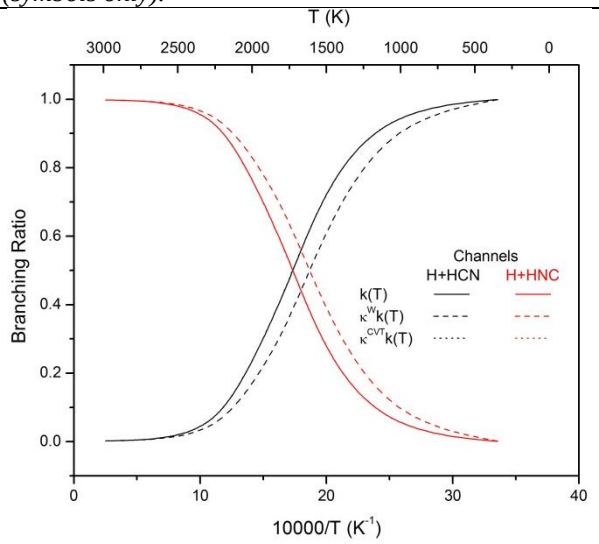

Fig. 4: *The branching ratios of the H_2+CN→ H+HCN and H_2+CN→ H+HNC reactions, at temperature range of 300-3000 K*

4. References

[1] Correa, E., da Silva, W.B., Barreto, P.R.P., Albernaz, A. F., J. Mol. Model. (2017) 23: 169.
[2] H. O. Euclides, P. R. P. Barreto, J. Mol. Model. (2017) 23: 176.
[3] M. A. ter Horst, G. C. Schatz, and L. B. Harding. J. Chem. Phys., (1996) 105:558.
[4] A. F. Wagner and R. A. Bair. Int. Chem. Kinet., (1986) 18:473.
[5] W. Tsang. J. Phys. Chem. Ref. Data, (1992) 21:753.
[6] I. R. Sims and I. W. M. Smith. Chem. Phys. Lett., (1988) 149:565.
[7] B. Atakan, A. Jacobs, M. Wahl, R. Weller, and J. Wolfrum. Chem. Phys. Lett., (1989)154:449.
[8] Q. Sun and J. M. Bowman. J. Chem. Phys., (1990) 92:5201.
[9] J. de Juan, I. W. M. Smith, and B. Veyrets. J. Phys. Chem., (1987) 91: 69.
[10] X. Li, N. Sayah, and W. M. Jacson. J. Chem. Phys., (1984) 81: 833.
[11] R. J. Balla and L. Pasternack. J. Phys. Chem., (1987) 91:73.

* alessandra@fis.unb.br

ID 103_1: THEORETICAL STUDY OF THE KINETICS AND MECHANISM OF THE $CH_3CH_2OH + H_2O$ REACTION

Alessandra F. Albernaz[1], Patricia R. P. Barreto[2]
[1]Instituto de Física, Universidade Brasília, CP04455, Brasília, DF, CEP 70919-970
[2]Laboratório Associado de Plasma, Instituto Nacional de Pesquisas Espaciais, CP515, São José dos Campos, SP, CEP 12247-970,

1. Introduction

Ethanol has been used as fuel additives to reduce automobile emissions of hydrocarbons. It is currently one of the most important renewable energy sources and an important green fuel. In Brazil, it has been used as a substitute for gasoline for decades. Flex fuel vehicles have been developed that operate on varying composition mixtures of ethanol and gasoline. Nevertheless, flex fuel vehicles in Brazil mean something very different from those being developed in much of the rest of the world. In Brazil, flex fuel vehicles are designed to operate using fuels that range from gasohol (in Brazil 20–25% anhydrous ethanol in gasoline) to hydrous ethanol approximately 95.5% ethanol with the rest being water), and any mixture of these fuels.[1]

The research on ethanol is relevant because molecular systems bound by hydrogen bonds are widely studied in many areas such as physics, chemistry and biochemistry. For example, they are the basis to explain, at a molecular level, the formation of molecular clusters such as those formed by the ethanol–water azeotrope (96% of ethanol and 4% of water). This azeotrope has received a lot of attention due to the use of anhydrous ethanol as additive in gasoline, which requires a high degree of separation of the ethanol-water mixture. Acetaldehyde and ethanol increase in vehicle emissions and nitrogen oxides (NO_x) may increase when ethanol fuels are used. Both CH_3CHO and NO_x are very important contributors to photochemical air pollution and ozone (O_3) formation.

In this paper, we study alternative mechanisms of the $CH_3CH_2OH + H_2O$ reaction to explain the origin of high reactivity and the formation of radicals and/or molecules with significant impacts on atmospheric pollution and, consequently, on the destruction of the ozone shell. The potential energy surface of the reaction of $CH_3CH_2OH + H_2O$ was study through of the eight possible.

2. Computational Methods

An extensive quantum chemical study of the potential energy surface for the different pathways of the reactions of $CH_3CH_2OH + H_2O$ has been studied. We investigated eight possible pathways, with a detailed mapping of the PES of the system; used CBS-QB3 Method to all species (reactants, transition states and products) involved in the $CH_3CH_2OH + H_2O$ reaction, and are show in the Figure 1. Vibrational frequencies calculated at CBS–QB3 level were used for characterization of stationary points as minimum and saddle points. The equilibrium structures possess all real frequencies, whereas transition states possess one and only one imaginary frequency indicates whether a transition state has been located. To confirm that the transition state really connects with designated intermediates along the reaction path, the intrinsic reaction coordinate (IRC) calculations were performed. All quantum chemistry calculations were conducted using Gaussian 09 program. The rate constants for the present simple mathematical reactions have been calculated by conventional transition state theory (TST) and canonical variational transition state theory (CVT) with the APUAMA program [2]. The quantum effect corrections for the CVT rate constants have been made by zero-curvature tunneling (ZCT) and small-curvature tunneling (SCT) calculations and the results are compared with reference data, when available.

3. Results and Discussions

The all geometrical parameters, as well as, frequencies, were obtained at the B3LYP/6-311G(2d,d,p) level, internal of CBS-QB3 method. The transition state found for the channel 1 (TS_1) was obtained from the abstraction of hydrogen from CH_3 group and the abstraction of OH from CH_2 group in the CH_3CH_2OH molecule. For the channel 2, the breaking of CH bound in the CH_2 group to form $CH_3CHO + H_2O + H_2$. formed the transition state. While for channel 3 (TS_3), the transition state was formed by abstraction of hydrogen from CH_2 group and break CC bond in the CH_3CH_2OH to form $CH_4 + H_2OH_2CO$. The configuration of the TS_4, of the channel 4, is similar to configuration of the TS_1 however; we have the formation of the two H_2O molecules and CH_3CH instead of C_2H_4. As to transition state of the channel 5 (TS_5), occur by breaking the HC bond (in CH_2 group) by water as products, we have $CH_4 + HCOH\ldots OH_2$. In channel 6, there was the breaking of the CC bound, forming the CH_4 and the forming of CO bound forming $CH_2(OH)_2$. Channel 7 was formed the abstraction of oxygen by the H_2O, forming H_2O_2 and C_2H_6. Finally,

* alessandra@fis.unb.br

the channel 8, the transition state was formed by abstractions of hydrogen-atoms from OH groups in the CH_3CH_2OH and H_2O to form $CH_3CH_2OOH + H_2$ (TS_8).

We calculated the zero-point energy corrections, inertial moment, and vibrational frequencies of all geometries of the reactants, transition states and products at B3LYP/6-311G(2d,d,p). The relative energies (RE) of species involved in the eight channels of the reaction are calculated at the CBS–QB3 with zero-point energy correction are visualized in Fig. 1. The schematic potential energy surfaces for the reaction between CH_3CH_2OH and H_2O are plotted in Fig. 1 with the following products: $C_2H_4 + (H_2O)_2$, $CH_3CHO + H_2O + H_2$, $CH_4 + H_2OH_2CO$, $CH_3CH + (H_2O)_2$, $CH_4 + HCOH\ldots OH_2$, $CH_4 + CH_2(OH)_2$, $C_2H_6 + H_2O_2$, $CH_3CH_2OOH + H_2$. Note that energy of reactants is set to be zero as reference. The barrier among all transition state are $TS_1 < TS_2 < TS_3 < TS_4 < TS_5 < TS_6 < TS_7 < TS_8$. The lower barrier is 53.9 kcal $mol^{-1}$and the higher is 121.9 kcal mol^{-1}. The product energy goes from 1.5 kcal mol^{-1}, for channel 6 to 74.0 kcal mol^{-1} for channel 4. The rate constant, calculated as CVT, are presented in Fig. 4. In the low temperature region the rate constant are according the barrier, $k_1 > k_2 > k_3 > k_4 > k_5 > k_6 > k_7 > k_8$. However, in the higher temperature region there are an inversion for k_4 and k_7. For temperature of 1000 K $k_4 > k_3$, for T=1800 K, $k_4 > k_2$ and for T=3200 K, $k_4 > k_1$. In the case of channel 7, this inversion occurs for temperature of 2600, 3100 and 4000 K, for k_6, k_5 and k_3, respectively.

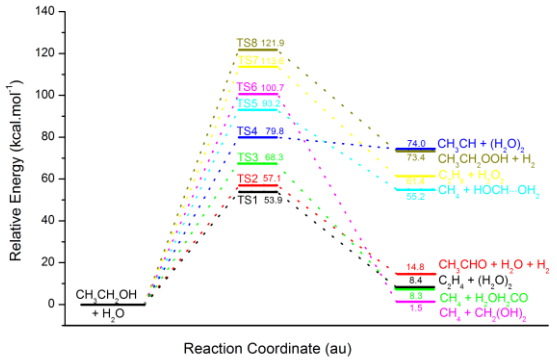

Fig. 1: *Representation of the Potential Energy Surface of the $CH_3CH_2OH+H_2O$ reactions using CBS–QB3 level, with ZPE correction.*

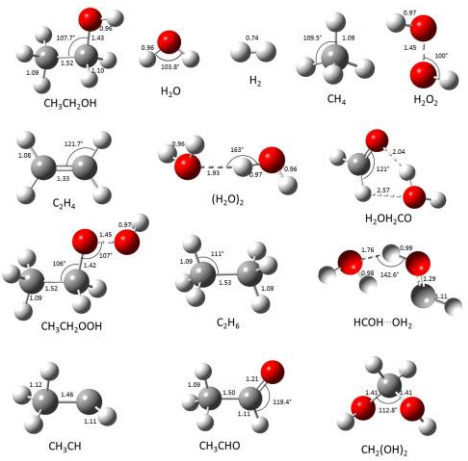

Fig. 2: *Optimized geometries of the reactants and products computed at the B3LYP/6-311G(2d,d,p) level. The units for the bonds lengths and bonds angles are Å and degrees, respectively.*

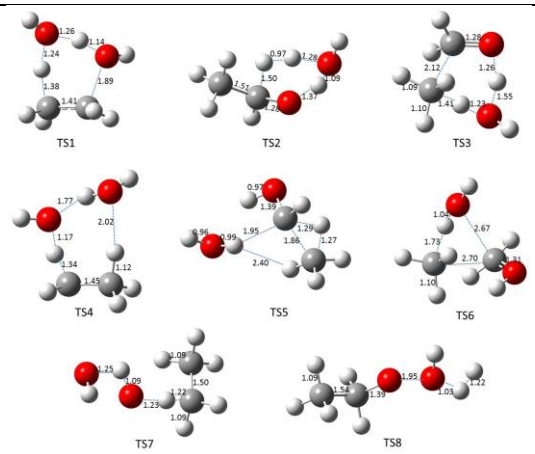

Fig. 3: *Optimized geometries of the transition states computed at the B3LYP/6-311G(2d,d,p) level. The units for the bonds lengths and bonds angles are Å and degrees, respectively.*

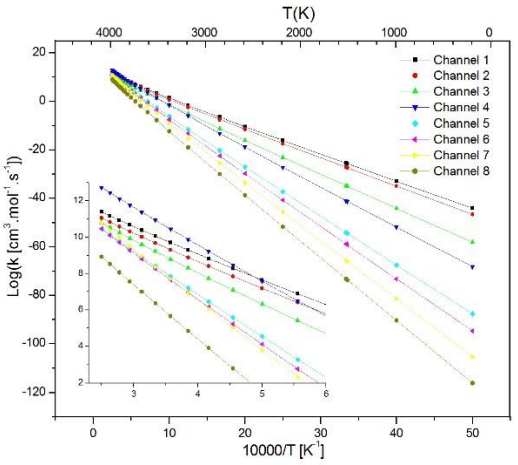

Fig. 4: *Potential energy diagram for the $CH_3CH_2OH+H_2O$ reaction at the CBS–QB3 level with ZPE corrections.*

4. References

[1] L. G. Anderson, Energy Environ. Sci. 2009, 2, 1015
[2] H. O. Euclides, P. R. P. Barreto, J. Mol. Model. (2017) 23: 176.

* alessandra@fis.unb.br

ID 104: POTENTIAL ENERGY SURFACES FOR INTERACTIONS OF H_2...HX AND H_2...X_2 SYSTEMS, USING A (HYPER)SPHERICAL HARMONICS REPRESENTATION

Cruz, A. C. P. S.* and Barreto, P. R. P.
[1]*Instituto Nacional de Pesquisas Espaciais – INPE/MCT, Laboratório Associado de Plasma – LAP, São José dos Campos, SP, CEP 12247-970, CP515, Brazil*

1. Introduction

The characterization of the intermolecular potential energy surfaces (PES's) of pairs of simple molecular systems and their compact representation through suitable analytic functions is an essential requirement for applications of classical, semiclassical, and quantum-mechanical approaches to molecular spectroscopy and dynamics. We report (i) the results of quantum-chemical *ab initio* calculations on a series of interactions between diatomic molecules, specifically, H_2…X_2 and H_2…HX, where X = H, F, Cl, Br; (ii) their use to assemble full dimensional intermolecular PES's in the framework of a spherical-harmonics expansion, and (iii) the optimized global minimum configuration.

2. Theory

The construction of the global intermolecular potential energy surface based on *ab initio* calculations of potential energy profiles for a series of leading configurations for H_2…X_2 and H_2…HX systems, with X = H, F, Cl and Br atoms, are defined by a spherical-harmonics expansion of the neutral-neutral molecular interaction [1, 2]. These *ab initio* calculations were performed at CCSD(T)/aug-cc-pVQZ level with counterpoise-corrected interaction energies, using the MOLPRO code [3]. The functional form depends on a radial coordinate *R* between centers-of-mass of the two molecules and the polar and dihedral angles (θ_1, θ_2, ϕ) and the moments of the spherical-harmonics expansion are determined by choosing a certain number of representative configurations (leading configurations) based on geometrical and symmetry considerations, which allow the solution of a system of linear equations. Figure 1 define the coordinate system used in this case, see reference 1 and 2 (and reference cited in this papers) for more details about the leading configurations and potential development. Then, we adjust the points found with Pirani potential function [4, 5] and, also, the generalized Rydberg function [6], which allows us to explore important parameters contained in the molecular interaction, generating efficient and simplified models for both the isotropic term and the additional anisotropic terms derived from electrostatic contributions or charge-transfer. The PES was minimized in order to find the global minimum representing the least energy point. After that, we select the most stable principal configuration and calculate the energy considering floppy diatoms where the length of their chemical bonds could vary and we compare the results obtained.

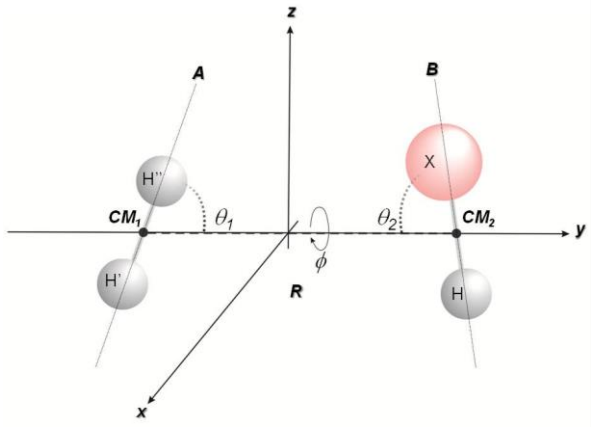

Fig.1: *The mutual position of the H_2 and X_2 or HX molecules is expressed by four coordinates in the Cartesian coordinate framework x,y,z. The radial coordinate **R** is defined as the distance between the center of mass of H_2, CM_1, and the center of mass of X_2 or HX, CM_2, θ_1 and θ_2 are the angles between the HH bound and y axes and XX or XH bound and y axes, respectively, and they vary between 0 and π, φ is the dihedral angle, and its value varies between 0 and π.*

3. Results and Discussions

Accurate results for this system have a high computational cost. Here, we show that the calculation of a small number of selected geometry allows the precise construction of the PES. We can verify that the rotor-rigid methodology can be considered in these cases of non-reactive systems with van der Waals type bonds, since the presented results differ minimally from one another. Nevertheless, it must be rethought when the system has a reactive character, since it presents values with considerable differences.

Table 1 compared the global minimum of the PES with the minimization calculation. It can be seen that the center of mass distance of H_2…X_2 systems decreases by 99.63%, while for the H_2…HX systems this

*anaclaudia.ps.cruz@gmail.com

distance increases by 82.43%, on average. The energy increases by 99.72 and 99.31% for the $H_2…X_2$ and $H_2…HX$ systems, respectively.

Table 1: *Minimum distance and energy among the $H_2…X_2$ and $H_2…HX$ systems when compared the PES and the minimized calculation*

System	T_b for $H_2…X_2$ and T_c for $H_2…HX$		Minimized	
$H_2…H_2$	3.380	-35.258	3.366	-35.526
$H_2…F_2$	3.497	-99.587	3.484	-99.615
$H_2…Cl_2$	4.019	-191.877	4.004	-191.801
$H_2…Br_2$	4.229	-226.098	4.215	-226.975
$H_2…HF$	2.477	-359.349	3.576	-361.299
$H_2…HCl$	2.983	-201.380	3.400	-202.538
$H_2…HBr$	3.160	-168.674	3.500	-170.271

Figure 2 and Figure 3 show the minimum configuration of the $H_2…X_2$ and $H_2…HX$ systems. One can see that the T configuration are the minimum configuration for all the systems.

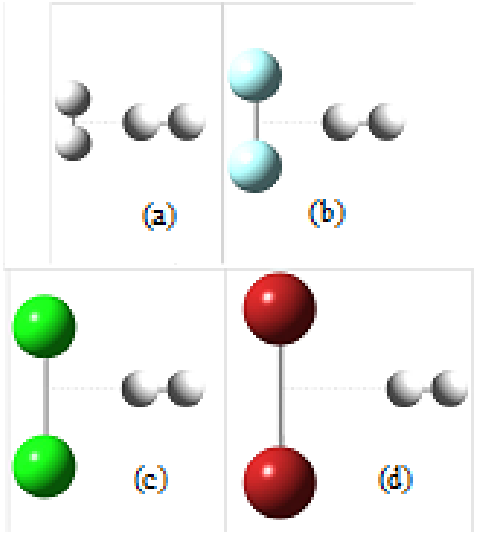

Fig. 2. *T_b configuration of $H_2…X_2$ system, where (a) X=H (b) X=F (c) X=Cl and (d) X=Br.*

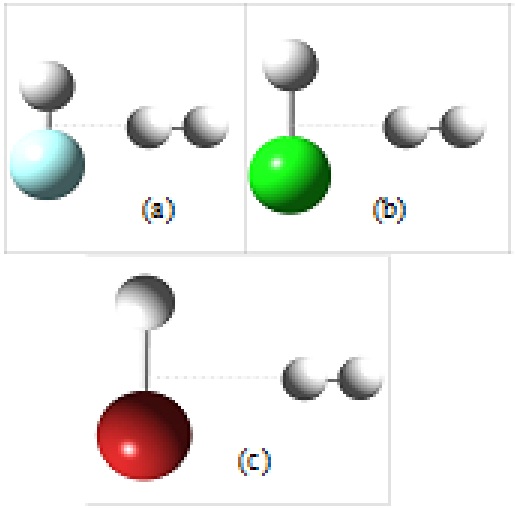

Fig. 3. *T_c configuration of $H_2…HX$ system, where (a) X=F (b) X=Cl and (c) X=Br.*

4. References

[1] P. R. P. Barreto; A. C. P. Cruz; R. Barreto; F. Palazzetti; A. Albernaz; A. Lombardi; G. Maciel and V. Aquilanti. The Spherical-Harmonics Representation for the Interaction Between Diatomic Molecules: The General Case and Applications to CO-CO and CO-HF. accept in May, **2017**, (2017).

[2] A. F. Albernaz, V. Aquilanti, P. R. P. Barreto, C. Caglioti, A. C. P. S. Cruz, G. Grossi and A. Lombardi, J. Phys. Chem. A, **2016**, 120, 5315, (2016).

[3] H. J. Werner; P. J. Knowles; G. Knizia; F. R. Manby; M. Schutz; P. Celani; T. Korona; R. Lindh; A. Mitrushenkov; G. Rauhut; K. R. Shamasundar; T. B. Adler; R. D. Amos; A. Bernhardsson; A. Berning; D. L. Cooper; M. J. O. Deegan; A. J. Dobbyn; F. Eckert; E. Goll; C. Hampel; A. Hesselmann; G. Hetzer; T. Hrenar; G. Jansen; C. Köppl; Y. Liu; A. W. Lloyd; R. A. Mata; A. J. May; S. J. Mcnicholas; W. Meyer; M. E. Mura; A. Nicklass; D. P. O. Neill; P. Palmieri; D. Peng; K. Pflüger; R. Pitzer; M. Reiher; T. Shiozaki; H. Stoll; A. J. Stone; R. Tarroni; T. Thorsteinsson and M. Wang, MOLPRO, a package of ab initio programs. version 2012.1, (2012).

[4] F. Pirani; M. Albertí; A. Castro; M. Moix Teixidor and D. Cappelletti, Chem. Phys. Lett., **2004**, 394, 37, (2004).

[5] F. Pirani; S. Brizi; L. F. Roncaratti; P. Casavecchia; D. Cappelletti and F. Vecchiocattivi, Phys. Chem. Chem. Phys., **2008**, 10, 5489, (2008).

[6] R. Z. Rydberg, Fur Physik, **31**, 73, 376, (1931).

Acknowledgments

The authors thanks for CAPES for financial support.

*anaclaudia.ps.cruz@gmail.com

ID 105: REACTION RATE OF H+HOC = H_2+CO

H. O. Euclides* and P. R. P. Barreto
[1]*Instituto Nacional de Pesquisas Espaciais (INPE/MCT), Laboratório Associado de Plasma (LAP), São José dos Campos, SP, CEP 12247-970, CP515, Brasil*

1. Introduction

Formyl radical HCO is a very important molecule in many fields as atmospheric chemistry [1], combustion science [2] and interstellar space [3], but its isomer HOC is not well studied, and it is stable only at high temperature. To understand the complete dissociation of HOC and the possible products formation of reaction H+HOC, consequently, H+HCO, that is well studied in the literature, a complete analyzes of potential energy surface (PES) is necessary. This work presents the rate constant for the reaction H+HOC = H_2+CO.

2. Theory

This study aims to obtain the reaction rate of H+HOC = H_2+CO, applying the tunneling correction of Wigner, Eckart and small curvature transmission coefficient [4, 5], which is presented in the Arrhenius' form. First of all a base set study was carried out in order to choose the best calculation level to conduct the rate constant calculation, that was determined using the APUAMA code [6].

The geometry are optimizes at MP2/aug-cc-pVDZ and MP2/aug-cc-pVTZ, and the frequencies are determined in the same level, while the energies are, also, calculated at CCSD(T)/aug-cc-pVQZ, in the GAUSSIAN09 program.

3. Results and Discussions

In table 1, we compare the forward and reverses barrier energies without the inclusion of rovibrational levels [7, 8] and the heat of reaction obtained in all bases set studies here. For comparison we included the heat of reaction obtained based in the experimental heat of formation of the reactant and products. One can see that the smallest error among the heat of reaction is given for the MP2/aug-cc-pVTZ, and it will be the basis set used in these studies.

Tab. 1. Comparison of barriers in the forward and reverse direction and the heat of reaction (in kcal mol^{-1})

base	Barrier Forward	Barrier Reverse	ΔH
MP2/aug-cc-pVDZ	80.78695	165.3715	-84.5846
MP2/aug-cc-pVTZ	79.27936	166.453	-87.1737
CCSD(T)/aug-cc-pVQZ	48.32118	151.5706	-103.249
Exp[9]	–	–	-89.7822

Experimental data based in the heat of formation of the reactant and products

We can observe a barrier of 79.3 *kcal mol^{-1}* in the forward direction versus *166.4 kcal mol^{-1}* in the reverse direction, we can include rovibrational levels of products the reverse barrier decrease, as well as, the heat of reaction, according to the rovibrational levels included. For the CO we used 10 vibrational and 2 rotational level, while for the H_2, we use 5 vibrational and rotational level. In this case, the reverse barrier decreases from *166.4 kcal mol^{-1}* to *60 kcal mol^{-1}*.

Figure 1 shows the most important variable of the intrinsic reaction coordinate (IRC) calculation, the bond HC increases while the bond HH decreases, showing the breaking of the HC bond in the HOC and the formation of HH bonding in the H_2.

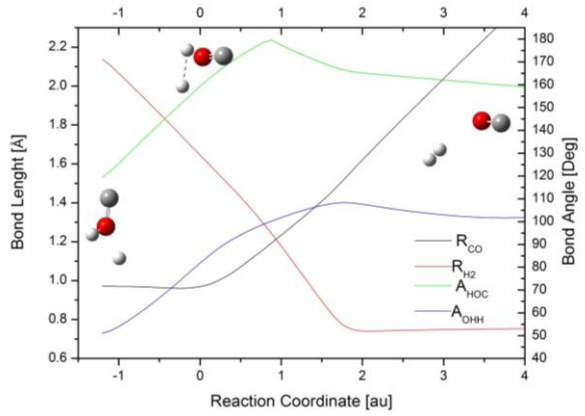

Fig. 1: *IRC results for reaction HOC+H=H_2+CO, calculated at MP2/aug-pVTZ*

*Corresponding author: henriqueuclides@gmail.com

Figure 2 compares the rate constant using the tunneling correction, as mentioned previous, for products in the rovibrational level (10,2) for CO and (5,5) for H_2. As we are working the hydrogen, one can expect a bigger tunneling effect, as present by Eckart correction. Figure 3 compares MEP (minimum energy path) and V_a^G (zero point correction) for the title reaction using the rovibrational level, as mentioned. The rate constant in the Arrhenius' form is given by $k_{TST_{0,0}} = 5.68 \times 10^9 T^{1.364} \exp(-80.59/RT)$, $k_{TST_{(10,2)(5,5)}} = 5.68 \times 10^9 T^{1.364} \exp(-80.58/RT)$ and $k_{E_{(10,2)(5,5)}} = 2.69 \times 10^{-17} T^{8.47} \exp(-30.77/RT)$.

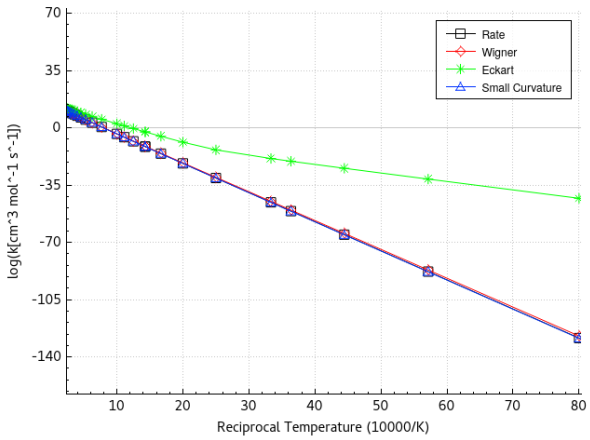

Fig. 2: *Reaction rate for H+HCO=H_2+CO with rovibrational level (10,2) for CO and (5,5) for H_2*

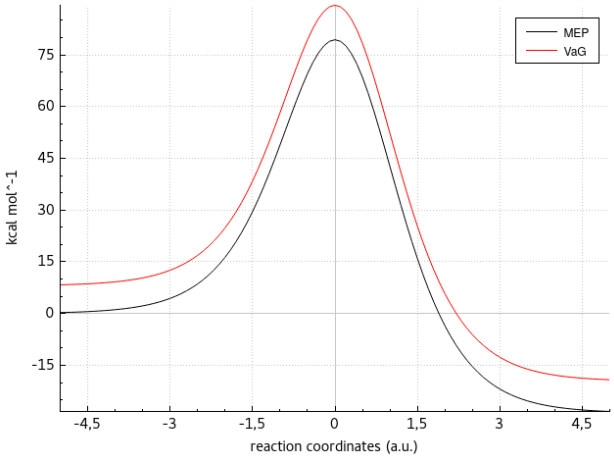

Fig. 3: *MEP and V_a^G for H+HCO=H_2+CO with rovibrational level (10,2) for CO and (5,5) for H_2*

Figures 4 and 5 compares the enthalpy and entropy, respectively, for species H, HCO, H_2 and CO.

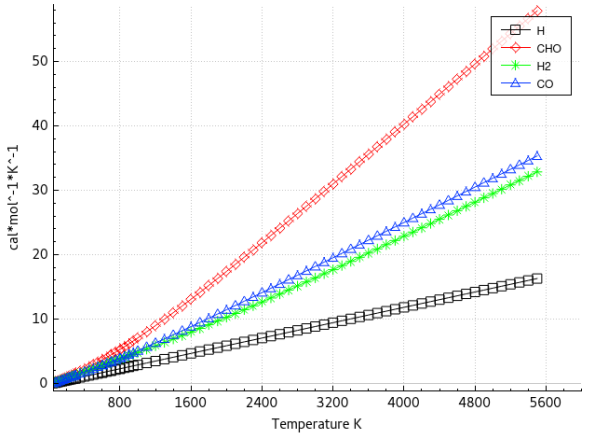

Fig. 4: *Comparison of enthalpy of reaction for all species*

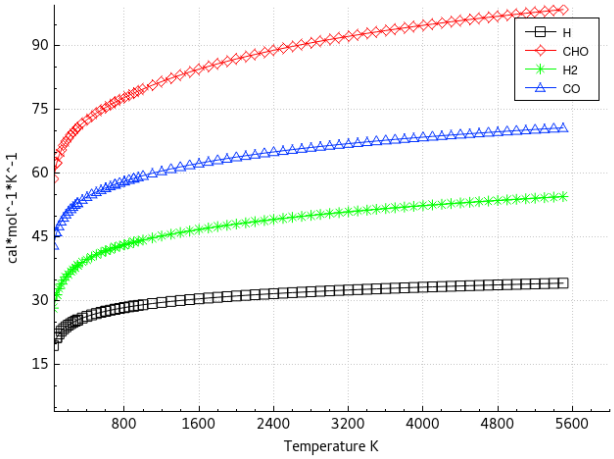

Fig. 5: *Comparison of entropy of reaction for all species*

4. References

[1] P. S. Peters, D. Duot, L. Wiesenfeld, C. Toubin, J. Chem. Phys. 139 (2013) 164310.
[2] J. A. Miller, R. J. Kee, C. K. Westbrook, Annu. Rev. Phys. Chem. 41 (1990) 345.
[3] S. Chu, A. Dalgarno, Proc. Roy. Soc. A 342 (1975) 194.
[4] Gonzalez-Lafont A., Truong T. N., Truhlar D. G. J. Chem. Phys. 95 (1991) 8875.
[5] Duncan W. T., Bell R. L., Truong T. N. J. Comput. Chem. 19 (1998) 1038.
[6] Euclides, H.O., P. Barreto, P.R. J Mol Model 23 (2017) 176.
[7] Dunham J. L., Phys. Rev., 41 (1932) 713.
[8] Dunham J. L., Phys. Rev., 41 (1932) 721.
[9] http://cccbdb.nist.gov/introx.asp

Acknowledgments

This research was funded by the CAPES.

*Corresponding author: henriqueuclides@gmail.com

ID 108: HFCVD DIAMOND PARAMETERS GROWTED ON TOOL STEEL APLAING VANADIUM CARBIDE INTERMEDIATE LAYER

D. D. Damm[1*], A. Contin[2], A. E. N. Andrade[3], V. J. Trava-Airoldi[2], D. M. Barquete[4], E. J. Corat[2].
[1]*São Paulo Federal University, São José dos Campos, São Paulo, Brazil*
[2]*Institute Nacional for Space Research, São José dos Campos, São Paulo, Brazil*
[3]*ETEP Faculty of Technolog , São José dos Campos, São Paulo, Brazil*
[4]*Santa Cruz State University , Ilhéus, Bahia, Brazil*
**djoilled.damm@hotmail.com*

1. Introduction

An intermediate material to growth diamond on steel substrate had been studied by many researchers [1]. The ideal interlayer have to full fill three requirements: reduce thermal residual compressive stress after cooling; block the iron diffusion from substrate to material surface; and block the carbon diffusion from gas phase to substrate during HFCVD diamond growth. The vanadium carbide (VC) interlayer was proposed by Barquete et al [2] as a great solution to CVD diamond deposition. The mismatch between diamond coefficient thermal expansion (CTE) ($0.8x10^{-6}K^{-1}$) and steel ($11.6x10^{-6}K^{-1}$) after cooling causes a high compressive stress in the diamond film. The VC CET around $6.06x10^{-6}K^{-1}$ [3], intermediate, can mitigate the residual stress. Also, the VC layer has elevate mechanicals properties (2600-3200HV) [4] and can act as an efficient diffusional barrier[5]. Iron in the diamond growth reactive region acts as catalyze for graphite formation (sp^2 bond) and the presence of graphite at the material surface reduces adhesion and diamond film quality[6].

Adherent and continuous diamond coatings on steel substrates with VC interlayers is determined by several parameters such as: surface morphology; interlayer thickness; substrate temperature; chamber pressure; total gas flow; work distance; CH_4 concentration and diamond deposition time. In this work a detailed study is carried out to probe the effect of some these parameters on diamond nucleation and growth over VC coating. The VC layer deposited on AISI O1 tool steel substrates and the HFCVD diamond film were characterized by scanning electron microscopy (SEM-EDS), X-ray diffraction and Raman spectoscropy. The results showed that VC layer has a strong bond with both materials: diamond and principally steel substrate. A well adherent diamond film with high quality and purity could be grouted on the VC interlayer.

2. Experimental Procedures

Thermo reactive diffusion is a deposition process which carbide coating using a borax bath grows onto carbon-containing substrates, through the combination of the carbide-forming element atoms in the bath with carbon atoms supplied from the substrates[7]–[9]. In this experiment the salt bath composition was borax ($Na_2B_4O_7.10H_2O$), vanadium pentoxide (V_2O_5) and boron carbide (B_4C) mixture in a melting pot, which is heated at 1050°C for 3h of TD-VC deposition time. After vanadium carbide deposition the samples are cleaned in boiling water and in the ultrasonic acetone bath.

The thermodiffused samples are submitted to diamond seeding process to improve diamond nucleation and the growth rate in the HFCVD reactor. Once introduced in the HFCVD reactor, the diamond deposition was conducted with the following parameters: 1-3% of CH_4; total flux of 100sccm; 50 torr; work distance of 5mm; substrate temperature at 650°C - 750°C; and deposition time of 3h.

3. Results and Discussions

A continuous and homogeneous vanadium carbide film was obtained on the AISI O1 tool steel and the carbide covered the entire samples surface with 16-18μm thickness (Fig.2). The film showed the formation of the phase VC, it can be happening as function of borax concentration. The borax acts reducing the melting point and give freedom to the salt bath elements to combine forming the VC phase (Fig.1). An EDS semi quantitative characterization on the vanadium carbide surface showed a residual iron concentration below 3%, it probe the efficiency of the VC diffusional barrier. In large proportions the iron catalyzes the CVD diamond reaction forming sp^2 bonds characteristics of graphite. However, on a small scale it acts as an accelerator, increasing the nucleation and CVD diamond growth.

We noted that as the temperature was increased the higher was the rate of the growth. However, under some conditions with elevate temperature, a high graphite formation was seeing in some sites. With 1% of methane a high quality of the diamond crystals was reached (Fig.4). The hydrogen was more reactive with this gas mixture controlling better the graphite formation. Increasing the methane concentration up 2% and 3% the quality of the film was reduced. On the other hand, the adhesion of diamond film to the VC surface

*Corresponding author: djoilled.damm@hotmail.com

increases, reducing cracks and the residual thermal stress after cooling. The Raman spectrum obtained with 2% of methane at 700°C showed a peak centered around 1341 cm^{-1} (Fig. 3.).

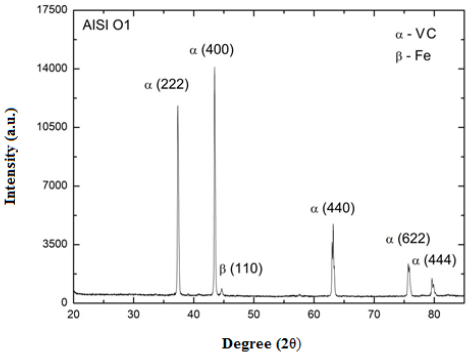

Fig. 1. Vanadium carbide phase.

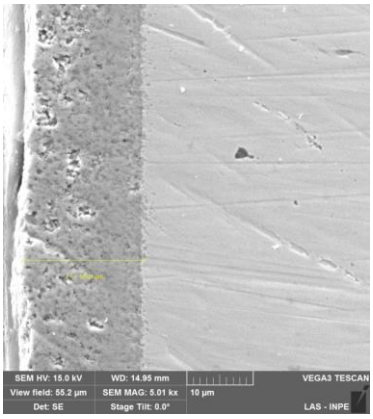

Fig. 2. Vanadium carbide thickness.

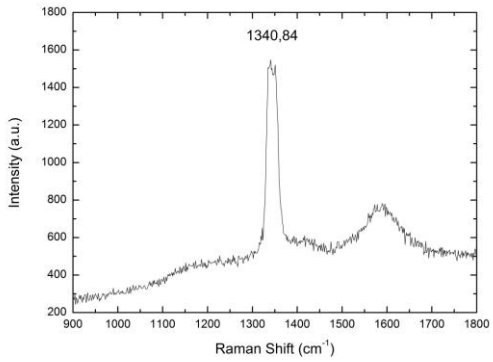

Fig. 3. HFCVD diamond Raman spectrum.

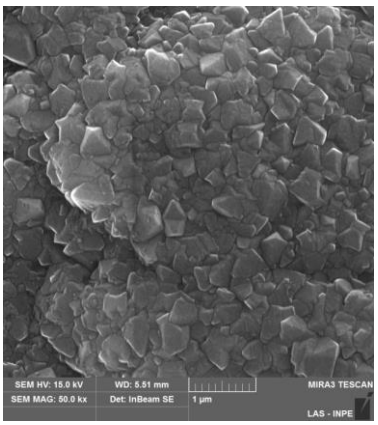

Fig. 4. HFCVD diamond morphology.

4. References

[1] M. Chandran and A. Hoffman, "Diamond film deposition on WC – Co and steel substrates with a CrN interlayer for tribological applications," *J. Phys. D. Appl. Phys.*, vol. 213002, p. 213002.

[2] D. M. Barquete, E. J. Corat, R. a. Campos, C. Moura Neto, and V. J. Trava-Airoldi, "Thermodiffused vanadium carbide interface for diamond films on steel and cemented carbides substrates," *Surf. Eng.*, vol. 26, no. 7, pp. 506–510, 2010.

[3] A. Krajewski, L. D'Alessio, and G. De Maria, "Physiso-chemical and thermophysical properties of cubic binary carbides," *Cryst. Res. Technol.*, vol. 33, pp. 341–374, 1997.

[4] L. Wu, T. Yao, Y. Wang, J. Zhang, F. Xiao, and B. Liao, "Understanding the mechanical properties of vanadium carbides: Nano-indentation measurement and first-principles calculations," *J. Alloys Compd.*, vol. 548, pp. 60–64, 2013.

[5] K. F. Almeida *et al.*, "Thickness study of vanadium carbide interface for deposition of dlc films," *RBAV*, vol. 35, pp. 47–52, 2016.

[6] A. Contin, G. De Vasconcelos, D. M. I. Barquete, R. A. Campos, V. J. Trava-Airoldi, and E. J. Corat, "Laser cladding of SiC multilayers for diamond deposition on steel substrates," *Diam. Relat. Mater.*, vol. 65, pp. 105–114, 2016.

[7] T. Arai and S. Moriyama, "Growth behavior of chromium carbide and niobium carbide layers on steel substrate, obtained by salt bath immersion coating process," *Thin Solid Films*, vol. 259, no. 2, pp. 174–180, 1995.

[8] B. Chicco, W. E. Borbidge, and E. Summerville, "Experimental study of vanadium carbide and carbonitride coatings," *Mater. Sci. Eng. A*, vol. 266, no. 1–2, pp. 62–72, 1999.

[9] D. KONG and C. ZHOU, "the Surface and Interface Properties of Vanadium Carbide Coating Prepared By Thermal Diffusion Process," *J. Adv. Manuf. Syst.*, vol. 10, no. 1, pp. 183–190, 2011.

Acknowledgments

*Corresponding author: djoilled.damm@hotmail.com

The authors wish to Foundation Support to the São Paulo State Research (FAPESP), Federal University of São Paulo (UNIFESP), the National Institute for Space Research (INPE) and Associated Laboratory of Sensors and Materials (LAS) for supporting this scientific research.

*Corresponding author: djoilled.damm@hotmail.com

ID 110: GROWTH OF DLC FILM IN A METALLIC TUBE WITH HIGH ASPECT

RATIO E. J. D. M, Pillaca*[1], Jesus Manuel Gutierrez Bernal[2] and Vladimir J. Trava-Airoldi[1]

[1]*Sensor and Materials Associated Laboratory, National Institute for Space Research, S. J. Campos, São Paulo, Brazil*

[2]*Universidad Nacional de Colombia, Facultad de Ingeniería, Colombia.*

1. Introduction

PECVD is a well-established method for the growth of DLC films on substrates with complex shapes, in a fast and efficient way [1]. By this technique, thick layers of DLC are coated on the surfaces of mechanical components. However, it was pointed out in the literature that plasma-based treatments inside pieces with hollow cylindrical geometry, such as pipes or tubes result quite difficult to be performed [2]. On the other hand, plasma-based coatings on the tube interior are usually restricted to be performed inside of a vacuum chamber. This limit the treatment of tubes with long length, considering that a vacuum chamber with higher dimension than the tube itself is required; in practice, it becomes expensive from the economic viewpoint. This situation has led to the use of the tube as a deposition chamber. Under this idea, the system shown in Fig. 1 was constructed aiming the use of a Stainless Steel (AISI 304) tube with high aspect ratio (200 cm in length and 10 cm in diameter) as a deposition chamber. So, in this work is reported the results of the study of the longitudinal distribution of DLC film coated on the inner surface of the tube. Issues such as current discharge, gas flow and temperature were studied too.

2. Experimental

For the characterization of the surface coated, five samples of AISI 304 were longitudinally distributed on the inner surface of the tube. The coating was performed by using the Plasma enhanced Chemical Vapor Deposition (PECVD) process and the acetylene gas, as precursor. The system was pumped down to a base pressure of the order of 10^{-4} Torr by a set of mechanical and diffusion pump. The discharge is carried out by a bipolar pulsed voltage feed. The pulse width, the repetition rate, the voltage and the working pressure were kept constant during all experiments at 15 μs, 21 kHz, 500 V and 70 mTorr, respectively.

3. Results and Discussions

Our measurements of current have shown the presence of a low discharge current. This result, in particular, it is interesting for DLC growth (thermal viewpoint) due that the ion impact on the inner wall of the tube has caused temperatures less than 50 °C. Growth of DLC film was carried out on the inner wall of the tube. Amorphous carbon hydrogenated (a-C:H) films were obtained. Raman analysis performed on the coated surface confirmed the presence of DLC film with good quality. However, it was not uniform along its longitudinal distribution.

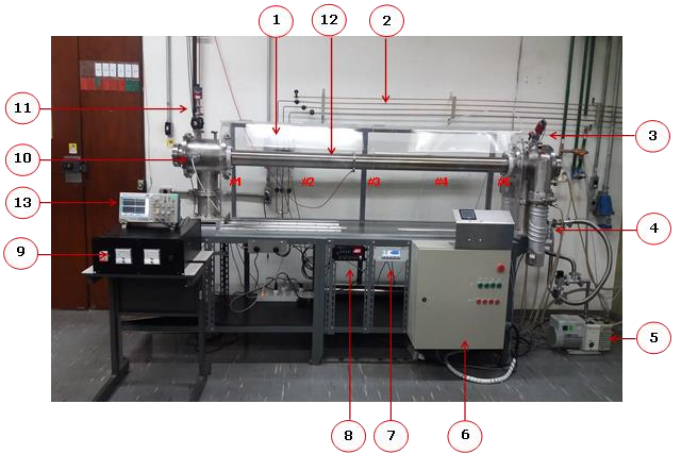

Fig. 1. Photograph of the system used as a deposition chamber for the growth of DLC film. The numbers in the circle indicate the components of the system; 1. Mass flow controller; 2. Gas line; 3. Pirani gauge; 4. Diffusion pumps; 5. Mechanical pump; 6. Electric control module; 7. Vacuum measurement; 8. Flow control module; 9. High voltage source; 10. Gas inlet; 11. Baratron; 12. Tube; 13. Oscilloscope. The typographic sign #1, #2, #3, #4 and #5 indicate the location of samples inside of the tube.

4. References

[1] K. Choy, Progress in Materials Science 48 (2003) 57.
[2] T. E. Sheridan, J. Appl. Phys. 80 (1996) 66.

Acknowledgments

This work was supported by grant #15/09781-0, São Paulo Research Foundation, FAPESP.

* mitma.elver@gmail.com

ID 111: PARTIALLY TRI-SULFATED CHITOSAN FILMS USING SODIUM SULFATE SALT AND CYTOTOXICITY EVALUATION ON HUMAN NEUTROPHILS

Anaftália Felismino Moraes[1*], Lyara Barbosa Nogueira Freitas[2], João Antonio C. Sousa [2], Antonio Carlos Guastaldi[3], Arcelina Pacheco Cunha[1], Luzia Kalyne Almeida Moreira LEAL[2], Rodrigo Silveira Vieira[1].

[1] Grupo de Pesquisa em Separação e Adsorção-Universidade Federal do Ceará
[2] Centro de Estudos Farmacêuticos e Cosméticos– Universidade Federal do Ceará;
[3] Grupo de Biomateriais – Universidade Estadual Paulista

1. Introduction

Medical devices of blood contact can induce thrombus formation and restenosis after implant. One strategy to avoid these drawbacks is surface coating with hemocompatible polymers. Scientists have interest in sulfated chitosan study due it present biocompatible properties [1]. However, the acid used in the sulfation reaction has some disadvantages, such as care with manipulation and chemical degradation of polymer. In addition, the use of anhydrous medium brings more costs for the final product. This work proposes to synthesize sulfated chitosan using the sodium sulfate salt as a sulfating agent in order to obtain thin films of partially tri-sulfated chitosan with chemical characteristics similar to those of sulfated chitosan obtained by conventional sulfating agents (chlorosulphonic acid) and non-toxic properties for human neutrophils, presenting potential for future coating applications in the blood devices, however, at lower cost.

2. Experimental

2.1 Characterization and film preparation of sulfated chitosan using sodium sulfate salt (SSC)

SSC was prepared from mix of 4% $NaSO_4^{2+}$ solution (w/v) and 2% chitosan solution (3% acetic acid, w/v) under stirring at room temperature (25 °C). For comparison purposes, it was used 2% natural chitosan solution (w/v) (NC) and sulfated chitosan obtained by chlorosulphonic acid (SC) according to [2]. To obtain the film, SSC solution was dispersed in polystyrene dish and keep at room temperature (25 °C) until drying. The chemical analysis of NC, SC and SSC was performed by elemental analysis and solid state ^{13}C Nuclear Magnetic Resonance spectra (^{13}C-NMR).

2.2 Cytotoxicity evaluation of human neutrophil

Neutrophils were isolated according to the method described by [3] and suspended in Hanks balanced salt solution (HBSS) containing 0.1% gelatin (HBSS-gel). The evaluation of cytotoxicity of NC, SC, SSC and triton X100 (cytotoxic standard) was performed by determination of lactate dehydrogenase (LDH) activity. In the control group, the cells were incubated with the vehicle (0.5% acetic acid neutralized with 2M NaOH), while the untreated group the cells were exposed only to the culture medium, HBSS. The analyses were performed according to the method described by the manufacturer (Labtest, Brazil).

3. Results and Discussions

The chemical modification was evidenced by the appearance of sulfur (S) in the elemental composition of chitosan (TABLE 1), showing that the SSC developed in this study reached % S equivalent to half of the SC prepared according to the method described above, which has a higher cost and risk during the preparation. However, it should be noted that the degree of sulfation (DS) found in the SSC, reach the proposed objective.

POLYMERS	%C	%H	%N	%S	DS
NC	38.9	7.1	2.9	-	-
SC	21.6	4.5	4.1	12.9	1.19
SSC	22.8	4.3	3.6	6.8	0.82

Table 1 – Elemental analysis of NC, SC and SSC.

A transparent and thin film was obtained and can be seen in the Figure 1. Through the ^{13}C-NMR spectrum (FIGURE 2), it was observed chemical shifts of carbons indicating a partial 2, N-3,6, O-sulfated chitosan (tri-sulfated).

*anaf_moraes@hotmail.com

Fig. 1. *Visual image of SSC film.*

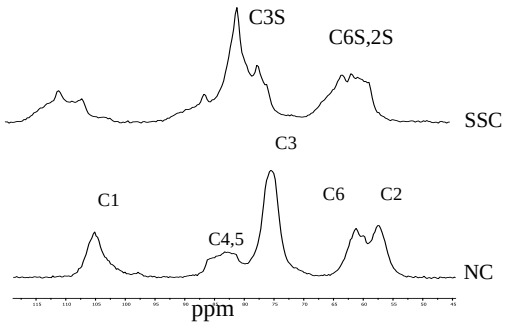

Fig. 2. Solid ^{13}*C-NMR spectra of NC and SSC*

The Figure 3 showed the effect of NC, SC and SSC (1-100 μg/mL) on the viability of human neutrophils. The vehicle (control group) not interfered significantly in the cell viability in relation to the HBSS group. The concentrations of SSC evaluated not increase the LDH activity significantly in the extracellular medium and similar results were observed for the NC and SC groups, relative to the control group. On the other hand, Triton X-100 (cytotoxic standard) significantly increased LDH activity. LDH is a cytosolic enzyme, and only is released for extracellular medium when occur damage of membrane integrity. Thus, the results suggest that the new sulfated chitosan (SSC), like the others, NC and SC, are non-toxic to the plasma membrane of human neutrophil.

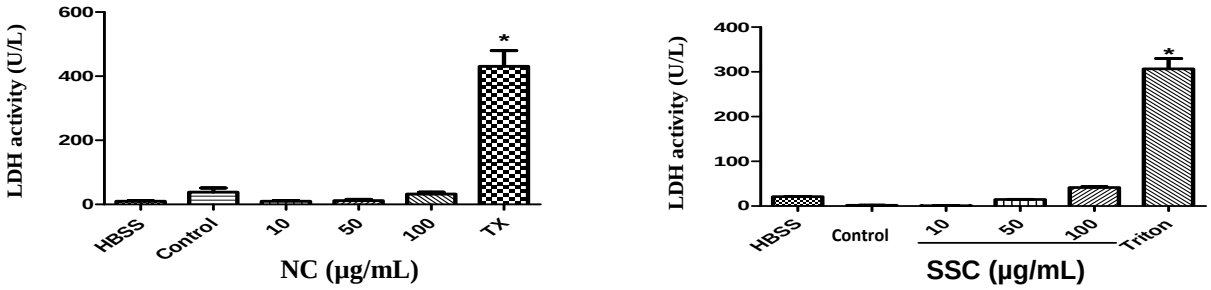

Fig. 3. *LDH effect of NC and SSC in human neutrophils*.

The results obtained in this study indicated that it was possible to obtain a sulfated chitosan (SSC) in a simpler way and at a lower cost than the previous sulfation method (SC) used by our laboratory. In addition, the SSC showed physical-chemical characteristics proving the sulfation and non-cytotoxicity in human neutrophil. Thus, the SSC showed potential for future biomedical applications.

4. References

[1] V. Balan and L. Verestiuc, European Polymer Journal, **53**, 171–188, (2014).

[2] A.F. Moraes, "Quitosana sulfatada: caracterização e estudo da hemocompatibilidade", Dissertação de mestrado, 94f. Universidade Federal do Ceará, Fortaleza, 2016.

[3] Y. M., Lucisano and B. Mantovani. Journal Immunology, **132**, 2015–2020, (1984).

*anaf_moraes@hotmail.com

ID 112: TI-6AL-4V ALLOY FATIGUE BEHAVIOR SUBJECTED TO SHOT PEENING AND PLASMA IMMERSION ION IMPLATATION (PIII) TREATMENTS

Leonardo Haruo Nozaki[1]*, Verônica Mara de Oliveira Velloso[1], Diego Cris Ashly Rey Tapia[2], Maria Odila Hilário Cioffi[1], Herman Jacobus Cornelis Voorwald[1]
[1]*Faculdade de Engenharia de Gauratinguetá, FEG – UNESP.*
[2]*National University of Engineering*

1. Introduction

Ti-6Al-4V alloy is used in aeronautical and biomedical fields due to its high strength/weight ratio, high biocompatibility, high corrosion resistance, low density, and superior heat resistance [1, 2, 3, 4]. However, its tribological properties are poor (low wear and friction resistances) [1]. Therefore, this alloy is usually submitted to surface treatments, in order to enhance its tribological properties.

In this research, Ti-6Al-4V alloy was submitted to shot peening (SP) and PIII treatments in order to increase its fatigue life.

Shot peening is a cold working process, which high-speed shots hit the piece surface, inducing compressive residual stress (CRS). The CRS can inhibit fatigue crack growth, increasing material's fatigue life [5]. Shot peening can also reduce the grain size of material surface, improving its fatigue strength. However, this treatment also increases material's roughness, which can induce stress concentration, resulting in crack initiation under cyclic loading [6].

Plasma Immersion Ion Implantation is a surface treatment, which consists in a three-dimensional ion implantation in complex shape pieces. PIII is used in order to enhance wear resistance and reduce friction coefficient. [7].

2. Experimental

The objective of this research is to compare the microstructure and fatigue behavior of Ti-6Al-4V alloy as received, treated by shot peening, and treated by PIII.

The SP intensity used was 0,41-0,49A, and the coverage was 100%. It was used steel balls S230 with diameter of 0,7 mm. The treatment was carried out according to ASM 2430, and the ball granulometry according to SAE J444.

The PIII parameters were: tension 9,5KV; frequency 1,5KHz; pressure 6,5 x 10^{-3} mbar, intensity of 110 mA.

The samples were observed using the optical microscope Nikon Epiphot 200. They were also observed using the Scanning Electron Microscopy (SEM) Leo device model 1450-VP.

Vickers microhardness measures were carried out on the top surface and cross-section of samples in each condition, using the device Shimadzu HMV-2T.

Profilometry was conducted to obtain arithmetic average roughness (Ra) in each condition. It was used the profilometer model Leica DCM 3D.

The samples were submitted to axial fatigue tests in the Instron 8801 machine, in order to obtain the fatigue strength in each condition.

3. Results and Discussions

According to the images obtained using Optical Microscopy and SEM, it was observed the presence of both phases (α-Ti and β-Ti) in the microstructure of Ti-6Al-4V, which can be seen in figures 1 and 2. It is possible to notice the grain refinement of the specimen treated by SP (Fig.1) compared to the sample submitted to PIII process (Fig.2).

The Vickers microhardness measures obtained on the surface region of the sample in SP condition were about 7% higher than the values obtained on the surface region in as received condition. However, in the middle of the samples, no significant difference was noticed, which has been already expected, since SP just change the material surface.

By analyzing profilometry results, it was observed that the specimen treated by SP had an increase in more than 500% in roughness, compared to non-treated sample. PIII treatment increased in about 25% the roughness compared to as received material. Therefore, it is important to notice that both treatments increase material's roughness; however, SP process increases it more than PIII treatment, which can be explained by the fact that the ion implantation of PIII causes almost no dimensional change, inducing less roughness increase compared to SP condition.

Surface roughness may induce stress concentration, which can result in crack nucleation under fatigue loading, reducing material's fatigue life. However, in case of the samples treated by SP, the compressive

*Corresponding author: leo.nozaki@hotmail.com

residual stress induced in the surface layer of the material (which can be noticed in the increase of residual microhardness) improves its fatigue strength.

Considering fatigue tests for stress level of 950 MPa, the following results were obtained: 30537 cycles (as received condition), 8666 cycles (PIII condition) and 110000 cycles (SP condition). It is possible to notice the fatigue life increase in the specimen submitted to SP treatment, and a decrease in fatigue life of the sample treated by PIII process, both compared to as received condition.

Due to the superior grain refinement and microhardness of SP specimen, the fatigue life of the sample in SP condition is superior to the fatigue life of the specimen in PIII condition.

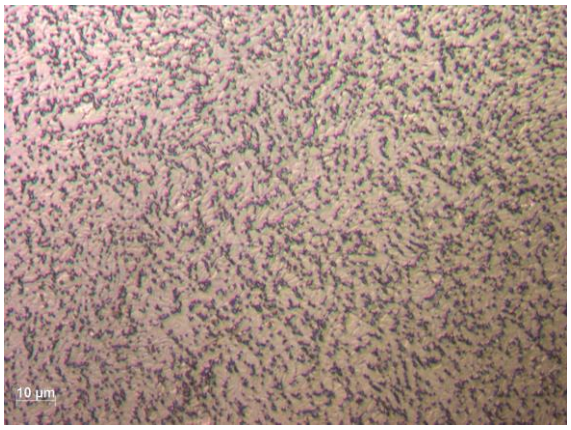

Fig. 1. *Ti-6Al-4V + SP , 50x magnification*

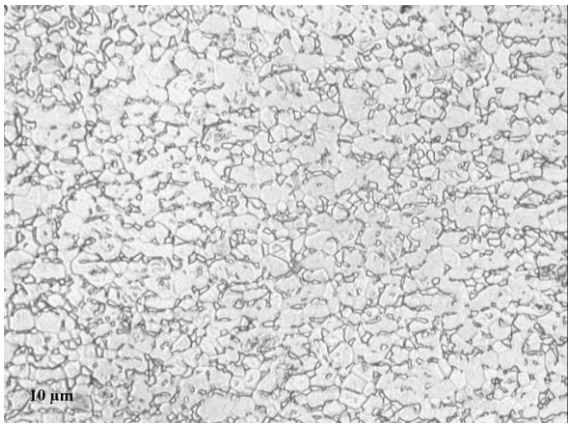

Fig. 2. *Ti-6Al-4V + PIII, 50x magnification*

4. References

[1] D. Cressman; B. Tury; G.L. Doll, Surf. & Coat. Tech, **290**, 110-115, (2016).
[2] P.L. Huang; J.F. Li; J. Sun; J. Zhou, Journal of Cleaner Production, **67**, 258-264, (2014).
[3] H.H. Tong; O.R. Monteiro; R.A. Macgill; I.G. Brown; G.F. Yin; J.M. Luo, Curent Applied Physics, **1**, 197-201, (2001).
[4] W. Li; S. Karnati; C. Kriewall; F. Liou; J. Newkirk; K.M.B. Taminger; W.J. Seufzer, Additive Manufacturing, **14,** 95-104, (2017).
[5] C. Wang; C. Jiang; F. Cai; Y. Zhao; K. Zhu; Z. Chai, Materials and Design, **95**, 159-164, (2016).
[6] Y.G. Liu; M.Q. Li; H.J. Liu, Materials Characterization, **123**, 83-90, (2017).
[7] C.B. Mello; M. Ueda; M.M. Silva; H. Reuther; L. Pichon; C.M. Lepienski, Wear, **267**, 867-873, (2009).

Acknowledgments

Acknowledgments to Fapesp (2016/18500-8) for the financial assistance.

*Corresponding author: leo.nozaki@hotmail.com

ID 113: THE INFLUENCE OF CONTROLLED THERMAL OXIDATION ON THE MORPHOLOGY AND PHOTOLUMINESCENCE OF POROUS SILICON

PAES, T.F.[1]*, BERNI, L. A.[2], BELOTO, A. F.[2]
[1]*Federal University of Bahia, Salvador, BA, Brazil*
[2]*National Institute for Space Research, São José dos Campos, SP, Brazil*

1. Introduction

Porous silicon (PSi) is a peculiar material with structural characteristics that provides study to develop many technological applications. The photoluminescence (PL) emission at room temperature is a feature of the PSi defined by its porous structure, which is the most investigated property from both views: theoretical and experimental. The PL property is also influenced by the oxidation process that creates a surface "shell" around the silicon (Si) core and changes the surface species, which is passivated [1]. This work was to analyses the influence of thermal oxidation controlled process on the morphological and photoluminescence emission of the PSi layer before and after the oxidation process and verify the viability of the formed structures for potential applications in sensors.

2. Experimental

PSi samples were produced from the electrochemical etching of p-type boron-doped monocrystalline silicon wafer <100>, resistivity between 0.01 and 0.02 Ωcm, using different anodizing parameters. A detailed sequence for the fabrication of PSi samples is published in reference [2]. The thermal oxidation procedure used an open-quartz tube furnace with digital temperature control set at 800 °C. The samples were annealing during 1 hour in air dry by an Edwards diaphragm pump, model D-Lab 10-100. This technique was chosen because it is a simple and widely used technique in surface passivation studies for the native oxidation control of PSi. For the PL measurements, it was developed a system capable to measure, in high resolution, the emission of the PSi samples at room temperature. The system uses a 365nm LED as an excitation source and a monochromator Shamrock SR-303i connected into a CCD camera iDUO DU-401A for the detection of the spectrum. High resolution images of the PSi structures were obtained by Field Emission Scanning Electron Microscopy (FESEM) by Shimadzu, model Mira LM. Other techniques as a Raman and X-ray Spectroscopy were used to verify and compare morphologies and PL characteristics of PSi samples.

3. Results and Discussions

Analyzing the controlled thermal oxidation, it was verified that there were variations of the original structures of the PSi because of the SiO_2 layer formed during the oxidation process. This change was observed in the several characterizations performed when compared to the characteristics of the non-oxidized PSi samples. The way in which these changes were made led to changes the optical, chemical and morphological properties of PSi, such as PL, which appeared in several samples when nonexistent (Fig 1). The field emission scanning electron microscopy (FESEM) analysis of oxidized porous structures does not reveal any considerable changes compared to the non-oxidized PSi samples. Otherwise, the imagens of surface structure show some physical changes that could be responsible for the morphology changes as pore size and surface area (Fig.2).

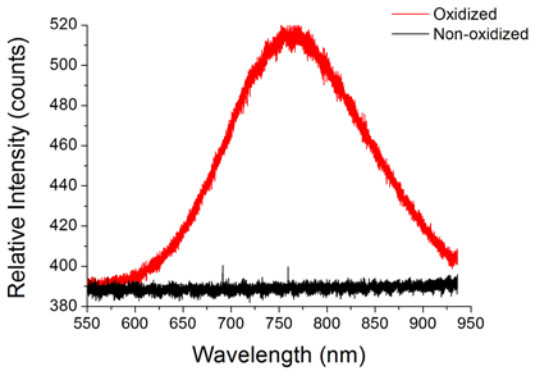

Fig. 1. *Photoluminescence spectrum of PSi Sample before and after oxidation.*

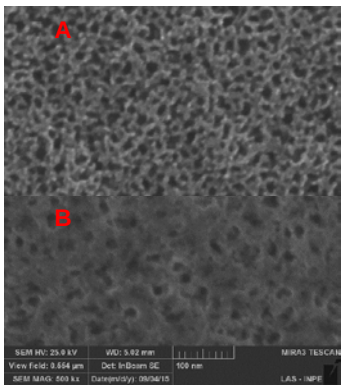

Fig. 2. *FESEM images of PSi Surface A before B after oxidation process. Magnification: 500kX.*

*Corresponding author: tfpaes@ufba.br

Another important fact that came after the oxidation process was the passivation of the porous layer, which inhibits the continuous oxidation and guarantees the characteristics of the formed oxide [3]. Using other techniques, it also has observed the variation of the refractive indexes of PSi, which favors for applications in optical systems. The results show that the non-oxidized samples have a higher refractive index than the thermally oxidized samples. A curious point in this analysis was the finding that the oxidized samples lost the structural properties of the crystalline silicon which, unlike the non-oxidized samples, suffered different deformations, due to the temperature and the structural difference between the porous and substrate layers. This study allowed to prove the effectiveness of the use of the methods of analysis developed, as it enabled a detailed assessment of the changes occurred in the structures caused by the influence of oxidation.

4. References

[1] Jinmyoung Joo, et. Al. Photoluminescent Porous Si/SiO 2 Core/Shell Nanoparticles Prepared by Borate Oxidation. Adv. Funct. Mater. 2014.

[2] PAES, T. F. Silício poroso: estudo de estruturas e fotoluminescência para possíveis aplicações em sensores. 2016. 167 p. Tese (Doutorado em Ciência e Tecnologia de Materiais e Sensores) - Instituto Nacional de Pesquisas Espaciais (INPE), São José dos Campos, 2016.

[3] PAP, Andrea E. et al. Thermal oxidation of porous silicon: study on structure. Applied Physics Letters, v. 86, n. 4, p. 041501, 2005.

Acknowledgments

Institute of Physics of the Federal University of Bahia (IF-UFBA) and Photovoltaic Devices Group of the National Institute for Space Research (DFG-INPE).

*Corresponding author: tfpaes@ufba.br

ID 114: THE EFFECTS OF CYCLING THE ATMOSPHERE NITRIDING ABILITY ON THE STRUCTURE OF THE NITRIDED REGION OF AN AISI 1015 STEEL PLASMA NITRIDED

Deivison Daros Paim [1]*, Luis Cesar Fontana [1], Abel André Cândido Recco [1]

[1]*Laboratory of Plasmas, Films, and Surfaces – Santa Catarina State University, Joinville, SC, Brazil*

1. Introduction

The nitriding structure of plain carbon steels is highly dependent on nitriding potential (i.e., the actual nitrogen flux, arc discharge voltage and current density, among others), treatment temperature and exposure time. Those steels are commonly nitrided at temperatures around 500°C, for periods typically as long as 20 h. The exposure of the steel to such demanding combination of high temperature and long treatment time induces excessive softening at the core region of the steel.

Processes for inducing improved nitrogen diffusivity inside the steel structure have been developed, with the aim of restraining both the nitriding temperature and time. One of those processes consists on refining the steel surface structure up to the nanometer length, through of nanocrystallization [1]. In this contribution, we report the nitriding treatment of a steel which surface was severely work-hardened. Thus, thick nitriding layers were obtained at a nitriding temperature as low as 350°C.

This contribution deals with the plasma nitriding treatment of an AISI 1015 steel, which was previously work-hardened at the near surface region. Several nitriding treatments, all of them with a total processing time of 3h were studied, having as parameter the nitrogen fraction of the gas atmosphere. The aim of this research was to assess the effects of cycling the nitrogen gas fraction in the nitriding atmosphere on the structure of the nitrided region of the aforementioned steel.

2. Experimental

Test samples of the AISI 1015 low carbon steel were obtained from the head of bolts with 12mm in diameter, which presented severe plastic deformation at the near surface region. Six different sets of samples were plasma nitrided at 350°C, with a total processing time of 3h, under H_2+N_2+Ar gas atmospheres, containing variable fractions of the N_2 gas, as depicted in Table 1. The atmosphere composition was modified during the treatment: a nitriding step and a diffusion step. The nitriding step was carried out in the presence of N_2 gas in the atmosphere, while the diffusion step was carried out with no N_2 gas (Table 1). For comparison, two samples (so-called S5 and S6 in Table 1) were obtained with conventional nitriding treatments, which were comprised of just the nitriding step.

Sample	Nitriding step	Diffusion step	Sample	Nitriding step	Diffusion step
S1	3 x 1,0h: 20% N_2 + 80% H_2	3 x :1,0h: 20% Ar + 80% H_2	S4	6 x 0,5 h: 80% N_2 + 20% H_2	6 x 0,5h: 80% Ar + 20% H_2
S2	6 x 0,5h: 20% N_2 + 80% H_2	6 x 0,5h: 20% Ar+ 80% H_2	S5	1 x 3,0h: 20% N_2 + 80% H_2	-
S3	3 x 1,0h: 80% N_2 + 20% H_2	3 x 1,0h: 80% Ar+ 20% H_2	S6	1 x 3,0h: 80% N_2 + 20% H_2	-

Tab. 1. *Atmosphere composition at the nitriding step and the diffusion step during the cycling nitriding experiments.*

3. Results and Discussions

Figure 1 shows the appearance of the microstructure observed in the scanning electron microscope (SEM). The transversal section of the samples prepared by conventional metallographic techniques is shown in Fig. 1. An uppermost region containing the compound layer can be observed in all samples, disregarding the actual cycling treatment. However, the thickness and the morphology of such region are dependent on the actual cycling treatment, as well as the total thickness of the nitrided region. The low temperature of treatment and lack of alloy elements in the chemical composition of steel promotes the compound layer formation [2]. The compound layer and total nitrided region thickness are listed in Table 2.

Samples (S5 and S6) obtained with conventional nitriding treatments show a homogeneous thickness of the compound layer. Between the specimens treated with cycling atmosphere nitriding, only the S3 sample shows the same morphology. All other specimens show the compound layer growth in form of needles. However, only S4 sample emphasizes well the nitrogen diffusion throughout the grain boundary, as depicted in Figure 1(d).

The nitriding step (H_2+N_2) contributes to the growth of compound layer, delaying the development of the nitrided region (diffusion zone) [3]. Specimens treated with higher nitrogen fraction in the gas mixture show a thicker of compound layer, as depicted in Table 2.

The cycling between nitriding step and diffusion step contributes as an additional mechanism beyond of nanocrystallization, increasing the nitrogen diffusion. The diffusion step cycle (H_2+Ar) doesn't promote

*deivisonpaim@gmail.com

the compounds layer formation. However, it aids to increase the nitrided region through of nitrogen redistribution incorporated in the compound layer, in other words, the use of diffusion step cycle during the treatment allows that the compound layer be "dissolved" and the nitrogen be redistributed towards of core region of the steel through of nitrogen concentration gradient on the surface. This characteristic is emphasized well for S1 sample, where nitrided region thickness is around three times higher than S5 sample, both nitrided with 20% N_2, obtaining values near the S3 and S4 samples, both nitrided with 80%N_2, as depicted in Table 2. Samples S3 and S4 show the same behavior in comparison with the S6 sample.

The compound layer thickness between specimens treated with the same nitrogen fraction is smaller with the presence of diffusion step cycle. The use of diffusion step cycle allows that the compound layer contributes more effectively to the growth of the nitrided region.

Nitrogen fraction of the gas atmosphere shows influence on the nitrides formation in the compound layer. A nitrogen fraction with 20% N_2 inhibits the formation of ε-$Fe_{2-3}N$ nitrides [3]. The samples treated with the nitrogen fraction of 80%N_2 show two phases: the ε-$Fe_{2-3}N$ phase in an uppermost region followed of γ′-Fe_4N just below (figure 1).

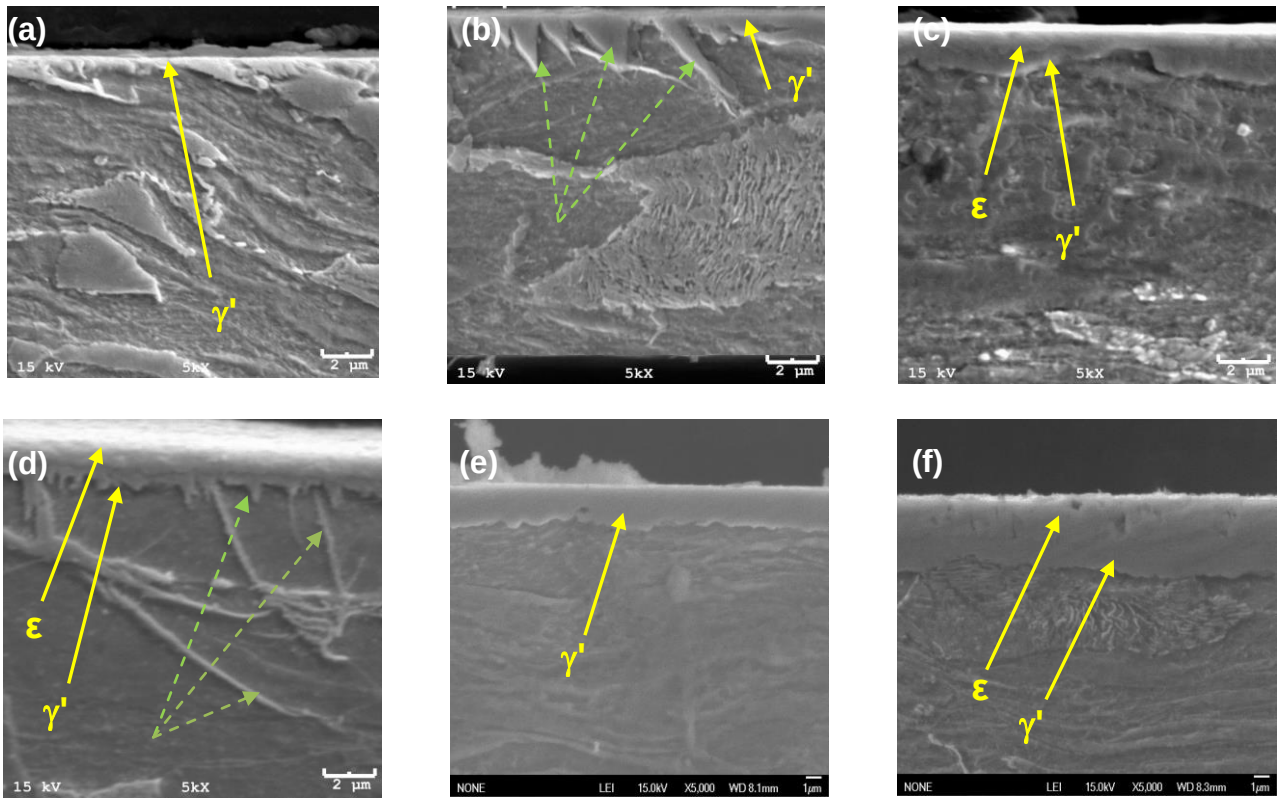

Fig. 1. *SEM photomicrographs (a) S1, (b) S2, (c) S3, (d) S4, (e) S5 and (f) S6. The γ'-Fe_4N and ε-$Fe_{2-3}N$ phases in compound layer (full line arrow) with small needles projections ahead of compound layer growth as well as diffusion of nitrogen in the grain boundaries in samples 0.5h treatment cycles (dashed arrow).*

Sample	Nitrided region	Compound layer	Sample	Nitrided region	Compound layer	Sample	Nitrided region	Compound layer
S1	170 ± 10 µm	1,5 ± 0,4 µm	S3	180 ± 10 µm	4,0 ± 0,4 µm	S5	50 ± 10 µm	2,5 ± 0,2 µm
S2	110 ± 10 µm	1,5 ± 0,4 µm	S4	180 ± 10 µm	4,0 ± 0,4 µm	S6	100 ± 10 µm	4,3 ± 0,4 µm

Tab. 2. *Results obtained through of microhardness profiles as DIN 50190.*

4. References

[1] P. W. TONG., R. N. TAO., B. Z. WANG., J. LU., K. LU "*Nitriding iron at lower temperatures*", Article in Science., **299**, 686-688, (2003).

[2] F. ASHRAFIZADEH "*Influence of plasma and gas nitriding on fatigue resistance of plain carbon (Ck45) steel*", Surf. & Coat. Tech., **174-175**, 1196-1200, (2003).

[3] L. C. FONTANA "*Nitretação iônica em aços baixo carbono*" Tese de M.Sc., CCFM/UFSC, Florianópolis, SC, Brasil, 1991.

Acknowledgments

The Santa Catarina State University for the financial support and CAPES for the scholarship awarded.

*deivisonpaim@gmail.com

ID 116: INFLUENCE OF THE 316L STAINLESS STEEL SUBSTRATE ROGHNESS ON THE MAGNETRON SPUTTER DEPOSITON OF TI-NB COATINGS

P.S. Sato[1]*, E.D. Gonzalez[1], A.L. Gobbi[2], P.A.P. Nascente[1,3]*

[1]*Universidade Federal de São Carlos, Programa de Pós-Graduação em Ciência e Engenharia de Materiais, 13565-905, São Carlos, SP, Brasil.*

[2]*Centro Nacional de Pesquisa em Energia e Materiais, Laboratório Nacional de Nanotecnologia, 13083-970, Campinas, SP, Brasil.*

[3]*Universidade Federal de São Carlos, Departamento de Engenharia de Materiais, 13565-905, São Carlos, SP, Brasil.*

1. Introduction

Titanium alloys are employed as orthopedic and dental implants. Niobium has been shown to be a nontoxic β-stabilizing agent, and β-Ti-Nb (body centered cubic structure) alloys have been reported to be promising for biomedical applications [1]. However, the cost of Ti-Nb implants is much higher than most of the metallic biomaterials, such as the 316L stainless steel (SS), although the later alloy do not have biocompatible characteristics as good as the ones presented by β-Ti-Nb. Thus, coating the SS implant with a Ti-Nb thin film would be an interesting option. A coating with adequate composition and thickness would enhance the material biocompatibility [2-4]. In the present study, Ti-Nb coatings were deposited on 316L SS substrates by magnetron sputtering. The substrates were polished and part of them was submitted to a chemical treatment with nitric acid. The changes in roughness and composition of the coatings were analyzed by atomic force microscopy (AFM), scanning electron microscopy (SEM), and X-ray photoelectron spectroscopy (XPS).

2. Experimental

A 316L SS bar having a diameter 15 mm was cut in disks with a thickness 2 mm for producing the substrates. The substrates were fine-ground with SiC sandpaper and then polished with diamond paste. Half of them was treated with a 10% nitric acid solution at 60°C for 20 minutes. The Ti-Nb coatings were deposited using an AJA Orion 8 Phase II J magnetron sputtering system, while the substrate temperature was kept at 200°C. The power applied to the Ti target was 300 W, and 56 and 100 W to the Nb target, producing coatings with two compositions: $Ti_{85}Nb_{15}$ (Ti-26 wt% Nb) and $Ti_{70}Nb_{30}$ (Ti-45 wt% Nb). The AFM, SEM, and XPS analyses were carried out using a Bruker NanoScope V, a FEI Inspect S 50, and a Thermo Scientific K-Alpha instruments, respectively.

3. Results and Discussions

AFM micrographs showed that the chemically treated substrates were flatter than the non-treated ones. SEM micrographs informed that the thickness was 800 nm for all Ti-Nb coatings. These relatively thick coatings presented similar morphologies, indicating that they were not influenced by the differences in the substrate roughness. The Ti 2p XPS spectra were fitted with components associated to TiO_2 and Ti. The Nb 3d XPS spectra for the $Ti_{85}Nb_{15}$ and $Ti_{70}Nb_{30}$ coatings revealed at least three chemical states: Nb_2O_5, Nb_2O_3, and Nb. After Ar^+ sputtering, most of the oxide surface layer was removed for both coatings deposited on either non-treated and chemically treated 316L SS substrates.

4. References

[1] D. Kuroda *et al.*, Mater. Sci. Eng. A, **243**, 244-249, (1998).
[2] D. A. Tallarico *et al.*, Mater. Sci. Eng. C, **43**, 45-49, (2014).
[3] E. D. Gonzalez *et al*., J. Vac. Sci. Technol. A, **34**, 021511, (2016).
[4] E. D. Gonzalez *et al*., Surf. Coat. Technol., in press, (2017).

Acknowledgments

The authors would like to thank Pedro I. Paulin Filho from UFSCar/DEMa and Bruna Massucato from CNPEM/LLNano, for their assistance in the AFM and XPS measurements, respectively. PSS tanks CAPES for a scholarship. CNPq and CNPEM are acknowledged for support.

*Corresponding author: nascente@ufscar.br

ID 117: MICROHARDNESS ANALYSIS NI $NI_{35}TI_{50}CU_{15}$ BY POWDER METALLURGY MODIFIED BY PLASMA IMMERSION ION IMPLANTATION TECHNIQUE

Eliene Nogueira de Camargo[1]*, Maria Margareth da Silva[1], Mario Ueda[2], Rogério de Moraes Oliveira[2], Luc Pichon[3] and Vinicius André Rodrigues Henriques[4].

[1]*Instituto Tecnológico de Aeronáutica, Praça Mal. Eduardo Gomes, 50 – Vila das Acácias, São Jose dos Campos, São Paulo, Brazil.*

[2]*Instituto Nacional de Pesquisas Espaciais. Centro de Tecnologia Espaciais. Laboratório Associado ao Plasma. Avenida dos Astronautas, 1758, São Jose dos Campos, São Paulo, Brazil.*

[3]*Institut Pprime (PPRIME) CNRS: UPR 3346, Université de Poitiers, ENSMA, Poitiers, France.*

[4]*Divisão de Materiais (AMR/IAE/CTA) Praça Mal. Eduardo Gomes, 50 Vila das Acácias, São José do Campos, São Paulo, Brazil.*

1. Introduction

The NiTiCu SMA produced by powder metallurgy (PM) is a promising material due to variety of advantages in practical use. The addition of cooper (Cu), as ternary element, in NiTi SMA Increases the characteristic temperatures of the martensitic transformation, cause good stability of characteristic temperature, good corrosion resistance and reduces of Ti_3Ni_4 precipitation [1-5].

When this type of alloy is utilized as biomedical material, such as implants, can be occurs the rejection on the human body. One possibility is the surface modification by Nitrogen Plasma Immersion Ion Implantation (N-PIII) technique.

The hardness measure in SMA is important properties because it is a strong indicator of mechanical performance. It is interesting to note that for in NiTiCu SMA the evaluating hardness depends on temperature since the mechanical properties of SMAs are temperature dependent [5].

2. Experimental

For production of the $Ni_{35}Ti_{50}Cu_{15}$ alloy by powder metallurgy were used as starting material elemental powders Ni, Ti and Cu. The powders were mixed in pharmaceutical mixer for 150 minutes. The sample was compressed in uniaxial press at 250 MPa in cylindrical form with 9 mm in diameter and 2 mm in thickness and after cold isostatic pressed at 450 MPa. The sintering was performed at 1000 ºC for 60 minutes. The N-PIII technique was realized at 770 ºC for 60 minutes.

The microstructure of as cast and implanted by PBII samples were observed with scanning electron microscope. The phase's identification and structural parameters were established using the X ray diffraction. The microhardness test were made in the as cast sample and the surface modified sample by N-PIII using a micro Vickers indenter and a 100 g load at room temperature.

3. Results and Discussions

The morphology in surface sample before N-PIII sintered at 1000 ºC for 60 minutes showed significant pores sizes and their distribution can be observed. The porous in surface are randomly distributes, rarely interconnected and has an irregular shape. The diffratogram of the sample presented Ti_2Ni and CuTi stables phases, the metastable phase$TiCu_3$ that disappears with the increase of sintering temperature and intermetallic NiTi phase important for shape memory effect.

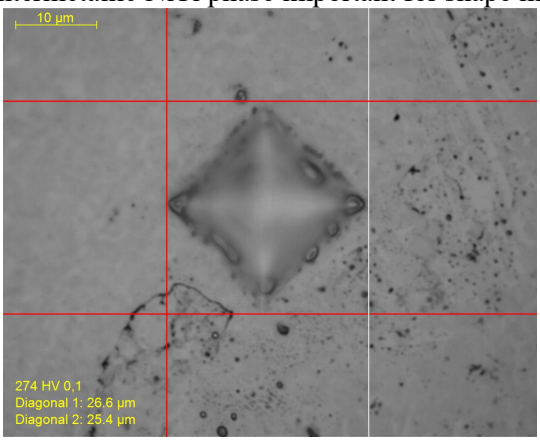

Fig. 1. *Hardness in $Ni_{35}Ti_{50}Cu_{15}$ sample sintered in 1000 C and for 120 minutes after N-PIII at 770 C for 60 minutes*

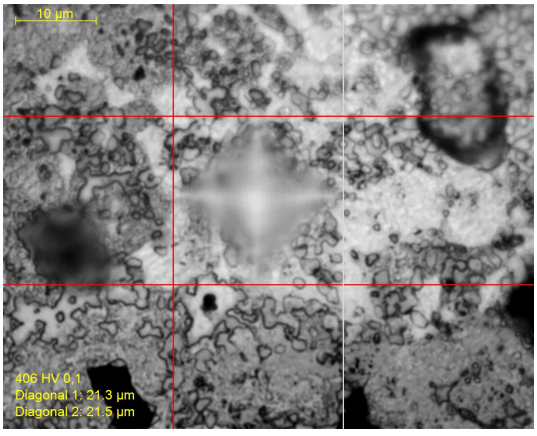

Fig. 2. *Hardness $Ni_{35}Ti_{50}Cu_{15}$ sample sintered in 1000 ° C and for 120 minutes and after N-PIII at 770 C for 60 minutes*

*elienencamargo@gmail.com

After surface modification by N-PIII at 770 ºC for 60 minutes, the implanted surface showed less quantified of porous and no presented residual particles inside. The surface demonstrated apparently roughness compared to surface sample before ion implantation (N-PIII). The diffratogram presented the TiN peaks demonstrating the surface modification occurs in the samples. However there is still the metastable phases Cu_3Ti and stable phases Ti_2Ni and Cu_2Ti affecting the mechanical properties.
In the microhardness test demonstrated that sample before surface implantation showed hardness near to 274HV and the N-PIII sample 406 HV, showed in figure 1 and 2 respectively.

4. References

[1] FUNAKUBO, H. Shape memory alloys. Translated from the Japanese by Kennedy, J. B., Stanford University. Tokyo: University of Tokyo, 1987.
[2] HUMBEECK, J.V. From a seed to a need: The growth of the shape memory application in Europe. *Material Research Society Proceedings*, v.246, p.377-387, dec. 1992.
[3] BANSIDDHI, T.D., SARGEANT, T.D., STUPP, S.I., DUNAND, D.C. Porous NiTi for bone implants: A review. *Acta Biomaterialia*, v.4, p. 773-782, dec. 2008.
[4] GANG, C., CAO, P., EDMONDS, N. Porous NiTi alloys produced by press-and-sinter from Ni/Ti and Ni/TiH_2 mixtures.
[5] GORYCZKA, T., HUMBEECK, J.V. NiTiCu shape memory alloy produced by powder technology. *Journal of Alloy and Compounds*, v.456, p.194-200, Feb. 2007.

Acknowledgments (bold face Times New Roman 11 pt)
The CNPq, INPE, ITA and PPRIME to support this project.

*elienencamargo@gmail.com

ID 119: COMPOSITE FILMS OF BARIUM-STRONTIUM TINATATE / SILVER DEPOSITED BY RF SPUTTERING: NEW SYSTEM TEST

Angel Fidel Vilche Pena*, Agda Eunice de Souza and Silvio Rainho Teixeira
Departamento de Física, Faculdade de Ciências e Tecnologia
UNESP campus de Presidente Prudente

1. Introduction

Barium-strontium titanate is a high dielectric constant material and used in many technological applications, where these dielectric properties are required. In our proposal, the composite silver / barium strontium can be very useful in view of the bactericidal properties of silver and therefore the interest of this work.

2. Experimental

We use a sputtering deposition system with targets in a confocal arrangement. A silver target was prepared with Barium-Strontium Titanate tablets placed with silver metallic adhesive. The 5 mm diameter tablets were arranged in an annular array to better utilize the 200 W RF discharge applied between the target and the substrate. For test purposes, the substrate used was a microscope slide.

3. Results and Discussions

This first film produced was made on a silver target with Barium- Strontium Titanate tablets. As the number of tablets was small, the RF deposition system of 200W during 15 min, privileged the deposition of silver in detriment of Barium- Strontium Titanate, as can be seen in the image of Figure 2. An interesting fact that will deserve later a deeper analysis is the amount of white light emitted during the deposition, which is significantly greater than any deposition of a material in a sputtering system..

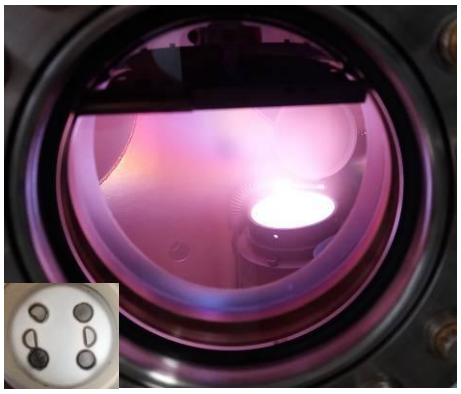

Fig. 1. *In the corner of this image, the arrangement of Bario / Strontium Titanate tablets glued to the silver target is shown. In the larger image, the RF discharge with argon gas. There is a great luminosity throughout the deposition chamber.*

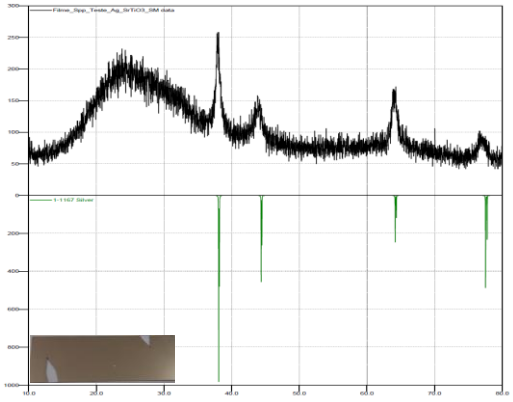

Fig. 2. *In the corner of this image, the composite film deposited on to the glass microscope slide. In the larger image, X-rays diffractometry analyze using Search Math software. Silver peaks are more significant as Titanate Barium strontium* That do not appear in this diffractogram.

Silver and Titanate Barium strontium has very different rates deposition, and the area covered by titanate was very small, favoring the growth of the silver film. Other configurations will be tested for obtaining these composites, for example Barium- Strontium Titanate target with silver plates or use of a Barium- Strontium Titanate target (RF deposition) with another silver target (DC deposition).

4. References

[1] Shih-Bin Lin, Chia-Che Chen, Li-Chen Chen, Hui-Huang Chen, The bioactive composite film prepared from bacterial cellulose and modified by hydrolyzed gelatin peptide, Jornal of Biomaterial Applications, **29**,1428-1438, (2015).

Acknowledgments
Fapesp 2013/07296-2 - CEPID - Centros de Pesquisa, Inovação e Difusão

*angel@fct.unesp.br

ID 120: TAILORING SURFACE PROPERTIES OF POLIAMIDE 6 BY PLASMA PROCESSES

Ricardo S. Hosokawa[1], Caíque Vendemiatti[1], Erica P. da Silva[1], Rafael P. Ribeiro[1], Janine S. G. de Camargo[1], Nilson C. Cruz[1], Elidiane C. Rangel[1]*

[1]*Science and Technology Institute of Sorocaba, Paulista State University, Av. Três de Março, 511 – Alto da Boa Vista, 18087-180, Sorocaba, SP.*

1. Introduction

A method largely employed to tailor the surface properties of polymers is the delineation of patterns on their surfaces. Patterned surfaces are of interest in designing sensors, for microfluidics, electronic and optical devices. Different and sophisticate approaches are normally associated to micro/nano-patterning a surface, attaining complexity and high costs to the process. In this work, integrated plasma methodologies are used for production of surfaces with regularly and randomly distributed patterns on the surface of the polyamide 6, PA-6, a widely diffused engineering thermoplastic.

2. Experimental

Commercial PA-6 pieces were submitted to different and sequential low pressure plasma treatments. Firstly, it was treated in radiofrequency (13.56 MHz, 150 W) Plasma Enhanced Chemical Vapor Deposition, PECVD, using hexamethyldisiloxane, HMDSO (70%), Ar (15%) and Oxygen (15%) mixtures. In a second methodology, samples were exposed to ablation in reactive oxygen plasma (13.56 MHz, 100 W) and subsequently to fluorination in SF_6 (13.56 MHz, 70 W) plasma. In a third procedure, PA was exposed to ablation in oxygen plasma but now using masks *(60 µm X 60 µm opening)* to remove material only from specific regions of the surface . In the last procedure describe here, PA was exposed to the PECVD process in HMDSO and Ar atmospheres using the same mask to selectively deposit the film on the surface. It was investigated the effect of these four different treatments on the surface chemical composition (EDS), molecular structure (IR), morphology (SEM), topography (AFM) and wettability (θ) of the samples.

3. Results and Discussions

Films deposited on the PA surface were characterized as organosilicon (50% C, 25% O and 25% of Si) containing Si-O, $Si(CH_3)_x$ and C-H groups. They changed morphology and topography of PA-6, attaining a hydrophobic character (100°) to the initially hydrophilic (64°) material. On the other hand, surfaces as hydrophobic as Teflon (~120°) were created as PA surface was ablated in oxygen plasma and aged in air (Fig.1). Upon fluorination contact angle further increased reaching around 154°. Surface morphology and topography are greatly changed by oxygen ablation but only slightly changed in the fluorination process. Patterns in the form of tanks and pillars were regularly defined on the surface of PA-6 by oxygen ablation and organosilicon film deposition, respectively, with the aid of masks. Structures height, surface topography and morphology were dependent on the plasma excitation parameters. Possible applications for the surfaces prepared here are proposed.

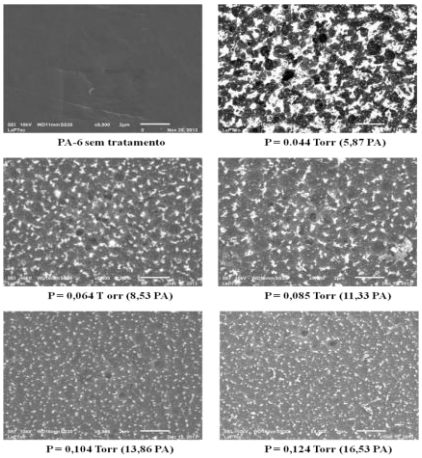

Fig. 1. *Secondary electrons micrographs of the PA-6 samples exposed to oxygen ablation using different plasma pressures. Bar scale in the micrographs are 2 µm long.*

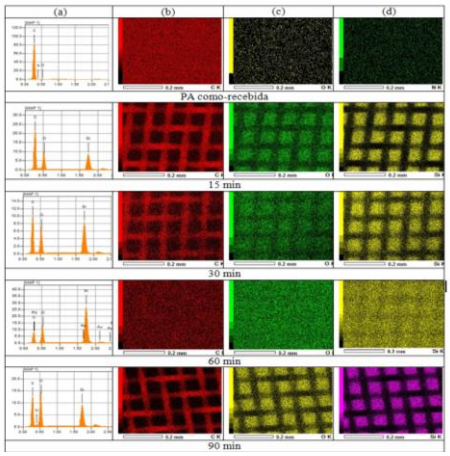

Fig. 2. *EDS spectra (a) and C (b), O (c) and Si (d) mapping of the as-received and organosilicon plasma deposited PA with the aid of masks. Mask opening 60 µm X 60 µm.*

*Corresponding author: place the email of the corresponding author here (bookman old style 9 pt)

Acknowledgments
Authors thank to the financial support supplied by FAPESP (2012/14708-2) and CNPq (PIBIC-25874 and 302446/2012-5).

* Corresponding Author: elidiane@sorocaba.unesp.br

*Corresponding author: place the email of the corresponding author here (bookman old style 9 pt)

ID 122: ELECTROCHEMICAL BEHAVIOR OF HMDSO POLYMER FILM DEPOSITED BY ATMOSPHERIC PRESSURE PLASMA JET

Leide Lili G. da Silva[1,2]*, Pedro V. M. Fagundes[1], Felipe V. P. Kodaira[2], and Konstantin G. Kostov[2]
[1] *Faculdade de Tecnologia de Pindamonhangaba – FATEC, Pindamonhangaba, SP, Brazil*
[2] *Faculdade de Engenharia de Guaratinguetá – FEG, Universidade Estadual Paulista – UNESP, Guaratinguetá, SP, Brazil*

1. Introduction

Nowadays there exist several methods to protect metallic surfaces from corrosion, such as, cathodic protection, paintings, anodization, film deposition, etc. Among these, polymer films are widely used in different industries because they are applied as adhesion promoted layers, barriers and also protection coatings [1]. The polymer films obtained by plasma processing possess great advantage compared to the painting layers, since do not require use of solvents and cure time for its application [2]. On the other hand the anodization process produces toxic sub-products to the environment. In this context, the aim of this work is to investigate electrochemical behavior of hexamethyldisiloxane (HMDSO) film obtained by Atmospheric Pressure Plasma Jet (APPJ) on SAE 1020 steel for the corrosion protection.

2. Experimental

The substrates used in this work were SAE 1020 steel discs. The plasma jet system consists of a 18.0-mm-diam Pyrex tube terminating with a horn-like nozzle, a HV electrode placed inside it and a grounded electrode covered by glass table that is placed beneath the tube. Plasma was excited by an AC power supply operating at 19.0 kHz and voltage amplitude of 15.0 kVp-p. The device was flushed with 1.0 L/min argon flow resulting in an approximately 10-mm-long plasma plume, which was extracted from the tube exit. In order to deposit polymer film a mixture of air/HMDSO at flow rate of 1.0 and 1.5 L/min was introduced into the discharge. Samples were exposed to the plasma jet for 5.0, 10 and 15 min using a nozzle-to-sample distance of 6.0 mm. The samples were characterized by electrochemical tests such as open circuit potential (OCP), impedance electrochemical spectroscopy (EIS) and polarization curves. These measurements were carried on an Autolab 302 N potenciostat using a conventional three-electrode glass cell. The reference and auxiliary electrodes were Ag/AgCl and Pt rod electrodes, respectively. All electrochemical experiments were conducted in 3.5% NaCl solution at room temperature.

3. Results and Discussions

Results of OCP as a function of the time showed similar constant potential behavior with the time for all samples. However, OCP values of coated samples are more positive (noble) when compared to the uncoated sample, which potential is around -0.65 V.

After OCP measurements, the Electrochemical Impedance Spectroscopy analysis was conducted and the capacitance of HMDSO film on the SAE 1020 steel substrate was calculated. According to some authors [3] the coating capacitance (C_c) reflects the electrolyte permeation in the coating. The smaller the diameter of the first semi-circle in the Nyquist diagram, the higher will be the solution permeation in the coating, which means that it will have higher values of Cc. On the other hand, when the first semi-circle diameter is larger, the solution permeation on the coating will be diminished and the Cc value will be smaller. Coated samples obtained smaller Cc values, thus it can be inferred that the HMDSO coating on SAE 1020 steel samples had lower electrolyte permeation when compared to the uncoated sample ($1.4x10^{-5}$ F/cm^2). After EIS measurements, polarization curves were obtained and the corrosion potential (E_{corr}) and current density (i_{corr}) were found. It is possible to see that, the HMDSO film on the SAE 1020 steel provided a decrease of the i_{corr} and an increase of E_{corr} when compared to the uncoated sample of 4.10^{-7} A/cm^2 and -0.67 V, respectively. It means that, the HMDSO coating on the substrate has a higher corrosion resistance.

Acknowledgments
The author thanks to the Plasma and Applications group, DFQ-UNESP by the polymer films depositions.

4. References

[1] U. Lommatzsch and J. Ihde, Plasma Processes and Polymers. **6**, 642, (2009).
[2] C. Regula, J.Ihde, U. Lommatzsch and R. Wilken, Surf. & Coat. Tech., **205**, 5355-5358 (2011).
[3] F. Fredrizzi, F.J. Rodriguez, S. Rossi, F. Deflorian and R.D. Maggio. Electrochim. Acta, **46,** 3715-3724 (2001).

*leide.kostov@fatec.sp.gov.br

ID 123: EFFECTS OF PLASMA IMMERSION ION IMPLATATION ON FATIGUE PROPERTIES OF TITANIUM ALLOY SURFACES

Maria Luiza Rinaldi de Souza[1,3]*, Bruno Bacci Fernandes[1,2,3], Stephan Mändl[2], Rogério Moraes Oliveira[1], Mario Ueda[1], Alfeu Saraiva Ramos[4]

[1] *Instituto Nacional de Pesquisas Espaciais, LAP/INPE, Av. dos Astronautas 1758, Caixa Postal 515, São José dos Campos, SP, Brazil*

[2] *Leibniz Institut für Oberflächenmodifizierung, Permoserstrasse 15, 04318 Leipzig, Germany*

[3] *Universidade Braz Cubas – Mogi das Cruzes, SP, 08773-380, Brazil.*

[4] *Universidade Federal de Alfenas, UNIFAL, Rod. José Aurélio Vilela, 11999, 37715-400, Poços de Caldas, MG, Brazil*

1. Introduction

Lightweight materials capable to withstand high temperatures with friction and/or oxidation are a demand imposed by several transportation and power generation systems, as in high speed aircrafts and engines, respectively. In order to comply with such requirements, the improvement of surface properties of these materials is essential, as well as the understanding of the links among their composition, processing method, microstructure and properties [1]. In addition, high temperature resistant alloys must combine two major requirements when thermal cycles are applied: low scale growth rate and adequate scale adherence [2]. Materials such as stainless steels, refractory metals and alloys, and superalloys are especially creep-resilient and commonly employed in high temperature service applications [3]. Nevertheless, modern surface functionalization is often applied. Ion implantation and its variants are still rarely commercially used for metal alloys – while they are state-of-the-art and indispensable for semiconductor applications. Especially the poor tribological properties of titanium alloys had hampered the increase of their technological applications [4], while PIII has been very effective in improving their tribological properties [5], and consequently in increasing their lifetime. PIII is especially promising because it allows the transference of laboratory processes to industrial applications. Three-dimensional characteristic is one of the reason for such possibility, i.e. the entire surface of parts with complex shapes can be treated without changing their masses [6]. Independent temperature control is another advantage, since simultaneous heating of the substrate is crucial for the treatment of Ti alloys to promote diffusion of the implanted ions [7] In this work, nanoindentation tests were employed to study the mechanical fatigue properties of titanium alloys (sintered Ti-Si-B and commercial Ti-6Al-4V) surface modified by HTPIII. The results after the plasma treatment are correlated with reciprocating wear tests and elemental depth profiles obtained by secondary ion mass spectroscopy (SIMS).

2. Experimental

High-purity elemental powders - Ti, Si and B - were used in this work to prepare four different powder mixtures: Ti-5.5Si-20.5B, Ti-7.5Si-22.5B, Ti-16Si-4B and Ti-18Si-6B. The milling process was carried out at room temperature in a Fritsch planetary ball mill under an argon atmosphere using rotary speed of 240-300 rpm, a ball-to-powder weight ratio of 10:1 and stainless steel vials (225 ml) and balls. The mechanically alloyed powders were uniaxially pressed for 2 minutes at 110 MPa and then isostatically pressed for 1 minute at 300 MPa, both operations being performed at room temperature. Subsequently, these green compacts were hot-pressed with 30 MPa and 1100oC for 20 minutes into a graphite die under argon atmosphere. Before HTPIII treatment, the samples were grounded on SiC papers and polished with colloidal silica suspension. Additional Ti-6Al-4V sample discs of 15-mm diameter and 3-mm thickness were also grounded, polished and cleaned in ultrasound acetone bath. For the present experiments, each titanium alloy sample was connected to a tungsten wire that in turn was fixed on a stainless steel rod playing the role of the discharge anode. This assembly was positively polarized to + 700 VDC in relation to the grounded chamber wall and simultaneously by negative HV pulses of -7 kV (length of 30 □s and repetition rate of 400 Hz). This process was operated in vacuum environment in nitrogen atmosphere at a working pressure of 10-3 Torr for 60 min. A thermionic oxide cathode generates primary electrons to ignite the glow discharge and to heat the substrate up to 800oC. The implantation of nitrogen ions takes place when the high negative voltage pulses are applied. The nitrogen depth profiles implanted into Ti alloys were measured using time-of-flight secondary ion mass spectrometry (ToF-SIMS). Tribological evaluations of the sample surfaces were conducted with a CSM tribometer with measurements of the dry friction coefficient accomplished in an oscillating ball-on-disk tribometer. The following parameters were used: load of 1 N with a 4.76-mm diameter alumina ball as a counterpart material, maximum speed of 10 cm/s and total track length of 2 mm. The afflicted surfaces after the wear test were examined using a scanning electron microscope employing the

*Corresponding author: mlrinaldis@hotmail.com

secondary electron detector mode to find out more information about the wear mechanisms. Roughness and surface profiles after wear test were measured with an optical profilometer. Additionally, dynamic nanoindentation was employed for surface characterization with conventional nanohardness being measured using a quasi-continuous stiffness measurement (QCSM). The employed indenter was a Berkovich three-sided pyramidal diamond. An average of 10 single measurements was used to determine the average hardness. Furthermore, the nanofatigue tests were conducted in the same nanoindentation equipment, however now with a spherical diamond indenter (tip radius of 10 μm). The samples were subjected to cyclic contact tests by repeatedly indenting the same area at maximum loads of 100-750 mN with minimum loads of 1.0-7.5 mN, respectively. A larger number of cycles were performed at the same position by repeating this 300-cycle experiment several times. Using the same spherical indenter, nanowear experiments were performed with loads of 10, 50 and 100 mN to make tracks with 80-μm length.

3. Results and Discussions

For the Ti-6Al-4V sample after HTPIII the SIMS experiments identify a nitrogen-rich layer with a thickness of about 1 μm. The untreated samples show a barely visible nitrogen signal below the surface oxide, indicating a large nitrogen uptake and retention during the HTPIII process. The roughness (Ra) is always increased after nitrogen implantation: for the commercial Ti alloy from 40 nm to up to 220 nm, as verified by optical profilometry. The sintered Ti-16Si-4B alloys present higher roughness in untreated condition (around 110 nm) and the HTPIII further increases this value to around 160 nm. Reducing the lengthscale of the experiments, nanowear experiments with a diamond tip also confirm that the HTPIII treatment significantly increased the wear resistance of the Ti-6Al-4V surface. Thus, a combination of resistance to plastic deformation (i.e. higher hardness) and resilience (increased wear resistance) can be inferred for both HTPIII treatments and Ti-Si-B alloys.The nitrogen implantation increased the hardness of the Ti-6Al-4V alloy three times, which is evidence of the presence of a titanium nitride phase in this surface region. However, the Ti-Si-B alloys had almost no increase of such property as the original hardness is already similar to the hardness of the nitrided Ti-6Al-4V alloy. It is concluded the process of nitrogen plasma immersion ion implantation at high temperature generates a surface layer rich in nitrogen that reduces the coefficient of friction and wear rate of a conventional Ti-6Al-4V alloy. This treatment also increases hardness, whilst it decreases the fatigue resistance due to surface embrittlement. In sintered Ti-Si-B alloys has a much smaller effect as a lower nitrogen amount is retained than in the commercial Ti-6Al-4V alloy, since in such alloy there are phases of high hardness and oxidation resistance, making difficult the implantation of the nitrogen at similar temperatures. These new alloys already present high hardness and wear resistance, but they also show low fatigue resistance, even without nitrogen addition at the surface. The results indicated that both HTPIII treated alloys showed improvements.

4. References

[1] J. C. Williams, E. A. Starke Jr., Acta Mater. 51 (2003) 5775-5799.
[2] F. Riffard, H. Buscail, E. Caudron, R. Cueff, C. Issartel, S. Perrier, Appl. Surf. Sci. 252 (2006) 3697-3706.
[3] W. D. Callister Jr., Materials Science and Engineering: An Introduction, John Wiley & Sons, Inc., New York, NY, 2007, p. 243.
[4] M. M. Khaled, B. S. Yilbas, I. Y. Al-Qaradawi, P. G. Coleman, D. Abdulmalik, Z. S. Seddigi, A. Abulkibash, B. F. Abu-Sharkh, M. M. Emad, Surf. Coat. Technol. 201 (2006) 932-937.
[5] R. Wei, T. Booker, C. Rincon, J. Arps, Surf. Coat. Technol. 186 (2004) 305-313.
[6] J.R. Conrad, J.L. Radtke, R.A. Dodd, F.J. Worzala, J. Appl. Phys. 62 (1987) 4591-4596.
[7] D. Manova, J.W. Gerlach, H. Neumann, W. Assmann, S. Mändl, Nucl. Instrum. Meth. B 242 (2006) 282–284

Acknowledgments

The authors acknowledge God for empowering them, and several other contributors. This work was partially supported by FAPESP and CNPq (National Research and Development Council) development agencies.

*Corresponding author: mlrinaldis@hotmail.com

ID 124: SiC/Cr THIN FILMS DEPOSITED BY HiPIMS ON Ti-6Al-4V USED AS PROTECTIVE COATING IN CREEP TESTS

Tarcila Sugahara[1], Fabiano E.Momtoro[2], Gislene Valdete Martins [3], Marcos Massi [3,4], Adriano Gonçalves dos Reis[5,6], Danieli Aparecida Pereira Reis[1,2]*

[1]*Universidade Federal de São Paulo (UNIFESP), Instituto de Ciência e Tecnologia, São José dos Campos.*
[2]*Laboratório Nacional de Nanotecnologia, CNPEM, Campinas, São Paulo, Brasil*
[3]*Instituto Tecnológico de Aeronáutica (ITA), Materiais e Processos de Fabricação, São José dos Campos.*
[4]*Universidade Presbiteriana Mackenzie (UPM), Engenharia de Materiais, São Paulo.*
[5]*Universidade Estadual Paulista (Unesp), Instituto de Ciência e Tecnologia, São José dos Campos.*
[6]*Instituto de Pesquisas Energéticas e Nucleares (IPEN), Ciência e Tecnologia de Materiais, São Paulo.*

1. Introduction

Ti-6Al-4V alloy is the most widely titanium alloy used in the aerospace industry due to its excellent properties such as high mechanical strength, corrosion and creep resistance. However one of the major factors limiting the life of titanium alloys in service is their degradation particularly in environments containing oxygen at elevated temperatures during long-term use causing oxidation and reducing creep resistance and consequently the lifetime [1,2]. In order to associate these two techniques (heating and surface treatments) and evaluate the Ti-6Al-4V creep behavior, SiC film was chosen like surface coating. SiC properties like good mechanical resistance, high hardness, high thermal conductivity and very high thermal stability make it attractive coating [3]. These SiC coatings can be used from protective layer against the corrosion of steel to microelectronic devices, and from X-ray mask materials to the protection of thermonuclear reactor walls, among others [4]. Costa et al. carried out an investigation of SiC films deposited by RF magnetron sputtering, with the aim of developing a material for applications as metallurgical and protective coatings. The results showed that films with hardness values larger than that of crystalline SiC can be produced, provided that Si and C sputtered atoms can reach the surface of the growing film with sufficient high energy and low deposition rates, ensuring a high surface mobility [5]. Thus, in this paper we carried out an investigation of SiC/Cr films deposited by HiPIMS on Ti-6Al-4V alloy with Widmanstätten microstructure in creep tests, aiming developing a material as protective coating. SiC/Cr film mechanical properties were evaluated through scratching test, SEM, STEM, EDS and creep test.

2. Experimental

SiC thin film and Cr interlayer were deposited by HiPIMS on Ti-6Al-4V surfaces samples. Initially, the depositions were made in blank samples for subsequent microstructural and tribological Si/Cr film characterization. After this first stage, SiC/Cr coatings were deposited on the creep tests samples surface. The coatings were deposited using a home-made stainless steel cylindrical reactor. An argon plasma was used to sputter high purity 4.00" targets of (99.95%) SiC and (99.95%) Cr.

3. Results and Discussions

Figure 1 show SEM images of SiC film deposited on Ti-6Al-4V alloy with Cr interlayer. From the images 1B and 1C, it can be observed that the thin films grow in a columnar shape and the surface is very compact and homogeneous. Spherical shaped small nodules were observed on the surface Fig.1A. A similar morphology with larger nodules also was observed on coatings grown at low Si target power, regardless of temperature for the SiCxNy coatings by Pettersson et al [6].

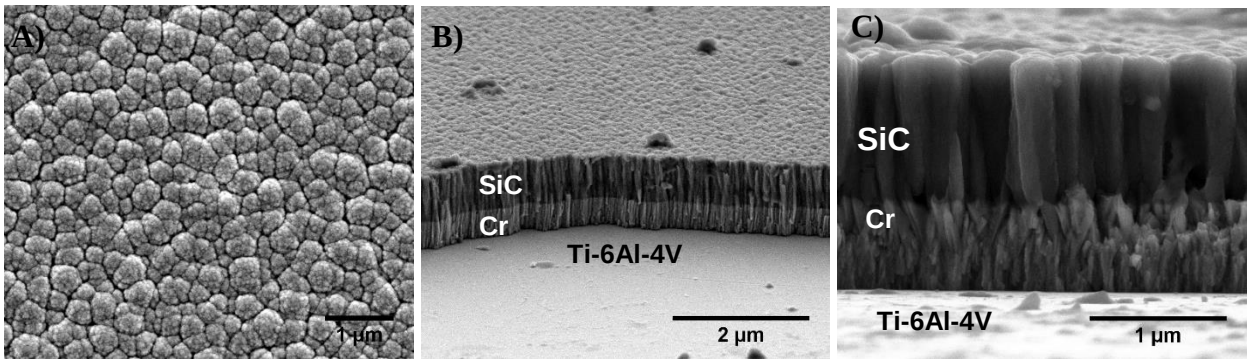

Fig. 1. *SiC film deposited on Ti-6Al-4V alloy with Cr interlayer, image obtained by SEM. (A) Overview, (B) Magnified overview and (C) Detailed layers view.*

*Corresponding author: danieli.reis@unifesp.br

Figure 2 presents creep curves at 600 °C and 250 MPa for Widmanstätten microstructure Ti-6Al-4V sample [7] and the Ti-6Al-4V sample with Widmanstätten microstructure and SiC film. It can be seen for the specimen with SiC film lifetime was higher, indicating a longer life in creep relative to the specimen without the SiC film. It is also observed that the creep rate in stationary stage is lower for SiC film specimen and the curve slope is lower than in specimen without SiC film curve, showing once more increasing creep resistance for the alloy with SiC film application. The improvement in steady state creep rate and time to fracture is attributed to the SiC coating presence, which is oxidation resistant. It can be concluded preliminarily by comparing the curves and creep parameters between the alloy with and without SiC film, that the SiC film was effective in protecting against oxidation of Ti-6Al-4V.

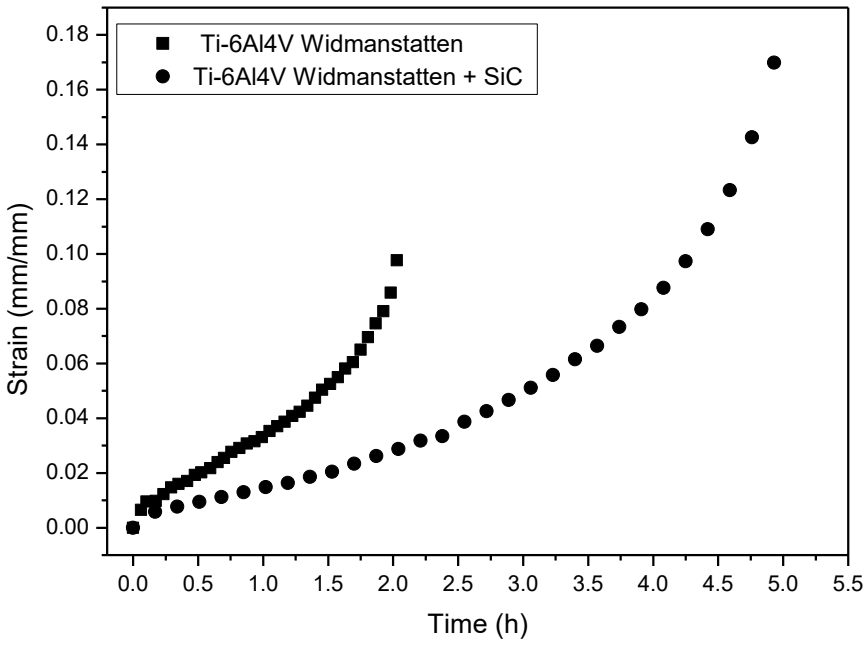

Fig. 2. *Creep curves at 600 ° C and 250 MPa of Widmanstätten microstructure Ti-6Al-4V sample [7] and Widmanstätten microstructure with SiC/Cr film Ti-6Al4V sample.*

4. References

[1] D.V.V. Satyanarayana and M.C. Pandey, Scripta Metallurgica et Materialia, **25**, 2273-2278, (1991).
[2] D. Eylon, S. Fujishiro, Pamela J. Postans, , F. H. Froes, Physical & Mechanical Metallurgy, **36**, 55–62, (1984).
[3] L. Gou, Ran J. Qi C and C. Zheng C. Thin Solid Films, **345**, 42-44, (1999).
[4] P.R. Chalker, C. Johnston, S. Romani, C.F. Ayres, I.M. Buckley- Golder, G. Kr¨otz, H. Angerer, G. Müller, S. Veprek, T. Kunstmann, W. Legner, L. Smith, A.B. Leesse, A.C. Jones, S.A. Rushworth, Diamond Relat. Mater. **4**, 632, (1995).
[5] A.K. Costa, S.S. Camargo Jr., C.A. Achete, R. Carius; Thin Solid Films, **377-378**, 243-248, (2000).
[6] M. Pettersson, T. Berlindb, S. Schmidt, S. Jacobsona, L. Hultmanc, C. Perssona, H. Engqvist, Surface & Coatings Technology **235**, 827–834, (2013).
[7] L.A.N.S Briguente, *Estudo de Tratamento térmico e recobrimento como forma de barreira térmica sobre o comportamento em fluência da liga Ti-6Al-4V*. 2012. 120 f. Dissertação (Mestrado em Engenharia Mecânica-Aeronáutica) - Instituto Tecnológico de Aeronáutica.

Acknowledgments

This work was supported by CAPES. The authors thank ITA for the use of the HiPIMS reactor and creep furnace, UNIVAP for the use of tribometer and LNNano/CNPEM for the use of SEM and FIB equipments.

*Corresponding author: danieli.reis@unifesp.br

ID 127: EFFECT OF PLASMA TREATMENT ON THE CORROSION RESISTANCE OF CARBON STEEL

Rafael Parra Ribeiro[1], Rita de Cássia Cipriano Rangel[1], Felipe Oliveira Fernandes[1], Guilherme Rodrigues Barbazza[1], Nilson Cristino Cruz[1], Steven Frederick Durrant[1] and Elidiane Cipriano Rangel[1]*

[1]*São Paulo State University (UNESP), Institute of Science and Technology, Sorocaba*

1. Introduction

Due to its excellent mechanical properties, weldability and low cost [1], carbon steel is a widely used material in a wide range of segments, such as civil construction, tools, transportation and household appliances. However, carbon steel is readily oxidized when exposed to the environment. To avoid this problem, some works suggest the development of protective coatings, using the plasma deposition technique based on HMDSO compound. Altering the plasma parameters, it is possible to deposit films with characteristics ranging from organic to oxide. Silicon oxide films are more resistant to corrosion than the organosilicon ones, however its physical stability is lower, which affect its efficiency and therefore its practical application. Aiming to associate the favorable properties of both, this work investigated the possibility of coating carbon steel with $SiO_xC_yH_z/SiO_2$ bilayer systems that have improved barrier properties by combining deposition and oxidation methodologies in low pressure plasmas.

2. Experimental

$SiO_xC_yH_z$ film was deposited for 1800 s by PECVD in an atmosphere composed by HMDSO (14 Pa), O_2 (4 Pa) and Ar (2 Pa). The total pressure of the gases was 20 Pa. The plasma was generated by applying radiofrequency signal (13.56 MHz, 150 W) to the sample holder. After deposition, the coating was treated by immersion in O_2 plasma (3.33 Pa, 13.56 MHz, 3600 s) in order to create a silica-type layer. It was investigated the effects of excitation power of the O_2 plasma (10-300 W) on the properties of the films. EIS were used to evaluate the layer protection against corrosion. The thickness of the films was measured by profilometry while the morphology and roughness was determined by AFM. The molecular structure and chemical composition of the samples were analyzed by FTIR. SEM and EDS were allied in this work to determine the surface morphology and elemental composition of samples prepared on carbon steel. Finally, the surface chemical composition and the chemical state of the detected elements were investigated by XPS.

3. Results and Discussions

The analysis of the molecular structure of the samples by FTIR allowed to verify the organosilicone nature of the starting material with degree of crosslinking greater than that found in conventional polydimethylsiloxane. The treatment with oxygen plasma has oxidative action on the layer when it removes methyl groups and incorporates oxygen and hydroxyl in the sites where initially methyl groups were found. Considering the results of XPS, it is noted that the as-deposited film has 47% C, 24% O and 29% Si. Conventional silicone ideally has a composition of 50% C, 25% O and 25% Si. With the treatment in oxygen plasma, the loss of C and the increase in the proportion of O and Si are noted. The thickness of the as-deposited film is around 1.5 μm. For treatments conducted on low power plasmas (<50W) no significant variations in thickness are observed. However, a clear downward trend appears for treatments with potencies above 25 W. These behaviors are due to the process of removal of species from the layer by the plasma being dependent on the excitation power of the O_2 plasma. In general, analysis of the morphology and topography of the samples showed that there is a clear reduction in the grain boundaries that constitute the organosilicone structure after the oxidation treatment, resulting in a more continuous surface than the untreated one. The analyzes obtained by EIS showed improvements in the performance of the system against corrosion by the deposition of the organosilicone layer. The oxidation process did not bring extra advantages when carried out under conditions of low (10 to 25 W) and high (100 to 300 W) energies. However, under conditions of moderate energy (50 W), the results point to the creation of a bilayer system with higher resistance to electrochemical attack than the organosilicone layer, even having a lower thickness than this one.

4. References

[1] J. R. Davis *"Corrosion:Understanding the Basics"*, 1nd edition, ASM International, USA, (2000).

Acknowledgments

Authors would like to thank CAPES and FAPESP for their support.

*Corresponding author: elidiane@sorocaba.unesp.br

ID 128: ATMOSPHERIC PLASMA TREATMENT FOR PCB ADHESION ENHANCEMENT

André Bianchi Laraia[1*], Milton Eiji Kayama, Luis Rogério de Oliveira Hein and Roberto Yzumi Honda
[1]*São Paulo State University (UNESP), Campus Guaratinguetá*

1. Introduction

Plasma produced by electric discharges in gases at atmospheric pressure has been intensively investigated for new technologies and industrial applications. On printed circuit board (PCB) and electronic assembly industry this is a dry and environmental friendly technique for removing residue (desmearing) left behind by laser drilling of vias and activate the material surface so strongly that it becomes receptive to all coating, printing or adhesive bonding process [1].The goal of the present project is to study how atmospheric plasma treatment can enhance the PCB manufacture process, by analyzing the contact angle of different substrates for PCB before and after plasma treatment and, later on, testing the adhesion of the metallization on the surface and in plated through hole.

2. Experimental

The device used is shown in Figure 1. It consists in a hollow-cathode electrode made with a needle and a borosilicate capillary in which argon gas flows through 0.75 l/min. The discharge is generated by a switching power supply in conjunction with a pulse transformer cascade, which supplies 5.5 kV peak-to-peak for dielectric breakdown.

The plasma jet is used to treat phenolic and fiberglass substrate samples cleaned with deionized water in the ultrasonic cleaner for 10 minutes. The major parameters are: plasma treatment time, varying from 1 second to 120 seconds and distance between plasma jet and surface (0 mm and 5 mm). The contact angle of the samples is measured and compared to the angle of an untreated control substrate sample.

3. Results and Discussions

As shown in Figure 2, the contact angle decays with the increase of the treatment time and increases with the distance between the sample surface and the plasma jet, just as expected. This decrease in contact angle shows that the surface has become more hydrophilic.

Therefore, the next step is to test different metallization methods, such as electrolysis and plasma deposition, in treated and untreated samples and to verify the adhesion force between the copper layer and the substrate.

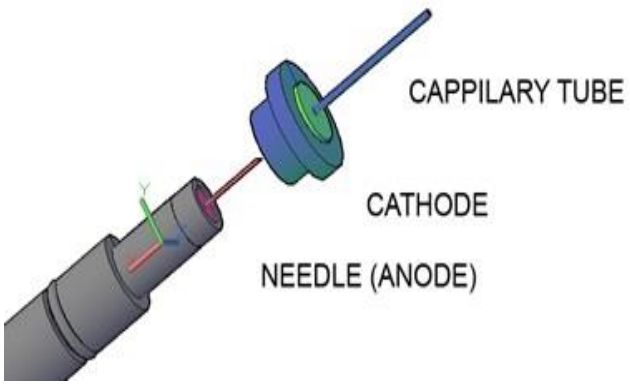

Fig. 1. *Schematic of the atmospheric plasma device used on surface treatment.*

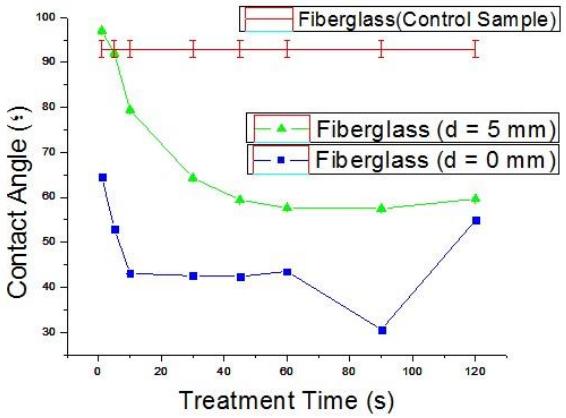

Fig. 2. *Contact angle with varying treatment time for different distances between jet and sample.*

4. References

[1] I. A. Melamies "Atmospheric Plasma Treatment". The PCB Magazine**,** v. 2, n. 8, p.68-74, ago. (2012).
[2] M. E. Kayama, L. J. Silva, V. Prysiazhnyi "Characteristics of Needle-Disk Electrodes Atmospheric Pressure Discharges Applied to Modify PET Wettability". IEEE Transactions on Plasma Science, p.843-848 (2017).

andreblaraia@yahoo.com.br

ID 130: STUDY OF ALUMINOS REFRACTORY MICROSTRUCTURE AFTER USE IN RACE CHANNEL

Ana Valéria de Sousa Costa[1], Antônio Renato Bigansolli[1]

[1] *Federal Rural University of Rio de Janeiro-UFRRJ*

1. Introduction

A ceramic is considered to be refractory when it withstands temperatures above 1500 ° C, without suffering any deformation or softening. Refractory materials have high melting point, are resistant to corrosion when subjected to severe environments with the presence of metals and slag [1]. For this reason they are present in several segments, such as civil construction in use in grills, and in the industry used as thermal insulation.

According to Lobato [2], the metallurgical industry is the main responsible for the consumption of refractories, in 2008 reached a level of 500 thousand tons mostly consumed by the steel mills. This number should reduce following a national and international trend, this is due to the technological advances occurred in the improvement and development of new materials.

The blast furnaces reach an internal temperature of 1500 ° C, for which thermal insulation is used with refractory bricks, in each region a type of refractory is used according to working temperature. The leakage of the furnace takes place in the race room through a hole that is subsequently buffered with a refractory mass responsible for the sealing of this hole. The iron leaks through a channel to the car torpedo, the temperature of the iron reaches 1600 ° C, the wear of this channel is due to thermal shock, iron abrasion in the refractory, with this there is a need to exchange this one every 150 thousand Tonnes of pig iron produced.

2. Experimental

2.1 X-Ray Diffraction

X-ray diffraction (XRD) is used to show the phases and the crystalline structure of the compounds present in the refractory if they are in the form of oxides or compounds. Therefore, the XRD technique is widely used to determine the phases present in the refractory after operation and, consequently, to determine the mechanism of failure in the scorification conditions [3]. The XRD analysis was performed using a MiniFlex II diffractometer using Cu-ka radiation (1.541870 A).

2.2 Infrared Fourier Transform Spectroscopy

. The alumina refractory sample was analyzed in the Brunker Vertex FT-IR ATR (Attenuated Total Reflectance). The analysis range was 500-4000 cm-¹.

3. Results and Discussions

3.1 DRX

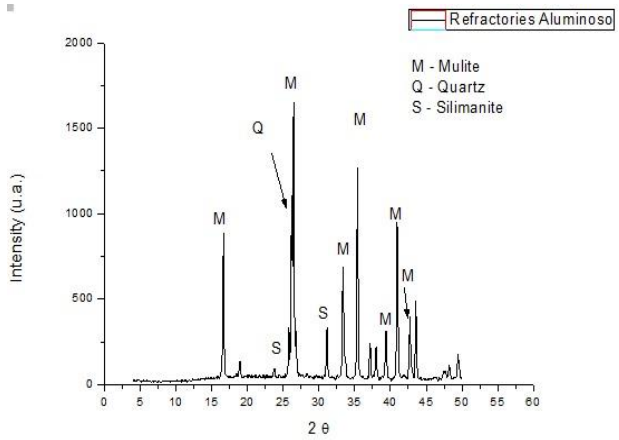

Fig. 1. *X-ray diffractogram of alumina refractory brick.*

3.2 FTIR

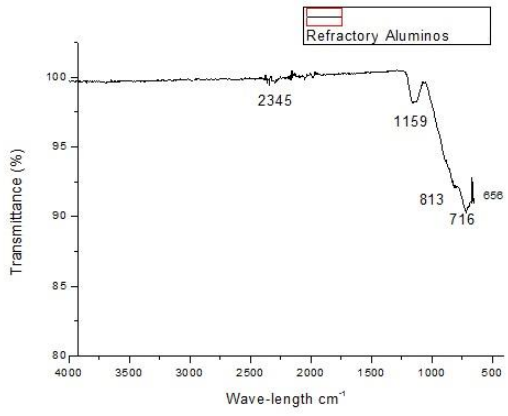

Fig. 2. *Spectrum of alumina refractory brick.*

valeriajw@hotmail.com

The mineralogical phases identified were mullite, quartz, and silimanite. Mullite is rarely found in nature, it is artificially obtained from silica and alumina. One of the ways of obtaining the mullite is by heating the silimanite that turns into mullite with liberation of silica, are found very pure, with only 1% of iron oxide and a little titanium. These impurities bind the liberated silica and the lumina to form the vitreous phase the quartz, their proportion will depend on the content of impurities and the temperature of the burning.

In the spectrum of the alumina refractory were identified at bands 1109 to 1062 cm -1 and at 813 and 653 cm -1. According to Low and MoPherson (1989, apud BONZANO, 1991, P.97) [5] the first bands are related to the vibrations and stretching of Si-O bonds and the other two are results of vibration $Al^{IV} - O$ e $Al^{VI} - O$, respectively.

4. References

[1]SILVA, G. Refratários para siderurgia. In: MOURÃO, M.: etal. **Introdução á Siderugia.** Edição 2007. São Paulo: Associação Brasileira de Metalurgia, Materiais e mineração (ABM). Capítulo n° 9. 257-265.

[2]LOBATO, E. **Refratários. Desenvolvimento de estudos para elaboração do Plano Duodenal (2010-2030) de Geologia, mineração e transformação mineral.** Brasília, 2009. 22p. Relatório Técnico 71: versão internet. Disponível em : HTTP://www.mme.gov.br. Acesso em 16 de abril de 2017.

[3] HANCOCK, J D. **Practical refractories.** Huddersfield:

Cartworth Industries, 1988. 371p.

[4]CRUZ, C.R.V. Definição e Generalidade. **Refratários para Siderurgia**. Edição 1979 São Paulo: Associação Brasileira de Metais (ABM), 1979.

[5] BOZANO, D.F, Dissertação de Mestrado. Preparação e Caracterização de Cerâmica Tipo Mulita Pelo Processo Sol-Gel, apresentada ao Instituto de Física e Química de São Carlos – USP, fevereiro de 1991

valeriajw@hotmail.com

ID 132: PLASMA POLYMERIZATION OF AMINE-CONTAINING THIN FILMS IN LOW PRESSURE ATMOSPHERES OF ETHYLENEDIAMINE (EDA) / ACETYLENE (C_2H_2) MIXTURE

P. W. P. Moreira Júnior*, F. V. P. Kodaira, A. H. R. Castro, R. E. Cortez, R. P. Mota
UNESP – Univ. Estadual Paulista, Av. Dr. Ariberto Pereira da Cunha, 333 - Guaratinguetá, SP, Brazil.

1. Introduction

Plasma polymers containing amine functionalized groups have been taken attention in the science and industry of biomedical applications. The main characteristic of this kind of materials is the capacity of improve the human cell attachment on its surface. In most cases their surfaces are hydrophilic and non-fouling. These key qualities lead to applications like implant coating, drug delivery and enzyme electrodes production [1]. The plasma polymerization process is a good way to manufacture these materials since it is a dry one-way step process, does not release any harmful waste by-products into the environment, it is solvent free and the polymerization can occur in a wide variety of substrates. Monomers like cyclopropylamine, allylamine, ethylenediamine (EDA), oxazoline among others, have been used as precursors of amine functionalized plasma polymers [2]. The EDA presents the same amount of nitrogen and carbon in its molecule, being a suitable candidate for this process. Nevertheless, one was observed that plasma polymers of EDA (ppEDA) present high solubility in water. In this work, the discharges of the mixture acetylene (C2H2)/EDA were performed to polymerize amine-containing thin films with low solubility.

2. Experimental

The thin films were generated in a stainless-steel plasma reactor chamber. The discharges were excited by an rf-power supply, RF-300 model – Tokyo Hy-Power, at 13.56 MHz and the applied power was varied from 5 to 30 W. The chamber was evacuated by a mechanical pump, M-18 model – Edwards, while the pressure was monitored by Penning™ and Pirani™ gauges. The discharges were performed at 100 and 200 mTorr of total pressure. It was utilized the EDA/C_2H_2 ratio of 3:7 to produce the thin films. To analyze the plasmas the actinometric optical emission spectroscopy (AOES) technique, argon was utilized as actnometer, it was performed by an Avantes USL 2048x64 device. The thin films were studied by Fourier transform infrared spectroscopy (FTIR), where the Perking Elmer FTIR Spectrometer Spectrum 100™ was utilized and the water contact angle (WCA) technique was carried out by a Ramé-Hart 300-F1™ goniometer.

3. Results and Discussions

The WCA measurements show that all thin films present hydrophilic character being around 56 degrees for the 5 W conditions and 66 degrees for the films produced at 30 W. The FTIR analyses reveal that the amount of NH (3300 - 3200 cm^{-1} stretching) and imine C=N (1690 - 1650 cm^{-1}) increase compared with C-C (1000 - 900 cm^{-1} stretching) and CH (1465 - 1375 cm^{-1}) bonds when the applied power rises. The main species analyzed by AOES were NH (336.0 nm $A^3\Sigma \rightarrow X^3\Sigma$), CN (382 - 388 nm $B^2\Sigma^+ \rightarrow X^2\Sigma^+$) and CH (431.3 nm $A^2\Delta \rightarrow X^2\Pi$). It was observed an increase in the ratios CN/CH and NH/CH when the applied power increases from 5 to 30 W. These results are in agreement with those observed in the FTIR analysis. It was noticed that the coatings produced at lower power conditions are less soluble in aqueous environments and it was assigned to the proportion of NH bonds in the molecular structure of the thin films when compared with C-C and CH bonds.

4. References

[1] H. Testrich, H. Rebl, B. Finke, F. Hempel, B. Nebe and J. Meichsner, Mat. Sci. and Eng. C, **33**, 3875-3880, (2013).
[2] J. Ryssy, E. Prioste-Amaral, D. F. N. Assuncao, N. Rogers, G. T. S. Kirby, L. E. Smith and A. Michelmore, Phys.Chem.Chem.Phys., **18**, 4496, (2016).

Acknowledgments

The authors would like to acknowledge CAPES for the financial support.

*Corresponding author: pedro_kcond28@hotmail.com

ID 135: DRY TRIBOLOGICAL BEHAVIOR OF LASER TEXTURED 4340 STEEL

Mansur, R.A.F.[1,3]*, Ribeiro, E.M.[2], Simões, J.G.A.B.[1,3], Jardim, V.R[3], Vasconcelos, G.[1,3], Lima, M.S.F.[1,3]
[1]*Instituto Tecnológico da Aeronáutica, São José dos Campos - SP*
[2]*Instituto Alpha Lumen, São José dos Campos - SP*
[3]*Instituto de Estudos Avançados, São José dos Campos - SP*

1. Introduction

The study of tribological properties is very important, since the majority of the mechanical components, such as car brakes, pistons and landing gears are submitted to constant friction forces during their work. An effective way to control the wear is the modification of the topology of the pieces with the use of lasers [1]. This work intends to analyze the effects of laser texturing in 4340 steel samples submitted to dry wear.

2. Experimental

In this work has used four samples of 4340 steel with a diameter of 25 mm and thickness of 5mm. The samples A, B and C were textured by a Nd:YAG pulsed laser, where the amount of passes and overlap varied as follows: A- overlap of 50% and 6 runs, B- overlap of 75% and 4 runs and sample C – overlap of 87,5% and 3 runs. For comparison, one sample (pattern) was not textured.

3. Results and Discussions

Pin on disc test was performed on all samples with a load of 1N, alumina sphere of diameter 6 mm, track diameter of 3 mm and 5000 laps (Fig. 1). For the samples A and B, the friction coefficient increased after one thousand laps, when compared to the untreated sample. Sample C presented an increase of the friction coefficient after 4000 laps. A thin oxide layer with low friction coefficient was formed in the textured surface samples, although after a certain number of laps, this layer was torn away, justifying the increase of the friction coefficient. The optical profilemeter showed an increase of 100% of roughness Ra of sample A, and 120% increase in the samples B and C. The SEM-FEG images (Fig.2) showed that for the sample A, the wear behaved in an abrasive manner, because the textured surface can be observed on the track, while for samples B and C the wear was adhesive because it was not possible to observe the surface below the non-textured layer.

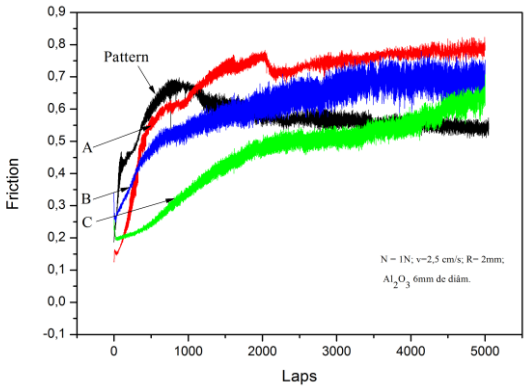

Fig. 1. Behavior wear pin-on-disk

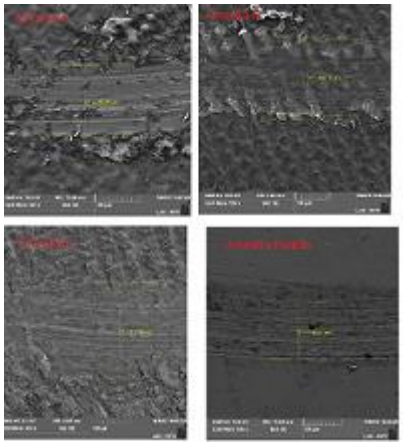

Fig. 2. Wear track images samples A,B,C and not texturized (pattern)

4. References

[1] Gachot, C. et al. *A critical assessment of surface texturing for friction and wear improvement*. Wear, v. 372, p. 21-41, 2017.

[2] Jones, Kyle; SCHMID, Steven R. *Experimental Investigation of Laser Texturing and its Effect on Friction and Lubrication*. Procedia Manufacturing, v. 5, p. 568-577, 2016.

Acknowledgments

CAPES, CNPQ, IEAV, INPE e ITA

*Raquel.alvim@gmail.com

ID 136: 300 MARAGING STEEL WELDED BY PLASMA PROCESS

A.C. Oliveira[1]*, P.R. Marqueti[1,2]

[1] *Instituto de Ciêcia e Tecnologia, Universidade Federal de São Paulo, São José dos Campos, SP, Brazil.*

[2] *Instituto de Aeronáutica e Espaço, Departamento de Ciênica e Tecnologia Aeroespacial, São José dos Campos, SP, Brazil*

1. Introduction

Maraging steels present good weldability and mechanical properties higher than those other ultra-high strength steels. These steels have a Fe-Ni array, having as mechanism of hardening, precipitation of intermetallic compounds by adequate aging heat treatment [1]. However, this process also can provide partial reversal of the martensite to austenite (austenite reversed), with reduction in mechanical strength and increased ductility of the material, making it unfit for use [2].

Once its mechanical properties are influenced by the heat treatment cycle employed, the heat generated by the welding process can change the final mechanical behavior of thermally treated alloy. In general, the welding of maraging steels presents, besides the fusion zone, three heat affected zones (HAZ), with distinct micro-structural changes [1]. In the cooling of the alloy, after the welding process, the structure of the fusion zone and thermally affected areas are soft. Moreover, the melting zone microstructure of maraging steels aged consists of dendrítes of martensite, with islands of austenite (γ) on the intersections of the edges [2], generating sharp decline of hardness in this region, when compared to the metal base (BM). The austenite located in this region is rich in Ni, Ti and Mo, while cells dendritic martensítes are poor of these elements. Therefore, the microstructural characterization and the mechanical properties of weld after post welding heat treatment is of importance for future technological application of this material.

In this context, welds in 300 maraging steel were produced by plasma arc welding process. The main objective of this work is to evaluate the microstructural and mechanical behavior of the alloy after the welding process.

2. Experimental

300 maraging steel sheets (solubilized to 820° C by 1h), with 3.3 mm x 600 mm x 100 mm, were used for this study. As filler metal was used the wire 300 SEA, with 0.89 mm of diameter. Initially all the samples were blasted sanded and cleaned with acetone. Plasma welding using filler metal was carried out with direct current, at room temperature, in the flat position and toward the transverse direction to the sense of the lamination plate. The welding parameters considered were: current and voltage of 222 A and 31.8 V, welding speed 500.0 mm/min, filler addition speed 700.0 mm/min, plasma and shielding gases of 1.0 L/min and 20.0 L/min, and distance torch-piece 3.5 mm.

After welding process, the joints had their microstructures characterized. For this purpose, samples were taken from the welded areas and their cross sections embedded in bakelite. After then, were sanded by water sandpapers with particles size of 180, 320, 600, and 1200 respectively, and polished with colloidal silica. Finally, the area was attacked with the 3% Nital (HNO3). A light microscope (ZEISS AXIO IMAGER model) was used for analysis and processing of images. In order, to quantify the austenite, we used the software IMAGE J. In this, the image obtained via optical microscopy was converted to grayscale, calculating the percentage of black areas against the white regions of the modified image.

The mechanical behavior of welded joints was analyzed by means of uniaxial tensile tests and hardness tests. For this, were conducted tests of Vickers microhardness (HV) mapping (EMCO TEST, DuraScan model), whereas constant load of 0.5 kgf.

3. Results and Discussions

Figure 1 shows the cross-section of the weld bead obtained in welding condition. Different regions of interaction in the material were obtained in the process of welding. In the molten zone (MZ) was observed the formation of dendrites oriented to the center of the weld bead, with two subsequent regions with larger grain size (Heat Affected Zones, HAZ 1 and HAZ 2). Then a third region, more darkened (averaging, HAZ 3) was obtained with martensitic microstructure with thin scattering of reversed austenite and stable.

In the fusion zone, the formation of dendrites oriented to the center of the strand, with two subsequent regions with larger grain size, which correspond to the Heat Affected Zones, HAZ1 and HAZ2. Then, the HAZ3, darker region, which features martensitic microstructure with a thin scattering of reversed austenite and stable. This region features characteristic of the phenomenon of averaging, promoted by heat involved during welding. Finally, the base metal (BM), where there occurs any microstructural transformation relative to the original aspect of the material. In relation to the melting zone (MZ),

*Corresponding author: alinecapella@gmail.com

microstructural variation was observed. It was observed the typical aspect of the melting zone microstructure of 300 maraging steels, with the formation of dendrites. As Lang and Kenyon, the austenite islands are not visible when tested on wending condition (Figure 2).

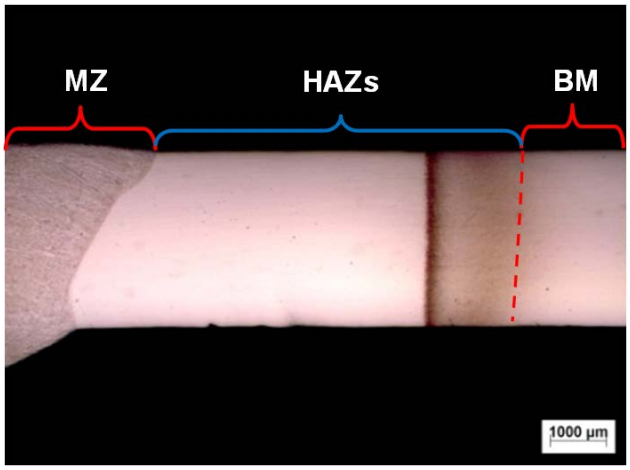

Fig. 1. *Morphology of the weld bead without subsequent heat treatment.*

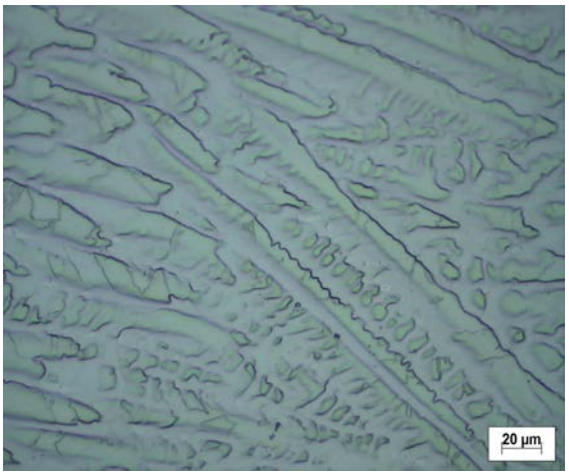

Fig. 2. *Microstructural aspect of the melting zone (MZ).*

The phenomenon of reversal of the martensite to austenite could be observed in heat affected zone (HAZ3), after welding process. It was observed an increase in hardness at HAZ3, resulting from precipitation of intermetallic compounds promoted by heating suffered during the welding process. The maximum hardness value found was 500 HV. As expected, the MZ presented a decrease of hardness with value 310 HV.

4. References

[1] A.M. Hall, C.J. Slunder. The metallurgy, behavior, and application of the 18-percent nickel maraging steels. Washington, D.C.: NASA, 1968. 137 p.

[2] U.K. Viswanathan, G.K.Dey, V. Sethumadhavan. Effects of austenite reversion during overageing on the mechanical properties of 18 Ni (350) maraging steel. Materials Science and Engineering: A, v. 398, n. 1, p. 367-372, 2005.

Acknowledgments

The authors thank IAE-DCTA by the use the welding system and to ITA by the hardness test equipment.

*Corresponding author: alinecapella@gmail.com

ID 138: RELATION BETWEEN SUBSTRATE FLOATING POTENTIAL AND GRID-TO-TARGET DISTANCE IN GRID ASSISTED MAGNETRON SPUTTERING

Rafael Fróis da Silva*, Julio César Sagás

Laboratório de Plasmas, Filmes e Superfícies, Universidade do Estado de Santa Catarina, Joinville - SC

1. Introduction

The magnetron sputter deposition is one of the most versatile techniques for film deposition. The technique is based on the sputtering of a cathode by ions generated in magnetically confined plasma. Among a great number of different configurations, it can be highlighted the triode magnetron sputtering [1-4], also called grid-assisted magnetron sputtering (GAMS) [5]. In this configuration, a grid is inserted between the target and the substrate, acting as an auxiliary anode when grounded. In reactive depositions, the grid reduces the hysteresis of process parameters (like pressure and voltage) as a function of reactive gas flow rate [2,4]. Previous works also show that the grounded grid improves the plasma confinement and change the current-voltage relations [3,5]. Using such configuration, the plasma is confined between the target and the grid. In this way the distance between plasma and substrate can be changed without modifying the target-to-substrate distance. It means that is possible to modify the charged particles flux to the substrate without change significantly the average energy of deposited atoms. The increase in the distance between plasma and substrate can be used for deposition in thermally sensitive substrates [6], once the charged particles flux is reduced.

However, to date, there is a lack of information about how fundamental parameters are affected by the introduction of the grid and the variation of grid-to-target distance. For example, there are no measurements about the substrate floating potential in such system. The deposition in floating substrates is usual in magnetron sputter deposition, in particular when using dielectric substrates. Modifications in the floating potential indicate variations not only in the charged particles flux, but also in the potential profile and in the electronic temperature.

The main purpose of this work is to investigate the relation between the substrate floating potential and the grid-to-target distance in grid-assisted magnetron sputtering. Once the floating potential is related with the energy transfer to the substrate, the deposition of stainless steel films was chosen for this study due to the technological interest in such films and the dependence of their properties with the energy flux.

2. Experimental

The measurements were carried out in a grid assisted magnetron sputtering chamber described elsewhere [3]. A 316L stainless steel target with 100 mm in diameter was used. The grid is a rectangular mesh (11.8 cm x 16.0 cm) with spacing of 2.0 mm between the wires and it was kept grounded in all measurements. The substrate has a diameter of 100 mm and it is located around 6.0 cm from the target. The base pressure was below 10^{-2} Pa. Argon (99.999% purity) was used as working gas and the flow rate was adjusted using a thermal mass flow controller. The working pressure was fixed to 0.40 Pa in all experiments and it was measured by a capacitive gauge. The plasma was powered with a DC power supply operating in constant power mode. The discharge power was varied in the range 200-1240 W. The choice for this range is based on previous studies about stainless steel film deposition [7]. The grid-to-target distance was varied between 1.5 cm and 4.0 cm. For comparison, measurements without the grid were made in the same discharge power range.

3. Results and Discussions

From the measurements of substrate floating potential as a function of discharge power for different grid-to-target distances and without the grid (figure 1), it is possible to see that the floating potential increases almost linearly when the discharge power is raised in the range 200-1240 W. Increasing the power both discharge voltage and current grow. Thus, it is expected a raise in the electron density. In the case without the grid, if the plasma potential remains constant during the power increasing, the raise in floating potential indicates a decrease in electron temperature in the vicinity of the substrate. However, it is unlikely that the plasma potential remains unchanged, thus further careful measurements are needed. It must be pointed also that in grid-assisted magnetron sputtering there is no plasma between the grid and the substrate.

Another feature observed is that moving away the grid from the target, the floating potential drops (becomes more negative) approaching the same level of the conventional system (without the grid). It must be highlighted that for a grid-to-target distance of 1.5 cm the floating potential is positive, i.e. more positive

*rfroisfisica@gmail.com

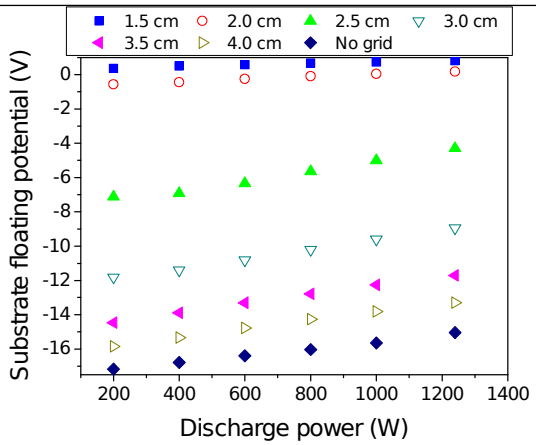

Fig. 1. *Substrate floating potential as a function of discharge power for different grid-to-target distances. The measurements without grid are also shown for comparison.*

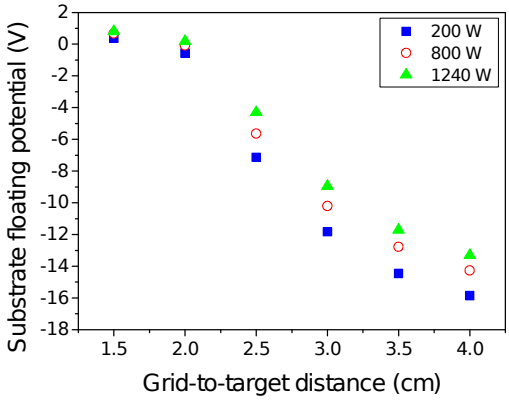

Fig. 2. *Behavior of substrate floating potential as a function of grid-to-target distance for different discharge powers.*

than the anode (grounded). The same is observed for 2.0 cm, but only for powers higher than 1000 W. This behavior is explained by the fact that the grounded grid drains electrons from the plasma reducing the electron flux to the substrate. The reduction in electron flux is greater for larger distances between plasma and substrate, i.e. small grid-to-target distances. It is expected that the ion flux is less affected by the grid, which leads the substrate floating potential to increase with decreased grid-to-target distance. It must be pointed out, however, that a complete understanding of the charged particles flux to the substrate is possible only with measurements of plasma potential.

4. References

[1] L. C. Fontana, J. L. R. Muzart. Surf. Coat. Technol., 107, **24–30**, (1998)

[2] L. C. Fontana, J. L. R. Muzart. Surf. Coat. Technol. 114, **7–12**, (1999)

[3] J. C. Sagás, L. C. Fontana, H. S. Maciel. Vacuum 85, **705–710**, (2011)

[4] J. C. Sagás, D. A. Duarte, D. R. Irala, L. C. Fontana, T. R. Rosa. Surf. Coat. Technol. 206, **1765–1770**, (2011)

[5] J. C. Sagás, D. A. Duarte, L. C. Fontana. J. Phy. D: Appl. Phys. 45, **505204**, (2012)

[6] D. A. Duarte, J. C. Sagás, L. C. Fontana, A. S. da Silva Sobrinho, M. J. Cinelli. Eur. Phys. J. Appl. Phys. 52, **31001** (2010).

[7] M. V. F. Schroeder. Obtenção e caracterização de filmes de aço inoxidável AISI 316 obtidos por pulverização catódica. Dissertação em Ciência e Engenharia de Materiais. Joinville, CCT/UDESC, (2017).

*rfroisfisica@gmail.com

ID 139-1: RADAR ABSORPTION MATERIAL BY POROUS CARBON PARTICULATE IN POLYMERIC MATRIX

B. H. K. Lopes[1]*, R. C. Portes[2,3], A. S. Monteiro[2,3], M. A. Amaral Jr [2], J. S. Marcuzzo[2,4], G. Amaral-Labat [5], E. S. Gonçalves[1], S. F. Quirino[3], M. R. Baldan[1,2]

[1]Instituto Tecnológico de Aeronáutica, São José dos Campos, SP, Brazil,
[2]Instituto Nacional de Pesquisas Aeroespaciais, São José dos Campos, SP, Brazil,
[3]ETEP Faculdades, São José dos Campos, SP, Brazil,
[4]Faculdade de Tecnologia Professor Jessen Vidal, São José dos Campos, SP, Brazil,
[5]Universidade de São Paulo, Escola Politécnica, São Paulo, SP, Brazil.

1. Introduction

Radar absorption materials are very common on aerospace industry because they are responsible to protect internal components on the satellites from external interferences. There are many studies that use carbon materials in polymeric matrix to add electromagnetic properties for electromagnetic shielding application [1]. The aim of this work is to perform electromagnetic characterization, by waveguide method, of a porous carbon particulate (PCP) synthesized by chemical polymerization of crude black liquor in alkaline medium [2].

2. Experimental

The materials will be prepared via chemical synthesis by modifying the methodology described in the literature [2] aiming at the integral use of the pulp and paper industry waste with a "polymerized resin". The acrylic polymer PMMA will be used in the medium in different granulometries in order to change the porosity. The materials produced will be crushed and the electric characterize will be performed through a network vector analysis combined with a waveguide in the microwave range.

3. Results and Discussions

Through reflectivity measurements it was possible to observe that there is no influence of granulometry of the samples in the attenuation of the incident wave. It was noticed that low porosities of the surface of the samples presented meaningfull improvement of the attenuation. According to Figures 1 and 2, it can be seen that the increase of the PCP concentration results in the increase of the attenuation. Similarly for all granulometry and porosity values, the attenuations for samples with 1% PCP were about 10.4% over the whole frequency range, whereas the samples with 5% and 10% PCP showed a non-linear behavior. The sample with 5% PCP presented a minimum attenuation of 9.7% in 8.2GHz and a maximum of 24.2% in 11.38GHz, while the 10% PCP showed a maximum attenuation of 30.1% in 8.2GHz and a minimum attenuation of 18.2% in 11.85 GHz.

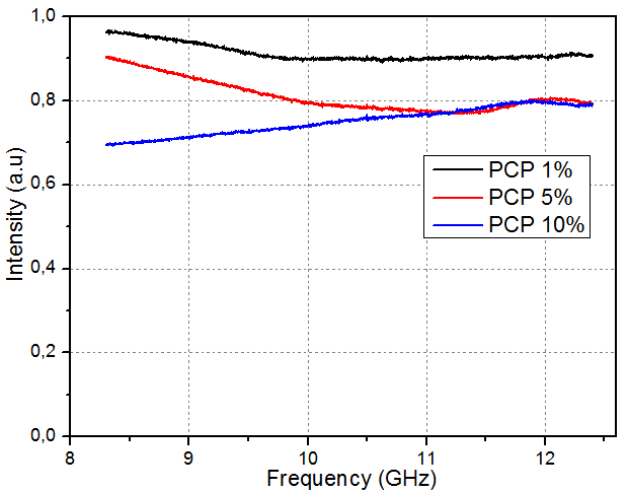

Fig. 1. *Reflectivity of the samples of 1%, 5% and 10% PCP with Granulometry less than 250 µm and pore less than 420µm*

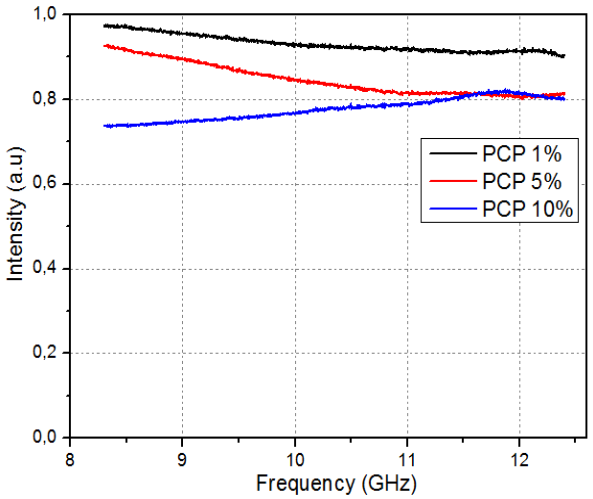

Fig. 2. *Reflectivity of the samples of 1%, 5% and 10% PCP with Granulometry less than 250 µm and pore greater than 420 µm*

*Corresponding author: brauliohkl@gmail.com

4. References

[1] D. Bychanok et al Appl. Phys. Lett, **108**, 013701, (2016).
[2] Seo J. et al Carbon, **76**, 357-367, (2014).

Acknowledgments

The author would like to thank ITA, INPE and USP for the support and infrastructure.

*Corresponding author: brauliohkl@gmail.com

ID 139: PRODUCTION OF LOW COST COMPOSITE BASED IN ATIVATED CARBON FIBER PARTICULATES APPLIED IN RADIATION ABSORBING MATERIALS IN X BAND FREQUENCY

Ariane A. T. Souza[1]*, Janaína S. Oliveira[1], Braulio H. K. Lopes[1], Emersom S. Gonçalves[2], Jossano S. Marcuzzo[1], Sandro F. Quirino[1], Miguel A. Amaral Jr[1] and Mauricio R. Baldan[1]

[1] Instituto Nacional de Pesquisas Espaciais – INPE
[2] Departamento de Ciência e Tecnologia Aeroespacial - DCTA

1. Introduction

Nowadays, radiation absorber materials (RAM) have received great attention from the industries and academic research centers, due to their applications in the most diverse areas, such as military, aeronautics, aerospace and telecommunications [1]. In aeronautical and military areas the RAMs have been extensively studied in the frequency bands of 8-12 GHz, known as X-Band [2]. Materials such as carbon, ceramic oxides, ferromagnetic and conductive polymers are traditionally applied to RAM and are thus used as absorber centers of unwanted radiation [3]. In particular, carbon is traditionally applied as RAM in the GHz frequency band because it is an excellent reflector of electromagnetic radiation [4]. Therefore, many researchers on this frequency were carried out with carbon in its different allotropic forms such as: activated carbon fibers [5], carbon fiber felt screens with rectangular shapes [6], particulates dispersed in a matrix [7] and cobalt oxide deposit [8].

Therefore, in this study the main objective was to produce a composite based on carbon fiber (CF) and activated carbon fiber (ACF) particulates, which is able to attenuate electromagnetic radiation in the frequency range of 8-12GHz. In order to perform the measurements a guided wave method coupled to a vector network analyzer (VNA) was used. Besides, a structural characterization of the fibers was performed using a Raman spectroscopy technique, in order to verify possible defects in carbon structure of the fibers.

2. Experimental

Textile PAN was used to produce CF, due to its low cost compared with other raw materials. The carbonization was performed in argon atmosphere at a final temperature of 1000°C by using a heating rate of 30°C/min. complete the carbonization process. The process time at maximum temperature was set in 20 min to complete the carbonization process. After the carbonization, the activation of the fibers is performed using two activation methods, the physical and chemical activation. The physical activation was carry out at the temperature of 1000°C in carbon oxide atmosphere for 50 minutes. Already the chemical activation was performed in KOH solution, the FC was impregnated with a 6 molar KOH solution, and then was placed in the furnace in an argon atmosphere. The heating ramp was 5 °C/min until reaching 600°C and remained for 1 hour. After the production process of the materials, the samples were produced to perform the electromagnetic measurements in a VNA. The samples of CF, ACF and ACF by KOH etching were powdered, and separated into particulates size between 25-53μm. After that, the samples were employed in a paraffin matrix, with thicknesses of 1.5mm with dimensions of 10.16x22.86mm.

3. Results and Discussions

Through Raman spectroscopy it was possible to observe that the samples of CF and ACF presented disorganization in the graphite structure due to the presence of peak D in the spectrum (Figure 1). However, peak G showed greater intensity in both cases. Although the Raman spectra were similar, it was observed that the FWHM of the ACF samples decreased, which is related to the decrease in the presence of heteroatoms on the surface of the fiber due to activation process. This result influenced the reflectivity of the material, causing an attenuation of approximately 50% of the incident radiation in the ACF sample, as showed in Figure 2. However, the chemical activation with KOH in the CF sample did not show attenuation of the radiation.

*Corresponding author: "miguel.junior.mat@hotmail.com"

Fig. 1. *Raman spectra of CF and ACF.*

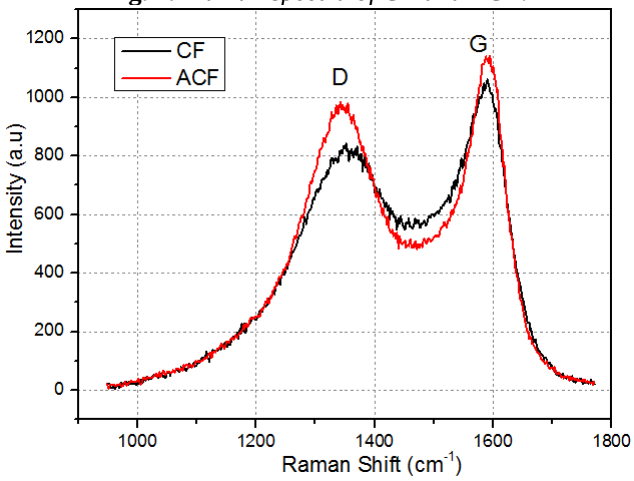

Fig. 2. *Reflectivity of the samples of CF, ACF and ACF (KOH)*

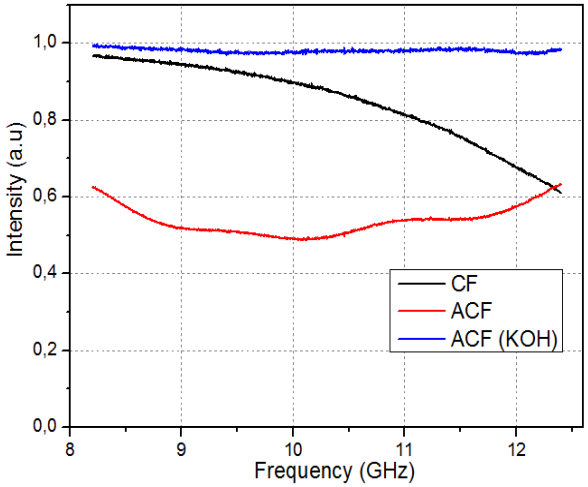

4. References

[1] HONG, W.; XIAO, P.; LUO, H.; LI, Z. Sci. Rep., Nature Publishing Group, v. 5, p. 14927, oct 2015

[2]LIU, Y.; LUO, F.; SU, J.; ZHOU, W.; ZHU, D., J. of Magnetism and Magnetic Materials, Elsevier BV, v. 365, p. 126–131, sep2014. 88

[3]Paula, A. L., Dissertação De Mestrado, INPE, São José Dos Campos, 2010.

[4]CHUNG, D. D. L., J. of Materials Science, Springer Nature, v. 39, n. 8, p. 2645–2661, apr 2004.

[5]Zang, Y., Xia, S., Li, L., Ren, G., Chen, Q., Quan, H., & Wu, Q., Composites Part B: Engineering, 77, 371-378, 2015

[6] Xia, S., Yao, B., Chen, Q., Yu, X., & Wu, Q., Composites Part B: Engineering, 105, 1-7, 2016.

[7] Dang, Z., Shen, Y., Fan, L., Cai, N., Nan, C., & Zhao, S., J. of applied physics, 93(9), 5543-5545, 2003.

[8] Liu, Y., Zhang, Z., Xiao, S., Qiang, C., Tian, L., & Xu, J., A. S. S, 257(17), 7678-7683, 2011.

Acknowledgments

The author would like to thank ITA and INPE for the support and infrastructure.

*Corresponding author: "miguel.junior.mat@hotmail.com"

ID 140: AN OVERVIEW OF MODIFIED PECVD TECHNIQUE FOR DLC GROWTH AND ITS NEW AREAS OF RESEARCH AND APPLICATION

Vladimir Jesus Trava-Airoldi[1*], Evaldo José Corat[1] , Marco Antonio Ramirez Ramos[2], and Luis Francisco Bonetti[3]

[1]*Insituto Nacional de Pesquisas Espaciais (INPE), Laboratório Associado de Sensores e Materiais (LAS), Av. dos Astronautas, 1758-São José dos Campos, 12227-010, SP, Brazil*
[2]*Universidade do Vale do Paraiba (UNIVAP), Av. Shishima Hifumi 2911, São Jose dos Campos, 12244-000, SP, Brazil.*
[3]*Clorovale Diamantes Ltda (CVD Vale), Estrada José Augusto Teixeira, 500 – Bairro Torrão de Ouro II – CEP:12229-840*

1. Introduction

DLC as an amorphous hydrogenated carbon (a-C:H) films have been used as protective coatings in many applications due to their superior properties such as: low coefficient of friction, high chemical inertness, high hardness, high wear resistance, biocompatibility, and bactericide (1). However, a very big challenge is to overcome the residual stresses that form during the growth process and to obtain high adhesion between the DLC and the different substrate materials, especially of metal. The PECVD technique modified with the addition of a cathode with the function of promoting confinement of electrons and ions in a plasma discharge was shown to be feasible for studies of the reduction of residual stresses that form inside of the DLC films structure, as well as showed, too, to be a prosperous technique to achieve high adhesion of DLC film on the most metal substrate surface besides being able to get harder films with less porosity and with lower friction coefficients. This technique proved to be, also, very promising for DLC deposition in the form of multilayers of thicker films. These results refer this technique to other areas of applications, enabling it to the applications in the space, aeronautic, and automotive area, besides to stand out in medical and dentistry areas.

2. Experimental

Basically, due to the possibility of operating at very low pressure (< 10-3 Torr) (2), this technique allows to grow DLC film in three dimensions in collision less regime. The operating parameters can be well controlled and allow easily scale studies. In this work will be presented a brief description of the operating principle, as shown in Fig. 1, where in a collision less regime, energy of ions generated in the plasma discharge is all used to the ion sub implantation process, and being primarily responsible for the high adhesion of DLC in most accessed metal substrates.

3. Results and Discussions

Due to the ease of control of adhesion and growth parameters of DLC films obtained by this technique allows to obtain very thick films in multilayer form, as shown in Fig. 2. These multilayers are responsible for low residual stress of the film, in spite of very thick. The thickness of the DLC film as high as to 10 microns correspond to an alternation of the film of amorphous silicon with the DLC film where the thickness of each layer, as well as, the concentration of silicon and carbon are well controlled. A summary of the studies that led to this DLC films growth technique optimization, not only thin films, but also thick films is an important area of new studies and new applications will be an important part of this work.

*vladimir.airoldi@inpe.br

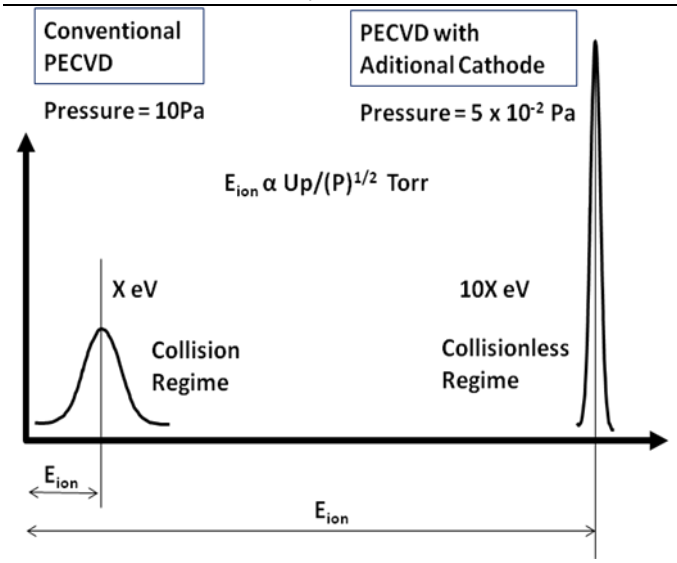

Figure 1. Collisions regime of operation

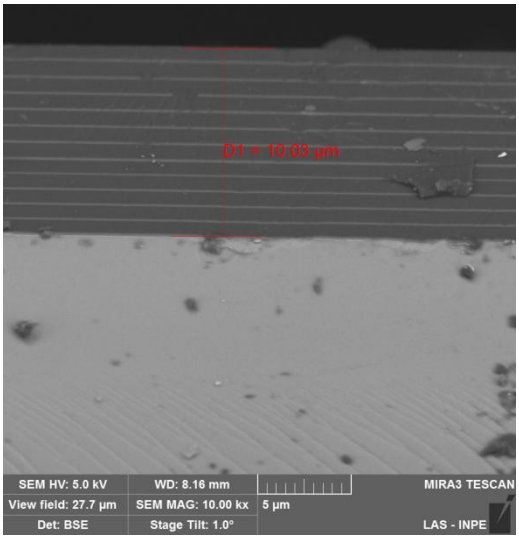

Figure 2. Multilayer DLC films on 316 SS

4. References

1 - Grill, A., Meyerson, B., in Syntetic Diamond: Emerging CVD Science and Technology , K. E. Spearand J. P. Dismukes, Eds., John Wiley & Sons, Inc., New York, 1994.

2 - Robertson, J., Material Science and Engineering, Review Journal, R 37, 129-281 2002.

3 - Capote, G.; Ramirez, M.A.; DA Silva, P.C.S.; Lugo, D.C.; Trava-Airoldi, V.J.. Improvement of the properties and the adherence of DLC coatings deposited using a modified pulsed-DC PECVD technique and an additional cathode. Surface & Coatings Technology, v. 308, p. 70-79, 2016.

*vladimir.airoldi@inpe.br

ID 141: CRYOGENIC UHV FAST-ENTRY CHAMBERS AT THE BRAZILIAN SYNCHROTRON LIGHT LABORATORY/LNLS

Horácio Ribeiro de Moraes[1]*, Laércio de Souza Jr.[1], Julio Criginski Cezar[1]
[1]*Laboratório Nacional de Luz Síncrotron (LNLS), Centro Nacional de Pesquisa em Energia e Materiais (CNPEM), CEP 13083-970, Campinas, São Paulo, Brasil*

1. Introduction

The Brazilian Synchrotron Light Laboratory, LNLS at Campinas, SP, provides the user community with several X-rays based experimental techniques that can be applied in the field of basic research and materials science. Among those techniques, those dealing with photons between 100 and 2000 eV are particularly sensitive to the sample surface. This spectral range is called soft X-rays, and its surface sensitivity makes it particularly suited to study surfaces and some interfaces of materials. On the other hand, to preserve the surface quality of the samples, these techniques have very stringent vacuum requirements, normally in the region of 10^{-9} mbar or better. Furthermore, at the LNLS we provide the users with some *in-situ* thin films growth facilities, which also operate in UHV conditions. For both experimental station and sample growth instrument, one must use load lock chambers to introduce the samples or substrates from air to the UHV chamber. The time needed to pump down these load locks to a suitable pressure level changes from system to system, but is not unusual for the user to wait around 6 hours prior to be able to introduce the sample in the UHV system. Also, some characterization instruments are not directly connected to the sample growth system. In these cases, the sample must be transferred inside a small UHV chamber that can be attached to both sample preparation and characterization systems without exposing the film to the atmosphere. This device is known as a vacuum suit case. Most of the time, transferring between chambers involved connecting the suit case through a small vacuum section that must be pumped and baked. Such procedure can take several hours what is not affordable in most of the synchrotron based experiments. Here we describe the development and first commissioning results of a fast entry based on a liquid nitrogen (LN_2) trap that acts as a cryo-pump. Such cryo-pumping precludes the need of baking in the case of vacuum suit cases and can reduce drastically the time needed to pump down the load locks.

2. Experimental

For the initial tests, we attached an existing LN_2 trap to a small volume chamber similar to the usual vacuum load locks we used in our instruments. The main components are numbered in figure 1 as: 1) main load lock chamber; 2) turbo pump; 3) vacuum gauge; 4) LN_2 trap. The system is initially pumped down with the aid of the turbo and backing pump to low 10^{-6} mbar. This initial pump down takes around 20 minutes. Then the LN_2 trap is filled and its walls act as a cryo pump. Our characterization involved to follow the variation of the internal load lock pressure as function of the time after filling the LN_2 trap. In this proof of concept test, after filling a 300 ml cold trap with LN_2, the pressure dropped by almost two orders of magnitude after one hour.

Fig. 1. *The experimental setup used during the proof of concept tests. The chamber 1 has a volume similar (5 liters) to what we expect for the fast entry. The system was pumped by a Pfeiffer HiPace 80 turbo molecular pump (2) and the pressure measured with a Pfeiffer PKR-261 full range gauge (3). The cryogenic pumping was obtained filling a 300 ml LN_2 trap (4).*

*Corresponding author: horacio.moraes@lnls.br

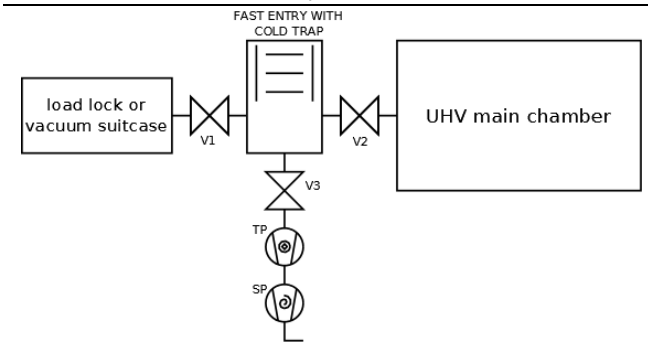

Fig. 2. *Diagram of a typical use of the fast entry. The components are described in the text.*

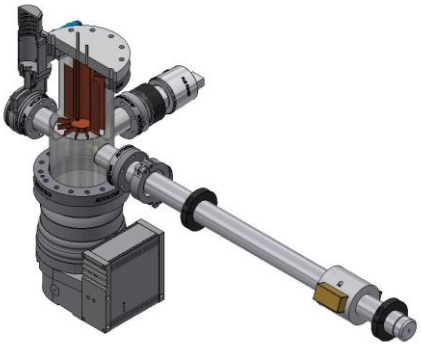

Fig. 3. *3D CAD drawing of the fast entry coupled with a load lock. In this case we don't use the V1 gate valve indicated in Fig. 1. More details in the text.*

3. Results and Discussions

The results obtained so far were good enough to allow us to develop further the idea. Figure 2 shows the vacuum diagram of the proposed experimental system. Figure 3 shows a CAD drawing of the final system under development. In this next version, we will address three main points that can be improved compared with our proof of concept experiments:

a) To introduce or take out samples from the main UHV chamber, the fast entry must be quick to drop the pressure but also to warm it up and vent. One can not afford to wait for the LN_2 to evaporate. Thus, instead of a reservoir, we will use a LN_2 circulating system.
b) Stainless steel is a very poor thermal conductor. We will use instead a cooper block.
c) The cylindrical reservoir has a limited surface to adsorb gases. For the final version we will mount several copper fins, directly brazed on the copper cooling block to increase the surface area of the cold trap.

In our contribution, we will present the results obtained with these improvements. We expect to reduce drastically the time needed to reduce the pressure to its final value after cooling. Furthermore, giving the more efficient heat exchange and greater trap surface, the final obtained pressure should also get in the 10^{-9} mbar range.

In any case, even the proof of concept used so far already allow us to reduce the time between sample transfers from several to around one hour. This reflects in a better use of the beam time of the synchrotron source.

Acknowledgments
We acknowledge the CNPEM/LNLS for allocating resources for this development as part of the SIRIUS project. The CNPEM is funded by the MCTIC.

*Corresponding author: horacio.moraes@lnls.br

ID 142: PLASMA POLYMERIZED HMDSO THIN FILMS INCORPORATEDWITH CHLOREXIDINE FOR DRUG RELEASE

F. V. P. Kodaira*, P. W. P. Moreira Júnior, R. P. Mota
UNESP – Univ. Estadual Paulista, Av. Dr. Ariberto Pereira da Cunha, 333 - Guaratinguetá, SP, Brazil

1. Introduction

Plasma polymers are known for its unique properties in comparison with the chemical polymerized ones, such as a high crosslinked structure, resistance to corrosion in mild acidic and basic media and adhesion to many kinds of substrates. [1] The plasma polymerization technique is also more environmentally friendly than the conventional chemical polymerization for it leaves no wastes and require no solvents in the process. The plasma polymerization of hexamethyldisiloxane (HMDSO) have been studied for many years and, despite its hydrophobicity, it is reported to be insoluble in water and non-cytotoxic, those characteristics makes it suitable for biomedical uses. [2], [3] One of the uses of a thin film is drug release, where a medicine is incorporated in the film and is released to the body with controlled time or condition. One possible drug is the chlorhexidine, a known antiseptic largely used in the pharmaceutical industry, it might be incorporated in the thin film to prevent infections in a period. In this work HMDSO was polymerized by plasma in a stablished condition and the chlorhexidine was incorporated to it. The FTIR and water contact angle (WCA) to evaluate the drug incorporation and release.

2. Experimental

The films were deposited inside a stainless-steel parallel plates reactor fed by a RF power supply at 15W, inside the chamber, a mixture HMDSO/Ar was admitted in the ratio of 9:1, the total pressure during the deposition was 100 mTorr, maintained by two mechanical vacuum pumps. The deposition process lasted 30 minutes. Two kinds of substrates were utilized, glass slices, for WCA measurements and aluminum foil for FTIR analyzes. For the medicine incorporation, a 2% chlorhexidine solution was used and three conditions were studied: a) the chlorhexidine was incorporated to the substrate and the film deposited on it; b) the chlorhexidine was incorporated on the deposited film; c) the chlorhexidine was incorporated between two layers of the film. The medicine incorporation was done by bathing the film in the solution for 30 minutes and then flushed with compressed air and dried for 24 hours. The FTIR was performed by a PerkinElmer Spectrum 100 spectrometer and the WCA by a Ramè-Hart 300-F1 goniometer. After those measurements, the samples were bathed in water for one hour and the measurements were performed again in order to verify if the drug was released.

3. Results and Discussions

For all the WCA measurements the samples maintained their hydrophobic character, with angles around 100 degrees, even after they were water washed. In the FTIR analysis, changes in functional groups related to the chlorhexidine were observed essentially in C-C (1450-1512 cm-1), C=N (1600-1670 cm-1) and phenyl group (1550 cm-1). After the water washing, the FTIR of the sample where the medicine was put on the film showed only trace elements of the chlorhexidine functional groups, meaning that they were washed away. The same behavior was observed for the sample where the drug was put between layers of HMDSO film, as the HMDSO film is hydrophobic, the chlorhexidine might have been flushed away after the incorporation. In the case where the chlorhexidine was put on the substrate, an slightly decrease was observed in the peaks relative to the drug, it was probably diffused to the water bath being released.

4. References

[1] H. K. Yasuda, *PLASMA POLYMERIZATION*. Elsevier Science, 2012.
[2] P. H. Li and P. K. Chu, "Thin film deposition technologies and processing of biomaterials," in *Thin Film Coatings for Biomaterials and Biomedical Applications*, Elsevier, 2016, pp. 3–28.
[3] C. Saulou, B. Despax, P. Raynaud, S. Zanna, P. Marcus, and M. Mercier-Bonin, "Plasma deposition of organosilicon polymer thin films with embedded nanosilver for prevention of microbial adhesion," *Appl. Surf. Sci.*, vol. 256, no. 3 SUPPL., 2009.

Acknowledgments (bold face Times New Roman 11 pt)
The authors would like to acknowledge CAPES for the financial support

*Corresponding author: kodaira.felipe@gmail.com

ID 143: STRUCTURAL AND MORPHOLOGICAL CHARACTERIZATION OF DLC FILMS DEPOSITED BY PLASMA IMMERSION ION IMPLANTATION AND DEPOSITION (PIII&D) WITH MAGNETIC FIELD INSIDE TUBES

Samantha de Fátima Magalhães Mariano[1, 2]*, Mario Ueda[2], Rogério de Moraes Oliveira[2]
[1]*National Institute for Space Research (INPE), Associated Laboratory of Sensors and Materials (LAS)*
[2]*National Institute for Space Research (INPE), Associated Laboratory of Plasma (LAP)*

1. Introduction

For the purpose of coating the inner side of metallic tubes, a magnetic field enhanced PIII&D process was used. A set of silicon-p type (100) samples were put inside a substrate steel (AISI 304) tube (150 mm length and 110 mm diameter), prior to the investigation of the PIII&D process affected by *ExB* drift. The structural analysis of the DLC as-coated samples were performed in order to observe the effects of the magnetic field on the properties of the obtained DLC film. In our previous work, hollow cathode discharges with argon, nitrogen, methane and acetylene plasmas were studied as regard to their I *versus* V characteristic curves, in the presence of the magnetic field [1]. As a continuation to that, the main objective of this work is to provide useful information about the molecular structure of the carbon bonds of DLC films, as well as, on their morphology along the inside of the tube, which are changed as the magnetic field is applied.

2. Experimental

Silicon wafers (15 mm x 15 mm) were fixed in the bottom of the tube, at its inner wall. Their positions were numbered from #1 to #4, from the left (back of the chamber) to the right (front of the chamber). For the two experiments, the substrate tubes were biased to 4 kV, with 20 μs of pulse width and 500 Hz of repetition rate, and at a working pressure of 4.5 Pa which was kept constant. The DLC growing steps were as follows: 15 min Ar PIII + 60 min N_2 PIII + 30 min CH_4 PIII + 30 min C_2H_2 deposition. Two experimental procedures were taken to compare the effectiveness of the magnetic field for the deposition. First, a standard discharge mode without magnetic field (0 G) was used with the four DLC growing steps. Later, a magnetic field of 22.5 G was applied during the whole PIII&D treatment. Then, Raman spectroscopy was used to analyze the structural arrangement of carbon bonds. The morphologies of the surfaces of DLC films were analyzed by SEM and optical profilometry.

3. Results and Discussions

In general, when the magnetic field is applied, the intensity of D band is greatly reduced and the G peak position is shifted to lower wavenumbers in comparison with the DLC films deposited without magnetic field (0 G). Also, a significant decrease in I_D/I_G ratio was observed for the second experiment. The I_D/I_G ratio decreased from 0.875 to 0.475 as we moved from the back samples towards the front ones of the tube. This result is ascribed to a disordering of carbon bonding structure and can be an indicative of hardness improvement in such films [2]. As regard to their hydrogenation, the same trend was observed for both experiments: the DLC as-coated samples placed on the edges of the tube showed higher at.% H, about 28 at.% H for deposition without magnetic field (0 G) and about 20 at.% H for DLC deposited with 22 G. For both experimental cases, the samples from the middle of the tube showed DLC films with the lowest values of hydrogen content. DLC films deposited using magnetically confined plasmas showed defect-free morphology on the surface. For the same sample position, the roughness was clearly reduced in the DLC films deposited in PIII&D with magnetic field.

4. References

[1] S. F. M. Mariano, M. Ueda, R. M. Oliveira, E. J. D. M. Pillaca and N. M. Santos, Surf. & Coat. Tech., 312, 47-54, (2017).
[2] C. Casiraghi, A. Ferrari and J. Robertson, Phys. Rev. B, 72, 85401, (2005).

Acknowledgments

This work was supported by CNPQ and CAPES.

*Corresponding author: samanthafmm@outlook.com

ID 145: DEPOSITION AND CHARACTERIZATION OF THIN FILMS BY ATMOSPHERIC PLASMA MICRO DISCHARGE

Daniela Araujo de Souza, Milton Eiji Kayama , Rogério Pinto Mota,
Mauricio Antonio Algatti, André Bianchi Laraia
UNESP – Campus de Guaratinguetá

1.Introduction

Ionic beams, cathodic erosion, cathodic arc and Plasma Enhanced Chemical Vapor Deposition (PECVD) are some methods used for the deposition of thin films; but currently the most used in laboratory is the PECVD, a technique that stands out due to the following factors: it is a dry, clean, speedy, inexpensive process easy to perform and with properties completely linked to the parameters of deposition, allowing the obtaining of uniform, homogeneous materials with low defects[1]. This technique is based on the deposition of thin films using non-thermal plasma and can be generated by radio frequency (RF), direct current (DC) or microwave (MW) applied to the precursor gas. In the present work, depositions will be performed using atmospheric plasma microchips, with the monomer Hexamethyldisiloxane (HMDSO), the precursor gas, which will be deposited on the glass substrate followed by the characterization of the same.

2. Experimental

The PECVD deposition technique was performed by means of a device, constructed in brass and polyacetal in cylindrical format connected to a flow valve, an Erlenmeyer and a voltage supply, shown in Figure 1. The DBD discharge occurs between a needle and grounded ring, insulated by a borosilicate capillary tube, at a frequency of 37 KHZ, voltage of maximum 5.5 KV peak-to-peak and gas flow 0.3 L / min and 0.15 L / min. The needle (anode) is connected to a brass body through which the gas flows[2]. The gas used was argon (Ar). Four samples of glass were cut in the following dimension 20x25 mm passing through a cleaning process. The depositions using the monomer HMDSO were characterized by contact angle measurements and Fourier Transform Infrared Spectroscopy (FTIR).

3. Results and Discussions

The wettability revealed that the films formed on the surfaces of the substrates in question exhibit a hydrophobic character. The angle of contact of the films were 90° in the central region of the deposition, and at the peripheral region was about 64º. Fourier transform infrared spectroscopy (FTIR) showed the presence of molecular groups present in the films formed by the HMDSO.

.

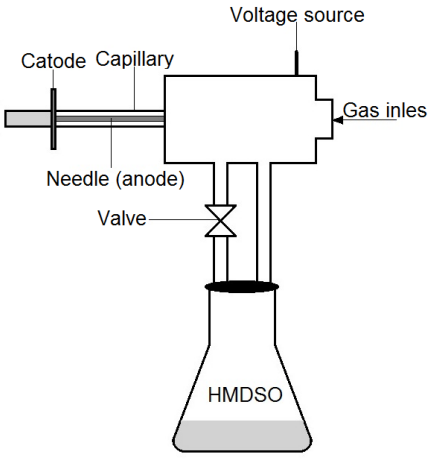

Fig.1. *Atmospheric pressure plasma plume device.*

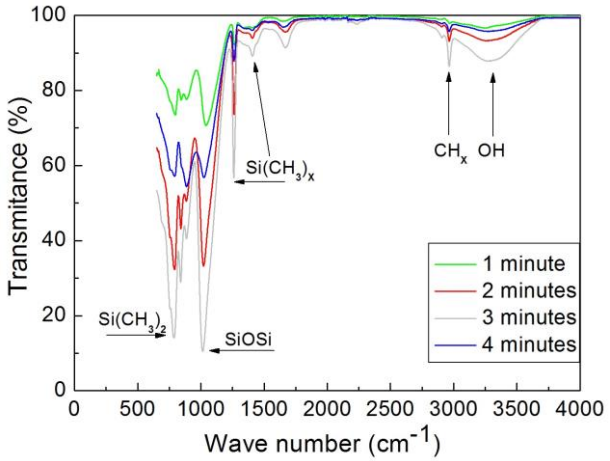

Fig. 2. *Spectrogram of the films formed by PECVD through micro-jets of atmospheric plasma.*

4. References

[1] Fanelli. F. Ar/HMDSO/O2 fed atmospheric pressure DBDs: Thin film deposition and GC-MS investigation of by- products. *Plasma Proc. Pol*.,**7**, 535-543, (2010) .

[2] Kayama. E.M., Silva. J.L, Prysiazhnyi. V, Kostov. G. K and Algatti. A. M. Characteristics of Needle-Disk Electrodes Atmospheric Pressure Discharges Applied to Modify Wettalility. *IEEE Trans. Plasma Sci.* 0093-3813, (2017).

daniela _araujo5@outlook.com

ID 147: CVD DIAMOND AND CARBON NANOTUBES NANOCOMPOSITES PRODUCTION AND APPLICATIONS

Evaldo José Corat[1]*, Romário Araújo Pinheiro[1], Cintia Macedo de Lima[2,3], Bruna C. Lourenção[4], Orlando Fatibello Filho[4], Marcos H. Mamoru O. Hamanaka[5] and Vladimir J. Trava-Airoldi[1]

[1]*Intistuto Nacional de Pesquisas Espaciais, São José dos Campos, SP, Brazil*

[2]*Universidade Federal de São Paulo, São José dos Campos, SP, Brazil*

[3]*Instituto Federal de São Paulo, Bragança Paulista, SP, Brazil*

[4]*Universidade Federal de São Carlos, São Carlos, SP, Brazil*

[5]*Centro de Pesquisas Renato Archer, Campinas, SP, Brazil*

1. Introduction

CVD diamond deposition on carbon nanotubes (CNT) has been studied for nearly 10 years, to gain synergy between both excellent materials properties. Most alternatives get a relevant synergy, but fail to preserve CNT nanometric structure. In this work, we show nanocomposites that preserve the original CNT structure to produce superior results, both in porous boron doped diamond (p-BDD) electrodes for electrochemistry and in electrons field emission [1].

2. Experimental

A modified Electrostatic Self Assembly (ESA) method provided the CNT seeding with nanodiamond (ND) particles. In this ESA method CNT oxidation introduced polar groups on its surface giving an anionic character to attract ND particles that have a cationic character. ND particles dispersed in a KCl solution, which supernatant was further diluted 10 times, produced the right amount for a subtle ND seeding of CNT upon submersion of oxidized CNT for few seconds. Short CVD diamond growth periods in Hot Filament Chemical Vapor Deposition (HFCVD) produced porous diamond surfaces closely resembling CNT morphology. BDD growth followed by bubbling hydrogen in a solution of boron oxide in methanol to mix to a CH_4/H2 gas mixture. Nitrogen doped diamond (NDD) growth replaces to urea in the methanol solution. Nanocomposites characterization involved field emission gun scanning electron microscopy (FEG-SEM) and Raman scattering spectroscopy (RSS). p-BDD electrodes were tested by cyclic voltammetry, electrochemical impedance spectroscopy and flow injection analysis. The NDD/CNT samples were tested for field emission.

3. Results and Discussions

Figure 1 shows the morphology of p-BDD electrode which resembles closely the original CNT morphology. CNT are covered by a thin diamond layer. p-BDD results show a surface area up to 400 times larger than an equivalent flat BDD electrode. Besides its viability as a large area electrode, its high sensitivity was shown by flow injection analysis. The field emission from NDD/CNT shows a threshold electron field as low as 0.75 V/μm, much lower than the best results in literature.

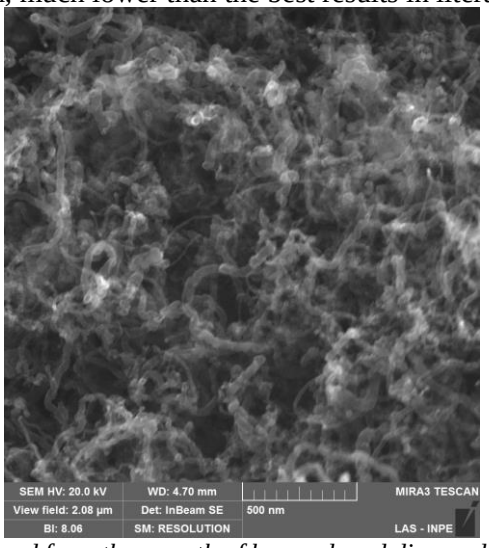

Figure1. *p-BDD diamond from the growth of boron doped diamond on carbon nanotubes.*

4. References

[1] RA Pinheiro, CM de Lima, LDR Cardoso, VJ Trava-Airoldi, EJ Corat – Diam. Relat. Mater. **65**(2016) 198.

Acknowledgments

We acknowledge FAPESP financial support.

*evaldo.corat@inpe.br

ID 148: WEAR RESISTANCE ANALYSIS $NI_{50,8}$TI SMA BY POWDER METALLURGY MODIFIED BY PLASMA IMMERSION ION IMPLANTATION TECHNIQUE

Caroline Borges de Sales*[1], Eliene Nogueira de Camargo[1], Maria Margareth da Silva[1], Mario Ueda[2], Rogério de Moraes Oliveira[2], Luc Pichon[3] and Daniel Rodrigues[4].

[1]*Instituto Tecnológico de Aeronáutica, Praça Mal. Eduardo Gomes, 50 – Vila das Acácias, São Jose dos Campos, São Paulo, Brazil.*

[2]*Instituto Nacional de Pesquisas Espaciais. Centro de Tecnologia Espaciais. Laboratório Associado ao Plasma. Avenida dos Astronautas, 1758, São Jose dos Campos, São Paulo, Brazil.*

[3]*Institut Pprime (PPRIME) CNRS: UPR 3346, Université de Poitiers, ENSMA, Poitiers, France.*

[4]*BRATS Filtros Sinterizados Pós Metálicos*

1. Introduction

The shape memory alloys have been application in some areas such as: naval, aeronautic, automobilist. This is a promissor material in biomedical areas due to shape memory effect and superelasticity proprieties. Actually, the porous alloys have been very interesting for utilized as biomaterial mainly for a hard bone tissue substitution by has structural characteristics similar the body bone. The shape memory alloys (SMA) porous produced by powder metallurgy has shape memory effect and shown better microstructure homogeneity, excellent finishing surface and controlled porosity this aspects improvement of the osteointegration and loss elastic modulus. However, studies indicate possibility nickel release that can be occurs toxic reactions and rejection as when used in form of prosthesis [1-4].

The Nitrogen Plasma Immersion Ion Implantation (N-PIII) technique is a possibility for reduction the nickel release and improves the tribological proprieties through of the modification structural and chemical that the change the growth oxides and nitrates rates in implanted alloys [3].

2. Experimental

For production of the $Ni_{50,8}Ti$ alloy by powder metallurgy were used as starting material elemental powders Ni (size 62 µm) and Ti (size 250 µm). The powders were manual mixed in 20 minutes. The sample was compressed varying the applied pressure between 50 MPa and 250 MPa in the cylindrical form with 10 mm in diameter and 2 mm in thickness .The sintering was performed at 900 ºC for 120 minutes. The N-PIII technique was realized at 770 ºC for 60 minutes.

The microstructure of as cast and implanted by PBII samples were observed with scanning electron microscope. The phase's identification and structural parameters were established using the X ray diffraction. The measurements of friction coefficient were accomplished in a CSM Instruments Pin-on-disc-Tribometer, computer controlled, SN 18-393, with 5 cm/s of linear speed, applied load of 1N, 3.18 mm of wear track radius, stopping at 5.000 revolutions at room temperature in air. Alumina ball-3 mm-diameter, supplied by CSM-Instruments was used. Disk volume loss and wear rate were calculated according to equations in the ASM G-99 norm.

3. Results and Discussions

The microstructure before N-PIII shows low heterogeneity and high porosity with open porous and interconnected. In XRD analysis, the difratogram demonstrated stable phase, $NiTi_3$ and $NiTi_2$ peaks and NiTi intermetalic phases, important for shape memory effect in these alloys. The microstructure of the sample after the N-PIII has less quantity of the porous in the surface. Furthmore it presented aleatory phases rich in Ni.

The wear resistance before and after plasma implantation were analyzed and the friction coefficient for the implanted sample presented an average around 0.2, showing low coefficient compared with as-cast sample which has coefficient close to 0.9.

4. References

[1] FUNAKUBO, H. Shape memory alloys. Translated from the Japanese by Kennedy, J. B., Stanford University. Tokyo: University of Tokyo, 1987.

[2] HUMBEECK, J.V. From a seed to a need: The growth of the shape memory application in Europe. *Material Research Society Proceedings*, v.246, p.377-387, dec. 1992.

[3] BANSIDDHI, T.D., SARGEANT, T.D., STUPP, S.I., DUNAND, D.C. Porous NiTi for bone implants: A review. *Acta Biomaterialia*, v.4, p. 773-782, dec. 2008.

[4] GANG, C., CAO, P., EDMONDS, N. Porous NiTi alloys produced by press-and-sinter from Ni/Ti and Ni/TiH_2 mixtures.

Carolinebsales94@gmail.com

Acknowledgments

The CNPq, INPE, ITA, BRATS and PPRIME to support this project.

Carolinebsales94@gmail.com

ID 151: CARBON NANOTUBE FUNCTIONALIZATION BY RF PLASMA

Daniela Becker[1]*, Teresa Tromm Steffen[2], Luis César Fontana[3]
[1,2,3]*Center for Technological Sciences, UDESC, Joinville, Santa Catarina, Brazil*

1. Introduction

Carbon nanotubes (CNTs) are nanoparticles with high electrical, thermal and mechanical properties, therefore are widely used as reinforcement in nanocomposites. However to efficiently act at matrices they need to have a good dispersion and interaction with the matrix, what could be reached by functionalization [1,2]. Radio frequency (RF) plasma is a fast and free of solvent process that can promote a wide variety of chemical modification in CNTs [3]. Therefore, the aim of this work is to functionalize carbon nanotubes by RF plasma, in way to promote the bond of functional groups in CNTs surface to improve the dispersion and interaction with nanocomposite matrices in further applications.

2. Experimental

Multi-walled carbon nanotubes (MWCNT) used in this work were purchased from Chengdu Organic Chemicals Co. Ltd (TNIM4), with 88% of purity, an external diameter range of 10-30. The plasma reactor, shown in Fig. 1, has 7 cm³ of internal volume and operate at 13,56 MHz. When the reactor reached 10^{-2} Torr, argon, oxygen and nitrogen gases were placed at the chamber to functionalize MWCNT, with power inputs of 40 and 20 W. The treatment time was 60 minutes. Table 1 shows the samples obtained.

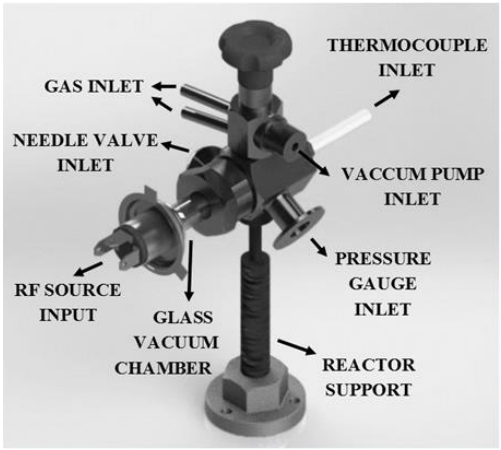

Fig. 1. *Plasma reactor utilized In MWCNT functionalization.*

SAMPLE	Power	Ar	O_2	N_2
CNT/pristine	-	-	-	-
CNT/40	40W	24sccm	6sccm	-
CNT/20	20W	24sccm	6sccm	-
CNT/N_2/40	40W	12sccm	6sccm	9sccm
CNT/N_2/20	20W	12sccm	6sccm	9sccm

Table. 1. *Samples conditions.*

3. Results and Discussions

FTIR spectra for all MWCNT samples treated by RF plasma are shown in Fig. 2. The peak at 3440 and 1435cm^{-1} can be assigned to the (O-H) stretch from (O=C-OH) and (C-OH). The infrared absorption at 2920, 2850 and 830cm^{-1} can be attributed to symmetric and asymmetric vibrations mode of (C-H) groups. The band in 1635cm^{-1} is associated to conjugated (C=C) stretching. The peaks 1210, 1090 and 1045cm^{-1} can be assigned to the (C-O) vibrations [4,5]. The presence of these bands including in MWCNT pristine is resulted from either atmospheric moisture of the raw material or oxidation during purification [6-8]. For all the samples treated in plasma there are a lightly peak at 1740cm^{-1} region (signed by vertical line) specially when the power supply is 20 W and nitrogen is present at the chamber. This peak can be attributed to (C=O) vibration mode of carboxylic groups [6,8-10]. The Raman spectra, shown in Fig. 3, indicates that for all the samples treated in plasma, there was an increase in D band, associated to increase of impurities and amorphous carbon, carbon nanotube oxidation and/or insertion of functional groups [11,12]. Besides that, the I_D/I_G ratio for samples treated had an increase in comparison with CNT/pristine. This increase, especially higher for CNT/N_2/40 sample, indicates the presence of defects in CNT surface and can be associated to an amorphous region [12] that can be seen in Fig. 4 provided by MET high-resolution image. XPS spectra show that the amount of oxygen increase in MWCNT for all samples treated in plasma. The sample CNT/40 present the higher amount in C-O functional group (~14% against ~7% of CNT/pristine sample) and the sample CNT/N_2/40 present the higher amount in O-C=O functional group (~4,6% against ~1,9% of CNT/pristine sample). This result show that the higher the power supply the higher the insert of oxygen functional groups in MWCNT surface. For sample CNT/N_2/20 was also found an atomic concentration of 0.1% of nitrogen and the presence of C-N bound, as shown in Fig. 5. The presence of this element, although

*Corresponding author: daniela.becker@udesc.br

small, indicates the capability of RF plasma in insert atomic nitrogen at MWCNT surface. Therefore, this work shows that RF plasma is an efficient tool to functionalize CNTs. The increase in oxygen and nitrogen amount in MWCNTs surface indicates that these nanoparticles can be further utilized to synthesize nanocomposites.

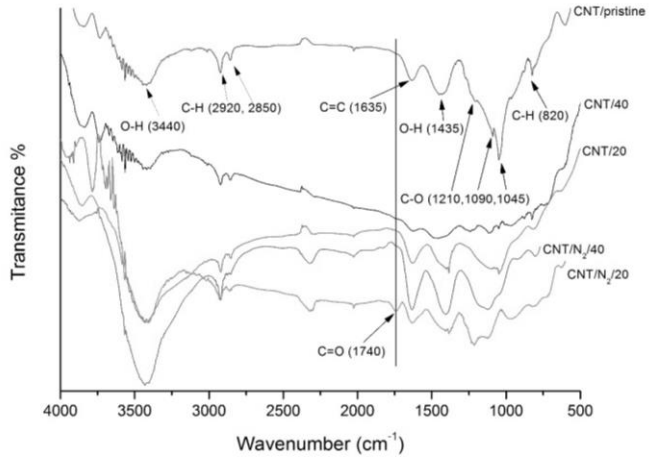

Fig. 2. *FTIR spectra showing a new peak around 1740cm^{-1} associated to (C=O) vibration mode of carboxylic groups*

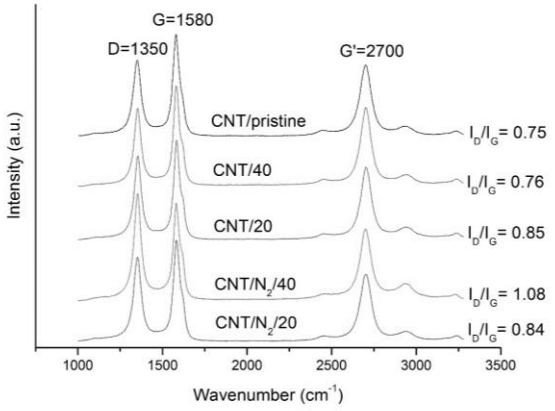

Fig. 3. *Raman spectra and I_D/I_G ratio for all samples of MWCNT*

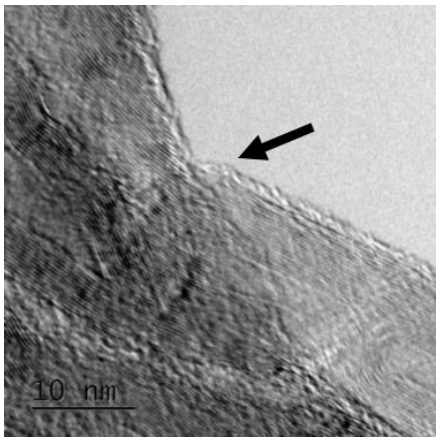

Fig. 4. *MET high resolution image, showing an amorphous region at CNT surface in CNT/N_2/40 sample*

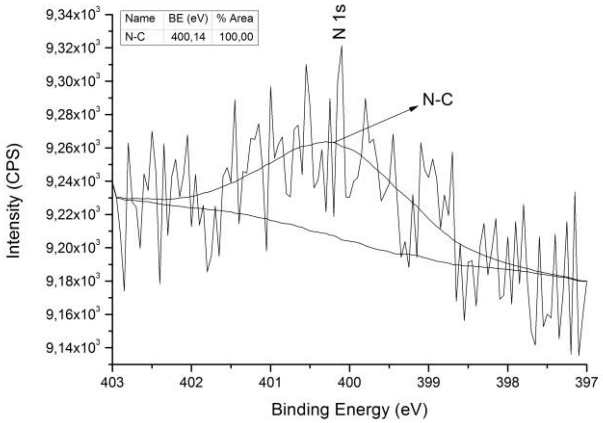

Fig. 5. *XPS spectra of CNT/N_2/20 sample, indicating nitrogen presence in MWCNT surface*

4. References

[1] J. N. Coleman, et al., Carbon, **44**, 1624–1652, (2006).
[2] S. W. Kim, et al., Carbon, **50**, 3–33, (2012).
[3] M. Loos; J. Nahorny; L. Fontana, Current Organic Chemistry, **17**, 1880–1893, (2013).
[4] M. Lavorgna, et al., European Polymer Journal, **49**, 428–438, (2013).
[5] M. Prodana, et al., Journal of Sustainable Energy, **3**, 62–66, (2012).
[6] J. Kathi; K. Y. Rhee, Journal of Materials Science, **43**, 33–37, (2008).
[7] T. Ramanathan, et al., Chemistry of Materials, **17**, 1290–1295, (2005).
[8] R. Scaffaro; A. Maio, Polymer Testing, **31**, 889–894, (2012).
[9] A. B. Gilman; M. Y. Yablokov; A. A. Kuznetsov, High Energy Chemistry, **46**, 219–228, (2012).
[10] A. U. Rehman, et al., Materials Letters, **108**, 253–256, (2013).
[11] X. Chen, et al., Journal of Materials Science, **51**, 5625–5634, (2016).
[12] G. Mercier, et al., The Journal of Physical Chemistry C, **117**, 8522–8529, (2013).

Acknowledgments The authors would like to thank the financial resources provided by CAPES by means of scholarships and CNPq by project Universal/445242/2014-0.

*Corresponding author: daniela.becker@udesc.br

ID 152: DYNAMIC FRICTION COEFFICIENT MEASUREMENT AND CONSTRUCTION OF A TRIBOMETER

Edgar Borali[1]*, Lucas Pereira Piedade[2], Carlos Alberto Fonzar Pintão[3]
[1, 2,3] *Departament of Physics-FC- UNESP-17033-360, SP, Brazil*

1. Introduction

Nowadays, the studies of tribology bring together knowledge acquired in physics, chemistry, mechanics, and material science to explain and predict the behavior of mechanical systems. These studies can be applied in several areas such as automotive, aerospace, electronics, biomedical and optics. There are estimates of reduced spending in these areas reducing wear loss [1]. The environmental aspect is also very important in the overall analysis of the losses due to wear, since it corresponds to an expressive reduction of CO_2 emitted into the atmosphere. Additionally, the discovery and existence of new materials, with surfaces previously prepared for a specific function, has required that efforts have to be made in characterizing them physically [2]. Thus, in this work a tribometer rotary with spherical body against was constructed (Fig. 1) to determine the coefficient of dynamic friction and to characterize some pairs of materials.

2. Experimental

To measure the coefficient of dynamic friction a tribometer was constructed with some characteristics to meet our needs (Fig. 1). The body against is spherical (diameter of 10 mm) and the sample is fixed to a chestnut. The system for measuring tangential or friction force is a force sensor (*FS*) Pasco, which will be in contact with a rod. Because of the relative motion between the sample and body against, there will be the dynamic frictional force ($F_{FRICTION}$) that is transmitted to this rod in contact with the *FS*. Through an interface, a *FS* and a specific program from PASCO, one can register this force (F_S) in function of time (t). The measurement of this force can be accomplished within a time interval of 60 minutes. Distinct normal forces (N) are applied by the body against on the surface of the sample by gravity by changing the weights respective. For each pair of materials (stainless steel 304 with Teflon or Titanium) the curve of the coefficient of dynamic friction (COF or μ) as a function of time is determined. In this case it is possible to define the relation: $\mu = F_{FRICTION} / N = F_S \; f_C / N$. The parameter f_C is the calibration factor.

3. Results and Discussions

As a first evaluation of the tribometer, the measurements of dynamic friction presented a good result. The COF versus time values is in agreement with the literature for all tested pairs. These facts open the possibility of characterization of new materials and future studies focused on tribology and tribocorrosion.

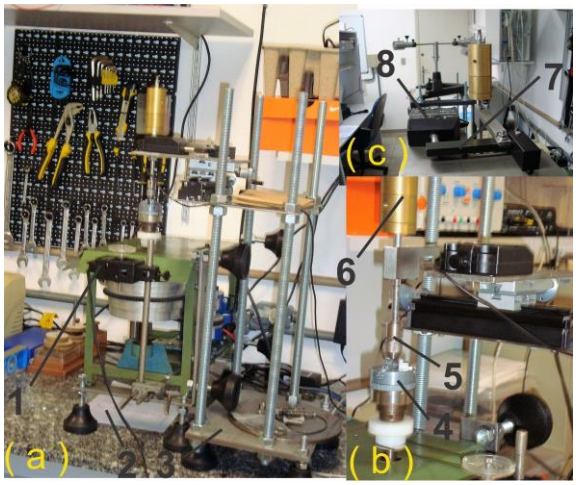

Fig. 1. *(a) Tribometer: (1) Rotary moviment sensor (RMS); (2) Base with the axis of rotation engine, belts, pulleys and nuts for fastening the specimen; (3) base of force sensor (FS) with rod, body against, weights and table XY. (b) Details of the chestnut for fixing the sample, body against and weights. (c) Details of force sensor and rod.*

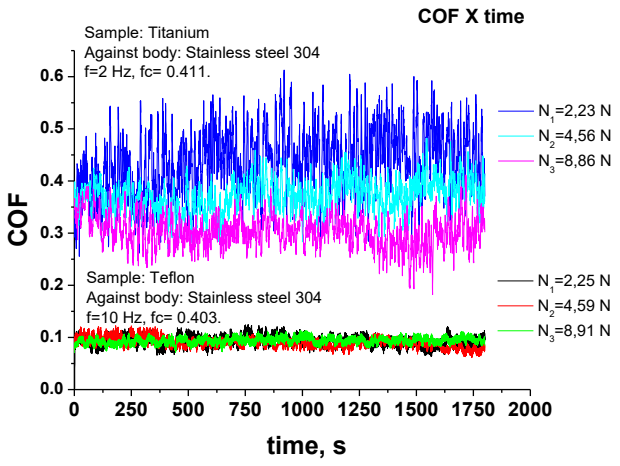

Fig. 2. *Results of dynamic friction coefficient to stainless steel 304 and titanium or Teflon.*

*fonzar@fc.unesp.br

4. References

[1] JOST, H. P. 1960, Lubrication (tribology) education and research, Jost Rep., Department of education and Science, HMSO, London, 1966, p.4. Citado em: SINATORA, A.,2005, "Tribologia: um resgate histórico e o estado da arte", Prova de erudição, São Paulo.

[2] BROSTOW, W. et al. Tribology with enphasis on polymers: Friction, Scratch resistance and wear. Journal of Materials Education. v. 24 (4-6): 119-132, 2003.

Acknowledgments

The authors thank the Brazilian funding agencies, FAPESP, process number: 2007/04094-9, and Capes, process number: BEX 6571/14-0.

*fonzar@fc.unesp.br

ID 155: CORROSION MORPHOLOGY STUDY OF DENTAL RESINS IMMERSED IN COLA

SANTOS,T.C.A[1], RADI,P.A[1,2] ,SOARES,L.E.S[1], VIEIRA,L*[1]
[1] *Universidade do Vale do Paraíba – UNIVAP, São José dos Campos, SP, Brazil*
[2] *Instituto Tecnológico de Aeronáutica – ITA, São José dos Campos - SP, Brazil*
**lucia.vieira@univap.br*

1. Introduction

Dental restorative materials, like resins, have been used in human teeth. They were developed in order to copy the teeth optical properties, not only the tooth color, but also their degree of translucency [1], but the mechanical and corrosion resistance are also important. Dental corrosion is defined as the progressive loss of dental hard tissue caused by acid and others erosive chemical substances, without bacteria involvement. This corrosion can be related to diets, especially in the consumption of acid from juice fruits and soft drinks and medicines (vitamin C, aspirin, hydrochloric acid) [2,3,4]. The diet is the most common acids source related to oral biodegradation. Hydroxyapatite crystals are calcium phosphate form present in inorganic portion of tooth constitution and any acid substance with low pH can improves corrosion in enamel and dentin. [6,7]. The dissolution of Hydroxyapatite crystals may occur depending on calcium concentration ions, saliva phosphate ions and starch availability[5]. Among the components of the diet with greater erosive capacity the pH value is below 5.5.

Fruit juices that has phosphoric acid could influence the pH. The phosphoric acid attack leads to an irreversible point of dental loss tissue duct, which is accompanied by progressive surface softening [8]. Some studies evaluates the erosive capacity of these drinks, not only pH measurement, but also the buffer acid effect, for ionic acid dissociation, calcium, phosphor, and fluorine concentration[9].

Studies published by United States General Academy of Dentistry alerts that the habit of consume energetic and isotonic drinks can cause an irreversible damage on the enamel tooth. The study explains the acid levels found on these types of drinks can originate, in some cases, the corrosive effect over the enamel after five days of consume[10].

2. Methods and Experiments

In this study were used two types of resins (Filtek z250 xt A3 and Filtek z350 A3E, both from 3M ESPE). These resins were prepared by a photopolymerizer and were immersed by seven days in coke soft drink and diet coke. After the immersion, the resins were stored in a stove at 37ºC without washing to check if the material has suffered some kind of waste. They were metalized by plasma using a thin golden layer to improves images contrast of phase. The resin morphology were analyzed using Scanning Electron Microscopy(SEM) to find differences. The resins samples were separated in three groups: Resins immersed in coke soft drink, diet coke and resins that weren't immersed in any liquid.

3. Results and Discussions

Figure 1 and 2 shows two images from *resin Filtek z250 XT A3 and resin Filtek z350 XT A3E* obtained by SEM. These resins weren't immersed in any liquid. From these images is possible to see that both resins presents porous.

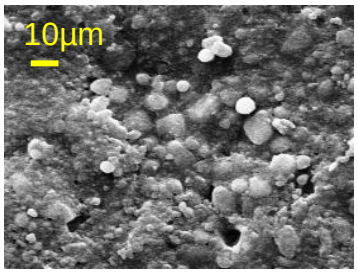

Fig. 1: *The resin Filtek z250 XT A3. Image with increasing of 2.00K.*

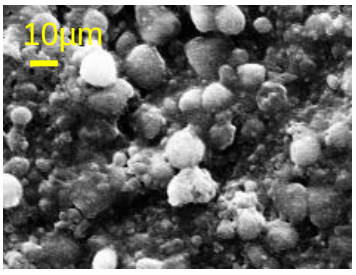

Fig. 2: *The resin Filtek z350 XT A3E. Image with increasing of 2.00K.*

Figure 3 and 4 shows two images from *resin Filtek z250 XT A3 and resin Filtek z350 XT A3E* obtained by SEM. Both resins were immersed in regular coke soda, and from this figure is possible to identify a layer with some cracks covering resin surface. The conclusion about this layer is concerned of sugar layer, since the resins weren't washed before being metallized.

E-mail: tataassis@hotmail.com

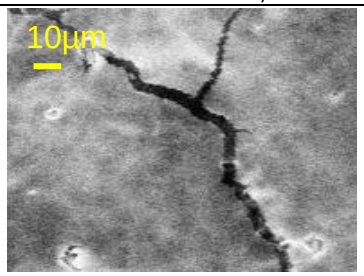

Fig. 3: *The resin Filtek z250 XT A3 immersed in coke soft drink. Image with increasing of 2.00K.*

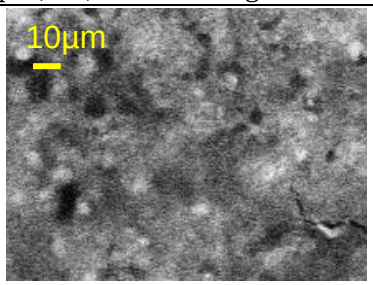

Fig. 4: *The resin Filtek z350 XT A3E immersed in coke soft drink. Image with increasing of 2.00K.*

Figure 5 and 6 shows two images from *resin Filtek z250 XT A3 and resin Filtek z350 XT A3E* obtained by SEM. Analyzing these images, it's possible to see a little layer of sugar, since the diet coke has smaller amount of sugar.

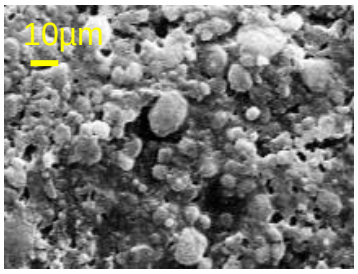

Fig. 5: *The resin Filtek z250 XT A3 immersed in diet coke. Image with increasing of 2.00K.*

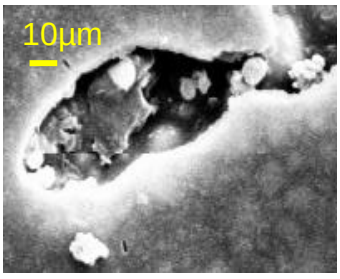

Fig. 6: *The resin Filtek z350 XT A3E immersed in diet coke. Image with increasing of 2.00K.*

4. Conclusions

Diet coke presented bigger porous than coke soda. The regular coke soft drink was responsible to improve a deposit of minerals on both studied resins. The minerals deposited in resins are provenient of sugars and others isotonic chemical constituents in soft drinks.

5. References

[1] Campos MIC,Campos CN,Vitral RWF. O uso de dentes bovinos como substitutos de dentes humanos em pesquisas odontológicas: uma revisão da literatura. Pesq Bras Odontopediatria Clín Integr. 2008;8:
[2] ECCLES, J. D. Dental erosion of nonindustrial origin. A clinical survey and classification. J Prosth Dent, Dec. 1979.
[3] GRANDO,J. L.;GABILAN,N. H.; PENTRY,A. *et al.* Erosão dental: estudo *in vitro* da erosão causada por refrigerantes e suco de limão no esmalte de dentes decíduos humanos. Análises bioquímicas. Ver Odontoped, v. 4, n 1,p. 1-10, jan./fev./mar./ 1995.
[4] LEVITCH, L. C.; BADER, J.D.; SHUGARS, D. A. *et al.* Non-carious cervical lesions. **J Dent,**v. 22, n. 4, p. 195-207,Aug. 1994.
[5]Gandara BK, Truelove EL, Diagnosis and management of dental erosion. J Contemp Dent Pract. 1999;15;16-23
[6]Grippo JO,Simring M, Schereiner S. Attrition, abrasion, corrosion and abfraction revisted: a new perspective on tooth surface lesions. J Am Dent Assoc.2004;135:1109-18; quiz 63-5.
[7] Barron RP, Carmichael RP, Marcon MA, Sandor GK. Dental erosion in gastroesophageal reflux disease. J Can Dent Assoc.2003;69;84-9.
[8] Stafne EC, Lovstedt SA, Rochester M. Dissolution of tooth substance by lemon juice, acid beverages ans acids some other sources. J Am Dent Assoc. 1947 May;34(9):586-92.
[9] Lussi, A.; Jaeggi, L.T.;Jaeggi-Scharer,S. The influence of different factors on in vitro enamel erosion.
[10] http://unieroradiologia.com.br/consumo-excessivo-de-energeticos-pode-prejudicar-o-esmalte-dentario/

Acknowledgments

IP&D Univap, Nanotecplasma Group and CNPQ for the financial incentive.

E-mail: tataassis@hotmail.com

ID 156: DEPOSITION OF HMDSO-BASED FILMS ON ETCHED CELLULOSE FOR CREATION OF SUPERHYDROPHOBIC SURFACES

Janine S. G. de Camargo[1,2], Aparecido J. de Menezes[2], Elidiane C. Rangel[1], Nilson C. Cruz[1], Adriana de O. Delgado-Silva[2]*

[1]*Science and Technology Institute of Sorocaba, Paulista State University-UNESP, Sorocaba, SP, Brazil.*

[2]*Federal University of São Carlos- UFSCar, Sorocaba, SP, Brazil.*

1. Introduction

Several studies have been developed with the purpose of modifying the wettability characteristic of the cellulose, in order to make it superhydrophobic, which property depends on the combination of an adequate surface morphology and a low surface energy [1]. Thus, in this work, films based on hexamethyldisiloxane (HMDSO) were deposited on the etched cellulose surface to obtain the superhydrophobicity on surface material.

2. Experimental

Pulp kraft cellulose sheets (20 x 10 mm) were firstly exposed to the plasma etching with oxygen at a pressure of 13 Pa and exciting power of 150 W for 60 minutes, to create of adequate surface topography. Then, the treated samples were submitted to the PECVD (Plasma Enhanced Chemical Vapor Deposition) process, in which a film was deposited on the surface from the precursor HMDSO in the presence of argon, in a ratio of 70 and 30%, respectively. The deposition time was varied from 5 to 30 minutes to obtain films of different thickness, in order to verify the effect of the thickness of the deposited films on the modification of the morphology created by the etching process. The samples were analyzed by Scanning Electron Microscopy (SEM), profilometry, Energy Dispersive Spectroscopy (EDS), Fourier Transform Infrared Spectroscopy (FTIR), static contact angle measurements and hysteresis and sliding angle measurements.

3. Results and Discussions

The previous etching step provided an accentuated removal of material from the substrate, evidenced by the presence of grooves in the cellulose fibers and addition of nanoscale structures on its surface [2] (as shown in Fig. 1b), in contrast with non-treated cellulose in Fig. 1a), that presents fibers with a smooth surface. The second step promoted the deposition of films with organosilicon character, with thicknesses varying between 160 and 910 nm, on the surface. For the higher thicknesses, the films promoted a "smoothing effect" on the created morphology, in which the nanostructures are covered by the film, as shown in Fig. 1e) and 1f). However, for the thinner films, the topography previously created by the ablation process is not suppressed (Fig. 1c). According to the results obtained by the EDS analysis, presented in Fig. 2, was verified that for the oxygen element (O), the intensity of the detected photons in relation to the carbon (C) peak remains practically constant, independent of the thickness of the deposited films. However, for the chemical element silicon (Si), the same trend is not observed. The relative intensity is constant for films up to 403 nm of thickness while for the film with thickness of 910 nm, there is a significant increase in the intensity of detected photons of Si in relation to C, compared to the other conditions. The FTIR analysis (in Fig. 3) showed that for thicker films, the intensity of the absorption bands related to methylsilyl groups (located at 1255, 838 and 792 cm^{-1}) is higher than the others. In addition, it is possible to observe that for this film, when compared to the others, the band at 792 cm^{-1} becomes more intense than the band at 838 cm^{-1}, which indicates an increase in the proportion of di-substituted methyl groups. The increase of these groups, combined with the higher Si presence in film composition (as detected by the EDS analysis) indicates crosslinked chains and, consequently, the formation of a film with higher density. This behavior can also be confirmed by displacement of absorption band located at 1020 cm^{-1}, which suggests changes in the degree of substitution of the methyl radical, since the di-substituted radicals favor the polymerization of longer chains, modifying their arrangement on the surface of the material [3]. The combination of chemical results with topological characteristic led to the optimal contact angle results for surface coated with the thinner films, with $\theta = 150°$ for water and $\theta \sim 120°$ for diiodomethane (non-polar liquid). Besides, the low values obtained for hysteresis (7°) and sliding angle (~10°) confirm the creation of a superhydrophobic “roll-off” surface.

*Corresponding author: adelgado@ufscar.br

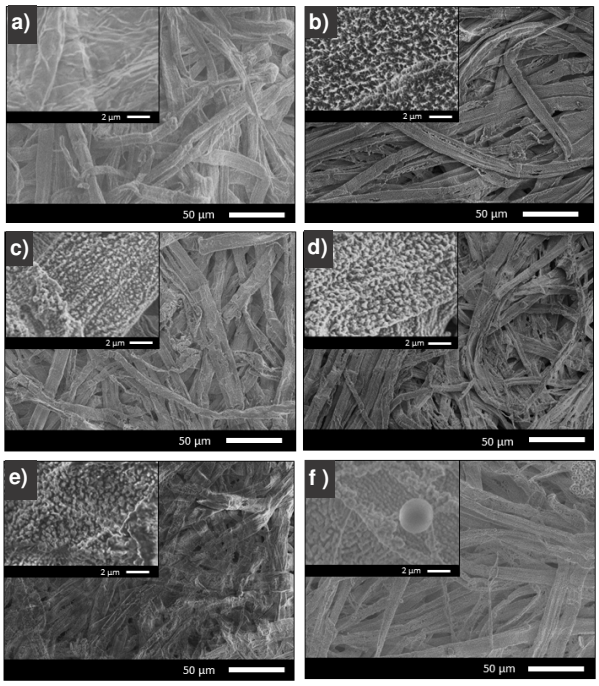

Fig. 1. *Secondary electrons micrographs of the cellulose surface a) as received, b) sample submitted to the etching process for 60 minutes; and covered with HMDSO-based film with thicknesses of c) 160 nm, d) 340 nm, e) 403 nm and f) 910 nm, after etching step.*

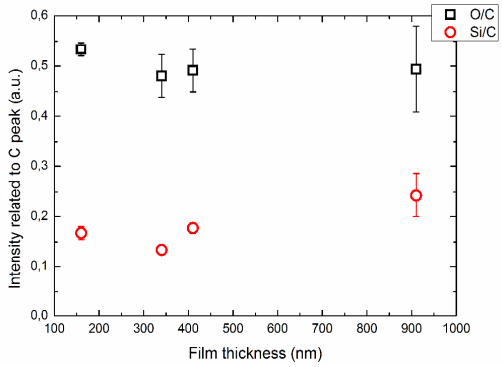

Fig. 2. *Intensity of the detected photons of the oxygen (O) and silicon (Si) elements on the surface of glass sheets covered with HMDSO-based film in relation to the peak of carbon (C), for films with different thicknesses.*

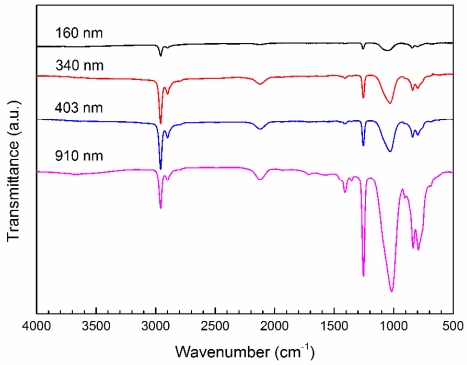

Fig. 3. *Infrared spectra of organosilicon films with different thickness deposited on mirror glass.*

4. References

[1] L. Li et al. Cellulose, **20**, 3219-3226, (2013).
[2] L. Xie et al. Surf. & Coat. Tech., **281**, 125-132, (2015).
[3] C. Vendemiatti et al. Surf. & Coat. Tech., **275**, 32-40, (2015).

Acknowledgments

Authors thank Capes, LMCMat and Votorantim Celulose e Papel (VCP).

*Corresponding author: adelgado@ufscar.br

ID 160: ALOE VERA INCORPORATION INTO ELECTROSPUN NANOFIBERS

Ana Neilde R. da Silva[1,2]*, Jaqueline Thiemy Awoky[2], Rogério Furlan[3], Maria Lúcia P. da Silva[1,2]

[1]*Department of Engineering of Electronic Systems, University of Sao Paulo, Sao Paulo, Brazil*
[2]*Departament of Electronic Systems, Faculty of Technology of São Paulo-FATEC-SP, CPS, Brasil*
[3]*Physics and Electronics Department, University of Puerto Rico at Humacao, Humacao, Puerto Rico*

1. Introduction

Electrospinning is a very simple, versatile and economic technique used for generating polymeric nanofibers in different fields. Polymeric nanofiber produced by electrospinning finds applications in several fields [1]. Tissue engineering, drug delivery and biomedical applications are the main fields where nanofibers have been extensively studied [2]. Considering nanoengineered tissues for biomedical therapeutics, the incorporation of aloe vera in nanofibers allows to obtain antibacterial, antifungal, antiviral, antidiabetic, antiinflammatory, and wound healing activities [3]. Different polymers and polymer combinations have been used with aloe vera (commercial powders, gel solutions) to obtain electrospun nanofiber mats [4-8]. Therefore this work aims the production and test the nanofiber mats with aloe vera incorporated.

2. Experimental

The precursor solutions were prepared with 2 g of polyvinylpirrolidone K90, commercial, dissolved in 10 mL of 3 different types of solvents: aloe vera juice, aloe vera and 2-propanol (IPA) and aloe vera with water. All solutions were stirred during 12h at room temperature, until complete polymer dissolution. The electrospinning process were conducted in an apparatus consisting in an DC high power supply (Gamma High Voltage Research Inc. 0-30 kV), a 3 mL syringe with a hypodermic needle 22G1 and a metal plate. The positive terminal of the power supply was connected to the needle and the ground terminal was connected to the metal plate where the sample is placed. The fibers were electrospun over silicon substrate from the three different precursor solutions. The needle was kept at 15 cm from the sample and a 15 kV was applied to the needle. The samples were analyzed by FTIRS and Raman microscopy in order to evaluate the interaction between the polymer, the aloe vera and the solvents. SEM analysis was performed aiming at verify the influence of the solvent in the fibers morphology. The solutions viscosity was measured in a Brookfield viscometer RVDVII with the small sample adapter.

3. Results and Discussions

The viscosity and conductivity of the precursor solution was evaluated in order to study the polymer solvent interactions. Also, the interest is to confirm if there is a strong interaction between the aloe vera and the polymer aiming the incorporation of the aloe vera in the fiber after electrospinning process. Table I resumes the viscosity values obtained for each solution studied.

Table I: Precursor solutions viscosity values

Aloe Vera/ Water/ IPA (ml)	Viscosity (MPa)
10 / 0 / 0	1356,7
5 / 5 / 0	1382,7
5 / 0 / 5	5591,7

Table II: Precursor solutions conductivity values

Aloe Vera /IPA /water (mL)	Condutivity (μS/cm)
10/0/0	1378
5/0/5	949
5/5/0	114
0/0/10	51,6
0/10/0	1,40

Table III: FTIRS absorption bands

Sample	Species					
	CHn	**C=O cyclic**	**1948**	**OH/C=O**	**CH2**	**CN**
Aloe Vera	--	2669	--	---	--	--
Aloe Vera + IPA	--	2553	interaction	--	--	--
Aloe Vera + Water	2954	2553	interaction	1674	1431	1288

The viscosity is five times higher for the solutions prepared with the mixture of aloe vera and 2-propanol confirming the influence of the solvent in the viscosity. However, the viscosity of the solutions prepared with pure aloe vera juice and a mixture of aloe vera and water is quite the same. Since that the extract of aloe vera has high concentration of water the measured values of viscosity for both solutions are similar. This result

*Corresponding author: neilde@lsi.usp.br

suggests that the interaction between the polymer and the solvent is mainly made by hydrogen bridge. The presence of this kind of chemical interaction prevents the polymer entanglement in the solution, lowering the viscosity.

The precursor solution conductivity was also evaluated. The conductivity is an important parameter for the electrospinning process, thus the higher the conductivity of the solution the more uniform are the fibers. The high conductivity of aloe vera extract is mainly due to the presence of dissolved salts, so in the table II is observed that the conductivity of the solutions decreases as the concentration of aloe vera decreases. Also, the values decrease as the amount of isopropyl alcohol increases.

The interaction between the polymer and the solvent was studied by FTIR and Raman. The Raman analysis did not show any significant variation between the solutions and FTIRS spectra are shown in Figure 1.

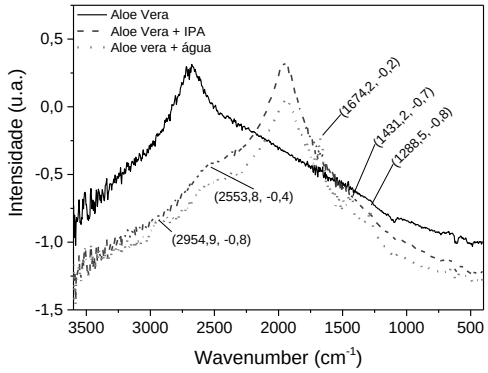

Fig. 1. *FTIRS Spectra from the fibers electrospun from solutions with different solvents and aloe vera.*

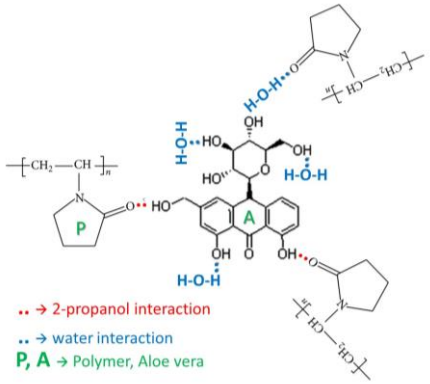

Fig. 2. *Illustrative model aloe vera polymer interaction in different solvents.*

The main characteristic bands of FTIRS, Figure 1, is depicted in Table III. The aloe vera spectrum shows only one prominent of the aloe vera absorption bands, the 2669 cm^{-1}, due to C=O cyclic species. On the other hand, aloe vera dispersed with water shows the main species due to PVP polymer that indicates low interaction among polymer and aloe vera components, which is also consistent with the low increase in viscosity. However, 2-propanol sample shows no bands at all, and considering the high increment on viscosity, is a good indication of high interaction among polymer/aloe vera components. Nevertheless, the most important appearance is the highly intense 1948 cm^{-1} band. Such value can be encountered in C=O bonds present in resonant structures of anhydrides, especially cyclic. Therefore, a most probable explanation for the interaction among polymer and aloe vera components is based in hydrogen bridge formation, which allows the existence of COH ….C=O … big structures, as shown in Figure 2. The main difference from water to 2-propanol interactions probably is that the small molecule, water, prevents this big structure to be done more efficiently, which permits to measure other bands on fiber spectrum. Due to conductivity and viscosity values, SEM analysis show that the fibers from solution with aloe vera and polymer has the thinner diameter

Based on the proposed model there are two different composed fibers to be tested on future works.

4. References

[1] Z.-M. Huang, Y.-Z. Zhangb, M. Kotakic, S. Ramakrishna, Composites Science and Technology, 63 (2003), pp.2223–2253

[2] J. Sharma, M. Lizu, M. Stewart, K. Zygula, Y. Lu, R. Chauhan, X. Yan, Z. Guo, E. K. Wujcik, S. Wei, Polymers, 7 (2015), pp. 186-219.

[3] B. Gupta, R. Agarwal, M. Sarwar Alam, Biomaterials and Tissue Engineering, 3 (2013), pp. 1-9.

[4] J. R. Venugopal, S. Sridhar, S Ramakrishna, Plant Science Today, 1(3) (2014), pp. 151-154.

[5] N. A. Abdullah@Shukry, K. A. Sekak, M. R. Ahmad, T. J. B. Effendi, Proceedings of the International Colloquium in Textile Engineering, Fashion, Apparel and Design 2014 (ICTEFAD 2014).

[6] I. Uslu, A. Aytimur, Journal of Applied Polymer Science, 124, (4) (2012), pp. 3520–3524.

[7] İ. Uslu, S. Keskin, A. Gül, T. C. Karabulut, M. L.t Aksu, Hacettepe, J. Biol. & Chem.,38 (1) (2010), pp. 19-25.

[8] Peel Narsih, Sri Kumalaningsih, Wignyanto, Susinggih Wijana, J. Agric. Food. Tech., 2(5)79-84, (2012)

Acknowledgments

The authors thanks to CNPq for the PIBIC scholarship.

*Corresponding author: neilde@lsi.usp.br

ID 162: SYNTHESIS AND CHARACTERIZATION OF N-DOPED TiO_2 THIN FILMS

E.A. de Souza Filho[1], E.G. de Araújo[2], O.V.Correa[1] and M.F.Pillis[1]
[1]*Instituto de Pesquisas Energéticas e Nucleares*
[2]*Universidade Federal de Pernambuco*

1. Introduction

Most of the metallic materials used in modern technology require certain properties of the alloy, and a different set of properties of the surface. The requirements for the alloy are toughness, tensile strength, among others, while those for the surface are resistance to oxidation, wear, erosion, etc. [1,2]. It is rare that this combination can be presented by a single material, hence the need for the use of coatings, which have the advantage of not altering the mechanical and microstructural properties of the alloys. A variety of techniques are available for deposition of thin films, such as ion implantation [3], sputtering [4], chemical vapor deposition (CVD) [5], sol gel [6], and metallorganic chemical vapor deposition (MOCVD) [7,8].

Titanium dioxide is a biologically and chemically inert material [9], nontoxic, exhibits photostability, good mechanical and corrosion resistance [7], and significant photocatalytic activity. It is used as dielectric material, anti-reflective coatings, anti-corrosive barriers [6,7], solar cells, biomaterials [10], and in optical devices [10]. The interest in Ti-N-O films has increased in recent years because the presence and control of oxygen in titanium nitride leads to the formation of gradient coatings ranging from TiO_2 to TiN, and where resistivity varies as a function of the N/O ratio [11]. Similarly, the increase of the nitrogen content incorporated into TiO_2 alters functional properties such as refractive index, electrical conductivity, hardness, and modulus of elasticity of the original oxide film because the metal-nitrogen bonds are less polar than the substituted metal-oxygen bonds [12].

This work reports the growth of TiO_2 and N-doped TiO_2 thin films at 500° C by MOCVD on stainless steel substrate. X-ray diffraction diagrams and XPS analysis of N-doped TiO_2 are presented and discussed in relation to the undoped TiO_2.

2. Experimental

Samples of AISI 316 stainless steel with 20x20x5 mm were used as substrate for the deposition of TiO_2 films and N-doped TiO_2 via MOCVD process. The samples were grounded with SiC abrasive discs up to 600 grit and polished with diamond paste until 3 μm. Substrates were ultrasonically cleaned in acetone, in ethanol, and rinsed in deionized water in abundance. They were then dried in nitrogen and immediately inserted into the reactor.

Titanium isopropoxide IV was used both as titanium and oxygen sources to obtain TiO_2. For the production of N-doped TiO_2 NH_3 was added in the reactor. Both reagents were introduced into the system simultaneously, and were mixed before reaching the reaction chamber. The growth parameters used were: nitrogen and ammonia flow 0.5 slm, titanium precursor temperature 39°C, chamber pressure 50 mbar, deposition temperature 500°C. The thickness of the films is close to 300 nm.

The samples were characterized by X-ray diffractometry (XRD) in a Rigaku equipament with incident angle of 3°, and by X-ray photoelectrons spectroscopy (XPS) in a thermoscientific equipment, model k-alpha.

3. Results and Discussions

XRD analysis, Figure 1, indicates that in the non-doped TiO_2 film anatase was formed, whereas N-doped TiO_2 sample presents the rutile phase. This fact suggests that nitrogen induces the anatase-rutile phase transformation. No peak relative to nitrogen-containing phases was observed. Similar results were obtained by F.Peng [13] and M. Sathish [14]. The XPS spectrum is shown in Figure 2. On the survey, it can be seen that the doped film is composed of Ti, O, and C as contaminant [13,15], in addition to nitrogen, which was incorporated in the ratio of 8.29 at%. N 1s linkage energy was detected at 396.9 eV resulting from the nitrogen substitution of the TiO_2 lattice. According to other researchers that agree on that N 1s peak at 396-397.5 eV is responsible for nitrogen atoms substitutionally doped into the TiO_2 lattice as characteristic peak of Ti-N-Ti linkages [14-17]. Further analyses are under way.

*Corresponding author: mfpillis@ipen.br

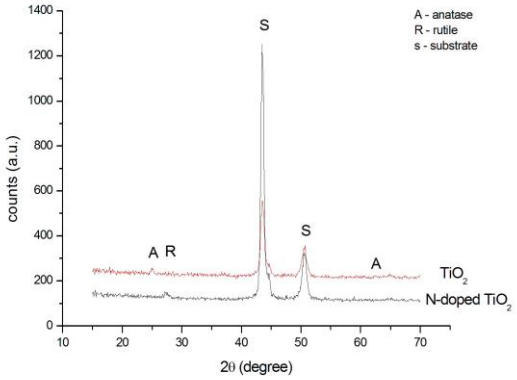

Fig. 1.. XRD diagram of samples.

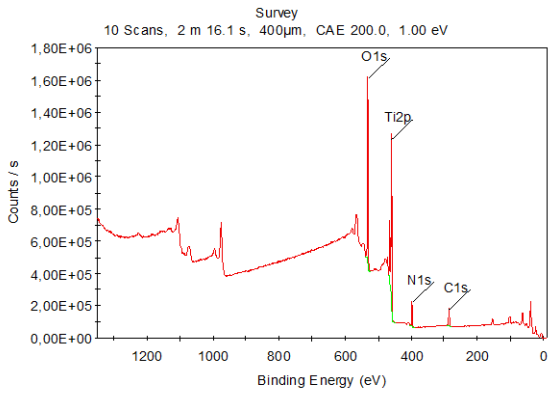

Fig.2. XPS spectrum of N-doped TiO_2 film.

TiO_2 and N-doped TiO_2 films depositions were performed in a single step by using the MOCVD technique. Titanium isopropoxide IV was used as a precursor of both titanium and oxygen, and NH_3 as a source of nitrogen. The growth was carried out at 500°C and the films presented about 300 nm of thickness. The nitrogen content incorporated into the film was 8.3 at%. Results of XRD indicate the formation of the anatase phase for the non-doped film, and rutile for the nitrogen-doped film, suggesting that the nitrogen induces the transformation of the anatase to rutile phase.

4. References

[1] D.G.Teer *"Evaporation and Sputter Techniques in: Coatings for high temperature applications"*. E.Lang (Eds.) Elsevier Applied Science Publishers, 1986.
[2] L.F. Pochet et al.Surf. & Coat. Technol, **94-95**, 70-75, (1997).
[3] I.G.Brown et al. Surf. & Coat. Technol., **112**, 271-277, (1999).
[4] M.F.Pillis et al. Corr. Sci., **102**, 317-325, (2016).
[5] H.M.Yates et al. J.Photochem and Photobiology A, **179**, 213-223, (2006).
[6] L. Curkovic et al.,Corr.Sci., **22**, 176-184, (2013).
[7] R.A.Antunes et al. Int. J. of Electrochem.Sci, **8**, 1487-1500, (2013).
[8] S.H.Namet al. Mat.Res.Bull., **47**, 2717-2721, (2012).
[9] F.D. Duminica et al. Surf. & Coat. Technol., **201**, 9304-9308, (2007).
[10] O. Carp et al. Progress in Solid State Chem., **32**, 33–177, (2004).
[11] F.Fabreguette et al., Appl. Surf. Sci., **175-176**, 685-690, (2001).
[12] F.Maury and F.-D.Duminica, Surf. &Coat. Technol., **205**, 1287-1293, (2010).
[13] F.Peng et al. J. of Solid State Chem., **181**, 130-136, (2008)
[14] M. Sathish et al. Chem. Mater., **17**,6349, (2005).
[15] J.Guillot et al. App. Surf. Sci., **6956**, 1-5, (2001).
[16] Feng M.S.Wong et al. Thin Solid Films, **494**,244, (2006)
[17] Feng S.Sakthivel et al. J.Phys. Chem. B **108**, 19384, (2004).

Acknowledgments
The authors are thankful to LnNano Lab.

*Corresponding author: mfpillis@ipen.br

ID 164_1: INTEGRATED LIGHT EMISSION STUDY ON ATMOSPHERIC NEEDLE PLASMA DISCHARGES

Gustavo G. Vasques, Milton E. Kayama, Marcelo H. Mello,
André B. Laraia and Mauricio Antonio A. Algatti
UNESP – Campus de Guaratinguetá

1.Introduction

The atmospheric plasmas have been used in the Science and industry in fields associated to material surface treatment. It has been used in medical field for treatments and sterilizations. In present work, we report the investigation of the measurements of integrated light emission by a micro plasma used for surface treatment and film deposition.

2. Experimental

The Fig.1 shows the schematic view of the experiment. The discharge device had two independent entrances for the gas with flow controlled by needle valves. The applied voltage had sinusoidal waveform with 5.8 kV peak-to-peak and frequency of 37 kHz. The voltage is applied between the needle and an external brass ring. The borosilicate capillary is located between them and a filamentary discharge type evolves at the site [1]. The light emitted by the filaments and the plume is collected by an optical cable with 1.0 mm diameter with polished surface. This system was also positioned side on to collect only the light emission of the plume. The cable was positioned on axis, 6 mm from the end of the capillary. Optical filters on red, green and blue was used to select different bands of the spectrum. The light is conducted thru the fiber and ends at the slit at entrance of the photomultiplier housing. The photomultiplier was the Hamamatsu model R374 with output coupled to an amplifying circuit.

3. Results and Discussions

The l signal photomultiplier signal is dominated by sequential fast spikes during the half-cycle of the applied voltage. The signal was numerically integrated assuming zero intensity at beginning of the half-cycle. Discharges were investigated for argon and helium at various flow rates. A typical result is shown in Fig. 2 The light intensity is higher for positive half-cycles due to the different mechanism involved on the discharges with positive and negative voltages. The intensity also rises with the flow rate in the needle. The helium gas at primary discharge site has shown higher integrated light intensity than discharges with argon.

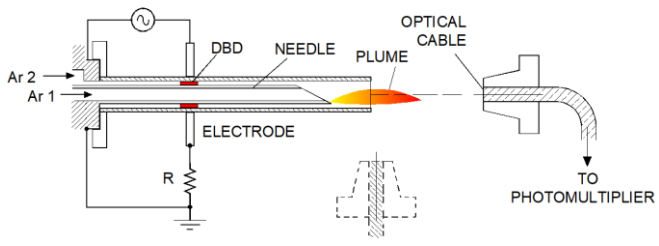

Fig.1 – Schematic view of the experiment

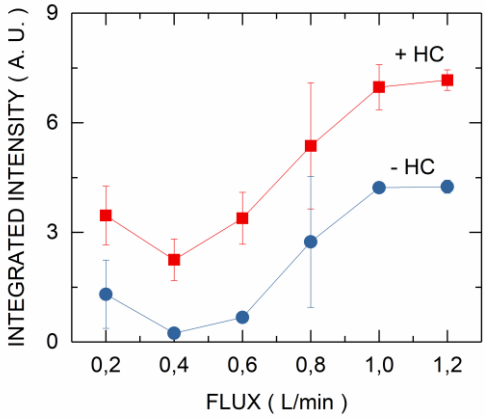

Fig.2 – Integrated light intensity during positive (+HC) and negative (-HC) half-cycles of applied voltage

4. References

[1] Kayama, M.E., Silva L.J., Prysiazhnyi. V, Kostov, K.G, and Algatti M.A., Characteristics of Needle-Disk Electrodes Atmospheric Pressure Discharges Applied to Modify Wettalility. *IEEE Trans. Plasma Sci.* 0093-3813, (2017).

ID 164: CHARATERISTICS OF DOUBLE GAS INJECTION NEEDLE MICRO DISCHARGES

Milton E. Kayama, Marcelo H. Mello, Gustavo G. Vasques,
Daniela A. Souza and Konstantin G. Kostov
UNESP – Campus de Guaratinguetá

1.Introduction

Micro plasmas are plasmas generated at atmospheric pressure where at least one dimension is less than 1 mm. They have high electron temperature, higher than the counterparts with large dimension. These high power density plasmas are appropriate to be used in application such as deposition process where molecular fragmentation by electron impact plays a major role. One architecture used to produce such micro-discharge is the arrangement of a surgical needle with capillary and an external ring. The dielectric-barrier-discharge (DBD) between the electrodes generates a plasma plume from the needle end that expands downstream the gas flow to the exit of capillary. The variation of the power of the discharge for various flow rates of argon and helium along the needle and in DBD zone is reported in the present work.

2. Experimental

The microdischarge is generated at the tip of the needle as shown in the Fig,1. It is promoted by a dielectric barrier discharge (DBD) between the body of the needle and an external electrode [1]. The dielectric is a borosilicate capillary. The needle has 0.7 mm outer diameter and the capillary 1.0 mm inner diameter. The applied voltage is a sinusoidal signal with 5 kV peak-to-peak and frequency of 37 kHz. The gases feed independently at DBD zone and the needle. Combined argon and helium gases were used in these lines. The mean power *p* was calculated according to the product voltage-current *vi* , integrated in time over one period of the signal. The voltage was measured with Tektronix 1000x probe and the current by the voltage drop on a 47 ohm resistor in series with the discharge.

3. Results and Discussions

. Fig.2 shows the variation of the power with the flow rate at DBD zone, calculated over 4480 values for each point. The flux in the needle was kept constant at 1,2 L/min.The mean value over 4480 values of p is shown in Fig.2. The increase of the power with flow rate suggests an augment of the filamentary discharges along the needle with the gas flow. The plume generated from the end of the needle extinguish at high flow rate. Once outside the capillary the plume shows reduction on the light emission due to the interaction with surrounding ambient gas. The investigation shows that the combination of both gases appropriate to produce high power plumes.

.

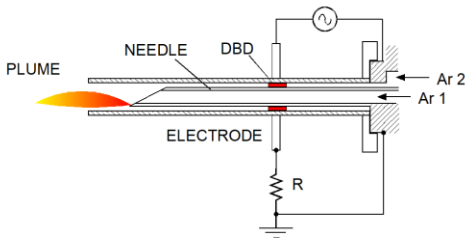

Fig.1 – Diagram of the experimental arrangement.

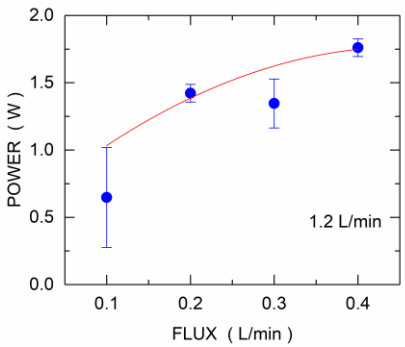

Fig.2 – Variation of the power with argon flow in DBD region and the needle.

4. References

[1] Kayama. E.M., Silva. J.L, Prysiazhnyi. V, Kostov. G. K and Algatti. A. M. Characteristics of Needle-Disk Electrodes Atmospheric Pressure Discharges Applied to Modify Wettalility. *IEEE Trans. Plasma Sci.* 0093-3813, (2017).

daniela _araujo5@outlook.com

ID 165: SILICON INTERLAYER INFLUENCE ON ADHESION OF DLC FILM DEPOSITED ON AA 7075 SUBSTRATE USING A MODIFIED PULSED-DC PECVD TECHNIQUE

Machado, S.L.[1]*, Machado, J.P.B.[1], Figueroa, C. A.[2], Nunes, C.A.O.[1], Gonzalez, D.C.L.[1], Ramírez, M.A.[1], Trava-Airoldi, V.J.[1]

[1]Instituto Nacional de Pesquisas Espaciais (INPE), São José dos Campos-SP, Brazil
[2]Universidade de Caxias do Sul, Caxias do Sul-RS, Brazil

1. Introduction

Aluminum and aluminum alloys have been widely used as structural materials in the aerospace and automotive industries because of their low density, good machinability and high mechanical strength-to-weight ratio [1, 2].

The choice for the AA 7075 aluminum alloy is due to its use in the space, aeronautics, automotive, biomedical and mainly because it is one of the most used alloys in the CBERS (China-Brazil Earth-Resources Satellite) family of the National Institute of Space Research (INPE). However, its low surface hardness as well as properties of low resistance to wear and corrosion reduces its lifetime in tribological contacts through wear and friction damage, limiting its application in several areas of surface engineering [3]. DLC (Diamond Like Carbon) is a metastable form of amorphous carbon with significant amount of sp3 bonds with high mechanical hardness, chemical inertia, optical transparency in addition to being a broadband semiconductor [4].

The focus of this study ison the silicon interlayer, seeking an interface with intermediary mechanical properties between substrate AA 7075 and DLC film, but with strong chemical bonds ensuring high adhesion.

2. Experimental

The deposition of DLC and Silicon interlayer films was made using a modified pulsed-DC PECVD technique (additional cathod) [5]. The applied self-bias voltage was -2 kV, -4 kV, -6kV, -8 kV and -10 kV, for Silicon interlayer growth. In order to increase the plasma densification of the technique an additional cathod was used [5]. All fifteen depositions was made using the same parameters as described in Table 1, the only changing parameter was the voltage for the Silicon deposition.

The film's atomic arrangements were analyzed by Raman Spectroscopy, and film adhesion was evaluated by Rockwell C Indentation with reference to VDI 3198 test (500, 1000, and 1500 N). DLC film and interlayer thickness was measured by Scanning Electron Microscopy (SEM / FEG) and Glow Discharge Optical Emission Spectroscopy (GDOES).

Tab. 1: Process parameters for all depositions.

ACTIVITIES	TIME (min)	PRESSURE (Torr)	VOLTAGE (V)	FLOW (sccm)
Sample cleaning (Argon)	25	$8{,}0 \times 10^{-4}$	-600	10,0
Silicon deposition (SiH_4)	15	$1{,}5 \times 10^{-4}$	variable	3,6
$SiH_4 + C_2H_2$	2	$1{,}0 \times 10^{-4}$	-800	3,6 / 9,8
$SiH_4 + C_2H_2$	3	$1{,}0 \times 10^{-4}$	-800	2,0 / 9,8
DLC deposition (C_2H_2)	40	$8{,}0 \times 10^{-4}$	-750	9,8

3. Results and Discussions

The growth in thickness of the silicon interlayer, measured by GDOES and SEM (Fig. 1, a and b, respectively), showed a near linear behavior as a function of the increase on the applied voltage. The thickness obtained by SEM showed smaller values but with the same (near) linearity. The thickness measurements of the films by SEM / FEG were made for films grown on Silicon [100] monocrystal substrate, and not on AA 7075, as it was made for GDOES. This is because when we cut the AA 7075 sample with DLC film, it was always observed a deformation of the metal above the film.

*soloma@globo.com

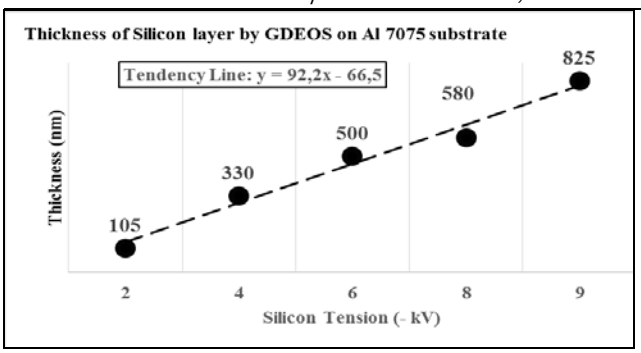

Fig. 1a. *Silicon thickness (GDOES) versus applied self-bias voltage.*

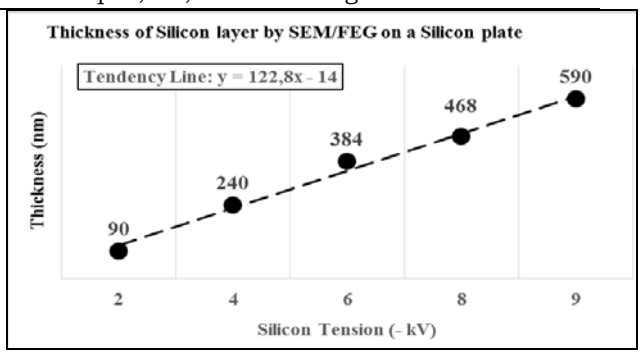

Fig. 1b. *Silicon thickness (SEM/FEG) versus applied self-bias voltage.*

The spectrum obtained through Raman spectroscopy for all processed samples is typically of a hydrogenated amorphous carbon (a-C: H) film, as it can be seen on Fig.2 for sample 23.

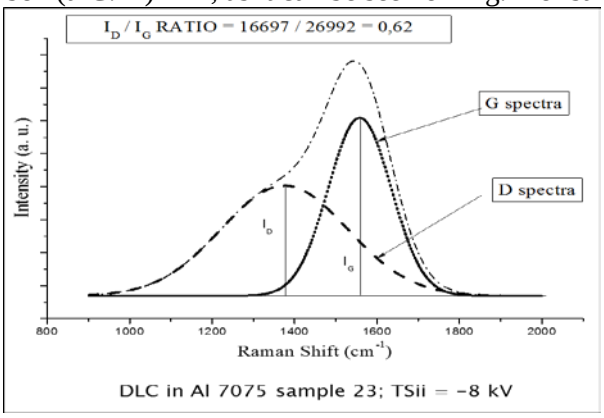

Fig.2. *Raman spectra with deconvoluted curves for sample 23.*

The adhesion results for the DLC films were satisfactory for all self-bias voltages applied in the silicon interlayer (VDI standard 3198). Fig. 4 shows the results of sample 13 -6 kV) for 1500 N.

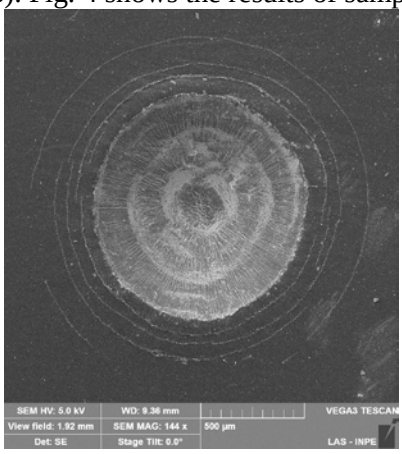

Fig.3. *Rockwell C indentation for the sample with sel-bias voltage of -6 kV.*

It can be concluded that, with the applied film growth methodology, it was possible to obtain high adherent DLC films on AA 7075 substrate, and that the silicon interlayer thickness did not affect the adhesion of the DLC film in the substrate.

4. References

[1] Miller WS, et al.Mater Sci Eng A, **280**, 37-49 (2000).
[2] Ashby MF, Bréchet YJM, Cebon D, Salvo L. Mater Des ,25, 51-67, (2004).
[3] Picas JA, Forn TA, Rilla R, Martín E. Surf Coat Technol 2005; 200: 1178-81.
[4] Robertson, J. Mater. Sci. and Eng. R., **37**, 129-281, (2002).
[5] Capote, G., et. al.. Surface & Coatings Technology, **308**, 70-79, (2016).

Acknowledgments

The author are grateful to UNIFESP, FAPESP and INPE for financial support.

*soloma@globo.com

ID 167: OPTICAL ABSORPTION SPECTRA OF VANADIUM MODIFIED BARIUM ZIRCONIUM TITANATE AND ZIRCONIUM-DOPED CALCIUM COPPER TITANATE POWDERS

M. A. Algatti[1]*, A. Z. Simões[2], M. Macias[3], A. Cruz-Orea[3]
[1]*FEG-DFQ-UNESP, Av. Ariberto Pereira da Cunha 333, 12516-410, Guaratinguetá, SP, Brazil*
[2]*FEG-DMT-UNESP, Av. Ariberto Pereira da Cunha 333, 12516-410, Guaratinguetá, SP, Brazil*
[3]*Physics Department, CINVESTAV- IPN, A.P. 14-740, C.P. 07360, Mexico City, Mexico*

1. Introduction

Barium titanate based materials are of great interest for a large range of applications in electronic devices. In addition, solid solutions of barium titanate with other perovskite-type materials, as vanadium modified barium zirconium titanate (BZT), offer a large range of possible modification of the dielectric properties [1]. By other hand another perovskite-type material in which has been observed an intense photoluminescence emission is the Zr-doped calcium copper titanate powders (CCTO)[2]. In these perovskite-type materials is important to study their optical properties which are related to their optical energy band gap. By using Photoacoustic Spectroscopy the optical absorption spectra of vanadium modified BZT and zirconium-doped CCTO powders were obtained.

2. Experimental

The optical absorption spectra of the samples were obtained in the range of 300 nm to 800 nm by using a homemade photoacoustic (PA) spectrometer. The experimental setup consisted of a 1000 W xenon lamp, a variable frequency mechanical chopper, set at 17 Hz, a monochromator, and an air-filled brass cell with a condenser microphone. The PA signal from the microphone provided the input to the signal channel of a lock-in amplifier which is interfaced to a personal computer, displaying the wavelength-dependent signal amplitude and phase simultaneously. In order to take into account the Xe lamp emission spectrum, the PA signal was normalized to the signal obtained from charcoal powder [3].

3. Results and Discussions

Figure 1 shows the optical absorption spectrum of CCTO, with 15% Zr, in this spectrum it is possible to observe two absorption bands. By other hand Figure 2 shows the optical absorption spectrum of vanadium modified BZT, with 0,5% V, in this case it is possible to observe a strong optical absorption band mainly in the UV region.

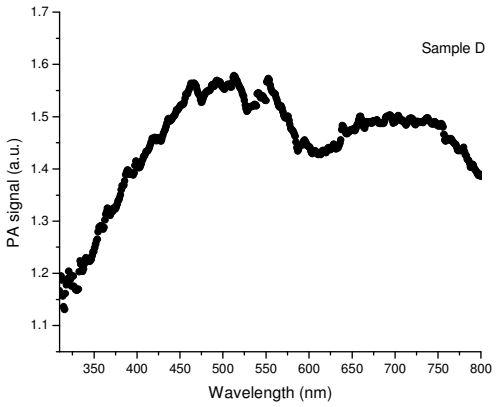

Fig. 1. *Optical absorption spectrum of CCTO w/ 15% Zr*

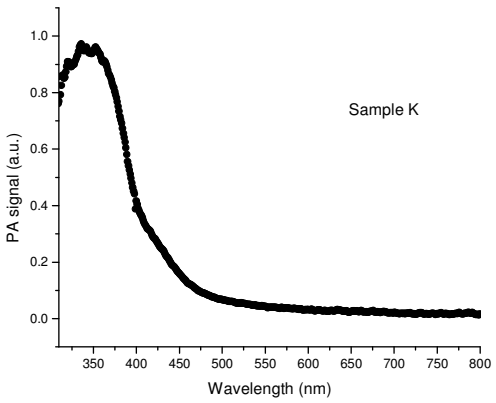

Fig. 2. *Optical absorption spectrum of BZT w/ 0.5% V*

4. References

[1]- F. Moura, A. Z. Simões, E. C. Aguiar, I. C. Nogueira, M. A. Zaghete, J. A. Varela, E. Longo, J. Alloys and Compounds, **479,** 280–283, (2009).
[2]- F. Moura, A. C. Cabral, L. S. R. Rocha, E. C. Aguiar, A. Z. Simões, E. Longo, Ceramics International, **42**, 4837-4844, (2016)
[3]- J. L. Jiménez-Pérez, J. Jiménez-Pérez, A. Bracamontes Cruz, A. Cruz-Orea, J. G. Mendoza-Alvarez, Int. J. Thermophys. **25**, 503–510 (2004)

Acknowledgments

Two of us, M. A. A. and A. Z. S., would like to thank FAPESP and CNPq for financial support.

*Corresponding author: algatti@feg.unesp.br or mauricio.algatti@gmail.com

ID 169: THE EFFECT OF VOLTAGE AND TIME ON THE FABRICATION OF TIO_2 NANOTUBE ON Ti-30Ta ALLOY BY ANODIC OXIDATION

Patricia Capellato[1]*, Gilbert Silva [2,] Ketul C. Popat [3,] and Ana P. R. Alves Claro[4]
[1,2]UNIFEI- Federal University of Itajubá, Av. BPS; 1303. Itajuba, Minas Gerais, Brazil,
[3]*School of Biomedical Engineering, Colorado State University, Fort Collins, USA,*
[4]*UNESP- Uni. Estadual Paulista, Faculty of Mechanical Engineering ,Guaratinguetá, São Paulo, Brazil*

1. Introduction

The ideal biomaterial specifically used for dental implants must exhibit biocompatibility, elastic modulus similar to natural bone, high strength, corrosion and wear resistance, high fatigue and ductility [1]. Current approaches for enhancing biomaterial osseointegration include topographical and biofunctional surface modifications [2]. Several studies have shown that by modifying the surface at a nanoscale or a microscale it can alter cellular response [3]. In this study, the self-ordered formation of nanotubular oxide layers on Ti–30Ta alloy was investigated.

2. Experimental

The Ti-30Ta alloy (Ti with 35wt% of Ta) was fabricated by mixing Titanium (grade 4) and Tantalum (99.9% purity). These metals were combined using a melting process in a high purity argon atmosphere. The resulting ingots were homogenized and then cold -worked by a rotary swaging process. The anodization process was performed using a electrolyte solution containing hydrofluoric acid (HF) + sulfuric acid (H_2SO_4) (1:9) + 5% dimethylsulfoxide (DMSO) on two different time and voltage. In the group A the samples was anodized at 12V for 20 min and group B applied 35V during 40 min. The nanotube layer was annealed in an oxygen ambient furnace at 530 ºC (5º C/min) for 3 hours to group A and B. All the surfaces were investigated using scanning electron microscopy (SEM), contact angle measurement and X-ray diffractometer (XRD).

3. Results and Discussions

The results indicated that the anodization process on Ti-30Ta alloy was highly influenced by time duration and voltage of the anodization process. SEM images confirm results of a parameter-driven surface topography. Ti-30Ta substrates anodized at 25 V for 20 min show a completely irregular surface layer covered with small cracking wells (see Figure 1 (a, b and c)). Figures 2 (a and b) shows Ti-30Ta substrates anodized with 35 V during 40 min with first signs of nanotube formation at lower and medium magnification. When the surface was analyzed in higher magnification clearly show irregular nanotube formation(see Figure 2 (c)). Figure 1 shows group A with the surface whitout nanotube and Figure 1B) we can see nanotube formation.

In order to obtain information on composition and structure of the different surface after anodization process, XRD was carried out using the samples before and after surface treatment. Figure 3 shows the XRD patterns , before (as-formed) and after annealing at 530 ◦C for 3h. Before annealing, all surface of the sample show an amorphous structure. After annealing all are transformed to crystalline phases. After annealing have been formed on all the surface of group A and B with anatase.

Figure 4 shows contact angle measurements on group A and B with hydrofilic interface which is preferable for eliciting a favorable environment for cellular interaction.The materials for biomedical application need to be more hydrophilic since they have higher surface energy which is desirable for biological interaction.

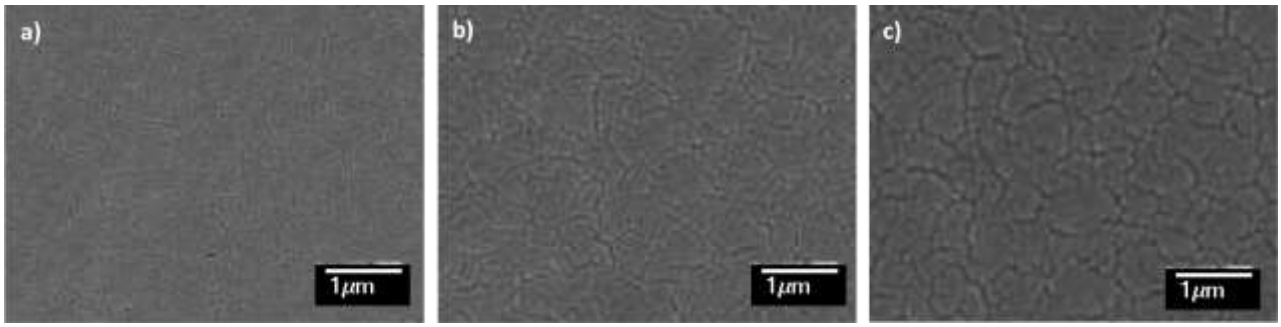

Fig. 1. *FE-SEM images of Ti-30Ta alloy surfaces after anodization in HF +H2SO4 (1:9) + 5% DMSO at 12V during 20 min (Group A). The anodized surface is shown in lower magnification (a), medium (b) and in higher magnification (c). All samples were annealed in an oxygen ambient furnace at 530 ºC for 3 hours.*

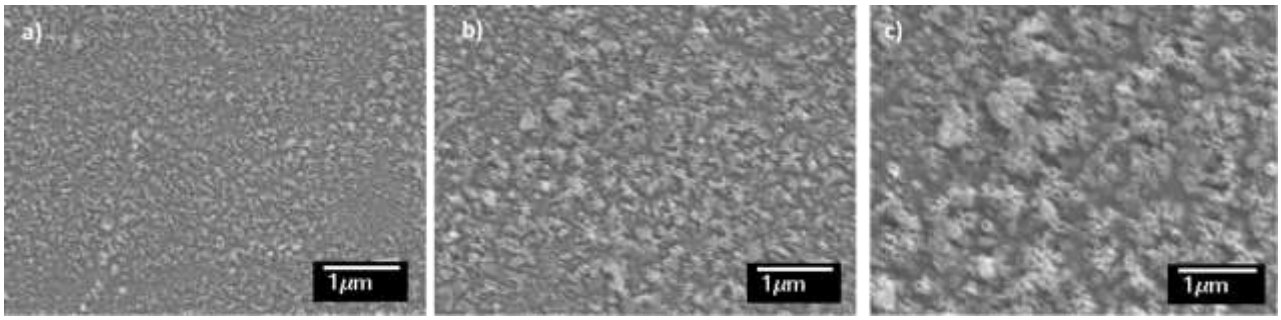

Fig. 2. *FE-SEM images of Ti-30Ta alloy surfaces after anodization in HF +H2SO4 (1:9) + 5% DMSO at 35V during 40 min (Group B). The anodized surface is shown in lower magnification (a), medium (b) and in higher magnification (c). All samples were annealed in an oxygen ambient furnace at 530 ºC for 3 hours.*

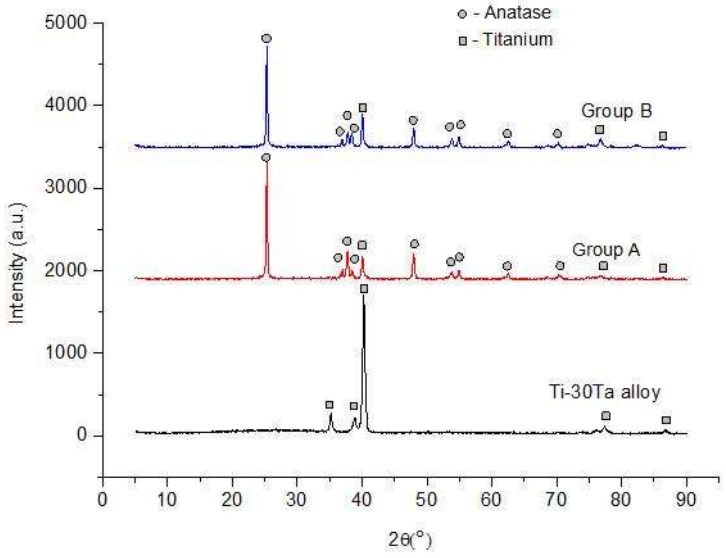

Fig. 3. *XRD spectra of the oxide nanotubes formed on Ti-30Ta alloy surfaces after anodization in HF +H2SO4 (1:9) + 5% DMSO at 12V during 20 min (Group A) and 35V during 40 min (Group B).*

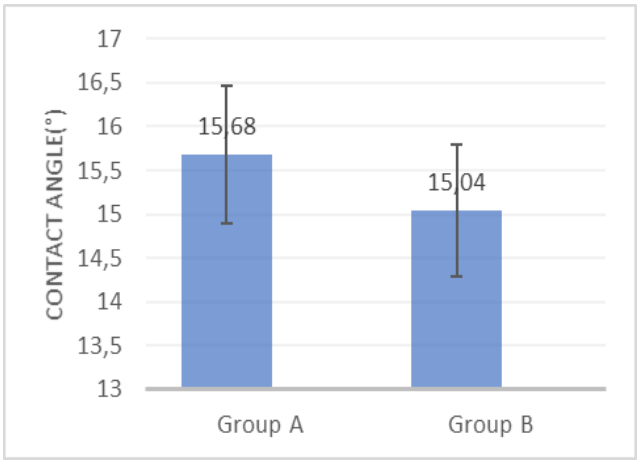

Fig. 4. *Contact angle measurements of the oxide nanotubes formed on Ti-30Ta alloy surfaces after anodization in HF +H2SO4 (1:9) + 5% DMSO at 12V during 20 min (Group A) and 35V during 40 min (Group B).*

References

[1] M. Geetha et al. Ti based biomaterials, the ultimate choice for orthopedic implants - A review. Progress in Materials Science, **54**, 397-425,(2009).

[2] P. Capellato et al. Interaction between mesenchymal stem cells and Ti-30Ta alloy after surface treatment. Journal of Biomedical Materials Research Part A, **102**, 2147-2156, (2014).

[3] P. Capellato et al. Fibroblast functionality on novel Ti30Ta nanotube array. Materials Science and Engineering: C , **32**, 2060- 2067,(2012).

Acknowledgments

Partial funding support for this work was provided by the Brazilian federal government, the National Council for Scientific and Technological Development (CNPq) and Fapesp.

*Corresponding author: pat_capellato@yahoo.com.br.

ID 170: GROWTH OF HYDROXYAPATITE COATINGS ON TANTALUM BY PLASMA ELECTROLYTIC OXIDATION

Rosana F. Antonio, Elidiane C. Rangel, Nilson C. Cruz*
Laboratory of Technological Plasmas, Unesp, Sorocaba, SP, Brazil

1. Introduction

Plasma electrolytic oxidation (PEO) is a technique that allows the production of ceramic surfaces with adjustable morphology and chemical composition. Owing to that, PEO is a very promising technique for the treatment of biomaterials. With such technique it is possible to produce porous surfaces containing calcium, phosphorous and other chemical species to stimulate cell adherence and proliferation.

2. Experimental

The treatments have been performed using water solution of disodium glycerophosphate and calcium acetate as electrolyte and it has been evaluated the influence of exposure time, which ranged from 60 to 600 s, on the chemical and structural characteristics of the coatings. Surface morphology, chemical and phase composition of oxide coatings were investigated by X-ray diffractometry (XRD), scanning electron microscopy (SEM), energy dispersive X-ray spectroscopy (EDS) and Fourier transform infrared spectroscopy (FTIR).

3. Results and Discussions

It has been observed that the characteristics of the surfaces are strongly influenced by the process parameters. For instance, as shown in figures 1 and 2, while treatments performed using 350 V resulted in a flat and porous surface, more complex structures have been formed when using 500 V. furthermore, varying the treatment time, it was possible to produce coatings predominantly composed by calcium and tantalum oxide or containing up to 84% of crystalline hydroxyapatite.

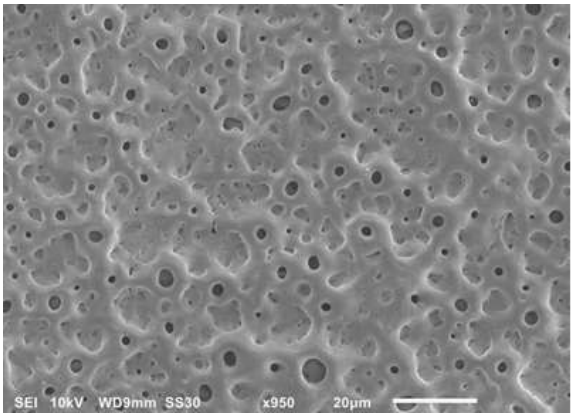

Fig. 1. *Scanning electron micrograph of a tantalum sample treated by PEO for 300 s at 350 V.*

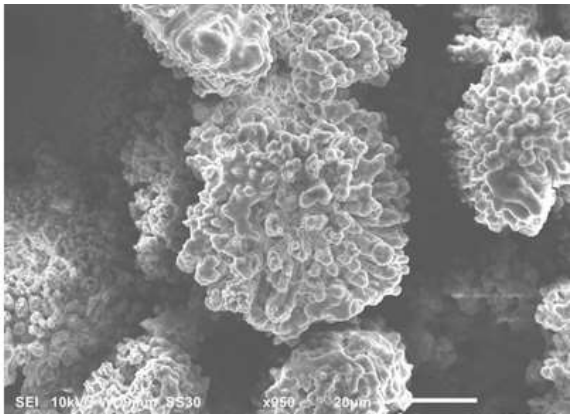

Fig. 2. *Scanning electron micrograph of a tantalum sample treated by PEO for 300 s at 500 V.*

Acknowledgments

The authors thank FAPESP and CNPq for financial support

*Corresponding author: place the email of the corresponding author here (bookman old style 9 pt)

ID 171: EFFECT OF THE TEMPERATURE ON CORROSION BEHAVIOR OF PLASMA-ANODIZED ALUMINIUM ALLOY

Pereira, G. A.*, Dinis, J. R. D. A, Silva, L.L.G., Santos, D. C. R
[1]*CEETEPS – Fatec Pindamonhangaba – College of Technology*

1. Introduction

Plasma electrolytic oxidation (PEO) is an electrochemical process that promotes the anodizing of valve metals by application of high voltage, which promotes the plasma breakdown [1]. Like conventional anodizing, the properties of PEO layers depend on chemical and electrical parameters, such as voltage, current, temperature, electrolyte, alloy composition, among others [1,2]. This work evaluated the effect of PEO temperature on corrosion resistance of plasma-anodized 5052 Al alloy.

2. Experimental

Electrolytic system is comprising a high-voltage DC power supply (20 kW) and a stainless-steel container (2000 ml) equipped with a mechanical stirrer and a cooling system. The container walls were used as cathode. Aqueous electrolytic solutions were prepared with 15 g/l sodium silicate (Na_2SiO_3) and 2 g/l sodium phosphate (Na_3PO_4). The anodizing treatments were performed in galvanostatic mode for 5 min at 10 A/dm^2 current density.

Corrosion tests were carried out in a conventional glass cell with three electrodes: Al samples (20 mm x 20 mm) as work-electrode, Pt wire as counter-electrode and Ag/AgCl (in KCl_{sat}) as reference-electrode. The corrosion electrolyte was NaCl solution (3.5 wt%).

3. Results and Discussions

In process A, the solution temperature increased from 25 to 40 °C and, in process B, the temperature increased from 20 to 30 °C, as can be seen in Fig.1. Fig. 2 shows the polarization curves obtained from corrosion tests. Process A led to higher corrosion potential and lower corrosion current density (E_{cor} = – 0.29 V; I_{cor} = 1.0 x 10^{-11} Adm^{-2}) compared to process B (E_{cor} = – 0.39 V; I_{cor} = 1.5 x 10^{-10} Adm^{-2}). Both processes improved the corrosion behavior of 5052 Al alloy (E_{cor} = – 0.79 V; I_{cor} = 3.5 x 10^{-8} Adm^{-2}). Temperature is responsible by diffusion of ions and contribute to electrochemical reactions which form the oxide layer. Besides, temperature elevation promotes the phase transformation of ceramic crystals and, consequently, improves the properties of the oxide layers [2]. Therefore, the results confirm that the process performed at highest temperature contributed to the best corrosion resistance of anodized 5052 Al alloy.

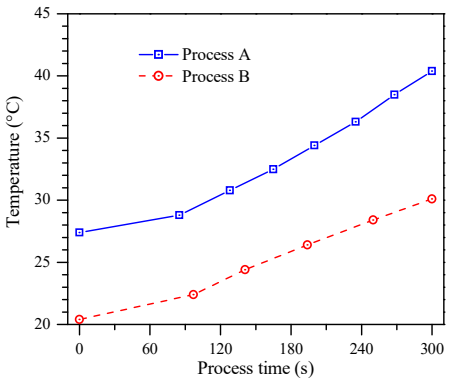

Fig. 1. *Solution temperature in function of plasma anodizing time.*

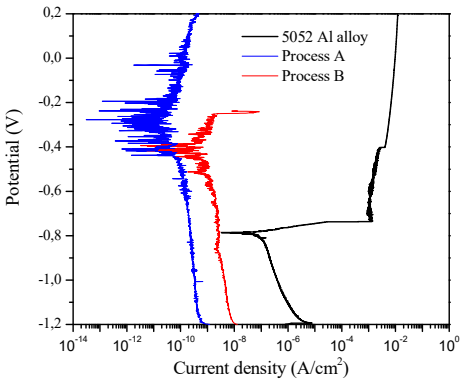

Fig. 2. *Potentiodynamic polarization curves of PA 5052 Al alloy in different temperatures.*

4. References

[1] A. Fattah-Alhosseini *et al.* **Acta Metall. Sin.** (Engl. Lett.), 2016, 29(3), 274–28.
[2] V. Dehnavi *et al.* **Surface & Coatings Technology 251** (2014) 106–114.

Acknowledgments

The authors thank to FAPESP for financial support.

*Corresponding author: gabriel.pereira30@fatec.sp.gov.br

ID 175: ANALYSIS OF GRANITE POWDER USING SEM

G. S. Damasceno[1], H. P. Gonçalves[1], A. D. Golanda[2], D. M. Carmo[1], A. R Bigansolli[1,*], B. B. Lima-Kühn[1]
[1]UFRRJ – Universidade Federal Rural do Rio de Janeiro.
Rodovia BR 465, Km 7, Seropédica, RJ, 23851-970, Brazil.
[2]EEL/USP – Escola de Engenharia de Lorena, Universidade de São Paulo.
Estrada Municipal do Campinho, s/n, Lorena, SP, 12600-000, Brazil.

1. Introduction

Brazil, besides having large reserves of ornamental stones is one of the main exporters of stones in the world. Linked to this production, it is observed the generation of a significant amount of waste from the cutting and processing of the rocks, which entails great environmental impacts. In this way, the great challenge of the ornamental stone sector is the rational use of this waste, making them an economically viable by-product for commercialization. The polymer industry, on the other hand, uses the incorporation of fillers to improve the thermo-mechanical properties, alter the surface appearance and, in particular, reduce the costs of the polymer composition. Thus, the knowledge of the characteristics of the load element and its influence on the polymer matrix is necessary [1]. The objective of the present work is to characterize the granite powder prepared by conventional milling that will used as reinforcing load on the thermo-mechanical properties of the epoxy resin.

2. Experimental

Granite sample was crushed to obtain a powder size less than 53 μm and characterized by backscattered electron (BSE) images. Sample micrographs were obtained in a Scanning Electron Microscopy (SEM) and the elements were identified through electron microanalysis using energy dispersive spectrometry (EDS). The microanalysis was then obtained using a Hitachi TM3000 model SEM, with an EDS Swift ED3000 system from Oxford Instruments.

3. Results and Discussions

Figures 1 and 2 show the BSE images for the granite powder, figure 2 presenting particles of different sizes, irregular and faceted morphology. Although the particles have very heterogeneous dimensions, the image shows that they are smaller than 100 μm. The results of EDS (O - 63.29 at%, Na – 1.53 at.%, Al – 6.00 at.%, Si – 26.00 at.%, K – 2.54 at.%, Ca – 0.68 at.%) show the high Si and O contents that indicates the presence of quartz in the analyzed granite.

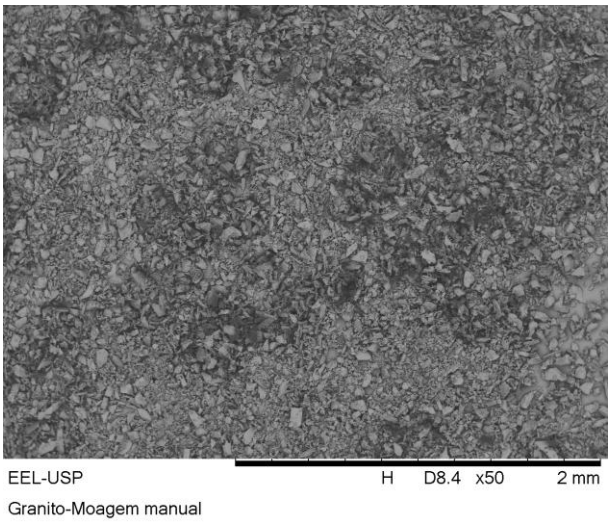

Fig. 1. *BSE images for the granite powder.*

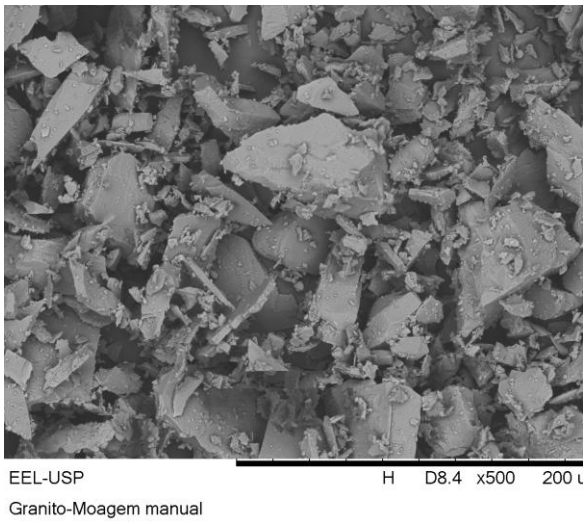

Fig. 2. *BSE images for the granite powder.*

4. References

[1] J. A. V. Gonçalves, D. T. Campos, G. J Oliveira, M. L. S. Rosa, M. A. Macedo, Materials Research, 17(4), 878-887, (2014).

Acknowledgments

The authors acknowledge Programa de Pós-Graduação de Engenharia de Materiais – PPGEM / EEL-USP and Universidade Federal Rural do Rio de Janeiro – UFRRJ.

*Corresponding author: bigansolli.arb@gmail.com

ID 176: INFLUENCE OF THE PROCESS AGENT ON THE HIGH ENERGY OF 7075T6 ALUMINUM ALLOY CHIPS.

Oliveira, L.A.; Mendonça, C.S.P; Capellato, P.; Dias. A,O. ; Corrêa, E.O.; Silva, G.
UNIFEI/IEM – Federal University of Itajubá. Avenue BPS, 1303, B. Pinheirinho,CEP 37500-903,

1. Introduction

Powder metallurgy is a promising route widely used to produce high strength to manufacture parts with complex shapes with less material and residues(SCHAFFER; SERCOMBE; LUMLEY, 2001).

The powder through collisions between the ball-powder-ball and ball-powder-jar systems causing severe plastic deformation, repeated fracturing and cold welding of the particles leading to a decrease in particles (SURYANARAYANA, 2001). One of the great problems of high energy grinding and cold welding where the particles of powders are joined together during the collisions, a way to avoid this phenomenon and the use of process controlling agents (SURYANARAYANA, 2001). The objective of this study to assess the effect of the agent in the milling process controller chip of aluminum 7075T6, performing a comparison of two control agents stearic acid and methanol.

2. Experimental

For the comparison of the ACPs, the parameters used in the survey were used; and other researchers, methanol with 3.2ml and stearic acid with 3% by weight of aluminum, using stainless steel balls of diameter 21mm and 12mm and jar of stainless steel under argon gas, with 10g of aluminum, with the time 10 hours , 250rpm, ratio 1:10 and without carbide. The choice of PCA to be used is related to the smaller particle size obtained. The raw material characterization involves the determination of size, particle distribution, and morphology of aluminium powder that was characterized by SEM,

3. Results and Discussions

The results of the comparison can be observed in table 1 where we can observe that the methanol process controller showed a better reduction in the part size of about 50%, in the D50 being also smaller in all the cumulative distributions: D10, D50, D95 Where this means that D10 means that 10% of the sample has particles of size smaller than this value, thus successively for D50 and D90.

Table 1 Result particle size.

	Size (µm)		
A.C.P	D10	D50	D95
Methanol	18,41	284	1795
Stearic Acid	374,6	1697	1955

The results of the comparison can be observed in table 1 where we can observe that the methanol process controller showed a better reduction in the part size of about 50%, in the D50 being also smaller in all the cumulative distributions: D10, D50, D95 Where this means that D10 means that 10% of the sample has particles of size smaller than this value, thus successively for D50 and D90.

The SEM analysis of figure 1 confirms the difference in the size of the powders when the methanol was used, we can also observe the irregular morphology of the powders of both conditions with the presence of agglomerations. Both conditions have particles larger than 100 microns and particles smaller than 5 microns.

According to research by RAMEZANI; Neitzert, (2012), methanol presents a better control of the process and, in its researches, the experiment that used methanol as controller of the process obtained the smallest particle size. Figure 1 Micrograph of the Figures of Position A as Methanol and Figure B with Stearic Acid.

Figure 1 Micrograph of the post A figures as Methanol and Figure B with Stearic Acid.

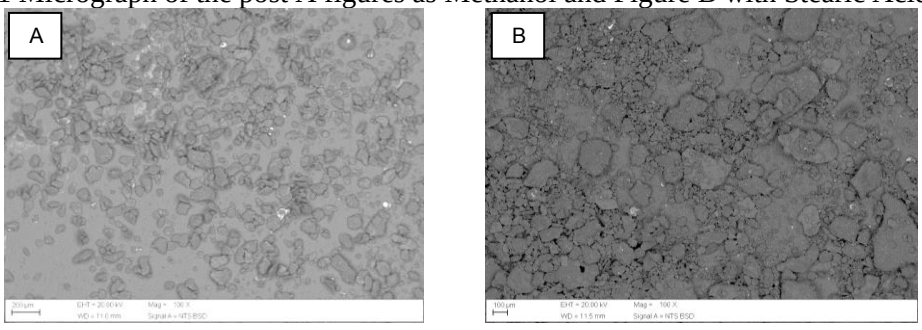

Leonardo A. Oliveira: Leonardoeng1@gmail.com

4. References

RAMEZANI, M.; NEITZERT, T. Mechanical milling of aluminum powder using planetary ball milling process. v. 55, n. 2, p. 790–798, 2012.

SCHAFFER, G. B.; SERCOMBE, T. B.; LUMLEY, R. N. Liquid phase sintering of aluminium alloys. v. 67, p. 85–91, 2001.

SURYANARAYANA, C. Mechanical alloying and milling. **Progress in Materials Science**, v. 46, n. 1–2, p. 1–184, 2001.

Acknowledgments

The author's acknowledgment support the CAPES and the financial support.

ID 177: OPTICAL AND CHEMICAL CHARACTERIZATION OF a-C:H:Si:O:Cl THIN FILMS OBTAINED BY PLASMA ENHACED CHEMICAL VAPOR DEPOSITION

Isabela Cristina Fernandes[1], Rafael Gustavo Turri[1], Milena Kowalczuk Manosso Amorim[1], Paulo Silas Oliveira[1], Fernando Mion Netto[1], Elidiane Cipriano Rangel[1], Steven Frederick Durrant[1]*

[1] Laboratório de Plasmas Tecnológicos, Instituto de Ciência e Tecnologia de Sorocaba, Universidade Estadual Paulista (UNESP), Avenida Três de Marco 511, Alto de Boa Vista, 18087-180, Sorocaba, SP, Brazil

1. Introduction

Plasma deposition of hydrogenated chlorinated amorphous carbon films in cold plasmas has received relatively little attention [1-3]. The interesting optical properties of these films need to be better understood and may have novel applications. Chlorinated films have been successfully produced using mixtures of acetylene, chloroform and argon, where Cl:C ratios close to one (1.0) were achieved [1]. Plasmas of propanol, chloroform and argon mixtures produced films with up to 8 at. % Cl [2]. Besides $CHCl_3$, C_4Cl_6 and $C_2H_2Cl_4$ have been used in atmospheric plasmas [3]. The use of HMDSO in PECVD is well established. Here, plasmas of HMDSO, O_2 e $CHCl_3$ were studied.

2. Experimental

For depositions, a cylindrical, steel reactor equipped with parallel-plate electrodes was used, with the upper electrode connected to a 13.56 MHz RF source. Thin films of the a-C:H:Si:O:Cl type were produced by PECVD, using HMDSO and O_2 at constant pressures of 42 mTorr and 8 mTorr, respectively, varying $CHCl_3$ pressure from 0 to 60 mTorr. All depositions were performed at 60 W. Film thicknesses were measured using profilometry. Contact angle measurements were made using the sessile drop method. Chemical characterizations of the films were carried out using IRS and EDS. Optical parameters (refractive index and optical gap) were obtained from Ultraviolet-visible Near Infrared spectral data.

3. Results and Discussions

The presence of chorine increased the wettability of the films. Deposition rates between 71 and 147 nm/min were obtained. For the pressures of HMDSO and oxygen used in this study, the presence of chloroform stabilized film structure. Transmission IR spectra of the films deposited at different percentages of $CHCl_3$ in the plasma feed are shown in Fig.1. Bands at around 780 cm^{-1} are attributed to $(Si-(CH_3)_2)$ groups, and those at around 1262 cm^{-1} and 1410 cm^{-1} are due to $SiCH_3$. The absorptions at 1120 and 1050 are due to Si-O-Si, while those centered at 2960 and 1716 cm^{-1}, are due, respectively, to C-H and C=O. Optical gaps of a few eV were observed.

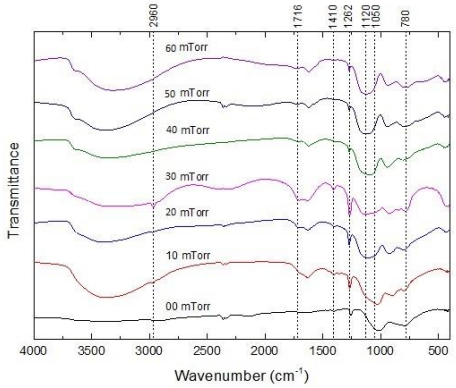

Fig. 1. *Infrared spectra of films deposited at different partial pressures of $CHCl_3$ in the plasma feed*

4. References

[1] Turri, R, Davanzo, CU, Schreiner, W, Dias da Silva, JH, Appolinario, MB e Durrant, SF, Thin Solid Films, 520, 1442, (2011).

[2] Rossi, D, Schreiner, WH, Durrant, SF, Surface & Coatings Technology, 289, 118, (2016).

[3] Hubert, J, Poleunis, C, Delacorte, A, Laha, P, Bossert, J, Lambeets, S, Okan, A, Bertrand, P, Terryn, H, Reniers, F, Polymer, 54, 4085, (2013).

Acknowledgments

We thank CNPq for concession of a Scientific Initiation grant (PIBIC) to Isabela Cristina Fernandes. We also thank FAPESP (2014/21594-9) and Capes for financial support.

*Corresponding author: steve@sorocaba.unesp.br

ID 179: HIGH VACUUM BRAZING AND MICROSTRUCTURAL ANALYSIS OF JUNCTION CuAG/Cu WITH SN100C ALLOY

Camili Ambrósio[1], Daniel Yukio Kakizaki[1,2], Felipe Silva[2], Marcelo M. Capovilla[2], Osmar Roberto Bagnato[1,2]*

[1]*Brazilian Synchrotron Light Laboratory, Brazilian Center for Research in Energy and Materials*

[2]*São Francisco University*

1. Introduction

The Brazilian Synchrotron Light Laboratory (LNLS) is in charge of designing and developing a new light source: Sirius, a circular electrons accelerator which has ultra-high vacuum chamber that delimits the transit region of the electrons and allow the beam remains stored in an unobstructed environment, as explained by CNPEM [1].

Sirius has operating characteristics which requires that the storage ring vacuum chambers will be manufactured with a copper and silver alloy. These chambers will dissipate the heat generated into them by water cooling channels. Intended to provide better heat transfer between the channels and chambers, the union of these components will be obtained from brazing in high vacuum environment, using SN100C alloy as the metal addition since it has low melting point (227ºC) when compared to the melting point of the chamber (1083ºC), which is made of copper and silver alloy.

2. Experimental

For the brazing was used a horizontal high vacuum furnace available at the laboratory of the Materials Group of LNLS-CNPEM as shown at Fig.1. All the materials were conducted to a specific cleaning process before assembly them for the brazing procedure.

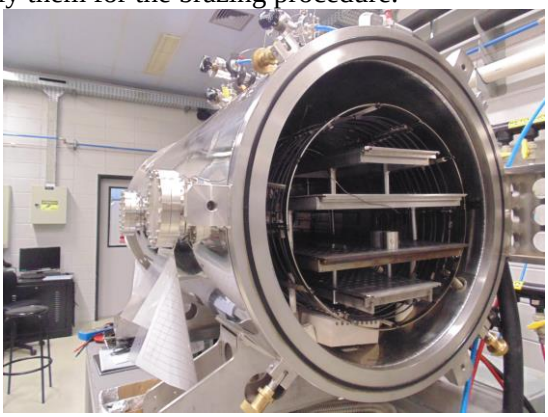

Fig. 1 *Horizontal high vacuum furnace of Material's Group at LNLS - CNPEM.*

The Fig.2 shows a special device that was used to gather the tubes and the metal alloy to guarantee the mechanical alignment before the sample being brazed inside the vacuum furnace. This procedure was made to achieve the best capillarity as possible and then reaching a quality brazing.

Fig. 2 *Detail of the assembly of the vacuum chamber, refrigeration tube and metal addition with the special device before brazing procedure.*

*Corresponding author: osmar.bagnato@lnls.br

Using the vacuum furnace with a pressure of 10^{-7} mbar, it started the process of ramping the temperature with three heat rate until reach 260ºC at the center of the sample. After this treatment, the furnace was cooled under nitrogen flux until the room temperature. All this process lasted about five hours.

The microstructure of the sample after brazed was analyzed by metallography and scanning electron microscopy (SEM). For metallography was used a Zeiss microscopy from the Materials group at LNLS while the SEM was performed with the experimental station of FEI Quanta at the electronic microscopy laboratory (LME) at Brazilian Nanotechnology National Laboratory (LNNano) at CNPEM using a 1500x magnification and, for EDS, X-Max detector with 10 keV of energy range.

3. Results and Discussions

After brazing, the samples were subjected to a first test: a visual inspection where were approved with satisfactory brazing due to the homogeneity observed in the brazed area along the length of the tubes. Then, a cross section of the brazed sample was analyzed by metallography, as shown at Fig. 3. A complementary study was at the microscope image of the brazed joint (Fig. 4) where it is possible to visualize at least two distinct phases (indicated as 1 and 2 at Fig. 4) in the region of the addition metal (region B), that are probably the intermetallic compound formation.

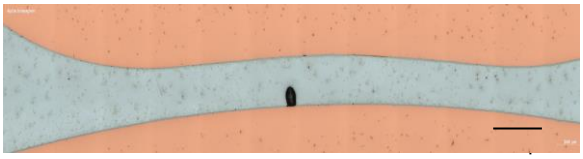

Fig. 3 *Metallographic cross section of brazed sample CuAg/Cu with SN100C alloy.*

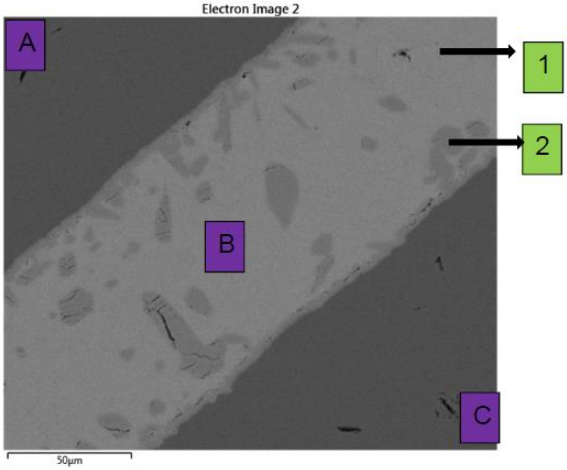

Fig. 4 *Microscopy image of the brazed joint. (A) Refrigeration tube (Cu), (B) Filler metal, (C) Vacuum Chamber (CuAg).*

In this contribution, we will detail the metallurgical results and it its implications to the vacuum performance of the system.

4. References

[1] Informations at http://lnls.cnpem.br/sirius Sirius: The New Brazilian Synchrotron Radiation Source, 05/05/2015.

[2] O. R. Bagnato, R. F. Francisco, A. L. Gobbi, T. Falvo, P. M. Pimentel. Defect and Diffusion Forum 367, 86-95 (2016).

Acknowledgments

We acknowledge the CNPEM/LNLS for allocating resources from the SIRIUS project for this development. The CNPEM is funded by the MCTIC.

*Corresponding author: osmar.bagnato@lnls.br

ID180: Development and Qualification Tests of Permanent Magnet Hall Thrusters for Future Brazilian Space Missions

Jose Leonardo Ferreira[1], Alexandre Alves Martins[1], Rodrigo Andres Miranda Cerda[1,2], Helbert de Oliveira Coelho Junior and Alvaro Queiroz dos Reis Silva,
[1]*Plasma Physics Laboratory of University of Brasilia(UnB),70910-900, Brasilia-DF, Brazil.*
[2]*Aerospace Department, Faculty of Technology of UnB, Gama-DF, Brazil.*

1. INTRODUCTION

The Plasma Physics Laboratory(PPL) of UnB has been developing a Permanent Magnet Hall Thruster (PHALL) for the UNIESPAÇO program, part of the Space Activities Program conducted by the Brazilian Space Agency (AEB) since 2004. Electric propulsion is now a very successful method for spacecraft propulsion systems that required high specific impulse. It is essential for several existing geostationary satellite station keeping systems and for deep space long duration solar system missions, where the thrust system can be designed to be used on orbit transfer maneuvering and/or for satellite attitude control in long term space missions. Applications of compact versions of Permanent Magnet Hall Thrusters on future Brazilian space missions are needed and foreseen for the coming years beginning with the use of small Divergent Cusp Field Hall (DCFH) Thrusters on CUBESATS (5-10 kg, 1-5 W power consumption) and on Microsatellites (50-100 kg, 10-100W). Brazilian (AEB) and German (DLR) space agencies and research institutions are developing a new rocket dedicated to small satellite launching known as the VLM - Microsatellite Launch Vehicle. The development of more compact versions of PHALL can also be very important for the recently proposed SBG system for a future Brazilian geostationary satellite that is presently being developed by international consortium of Brazilian and foreign space industries.

2. EXPERIMENT:

This work shows the study, development and qualification test planning of Permanent Magnets Hall Thrusters (PHALL IIa and PHALL IIb). Emphasis is given on the development and planning of compact electrical propulsion engines like Ambipolar Thrusters and DCFH PHALL III version. A new large vaccum chamber (Diam=1,5m , L= 3,0 m) is now being assembly at PPL, It was designed to perform life time and space qualification tests for Plasma Thrusters operating in the 20mN to 100 mN range. In order to perform these tests a new vacuum pumping system with higher capabilities is been developed. It contains a mechanical dry pump, a mechanical roots booster pump with 250 m^3/h velocity and turbo molecular pumping system within four pumps within 13.000 l/s as total and maximum pumping velocity. Several plasma diagnostics and PHALL parameters measuring systems are been developed at PPL. An interferometric laser beam system for ion velocity and specific impulse measurement and a thrust balance system for direct thrust measurements are been planned for the near future.

3. RESULTS:

We will show design and computer simulations results of PHALL IIa and IIb and a Compact Hall Thruster,.PHALL III, which is being designed with divergent cusped magnetic field principles for possible use on future Nanosatellites and Microsatellites space missions. We will also show possible applications of Permanent Magnet Hall Thrusters on geostationary satellites, planned to be applied on orbit and attitude control systems and on deep space missions spacecrafts used for low thrust trajectory mission maneuvering in the solar system.

A particular new permanent magnetic field design for PHALL III is going to be shown together with new computer simulations results using a particle-in-cell methodology, that predicts thrust performance characteristics and erosion lifetime. We will describe the expectations foreseen for these types of Hall thrusters, which were also used in the design process of this newly proposed cusped magnet field Hall Thruster. Based on our first calculated results we believe PHALL III will allow improvement of spacecraft performance on long duration space missions. We also foreseen applications of PHALL III on small size spacecraft's with limited or low electric power source consumption.

.

References:

Ferreira J. L.; Martins A. A.; Cerda R. M.; Schelin A. B.; Alves L.S.; Costa E.G.; Coelho H.O.; Serra A.C.B.and Nathan F. in **"Permanent magnet Hall thruster development for future Brazilian space missions,"***Computational and Applied Mathematics*, Springer SBMAC,December 2015.

ID 184: A FULLY AUTOMATED BAKEOUT SYSTEM FOR THE NEW SIRIUS SYNCHROTRON

Gustavo Vicentin[1], Adalberto Ferreira Melo Fontoura[1], Fernando H. Cardoso[1], Horácio Ribeiro de Moraes, Laís Pessine do Carmo[1], Julio Criginski Cezar[1]*

[1]*Laboratório Nacional de Luz Síncrotron (LNLS), Centro Nacional de Pesquisa em Energia e Materiais (CNPEM), CEP 13083-970, Campinas, São Paulo, Brasil*

1. Introduction

The bakeout procedure in ultra high vacuum (UHV) systems consists in heating the chamber ideally well above room temperature to speed up the desorption of gases that ultimately would limit the final pressure in the vessel. One can say that it is almost impossible to attain real UHV conditions without such bakeout procedure. There is several approaches to heat a vacuum chamber during the bakeout. In most of the cases one uses heating tapes to deliver the heat and thermal sensors to control the final temperature. There exist several commercial solutions that can use a closed control loop in order to maintain the temperature during the bakeout. Here we introduce a prototype of the solution to be adopted at the new synchrotron SIRIUS from LNLS. In this case we have a PLC (Programmable Logic Controller) based system, capable of controlling 4 loops of bakeout, and monitoring another 4 temperature sensors. The system is remotely controlled via Ethernet.

2. Experimental

Figure 1 shows the design of the system. It is mounted on a standard 19 inch electronics rack. It's interior is shared by the two main parts of the electronics: i) the low power, PLC based controller and associated circuitry; ii) the high power, based on solid state relays that effectively delivers power to the heating elements.

The system is based on a Siemens 1510SP-1 PN CLP [1] which has most of the logic to interface with the user and extra boards needed to read the temperature and actuate on power controllers. In total the system can control up to 4 independent power channels, each one fed by a solid state relay able to deliver up to 1500 W under 220V operation. All PID (Proportional-Integral-Derivative) control is done by the PLC, with different values of PID constants for each channel. The temperature reading can programmatically select between K type thermocouples (TC) or PT100 resistive sensors. Besides the 4 control channels, each with its TC or PT100 reading, there is another 4 temperature inputs for monitoring.

The system as built has no user interface other than an ON/OFF, reset and emergency switches. All the control is meant to be done via Ethernet communication between the PLC and a central control system. As this is the prototype of a system to be adopted at the new synchrotron machine SIRIUS, the bakeout controller is integrated in EPICS (Experimental Physics and Industrial Control System), the software framework used to control all machine and beam line hardware at the LNLS [2]. This allows to full flexibility in terms of operation of the bakeout controller. For example, a user graphical interface has been developed to interact with the controller, allowing to load different PID`s for different UHV systems, temperature ramp and bakeout time control. This same interface can be trigged by any of the four extra temperature monitors to stop the bakeout in case of over-heating. This is particularly important for intricated UHV chambers with large temperature lag among sections due to the thermal inertia. In any case, it is the PLC controller who is effectively in charge of bakeout process, and even if it loses the communication with the host computer, it can be set to keep the procedure until the communication is reestablished or switch off the bakeout altogheter until an external intervention takes place.

The bakeout controller is fitted with a second Ethernet port that can be used to connect it to a Human-Machine Interface (HMI) which is basically a touchscreen system. In this case, the bakeout controller can be operated in a fully stand alone mode.

For beam line operation, the remote computer operation is advantageous for the following reasons:

a) One has full versatility on the program of temperatures, ramps and bakeout duration;
b) It is possible to log the temperature for almost any amount of time and correlate with the UHV chamber pressure. This can give a benchmark of the vacuum behavior of the chamber, which can be used as diagnostics of the vacuum system;
c) The system can be operated remotely;
d) More complex procedures can be automated like flashing ion pumps or degassing filaments in the system.

*Corresponding author: julio.cezar@lnls.br

Fig. 1. *Front view of one of the two prototypes of the bakeout controllers mounted at the LNLS/CNPEM. Behind the plexiglass front one can see the rails with the CLP modules at the bottom, and the power part, with breakers and solid state relays at the top. On the front one can see the ON/OFF and reset switches, besides the Ethernet port (lower left).*

Fig. 2. *Distribution box or patch panel, permanently located close to the system to be baked out. The tapes and temperature sensors are connected to the bakeout controller using specific made cables.*

When mounted on smaller, wheeled racks, the bake out controller is quite portable and intended to be used at several places at the LNLS experimental hall. For the sake of safety, it is connected to the UHV system via cables that run from sockets located at the rear of its rack, to sockets found at distribution boxes (patch panels) located at each UHV chamber or beam line section. These boxes are then duly wired to the heating tapes and temperature sensors, which are permanently fixed at the UHV system (see figure 2).

3. Results and Discussions

We have assembled two prototype systems. Bench tests using the Siemens proprietary software to communicate with the controller showed that it performs as expected for the basic operations, like temperature reading and switching on and off the solid state relays. At present we are finishing the user interface to the controller and performing the first bakeout tests on UHV systems.
In this contribution we will detail the operation of the system, its capabilities and limitations, and discuss the impressions of its first months of operation.

4. References

[1] https://mall.industry.siemens.com/mall/en/WW/Catalog/Products/10239950 (checked on May,30,2017)
[2] http://www.aps.anl.gov/epics/ (checked on May,30,2017)

Acknowledgments

We acknowledge the CNPEM/LNLS for allocating resources for this development as part of the SIRIUS project. The CNPEM is funded by the MCTIC.

*Corresponding author: julio.cezar@lnls.br